NROCK2023

Nordic Rock Meeting

The IV Nordic Symposium on Rock Mechanics and Rock Engineering

Reykjavik Iceland
24 - 26 May 2023

PROCEEDINGS

ISRM Specialized Conference

The IV Nordic Symposium on Rock Mechanics and Rock Engineering

May 24-26, 2023
Reykjavik, Iceland

Editors

Haraldur Sigursteinsson
Atli Karl Ingimarsson

Organizers

The Icelandic Geotechnical Society, ISRM National Group
The Icelandic Tunneling Society

National Organizing Committee

Atli Karl Ingimarsson, Chair
Aldís Ingimarsdóttir
Haraldur Sigursteinsson
Jóhann Örn Friðsteinsson
Jón Smári Úlfarsson,
Matthías Loftsson
Oddur Sigurðsson
Stefán Geir Árnason

Nordic Advisory Committee

Søren Degn Eskesen, Denmark
Lauri Uotinen, Finland
Roger Olsson, Norway
Fredrik Johansson, Sweden

The Symposiums website: http://www.nrock2023.com

The documents are indexed with following numbers:
ISBN 978-9935-9436-2-0
DOI 10.33112/nrock2023

and each reviewed paper with individual DOI
DOI 10.33112/nrock2023.X

PREFACE

The Icelandic Geotechnical Society and The Icelandic Tunnelling Society are pleased to welcome you to the 4th Nordic Symposium on Rock Mechanics and Rock Engineering, the Nordic Rock Meeting (NROCK 2023), in Reykjavik, Iceland 24 - 26 of May 2023. The theme of the symposium covers all aspects of rock mechanics and rock engineering, e.g. utilization of underground space, tunnelling, foundation, mining, infrastructure, stability and geo hazards.

The first Nordic Rock Mechanics Symposium was held 2010 in Kongsberg in Norway, the second in Gothenburg in Sweden 2013 and the third in Helsinki in Finland 2017. The fourth symposium was originally planned in Reykjavík in 2021, but due to the Covid-19 pandemic it was postponed until now. The NROCK 2023 symposium is supported by ISRM (International Society for Rock Mechanics and Rock Engineering) and has a status as an ISRM-sponsored Specialized Conference.

We hope that the symposium exceeds your expectations, with interesting papers, presentations, and field excursions. The aim of the symposium is to strengthen the relationship between practicing experts in the Nordic region and the symposium is an opportunity of learning and sharing experience and knowledge with fellow colleagues about various challenges within the field of rock mechanics and rock engineering.

The participants are engineers, researchers, and scientists from the Nordic countries as well as other countries in the world. We have four keynote presentations, from Canada, Norway, and Iceland, and 22 technical oral presentations from 9 countries. All submitted papers are included in this publication. On the behalf of the Organizing Committee, I would like to use this opportunity to gratefully thank the speakers, authors, reviewers, Session Chairs, the Nordic Advisory Committee, Secretariat and last, but not the least, all the participants, for making these proceedings and symposium come to life.

We hope you have a pleasant stay in Iceland and look forward to seeing you again in the next host country of the Nordic Rock Mechanics Symposium!

Reykjavík, May 2023

Atli Karl Ingimarsson

Chair of the Organizing Committee

TABLE OF CONTENTS

Proceedings of the NROCK 2023
The IV Nordic Symposium on
Rock Mechanics and Rock Engineering
ISBN 978-9935-9436-2-0
DOI 10.33112/nrock2023.1

Ground Support for Extreme Conditions

John Hadjigeorgiou
University of Toronto, Toronto, Canada
John.Hadjigeorgiou@utoronto.ca

ABSTRACT

Ground support is routinely employed to maintain the structural integrity of excavations in rock. In extreme conditions, such as observed in seismically active mines, and in excavations in squeezing rock, this can be challenging. In seismic conditions, ground support is required to prevent excessive levels of rock mass dilation, sustain confinement around the reinforcement and absorb kinetic energy released through the process of brittle rock mass failure and ejection. This is only possible if the ground support works as an integrated system to maintain the load distribution between all elements. In extreme squeezing ground the role of support is to maintain access for the working life of the excavations. Recent years have seen the development of yielding or energy absorbing reinforcement and surface support elements that can perform better than conventional support in extreme conditions. An improved understanding of the loading mechanisms, and better data on the capacity of ground support, complemented by field observations, have resulted in improved ground support practice for extreme conditions. The long-term performance of ground support can be hindered when exposed to corrosive environments. In extreme corrosive environments ground support is susceptible to degradation that may severely reduce its capacity to meet its performance goals for the intended service life of the excavations. This requires protective processes to prolong the effectiveness of ground support, or to plan for rehabilitation when a reduction in capacity is deemed critical. This paper reviews recent developments in ground support strategies for extreme conditions, including mine seismicity, squeezing environment and corrosive environments. In this context, the role and timing of rehabilitation of ground support can have significant safety and economic implications.

KEYWORDS

Ground support; mine seismicity; squeezing ground; corrosive environments; rehabilitation strategies;

INTRODUCTION

Ground support is integral in maintaining the structural integrity of excavations in rock for their projected working life. Reinforcement is the process where rock bolts and cable bolts are applied internally to the rock mass, while surface support is a technique in which elements such as shotcrete, steel mesh, straps, are applied to excavation surfaces externally to the rock, Hadjigeorgiou and Potvin (2011). A successful ground support system employs both reinforcement and surface support elements that work as a system to maintain the stability of an excavation under the anticipated load and ground conditions.

Excavations developed at shallow to moderate depth, in relatively competent rock masses, are often characterised by relatively low stress and low convergence. These are often described as “normal conditions” and can be adequately supported by conventional reinforcement and surface ground support. Conventional rockbolts include mechanical bolts, (i.e., expansion shell bolts), fully grouted rebars and frictional bolts (e.g., friction rock stabilisers and expandable rockbolts). Li et al (2014) provided a useful performance comparison between conventional and energy absorbing, or yielding rockbolts, while Hadjigeorgiou and Potvin (2011) reviewed the range of surface support elements.

There are several ways to describe “extreme conditions” in underground hard rock excavations. For the purposes of ground support, extreme conditions are those where the potential failure mechanisms are such that maintaining the integrity of an excavation is challenging. Such conditions include seismically active and rockburst prone ground as well as excavations displaying very large deformations (squeezing rock). Highly corrosive environments that may result in degradation and loss of capacity of ground support, are also considered as extreme conditions.

A more nuanced definition of extreme conditions is one that may have severe safety and economic consequences for the operation. This paper focuses on issues associated with the use of ground support under extreme ground conditions in underground hard rock mines.

1. NORMAL GROUND CONDITIONS

A conventional definition of extreme is any condition that is situated at the farthest possible point from a center of a set of ground conditions. Excavations developed at shallow to moderate depth are often characterised by low stress and low convergence and can be adequately supported by conventional ground support systems. Empirical rock mass classification systems have been successfully employed in these conditions. The Q system by Barton et al (1974) uses six constitutive parameters and captures a large range of ground conditions. It has been successfully employed worldwide for a variety of characterization and design purposes in rock engineering, Barton (2002). The original ground support recommendations, Barton et al (1974), were based on ground support technology available to prior to 1973 that included plain shotcrete, steel-mesh reinforced shotcrete, or cast concrete arches along with conventional rock bolts. The updated ground support recommendations using the Q system, Grimstad and Barton (1993), use fibre reinforced shotcrete which is routinely used in tunneling applications. Although the Q system provides design recommendations for conditions that range from exceptionally poor to exceptionally good, it has been argued by Palmstrom and Broch (2006), its applicability is more limited, Figure 1a. They suggest that it should be used for normal hard rock ground conditions from “very poor” to “good”, i.e., 0.1 < Q < 40, and tunnels or caverns of 3 to – 30 m span or height.

Potvin and Hadjigeorgiou (2016) highlighted that the vast majority of constitutive case studies of the Q system, Grimstad and Barton (1993) were based in tunneling, with a limited number from mining. This is significant, given variations in the choice of ground support between tunneling and mining drives, as well inconsistencies by mining operators in assigning an ESR value. At the same time the Q system is used widely to characterise the rock mass in mining applications. Consequently, Potvin and Hadjigeorgiou reconciled rock mass quality data based on the Q system, with the ground support used for mining drives (4 to 6 m span). Based on an analysis from mines in Australia and Canada, Potvin and Hadjigeorgiou (2016) provided preliminary ground support recommendations for a range of Q values (0.01 to 100), Figure 1b. It was recognised that the developed ground support recommendations were not applicable for extreme conditions such as seismically active and squeezing ground conditions. These extreme conditions would require different ground support strategies.

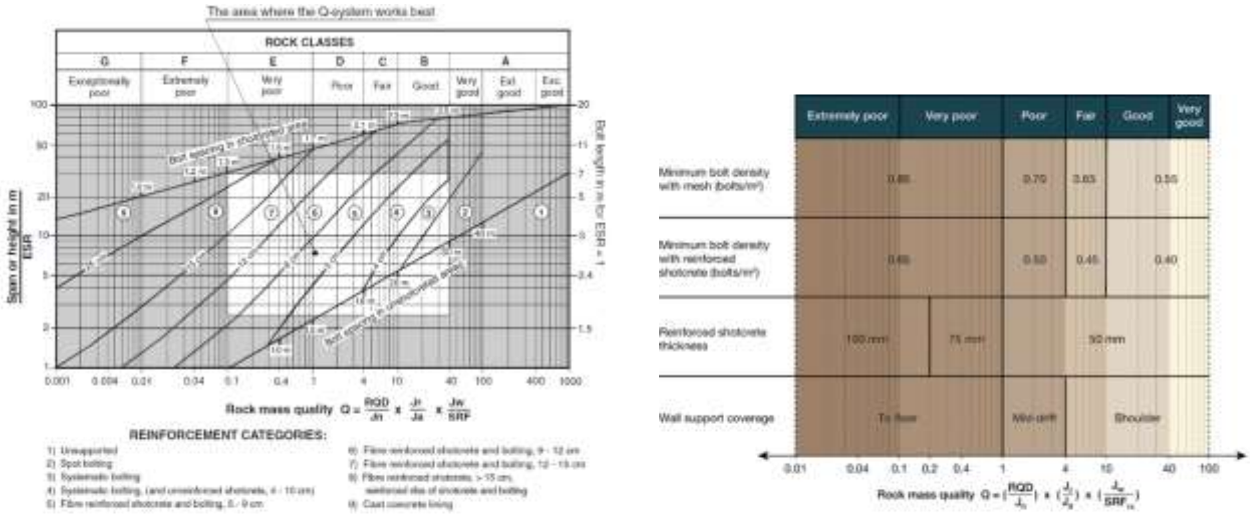

Figure 1. a) Applicability of Q system: a) tunneling, Palmstrom and Broch (2006); b) mining drives, Potvin and Hadjigeorgiou (2016).

Low stress and structurally defined ground are also defined as normal ground conditions. Rigid wedge gravity falls of ground can be routinely analysed using limit equilibrium tools such as UnWedge, Rocscience (2023) or a combination of DFN and limit equilibrium tools, Hadjigeorgiou and Grenon (2017), Figure 2. Both options can assess the impact of ground support to stabilize potentially unstable excavations. As in all design methods, provided the data quality is acceptable and their inherent limitations understood, they are useful. Conventional ground support systems are usually adequate to meet the desired support requirements.

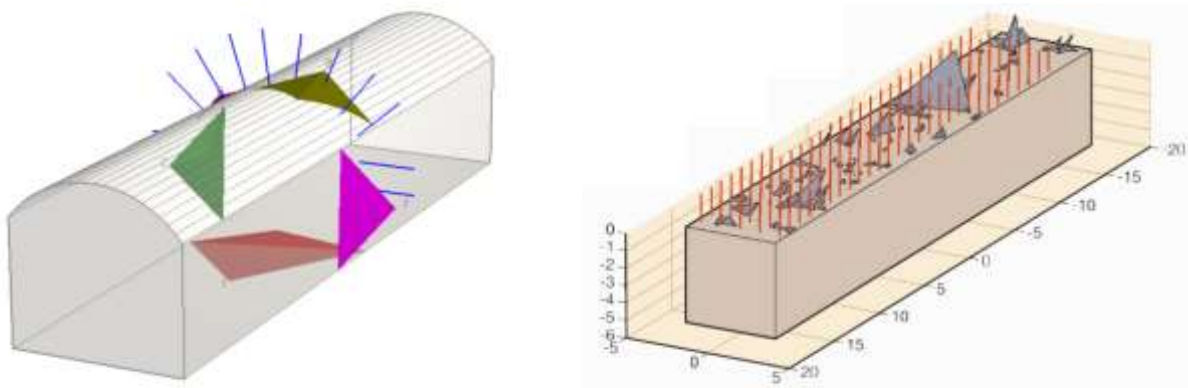

Figure 2. Limit Equilibrium Analysis including reinforcement: a) UnWedge, Rocscience (2023); b) DFN generated rock mass, Hadjigeorgiou and Grenon (2019).

Although high stress conditions can result in stress fracturing of the rock mass, Figure 3a, these are not always considered extreme conditions. The reason for this interpretation is that stress fracturing can be reasonably anticipated using stress modelling, and consequently supported by ensuring the length of reinforcement exceeds the fractured/broken ground zone, Wiles et al (1994). The basic assumption is that the broken/cracked ground has undergone stress driven failure and represents the dead weight that needs to be reinforced, Figure 3b. The use of borehole cameras to determine the extent of fracturing can provide a good indicator of the extent of the fractured zone as well "groundtruth" the results of the numerical models.

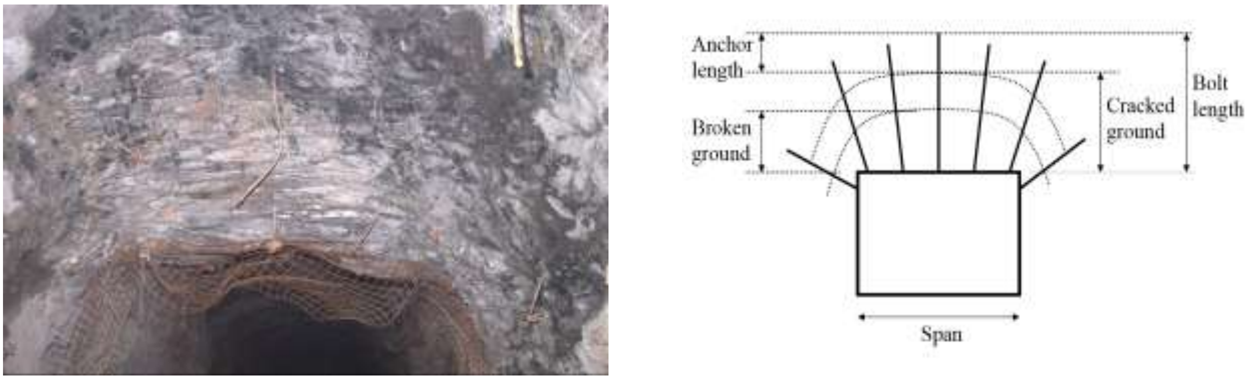

Figure 3.a) Stress fracturing at the back of an excavation, Simser (2023) b) Implicit reinforcement design using numerical modelling tools, Wiles et al (1994).

Several stress analysis tools allow for the explicit representation of ground support and can be used to compare different alternatives or the adequacy of a specific strategy, Sweby et al (2020). The choice of a numerical tool should be driven by the objectives of the analysis and definition of the problem. However, depending on the model requirements (elastic vs elasto-plastic; 2D vs 3D; continuum or discontinuum) the data and calibration requirements can be quite demanding. In several cases, a relatively simpler numerical model, capturing the salient problem requirements, may be adequate for most design purposes in normal ground conditions.

Although all analytical, empirical, and numerical modelling approaches have inherent limitations, there are multiple tools available that can be used with success in normal ground conditions. The recommended conventional ground support can usually be installed without major QA/QC issues and is typically able to maintain the stability of an excavation for its intended working life.

2. EXTREME CONDITIONS: MINE SEISMICITY AND ROCKBURSTS

2.1. Mine Seismicity and Rockbursts

In a rock engineering context, a seismic event may occur because of a movement, or creation of a new fracture within a rock mass. A useful classification of seismic events for underground excavations has been proposed by Ortlepp and Stacey (1994). Table 1. Any of these seismic events can potentially result in damage to the ground support.

Table 1.Classification of seismic event sources with respect to tunnels.

Seismic Event	Postulated Source	First motion from Seismic Records	Guideline Richter Magnitude ML
Strainbursting	Superficial spalling with violent ejection of fragments	Usually undetected; could be implosive	-0.2 to 0
Buckling	Outward expulsion of pre-existing larger slabs parallel to opening	Implosive	0 to 1.5
Face crush	Violent expulsion of rock from tunnel face	Implosive	1.0 to 2.5
Shear rupture	Violent propagation of shear fracture through intact rock mass	Double-couple shear	2.0 to 3.5
Fault-slip	Violent renewed movement on existing fault	Double-couple shear	2.5 to 5.0

A rockburst is a seismic event resulting in significant damage to a tunnel or an excavation of a mine. Although several seismic event mechanisms can cause damage, it is convenient to distinguish between strainbursts, in which the source of the seismicity and the location of the damage are coincident, and events in which the source of the seismicity and the location of the rockburst damage may be separated by substantial distances, Stacey (2016).

There are valuable lessons to be gained by reviewing the performance of ground support under seismic loads. Examples of damage following a strainburst are illustrated in Figure 4. In the first case, the ground support failed, while in the second case the installed ground support successfully contained the fractured material. The challenge from a practical perspective is to establish the remaining capacity of the ground support in the latter case, Figure 4b. This is extremely difficult to quantify but is important in deciding whether it is necessary to trigger rehabilitation of the installed ground support in the affected area.

Figure 4. Strainburst a) ground support failed; b) the support retained the ground, Simser (2023).

A characteristic of very large seismic events is that damage can occur at multiple levels. Boskovic (2022) reports on the extent of damage following the May 18, 2020, M_w 4.2 ± 0.2 seismic event at the LKAB Kiirunavaara mine. The aftershock activity that followed was widespread over a 1,000 m away from the hypocentre of the main event. The May 18, 2020, event damaged several kilometres of drifts on six mining levels and had an impact on several production areas at different levels. Figure 5 illustrates different degrees of damage following the seismic event.

Figure 5. Examples of severity of damage: (a) Heavily damaged area; (b) Area of major damage; (c) Area with the localized damage, Boskovic (2022).

Counter (2014) provides examples of significant damage to multiple levels following a M_N 3.8 seismic event in January 2009 at the Kidd Mine. Damage was significant in intersections which were not heavily reinforced at the time of capital development, Figure 6. An extensive rehabilitation program took approximately 18 months to complete, and upon resumption of mining, another M_N 3.8 event occurred on 13 September 2011, in almost the same location as the event of 2009, on the same poorly developed incipient structure. Damage during the second event was significantly reduced as compared to the first large event, as the density and type of support were modified during the 2009-2010 repairs to better withstand future events of similar magnitude, Figure 7.

Figure 6. Damage following the January 2009 M_N 3.8, Counter (2014).

Figure 7. a) Rehabilitation following the 2009 event; b) Damage following the 2011 event, Counter (2014).

The practical question that a mining operation has to address following a significant seismic event is whether the installed system has sufficient residual capacity. This is not a trivial problem although the use of LiDAR monitoring has shown potential, Jones and Hancock (2020). Counter (2019) provides site specific examples of areas beyond a certain threshold of deformation where the ground support is susceptible to increased risk of failure associated with subsequent seismicity.

An interpretation of the consumption of capacity following an impact load under controlled conditions has been provided by Hadjigeorgiou (2016). Figure 8 is a conceptual representation based on a series of impact loads on a high quality grouted threaded rebar. The first impact load resulted in a split of the tube, but the bolt did not fail. The bolt was subjected to a second impact load and this time failed. This however demonstrates the degradation-failure process in a reinforcement element, under axial loading in a controlled laboratory environment. It is difficult to demonstrate the same phenomenon in the field, where ground support is subjected to more complex loading mechanisms. In seismic mines, failure of the ground support system, is more likely to occur under its weakest link Simser (2007).

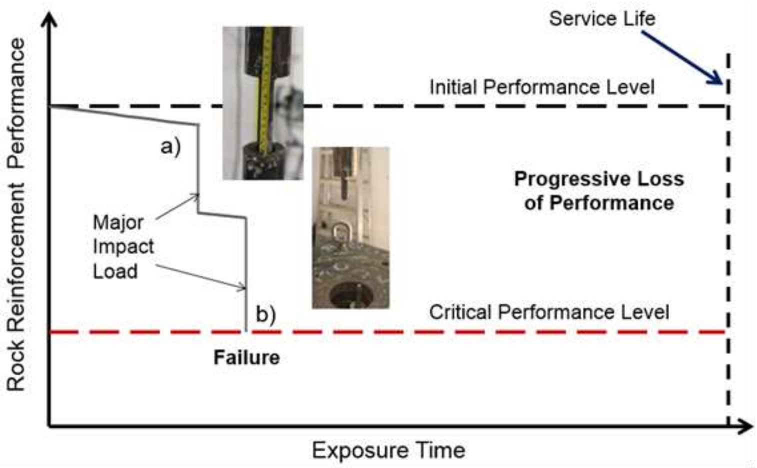

Figure 8. Degradation following an impact load (a) and failure following a subsequent impact load (b), Hadjigeorgiou (2016).

It should be reiterated that ground support is only one of the mitigation strategies in the management of seismicity. Other measures include changes in the mining sequence, destressing the rock mass and the implementation of exclusion protocols where the objective is to reduce the exposure of personnel.

2.2. Design Considerations

The design of ground support in seismic mines does not replace the requirements for maintaining the structural integrity of excavations between seismic events. The traditional design approach has been to extend the factor of safety concept used for static load to dynamic problems. It has been suggested to investigate the resulting factor of safety as a function of displacement capacity and demand, as well as energy capacity and demand, e.g., Kaiser et al (1996), Kaiser and Cai (2012). Other approaches for seismically active mines include the rockburst damage potential approach, Heal (2010), and the Western Australian School of Mines, Villaescusa et al (2013, 2014). Site specific approaches have also been developed by Mikula and Gebremedhin (2017) based on empirical charting, and by Morissette and Hadjigeorgiou (2019) using passive monitoring. All these approaches have merit and can provide useful insights, but they have inherent limitations, Potvin and Hadjigeorgiou (2020).

The performance of ground support, under seismic loads, has been difficult to predict reliably. This is illustrated by case studies where localised failure of the ground support can be observed following a seismic event, while adjacent areas remaining intact, Figure 9. There can be several reasons for these discrepancies, ranging from QA/QC, poor understanding of the seismic loads, inadequate load distribution between surface and reinforcement, yielding vs not yielding ground support, etc. Stacey (2012) concluded that since the dynamic capacity of ground support systems and the demand from seismically induced dynamic loading cannot be reliably quantified, then "…a clear case of design indeterminacy" results, making it "…impossible to determine the required support using the classical engineering design approach". Furthermore, in a rockburst event, it is essential that no component of the support system fails. This is consistent with the observations of Simser (2007) where a ground support system fails along its weakest link.

Figure 9. Examples of localised rockburst damage.

2.3. Energy Absorbing Ground Support

Under normal ground conditions conventional reinforcement and surface support provide confinement and limit the loosening of the rock mass. In seismically active ground conditions, the rock mass tends to display significant deformation as a result of impact loads. Under these conditions, energy absorbing ground support can better match the anticipated rock mass failure mechanism.

There is plethora of energy absorbing systems that have been introduced in the last twenty years. Examples of these include the use of debonding agents with threaded bars, debonded bars with anchors that are designed to slip or plough through the chemical bonding agent, and paddled energy absorbing rockbolts. Developments in surface support technology include applications using chainlink mesh, straps etc. The objective being to develop a system that can accommodate large deformations.

The development of new ground support elements for seismic ground conditions created the need for specialised testing facilities to quantify their "dynamic" performance. Hadjigeorgiou and Potvin (2011) provided a critical review of such facilities identifying variations in testing rigs and followed procedures. Most testing rigs currently use the direct impact method. In this configuration a free-falling mass impacts on a plate attached to the sample, thereby applying a load, Potvin and Hadjigeorgiou (2020), Li et al (2021). A different testing set-up is used by the WASM rig, Villaescusa et al (2014), where both mass and bolt free-fall at the beginning of the test. In this arrangement the bolt is then abruptly stopped, and the momentum of the mass is transferred to the rockbolt.

There are two fundamental configurations used during impact tests of rockbolts: continuous tube which simulates the application of an impact load directly applied onto the bolt plate; and split-tube used to reproduce the loading condition by impact thrust ejection on the rockbolt. In both setups, the energy dissipated per impact is equal to the area under the impact load and plate, Figure 10. Li et al (2021).

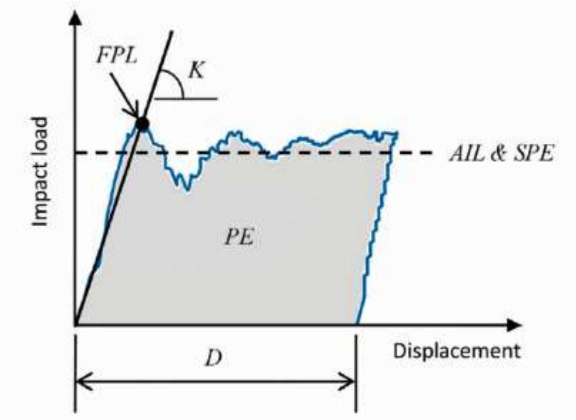

Definitions:

PE: plastic energy dissipation

D: permanent plastic displacement

AIL: average impact load

SPE: specific plastic energy dissipation

FPL: first peak load

K: initial stiffness

Figure 10. A typical impact load - displacement curve of a rockbolt, Li et al (2021).

Several authors have compiled the results from impact testing for various rigs, e.g., Potvin and Hadjigeorgiou (2020). Villaescusa et al (2014) compiled the results from the WASM rig. In results from both testing configurations, performance trends between yielding and non-yielding ground support elements are evident. The specifics of individual elements under impact loads should be subjected to greater scrutiny given the wide variety of ground support products and testing protocols. Li et al (2021) reported on a series of impact tests of identical rockbolts carried out using the direct impact method on the rigs in four laboratories. It was concluded that there was a degree of testing rig bias when comparing results from different laboratories.

Another useful source of information is through large-scale impact tests that can also investigate the interaction between reinforcement and surface support. The Walenstadt testing rig (Figure 11) has been used to investigate the relative performance under specific loading conditions of different ground support systems, Brändle and Luis Fonseca (2019, 2021). In this case it was possible to investigate the performance of a ground support system used at a specific mine site, providing an insight into the load distribution between reinforcement and surface support elements.

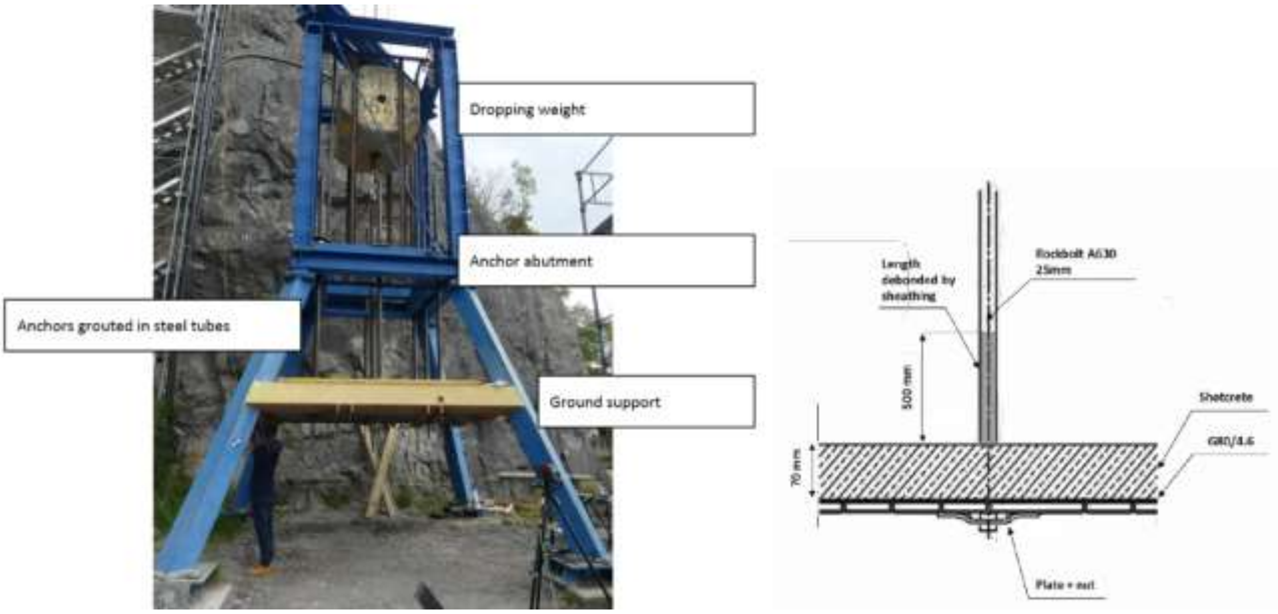

Figure 11. Walenstadt test arrangement (left), tested configuration (right), Brändle and Luis Fonseca (2021).

Although none of the testing systems can fully reproduce the rockburst mechanism they can still provide valuable insights and improve our understanding of ground support behaviour under impact loading. For example, Knox and Hadjigeorgiou (2022) explored the influence of both the presence and location of the split in a continuous tube for paddled energy absorbing rockbolts. Five split configurations were used (Figure 12) and the results are summarised in Table 2. The energy dissipated per impact is equal to the area under the impact load and plate, Li et al (2021). Figure 13 is longitudinal cross-section of a sample after testing using the indirect impact paddle split tube configuration and the location of a rupture point in the paddle set relative to the split in the host tube.

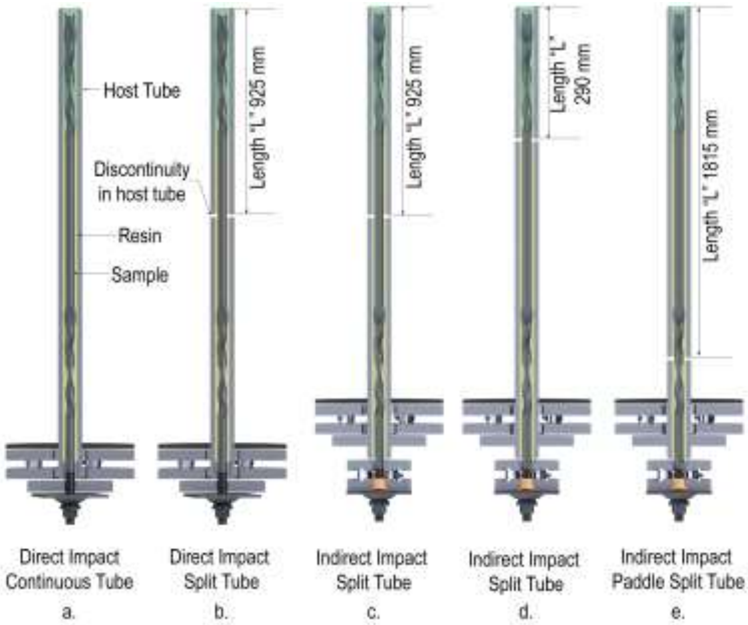

Figure 12. Illustration of split location along the tube for both direct and indirect impact test configurations, Knox and Hadjigeorgiou (2022).

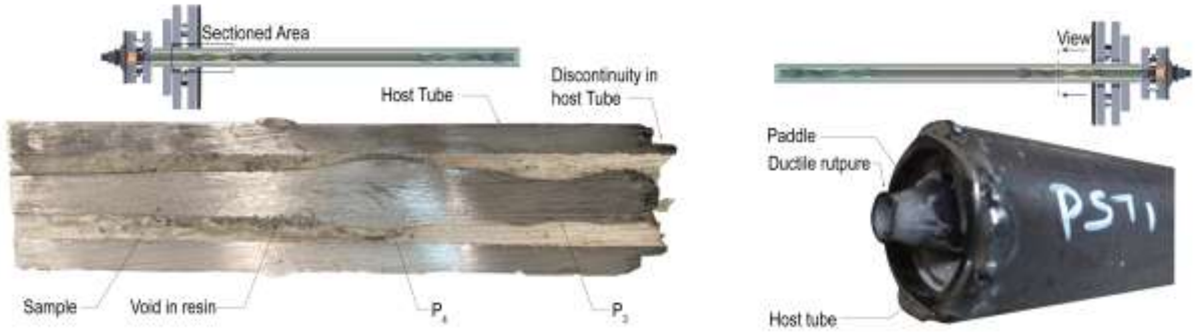

Figure 13. Cross-section of the proximal side of the split through the proximal anchor where the split was located; rupture of the bar on the distal side of the split, Knox and Hadjigeorgiou (2022).

Table 2. Testing Configuration and Results, Knox and Hadjigeorgiou (2022).

Sample	Split position	Avg. E_{total} (kJ)
Direct impact continuous tube	No Split	12
Direct impact split tube	At the centre of the distal stem L = 925 mm	52
Indirect impact split tube	At the centre of the distal stem L = 925 mm	56
Indirect impact split tube	At the distal stem L = 300 mm	49
Indirect impact paddle split tube	Between P2 & P3 of the proximal paddle set L=1845 mm	6

These experiments demonstrated that the split location, had a significant influence on both the maximum plate displacement and dissipated energy recorded prior to the rupture of paddled energy absorbing rockbolts. This has significant implications on the use of laboratory testing results to understand the field performance of energy-absorbing rockbolts under more complex seismic load mechanisms.

3. EXTREME CONDITIONS: SQUEEZING GROUND

Large deformations and squeezing ground conditions result in major operational problems often requiring major rehabilitation of existing support. Figure 14 illustrates examples of structurally controlled squeezing in mining drives at two Canadian hard rock mines, Hadjigeorgiou et al (2013). In general, after very large deformations the mines have to purge the broken rock mass and rehabilitate the area in order to keep the mining drives operational.

The last 15 years have seen significant developments in how mines manage large deformations. These include access to tools to anticipate the level of deformation, e.g., the Squeezing Index, Mercier Langevin and Hadjigeorgiou (2011) and increased use of numerical models. The Squeezing Index, in particular, was shown to facilitate proactive modifications to a mine’s ground support strategy, Marlow and Mikula (2013), Wooley and Andrews (2015).

Figure 15 highlights the influence of the angle of interception (ψ), defined as the angle between the normal to the foliation planes and the normal to the drive wall of interest, on the resulting total strain at the LaRonde and Lapa Mines. It is important to note that the observed severe squeezing at these mine sites would not have been tolerated in a tunneling project where values of 10% strain, are not acceptable.

Numerical models have been used frequently to predict the anticipated levels of squeezing as well to explore the influence of the type and time of installation of ground support as part of a mitigating strategy, e.g., Vakili et al (2013), Karampinos et al (2015, 2016), Bouzeran et al (2020). The complexity and assumptions of these models differs significantly for the given applications. This should be taken into consideration when interpreting the results and interpretation.

No squeezing

Low squeezing: rockbolts take load

Moderate squeezing: convergence

Extreme squeezing

Rehabilitated drift

Purged drift

Figure 14. Examples of structurally controlled squeezing, Hadjigeorgiou et al (2013).

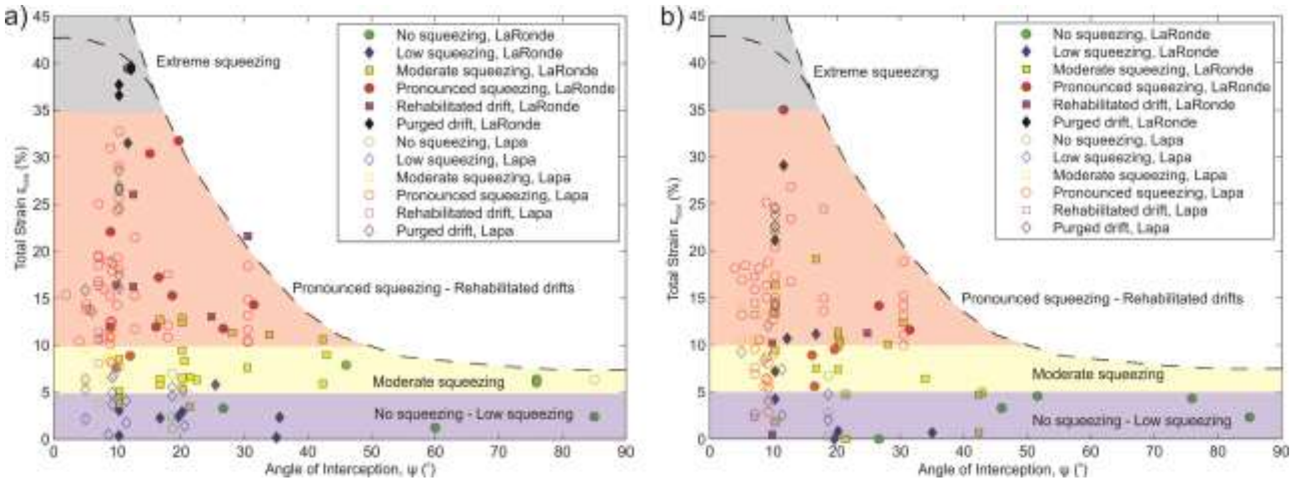

Figure 15. Influence of angle of interception (ψ) on resulting total strain at the LaRonde and Lapa Mines; (a) total wall-to-wall strain; and (b) total back-to-floor strain, Karampinos and Hadjigeorgiou (2018).

Both Lapa and LaRonde managed the high level of deformations (> 35% strain) over time by timing the installation of its reinforcement, using yielding ground support, and bringing the surface support close to the floor to prevent unravelling of the lower walls, Turcotte (2010), Mercier-Langevin and Wilson (2013).

3.1. Ground Support Strategies

In a benchmarking study Potvin and Hadjigeorgiou (2008) observed significant differences in ground support strategies between tunneling and mining. Applying some of the ground support strategies from tunneling to mining was deemed as prohibitively expensive and would result in significant delays in development and production. At the time it was also observed that Australian mines favoured the use of fibre reinforced shotcrete as the principal surface support while Canadian mines relied on welded mesh as part of their ground support to manage large deformations. As shown in Figure 16a, the fibre reinforced shotcrete keeps the rock mass together, is initially stiff until it cracks and the overlaying mesh restrains the large shotcrete plates produced by the excessive wall deformation. The use of weld mesh, Figure 16b, allows the rock mass to deform and shatter before retaining the rock fragments. Although mesh can accommodate considerable deformation it has more limited overall strength capacity. The use of straps is often used with mesh in extreme squeezing conditions.

Figure 16. a) mesh overlaying fibre reinforced shotcrete; b) welded mesh, Potvin and Hadjigeorgiou (2008).

Following a recent benchmarking study Hadjigeorgiou and Potvin (2023) provided a series of guidelines for a range of squeezing conditions. Mines now have access to the same range of energy absorbing ground support elements as for seismic conditions. A further characteristic of best practices includes the use of long reinforcement and installing ground support to the floor.

The influence of stiffness and time of installation of reinforcement to optimise its effectiveness in squeezing ground has been demonstrated by several people, including Turcotte (2010). Installing the hybrid bolt as a secondary support at LaRonde, resulted in significant reduction in rehabilitation.

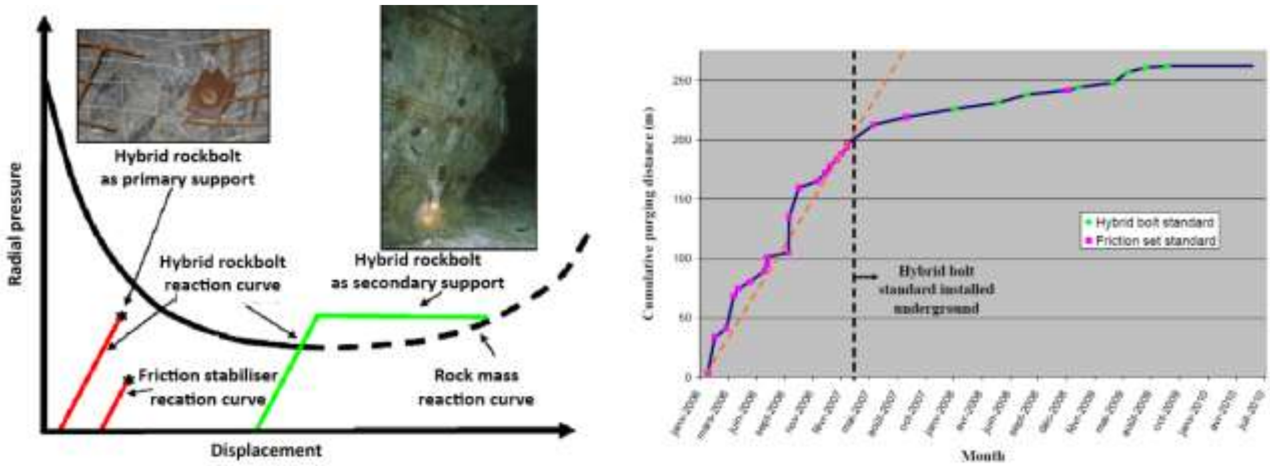

Figure 17. Conceptual reaction curve for the wall (left); cumulative distance purged under the 215 Level (right), Turcotte (2010).

Hadjigeorgiou and Potvin (2023) suggested that there are two fundamental ground support strategies available to mines experiencing very large deformations. The first one uses a sacrificial support, and the second requires a planned rehabilitation. The decision process is illustrated with reference to Figure 18 differentiating between convergence during development of the drive (phase 1), operational stage (phase 2) and phase 3 when mining of nearby stopes results in an increased rate of convergence.

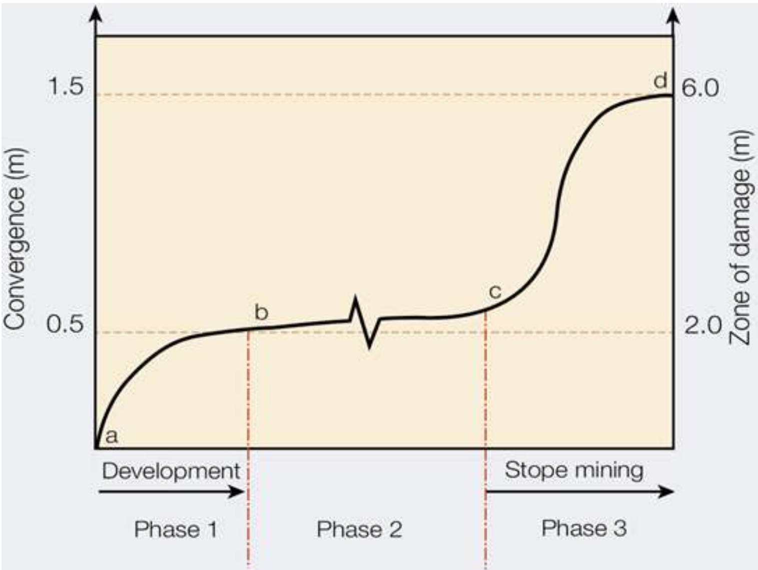

Figure 18. Mining-induced stress changes caused by the development of the drive followed by the mining of stopes nearby resulting in distinct deformation profiles, Hadjigeorgiou and Potvin (2023).

Sacrificial support is used to manage the convergence triggered by development mining. The convergence rate is relatively high immediately after the first development round and then slows down (Phase 1). Ground support is subsequently stripped towards the end of phase 1 and replaced with a system that can sustain the increased deformations associated with stope production (Phase 2 and 3). The convergence is relatively stable during Phase 2 and controlled by the ground support. Stope mining in the vicinity of the mining drive (Phase 3) results in increased convergence and damage within the rock mass. A planned rehabilitation strategy requires rehabilitation of the ground support just before the nearby stopes are extracted (Phase 3). The initial support must be able to manage convergence until just before the stope extraction phase.

4. EXTREME CONDITIONS: CORROSIVE ENVIRONMENTS

The preceding discussions focused on two types of extreme ground conditions, seismically active and squeezing ground. The challenge is to match the most appropriate ground support to these challenging conditions. A further consideration is degradation of a ground support system due to a multiple of extraneous factors including: material quality and the presence of manufacturing flaws; installation issues such as bolt orientation, grout quality; blast damage associated with explosive gases and flyrock; overload of individual reinforcement or surface support elements; damage to reinforcement and support caused by equipment; mine induced seismicity resulting in rockbursts, and corrosion of support systems.

A corrosive environment may invariably result in loss of capacity of installed ground support. However, its impact in seismically active and squeezing ground, can be greater as there is already the potential for reduced capacity due to increased demand, and damage to the ground support as well. Characterizing the corrosive environment is consequently important to evaluate the potential for degradation of different ground control elements. Atmospheric corrosion is the degradation of rock bolts exposed to air and pollutants present in an underground. The rate of atmospheric corrosion is a function of the relative humidity, temperature, and the presence of pollutants such as gas and particles. Aqueous corrosion is an electrochemical reaction that results in deterioration of the material and is influenced by both the characteristics of the solution and the material properties. Microbiologically influenced corrosion (MIC) is the condition where microorganisms present in the water can facilitate or inhibit corrosion.

Different types of ground control elements, exposed to the same corrosive environment, can have varying resistance to corrosion. For example, friction rock stabilisers are perceived to have higher corrosion rates than other ground support elements when exposed to atmospheric and aqueous corrosion, Figure 19.

Figure 19. Friction rock stabilizers showing signs of a) atmospheric corrosion; b) aqueous corrosion.

What is often overlooked are variations in corrosion rates between “similar” rockbolts. For example, it is possible for specific rockbolt types to have similar mechanical properties but different resistance to corrosion. This was demonstrated in accelerated corrosion studies where three similar expandable rockbolts, from different suppliers, exposed in an aggressive electrolyte, showed significant variations in their calculated corrosion rates, Hadjigeorgiou et al (2020). The benefits of corrosion inhibiting coating on rockbolts must be carefully addressed case by case. In an in-situ investigation of six coated expandable rockbolts completely immersed in two aggressive mine waters, there were clear signs of corrosion, Figure 20. A comparison of the performance of these rockbolts is provided in Figure 21 summarising the frequency of pitting attack (by colour) and the estimated corrosion rate, Hadjigeorgiou et al (2019). Although there were significant variations, all bolts performed much better in the less corrosive solution (site A). The other takeaway is that use of some of these rockbolts in these environments would result in premature failure and necessitate earlier rehabilitation of the ground support.

Figure 20. Observed corrosion types along the bolt length: a) general corrosion, b) pitting corrosion and c) pinpoint rusting, Hadjigeorgiou et al (2019).

Type	Site A	Site B
SA-CoatA2-12t	60 μm (120 μm/year)	30 μm (60 μm/year)
SA-CoatA1-24t	120 μm (240 μm/year)	750 μm (750 μm/year)
SB-CoatB1-12t	85 μm (170 μm/year)	470 μm (940 μm/year)
SB-CoatB2-12t	40 μm (80 μm/year)	1,980 μm (3,960 μm/year)
SC-CoatC1-12t	55 μm (110 μm/year)	1,655 μm (3,310 μm/year)
SC-CoatC2-24t	145 μm (290 μm/year)	295 μm (590 μm/year)

Note: **Pit Depth** μm; **Corrosion Rate** (μm/year)

Coating Condition (Pit Density)

- Light – Only few corrosion sites are present, typically due to mechanical damage
- Moderate – Some corrosion sites are present, typically due to mechanical damage
- Heavy - Many corrosion sites distributed on the entire surface of the bolt, closed blisters
- Severe – The whole surface covered with pits, open blisters

Figure 21. Performance of expandable bolts exposed in two solutions, Hadjigeorgiou et al (2019).

Although the long-term performance of ground support in corrosive environments is a complex process, it is still possible to provide some guidelines on when to trigger the rehabilitation process based on field observations, Figure 22. A good example of an effective use of the corrosion level chart is illustrated in Figure 23 where site inspections were used to zone areas of similar corrosion levels. This information allowed the mine to develop and prioritize its rehabilitation strategy. The same approach has been employed at another site by Dorion (2019), to develop a decision matrix to establish the mine's rehabilitation strategy, also considering the consequences of not achieving its production goals due to ground control issues. The mine then issues a rehabilitation plan.

Corrosion Level	Description	Corrosion rate	Loss of capacity	#6 Mesh diam.	Required Intervention
	**C1: Negligible corrosion** Steel is in excellent condition and corrosion evident only on the surface. A few localized spots, less than 10% of the surface is corroded.	< 0.02 mm/yr	< 10%	> 4.75 mm	None
	**C2: Localized corrosion** Corrosion is characterized by localized spots on the surface. Between 10% and 75% of the surface is corroded. Steel is in good condition.	0.02 to 0.04 mm/yr	10 to 20%	4.50 to 4.75 mm	None
	**C3: Surface corrosion** Corrosion over 75% of the surface. Corrosion is only on surface. If a corrosion crust is present, it is very thin. Can identify blisters.	0.04 to 0.15 mm/yr	20 to 35%	4.00 to 4.50 mm	None to follow up.
	**C4: Advanced corrosion** 100% of the surface is corroded. Can identify blisters. Thin corrosion crust (< 1 mm) easily removed.	0.15 to 0.30 mm/yr	35 to 50%	3.50 to 4.50 mm	Follow up. If installed over 12 months, it will display signs of severe corrosion.
	**C5: Very advanced corrosion** 100% of the surface is corroded. Thick corrosion crust (> 1 mm) and flaky.	0.30 to 0.60 mm/yr	50 to 75%	2.50 to 3.50 mm	Consider replacement of installed units.
	**C6: Extreme corrosion** Corrosion goes through the steel. Integrity of steel has been damaged. Pieces are easily breakable by hand.	>0.60 mm/yr	>75%	<2.50 mm	Reconditioning. May require immediate intervention.

Figure 22. Linking on site observations to resulting loss of capacity and required intervention, after Dorion and Hadjigeorgiou (2014)

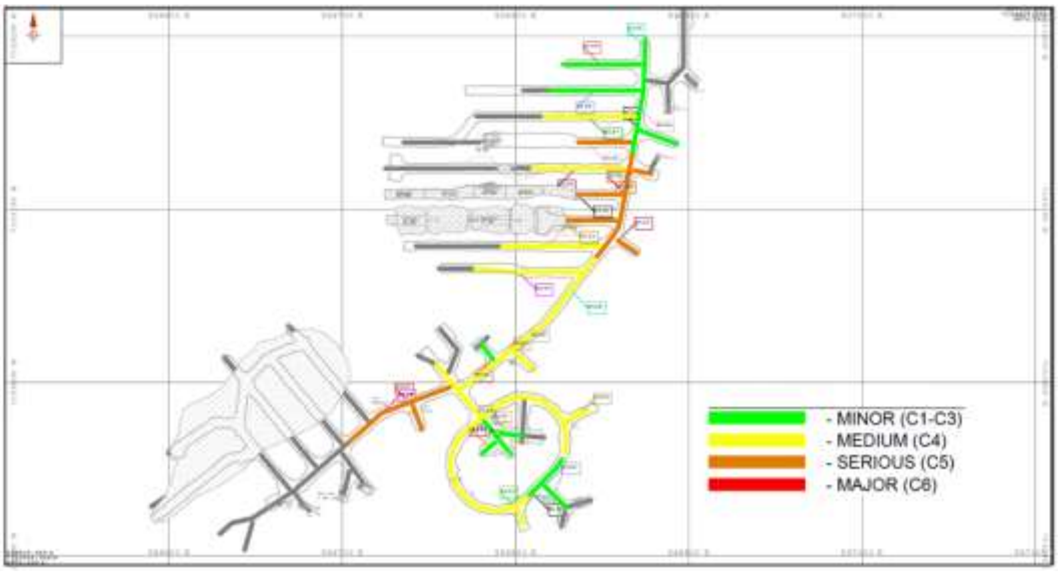

Figure 23. Observed level of ground support corrosion in an underground hard rock mine.

4.1. Interaction of degradation with other extreme conditions

The preceding discussion focused on the degradation of ground support when exposed to corrosive environments. In operating mines, exposed to mine seismicity or extreme squeezing, a corrosive environment can be detrimental to the long-term performance of ground support. For example, a corroded ground support may limit its capacity to withstand a seismic load. This is illustrated conceptually in Figure 24 where a degraded support can fail following a major impact load. This has been observed in field investigations following falls of ground, but it is very difficult to quantify the degree of influence of degradation in the process.

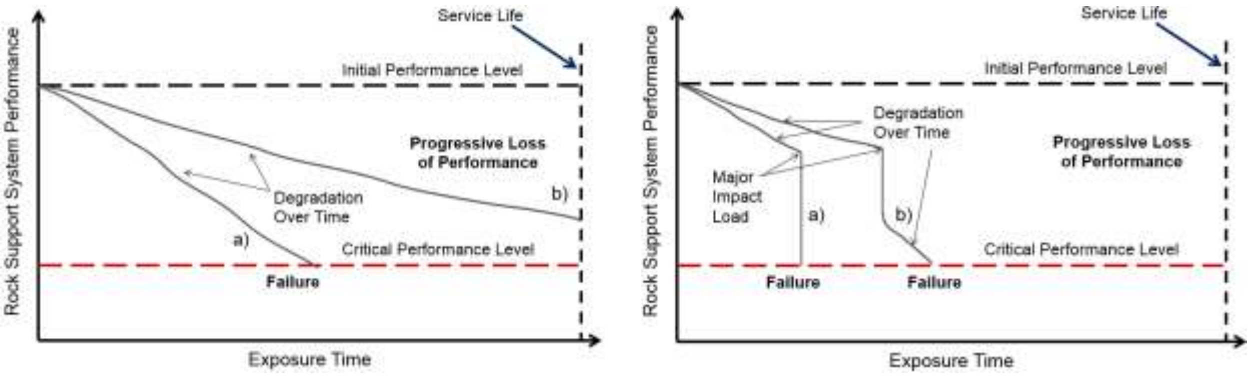

Figure 24. a) Degradation over time resulting in failure; b) Degradation over time, major impact load, and further degradation resulting in failure, Hadjigeorgiou (2016).

Localised corrosion of ground support may also result in developing a weakest link in the system. This can further compromise the structural integrity of the system under additional loading.

5. CONCLUSIONS

Excavations developed at shallow to moderate depth, in relatively competent rock masses, are often characterised by relatively low stress and low convergence. These are often described as “normal conditions” and there are several analytical, empirical, and numerical tools that can be used for the design of ground support. Conventional reinforcement and surface support elements are typically adequate to ensure the structural integrity of excavations in normal ground conditions.

Designing for extreme ground conditions poses significant challenges given the complexity of the loading mechanisms, as well as determining the ground support system capacity. Conventional ground support systems are often inadequate for seismic and squeezing ground, necessitating the use of energy absorbing ground support systems capable of accommodating large deformations. Even when installing energy absorbing ground support systems, it may be necessary to rehabilitate under extreme conditions. The case is made in this paper that determining the threshold and planning for rehabilitation should be an integral part of a ground support strategy for extreme ground conditions.

6. ACKNOWLEDGEMENTS

The financial support of the Natural Science and Engineering Research Council of Canada and multiple mining companies that have financed elements of this work is greatly appreciated. The author is grateful to have had the opportunity to collaborate with outstanding industry and research colleagues over the last thirty years.

REFERENCES

Barton, N, Lien, R & Lunde, J (1974). *Engineering classification of rock masses for design of tunnel support. Rock Mechanics and Rock Engineering*, vol. 6, no. 4, pp. 189–236.

Barton, N. (2002). Some new Q-value correlations to assist in site characterisation and tunnel design. International Journal of Rock Mechanics & Mining Sciences 39 (2002) 185–216.

Boskovic M. (2022). *Challenges of Resuming the Production After a Major Seismic Event at LKAB's Kiirunavaara Mine. Proceedings of the Tenth International Conference on Rockburst and Seismicity in Mines.* Tucson, Arizona, The Society for Mining, Metallurgy & Exploration (SME).

Brändle R. and R Luis Fonseca (2019). *Dynamic testing of surface support systems. Proceedings of the Ninth International Symposium on Ground Support in Mining and Underground Construction*. J Hadjigeorgiou & M Hudyma (eds), Australian Centre for Geomechanics pp. 243-250.

Brändle, R., Luis Fonseca, R., von Rickenbach, G., Fischer, G., Vallejos, J., Marambio, E., Burgos, L. and Cuello, D. (2021). Single impact dynamic test of a ground support system with a high-tensile steel wire mesh at the Walenstadt testing facility. *Proceedings of the Tenth International Conference on Rockburst and Seismicity in Mines, RaSim10. Tucson, Arizona, The Society for Mining, Metallurgy & Exploration (SME).*

Bouzeran, L., Pierce, M., Andrieux, P. and Williams, E. (2020). *The role of rock mass heterogeneity and buckling mechanisms in excavation performance in foliated ground at Westwood Mine, Quebec. The Southern African Institute of Mining and Metallurgy*. Vol. 120, pp. 41-48.

Counter DB 2019. *Laser-based scanning to manage geotechnical risk in deep mines. Proceedings of the Ninth International Symposium on Ground Support in Mining and Underground Construction*. J Hadjigeorgiou & M Hudyma (eds), J Hadjigeorgiou & M Hudyma (eds). Australian Centre for Geomechanics, pp. 43-58.

Counter DB (2014). *Kidd Mine – dealing with the issues of deep and high stress mining – past, present and future.* Deep Mining 2014 – M Hudyma and Y Potvin (eds). pp. 3-22.

Dorion, J.F. (2019). *Corroded rock support issues: implementation of an investigation and rehabilitation program. Proceedings of the Ninth International Symposium on Ground Support in Mining and Underground Construction*. J Hadjigeorgiou & M Hudyma (eds), Australian Centre for Geomechanics pp. 401-417.

Dorion J.F. and J. Hadjigeorgiou (2014). *Corrosion considerations in design and operation of rock support systems. Mining Technology* 2014 Vol. 23 No 2 pp. 59-68.

Grimstad, E. & Barton, N. (1993). *Updating the Q-system for NMT.* Proceedings of the International Symposium on Sprayed Concrete C Kompen, SL Opsahl & SL Berg (eds), Norwegian Concrete Association, p. 21.

Hadjigeorgiou J. and Grenon M. (2017). *Drift reinforcement design based on Discrete Fracture Network (DFN) modelling. Rock Mechanics and Engineering*. Edited by Xia ‐ Ting Feng. Chapter 4. CRC Press/Balkema, Taylor & Francis Group, pp. 123-146.

Hadjigeorgiou J. and Y. Potvin (2011). *Hard Rock Ground Control with Screen and Shotcrete. Chapter 8.6 in the SME Mining Engineering Handbook.* Society of Mining Engineers. pp. 573-594.

Hadjigeorgiou, J. and Potvin, Y. (2011). *A critical assessment of dynamic rock reinforcement and support testing facilities, Rock Mechanics and Rock Engineering*, vol. 44, no. 5, pp. 565–578.

Hadjigeorgiou, J. and Potvin, Y. (2023). *Ground support guidelines for squeezing rock conditions.* (Submitted for publication).

Hadjigeorgiou, J., Karampinos, E., Turcotte, P. and Mercier-Langevin, F. (2013). *Assessment of the influence of drift orientation on observed levels of squeezing in hard rock mines. Proceedings of the Seventh International Symposium on Ground Support in Mining and Underground Construction*, B Brady & Y Potvin (eds), Australian Centre for Geomechanics, Perth, pp. 109–118.

Hadjigeorgiou, J. (2016). *Rock support: degradation and failure*. *Proceedings of the Eighth International Symposium on Ground Support in Mining and Underground Construction*, E Nordlund, TH Jones & A Eitzenberger (eds), Luleå University of Technology, Luleå, 21 p.

Hadjigeorgiou J., Savguira Y. and Thorpe S. J (2020). *Impact of Steel Properties on the Corrosion of Expandable Rock Bolts. Rock Mechanics and Rock Engineering*, 53:705-721.

Hadjigeorgiou, J., Savguira, Y. and Thorpe, S.J. (2019). *Comparative susceptibility to corrosion of coated expandable bolts', Rock Engineering, Rock Mechanics and Rock Engineering*, vol. 52, issue 8, pp. 2665–2680.

Heal, D. (2010). *Observations and Analysis of Incidences of Rockburst Damage in Underground Mines, PhD thesis*, The University of Western Australia, Perth.

Jones, E. and Hancock E. (2020). *Managing the deformation of ground support and reinforcement. Rock Mechanics for Natural Resources and Infrastructure Development.* Fontoura, Rocca & Pavón Mendoza (Eds). pp. 822-829.

Kaiser, P. and Cai, M. (2012). *Design of rock support system under rockburst condition. Journal of Rock Mechanics and Geotechnical Engineering*, vol. 4, no. 3, pp. 215–227.

Kaiser, P.K., McCreath, D.R. and Tannant, D.D. (1996). *Canadian Rockburst Support Handbook, Canadian Mining Industry Research Organization*, Sudbury.

Karampinos E., J. Hadjigeorgiou, J. Hazzard and P. Turcotte (2015). *Discrete element modelling of the buckling phenomenon in deep hard rock mines. International Journal of Rock Mechanics & Mining Sciences* 80 (2015) 346–356.

Karampinos E., Hadjigeorgiou J., and P. Turcotte (2016). *Discrete element modelling of the influence of reinforcement in squeezing conditions in a hard rock mine. Rock Mech Rock Eng* 49:4869–4892.

Karampinos, E. and Hadjigeorgiou, J. (2018). *Quantifying the influence of structure, rock mass strength and mining development of drives in squeezing ground. Transactions of the Institutions of Mining and Metallurgy, Mining Technology*, vol. 127, issue 4, pp. 177–194.

Knox, G. and Hadjigeorgiou, J. (2022). *Influence of testing configuration on the performance of paddled energy-absorbing rockbolts under impact loading. Rock Mechanics and Rock Engineering*. 55:5705–5721.

Li, C., Hadjigeorgiou, J., Mikula, P., Knox, G., Darlington, B., Royer, R., Pytlik, A., Hosp M. (2021). *Performance of Identical Rockbolts Tested on Four Dynamic Testing Rigs Employing the Direct Impact Method. Journal of Rock Mechanics and Geotechnical Engineering*. Volume 13, Issue 4, August 2021, pp. 745-754.

Li, C.C., Stjern, G. and Myrvang, A. (2014). *A review on the performance of conventional and energy-absorbing rockbolts. Journal of Rock Mechanics and Geotechnical Engineering*, vol. 6, issue 4, pp. 315–327.

Marlow, P. and Mikula, P.A. (2013). *Shotcrete ribs and cemented rock fill ground control methods for stoping in weak squeezing rock at Wattle Dam Gold Mine. Proceedings of the Seventh International Symposium on Ground Support in Mining and Underground Construction.* Y Potvin & B Brady (eds), Australian Centre for Geomechanics, Perth, pp. 133–148.

Mercier-Langevin, F. and Hadjigeorgiou, J. (2011). *Towards a better understanding of squeezing potential in hard rock mines. Transactions of the Institutions of Mining and Metallurgy: Section A – Mining Technology*, vol. 120, no. 1, pp. 36–44.

Mercier-Langevin, F. and Wilson, D. (2013). Lapa Mine – ground control practices in extreme squeezing ground. *Proceedings of the Seventh International Symposium on Ground Support in Mining and Underground Construction*, B Brady & Y Potvin (eds), Australian Centre for Geomechanics, Perth, pp. 119–131.

Mikula, P. and Gebremedhin, B. (2017). *Empirical selection of ground support for dynamic conditions using charting of support performance at Hamlet mine. Proceedings of the Eighth International Conference on Deep and High Stress Mining*, J Wesseloo (ed.), Australian Centre for Geomechanics, Perth, pp. 625–636.

Morissette P., Hadjigeorgiou J. (2019). *Ground support design for dynamic-loading conditions: A quantitative data-driven approach based on rockburst case studies. Journal of Rock Mechanics and Geotechnical Engineering,* 11 (2019) 909-919.

Ortlepp W. D. and T. R. Stacey (1994). *Rockburst Mechanisms in Tunnels and Shafts. Tunnelling and Underground Space Technology*, Vol. 9, No. 1, pp. 59-65.

Palmstrom, A. and Broch E. (2006). *Use and misuse of rock mass classification systems with particular reference to the Q-system. Tunnelling and Underground Space Technology* 21, 575–593.

Potvin, Y. and Hadjigeorgiou J. (2008). *Ground Support Strategies to Control Large Deformations in Mining Excavations. The Journal of the Southern African Institute of Mining and Metallurgy*. Vol. 108, July 2008 pp. 393-400.

Potvin, Y. and Hadjigeorgiou, J. (2016). *Selection of ground support for mining drives based on the Q-System. Proceedings of the Eighth International Symposium on Ground Support in Mining and Underground Construction*, E Nordlund, T Jones & A Eitzenberger (eds), Luleå University of Technology, Luleå.

Potvin, Y. and Hadjigeorgiou, J. (2020). *Ground Support for underground mines*. Australian Centre for Geomechanics p. 520.

RocScience 2023. *UnWedge: Underground Wedge Stability Analysis Software Package*. Rocscience Inc., Toronto.

Simser, B.P. (2007). The weakest link—ground support observations at some Canadian Shield hard rock mines. In: Potvin Y (ed). Proceedings 4th International Seminar on Deep and High Stress Mining. Australian Centre for Geomechanics, Perth, pp 335–348.

Simser, B.P. (2023). Personal communication.
Stacey T. R. (2016). *Addressing the Consequences of Dynamic Rock Failure in Underground Excavations. Rock Mech Rock Eng* (2016) 49:4091–4101.
Stacey, T.R. (2012). *Support of excavations subjected to dynamic (rockburst) loading. Proc. 12th Int. Cong. Int. Soc. Rock Mech.*, Beijing, CRC Press/Balkema, pp 137–145.
Sweby, G., Hadjigeorgiou, J., Wesseloo J. and Y Potvin (2020). *Numerical modelling for ground support design – mining applications.* Chapter 11 in Ground Support for underground mines. Potvin Y. J. Hadjigeorgiou. Australian Centre for Geomechanics pp. 237-265.
Turcotte, P. (2010). *Field behaviour of hybrid bolt at LaRonde Mine*. *Deep Mining 2010*, M. Van Sint Jan and Y. Potvin (eds). Santiago, Chile. Australian Centre for Geomechanics, 309-319.
Vakili, A., Sandy, M.P., Mathews, M. and Rodda, B. (2013). *Ground support design under high stressed conditions. Proceedings of the Seventh International Symposium on Ground Support in Mining and Underground Construction*. Y Potvin & B Brady (eds), Australian Centre for Geomechanics, Perth, pp. 551–564.
Villaescusa, E, Player, J.R. and Thompson, A.G. (2014). *A reinforcement design methodology for highly stressed rock mass. Proceedings of the 8th Asian Rock Mechanics Symposium,* N Shimizu, K Kanedo & J Kodama (eds), Japanese Society for Rock Mechanics, Tokyo, pp. 87–94.
Villaescusa, E., Thompson, A.G. and Player, J.R. 2013. *A decade of ground support research at the WA School of Mines. Proceedings of the Seventh International Symposium on Ground Support in Mining and Underground Construction*. Y Potvin and B Brady (eds), Australian Centre for Geomechanics, Perth, pp. 233–245.
Wiles, T.D., Villaescusa, E. and Windsor, C. (2004). *Rock reinforcement design for overstressed rock using three dimensional numerical modelling. Proceedings of the Fifth International Symposium on Ground Support in Mining and Underground Construction*. E Villaescusa & Y Potvin (eds), Perth, pp. 483–489.
Wolley, C.E. and Andrews, P. (2015). *Short term solution to squeezing ground at Agnew Gold Mine. Proceedings of the International Seminar on Design Methods in Underground Mining.* Y Potvin (ed.), Australian Centre for Geomechanics, Perth, pp. 199–214.

Proceedings of the NROCK 2023
The IV Nordic Symposium on Rock Mechanics and Rock Engineering
ISBN 978-9935-9436-2-0
DOI 10.33112/nrock2023

ABSTRACT
Session K1.2

Carbfix - CO_2 mineral storage in basaltic rocks

Sandra Ósk Snæbjörnsdóttir
(Sandra.Osk.Snaebjornsdottir@carbfix.com)

Substantial and sustained reduction of anthropogenic CO_2 emissions to the atmosphere are needed to achieve the goals of the Paris agreement and constrain the current rapid warming to 1,5-2°C. Carbon capture and storage (CCS) solutions play an important role in the transition towards carbon neutrality. CCS includes a range of processes for CO_2 capture, separation, transport, storage, and monitoring, and is considered the key technology for reducing emissions from fossil fuel power plants while these are still part of the energy systems, limiting emissions from many industrial processes such as steel, aluminium and cement production, and to deliver "negative emissions" by removing and permanently storing CO_2 captured directly from air by the second half of the century.

What we do

Despite the urgent need for rapid deployment of widespread carbon storage sites, experience demonstrates that low public acceptance, high upfront investment costs and uncertain future liabilities have hindered the implementation of conventional carbon storage methods in Europe. The success of CO_2 storage depends on its long-term security. Injection of CO_2 into young basaltic formations provides significant advantages, including great storage potential, and permanent storage by mineralization by combining the injected CO_2 with metals contained in the basalts to form stable carbonate minerals.

Mineral carbonation is a part of the natural carbon cycle, where the carbon moves from one terrestrial reservoir to another. Within the natural cycle, carbon has few years average residence time in the atmosphere, decades in vegetation, decades to tens of thousands of years in soils and in the oceans, and thousands to millions of years in rocks, which is by far largest carbon reservoir on Earth. Mineral carbon storage, however, will only be practical if it is possible to accelerate this process at large enough scales to address the current global challenge. Within this approach the captured carbon is stored via injection into reactive rocks such as mafic or ultra-mafic rocks for rapid mineralisation. Mineral carbonation can be promoted by the dissolution of CO2 into water before or during its injection. No cap rock is required when injecting water charged CO2, as it is denser than CO2-free water. As such it does not have the tendency to migrate back to the surface. By dissolving CO2 into water before or during its injection, solubility trapping is achieved immediately, and the bulk of the carbon is trapped in carbonate minerals within two years of injection at 20-50°C. By provoking the mineralisation of the injected CO2 into carbonate minerals such as calcite (CaCO3), dolomite (CaMg(CO3)2) or magnesite (MgCO3) via its injection into reactive host-rocks, the injected carbon is permanently fixed and there is a negligible risk of it returning to the atmosphere.

Mineral CO2 storage offers a vast storage potential and unlocks large regions in the world where CCS has until now not been considered possible. The largest potential lies offshore within the sub-marine basaltic crust, but suitable formations are also widespread onshore, including volcanic formations, mine tailings and unconventional petroleum reservoirs.

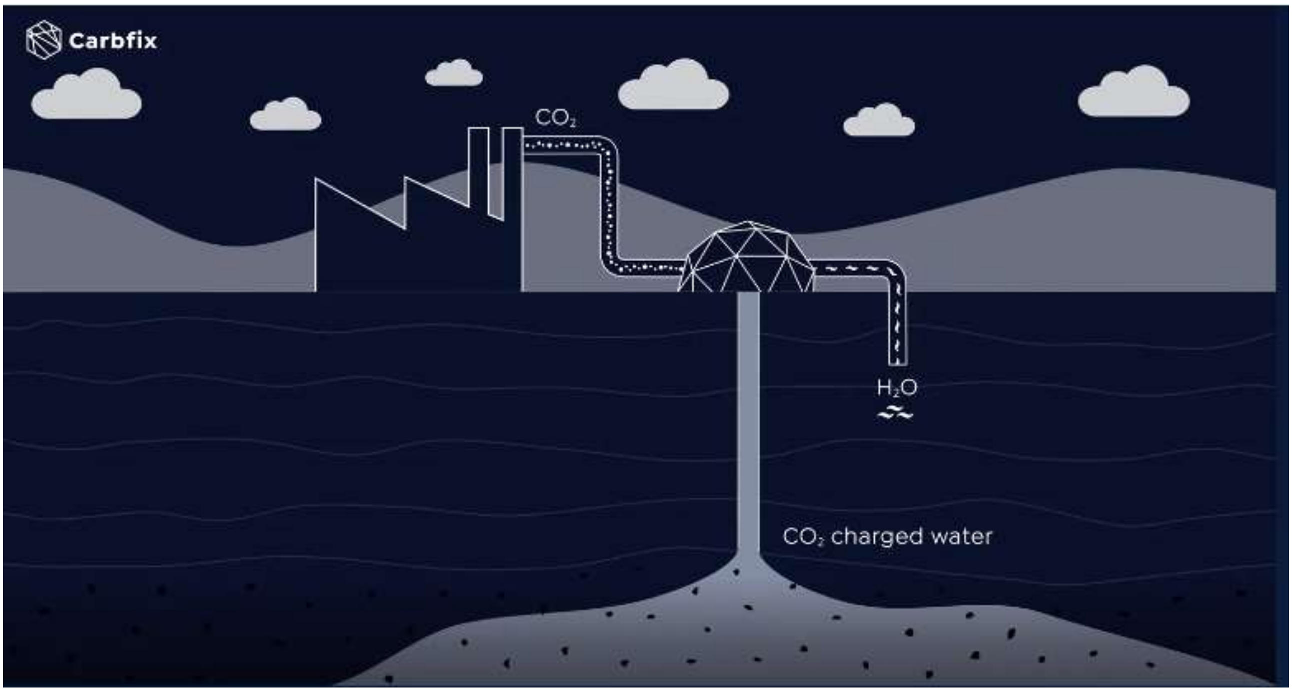

How we do it

Carbfix has since 2014 injected over 90,000 tonnes of CO2 from the Hellisheidi geothermal plant in SW-Iceland into the basaltic reservoir for mineral CO2 storage. Emphasis is currently being placed on making this technology more cost effective and exploring its limits in terms of potential sites and injection methods, including injection of CO2 captured directly from the atmosphere.

Proceedings of the NROCK 2023
The IV Nordic Symposium on
Rock Mechanics and Rock Engineering
ISBN 978-9935-9436-2-0
DOI 10.33112/nrock2023.2

Engineering Geology in Hydropower Engineering

Krishna Kanta Panthi
Department of Geoscience and Petroleum
Norwegian University of Science and Technology (NTNU)
S.P. Andersen vei 15a, Trondheim, Norway
email: krishna.panthi@ntnu.no

ABSTRACT

Norway has more than 100 years of experience in the design and construction of hydropower plants consisting waterway systems that included unlined pressure tunnels and shafts. The waterway systems are in general very long and consist of unlined pressurized headrace tunnels, unlined high-pressure shafts, underground powerhouse caverns, access, and tailrace tunnels. The maximum static head that the unlined pressure tunnel has reached is 1047 meter, which is equivalent to almost 10.5 MPa. This is a world record, and it is obvious that the rock mass in the periphery of unlined pressure tunnels and shafts experience high hydrostatic pressure exerted by the flowing water discharge. Experienced gained from the construction and operation of these unlined pressure tunnels and shafts were the key to develop design criteria and stability assessment principles by giving focus on engineering geology, rock mass quality and geo-tectonic environment. As a result, these criteria and principals have got worldwide acceptance. However, the success of these criteria depends on the engineering geological and geo-tectonic environment prevailing in the are of concern and the operational regime adopted in the hydropower plants. This key-not lecture reviews some of the first attempts of the use of unlined pressure tunnels and shafts concept, highlights major failure cases, discusses the gradual development of design criteria for the unlined pressure tunnels and shafts and highlights recent operational trends that have direct influence on the stability of unlined pressure tunnels and shafts of hydropower plants.

KEYWORDS

Hydropower; Hard rock mass; Water pressure; Design criteria; Operation

1. INTRODUCTION

A typical layout of the hydropower schemes in Norway before 1920s consisted horizontal headrace tunnel, steel penstock along the surface topography and powerhouse on the bottom of the valley. Early 1920s attempts were made to build underground pressure shafts (both steel-lined and unlined) and underground powerhouse. The first such hydropower scheme with underground powerhouse was built in the year 1916. However, emphasis was given to keep all waterway system and powerhouses inside the mountain mainly after the completion of World War II. Today, according to Panthi and Broch (2022), Norway has over 200 underground powerhouse caverns and over 4300 km hydropower tunnels. Experiences gained through the design, construction and operation of hydropower schemes has made it possible to apply unlined high-pressure tunnels and shafts concept due to the favorable engineering geological and geo-tectonic conditions that persist in the Scandinavia. It is estimated that over 95% of the waterway length of Norwegian hydropower schemes are left unlined (Panthi, 2014; Panthi and Broch, 2022).

The success history of the development of hydropower schemes with unlined pressure tunnels and shafts in Norway used to be almost 99 percent with very little stability problems until the de-regulation of power market in early 1990s. However, after the de-regulation of power market the waterway systems are facing new operational challenges (Neupane et al., 2020). This key-note lecture highlights about the developed design criteria that consider geology, rock mass and in-situ stress. In addition, challenges associated to topography, geo-tectonic conditions, and changes in operation after de-regulation of power market are highlighted.

2. BRIEF HISTORY OF DEVELOPMENT

In Norway, the use of unlined pressure tunnel and shaft in hydropower projects started early 1920 (Vogt, 1922). Four projects were implemented around this time. Three out of these four projects had problems during initial water filling and these problems were solved by extending the penstock pipe and by carrying out extensive grouting. All four projects were designed with low pressure headrace tunnel, unlined inclined pressure shafts, and horizontal penstock tunnel as waterway system connecting the powerhouse located at surface (Figure 1a). Although three out of four hydropower schemes with unlined pressure shafts were operating perfectly after some initial problems were fixed, it took almost 40 years to beat the world record of static water head of 152 m with unlined high-pressure shaft of Svelgen hydropower project (Figure 2). The Tafjord K3 hydropower project with a static head of 286 m was the one to beat this record, which was successfully put into operation in 1958 (Broch, 1982). After the construction of this project the hydropower industry in Norway had a new confidence in the application of unlined pressure tunnels and shafts concept. The general layout design used for the design of hydropower schemes after Tafjord K3 is shown in Figure 1b. This type of design uses very limited length of steel lining near the powerhouse (mostly not exceeding 75m) in order to avoid the leakage from unlined pressure shaft to the underground powerhouse cavern. In areas where topography restricted the use of unlined high pressure shaft all the way from near powerhouse cavern to downstream end of headrace tunnel, an layout arrangement consisting steel lined lower pressure shaft and part of the horizontal pressure tunnel downstream of unlined upper pressure shaft and unlined headrace tunnel (Figure 1c) become common hydropower design solutions after around 1960.

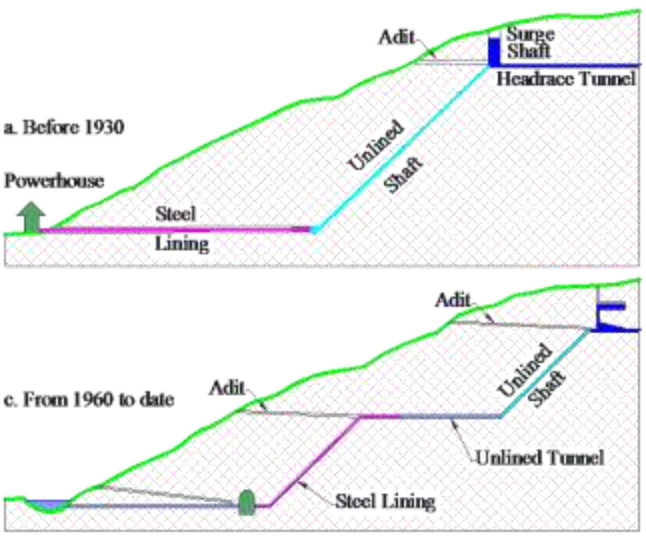

Figure 1. Layout design history of hydropower projects in Norway (Panthi and Basnet, 2016)

Until the beginning of 1970s, all the hydropower schemes consisted of the vented surge chamber to dampen the water hammer and oscillation waves (upsurge waves) produced due to sudden stoppage of turbines or operational changes in the turbine units. However, at Driva hydropower project which came in operation in 1973 had a very steep topography which restricted to build access road to intermediate adit and top of vented surge shaft. As a result, an Air Cushion Surge Chamber with a solution as indicated in Figure 1d was implemented (Selmer-Olsen, 1974; Panthi and Broch, 2022). Today, Norway has 10 hydropower schemes where Air Cushion Surge Cambers are used to control the water hammer and oscillation waves generated in the headrace system due to sudden changes in the operation mode of the plant.

The benefit of this solution is that a hydropower scheme can avoid an inclined or vertical shaft. Instead, a long unlined high-pressure headrace tunnel may connect the intake directly with underground powerhouse through a very short steel penstock shaft near the powerhouse. At present, Norway has many unlined pressure tunnels and shafts of varying static heads with maximum static water head of 1047m at Nye Tyin hydropower project, which came in operation in 2004 (Figure 2).

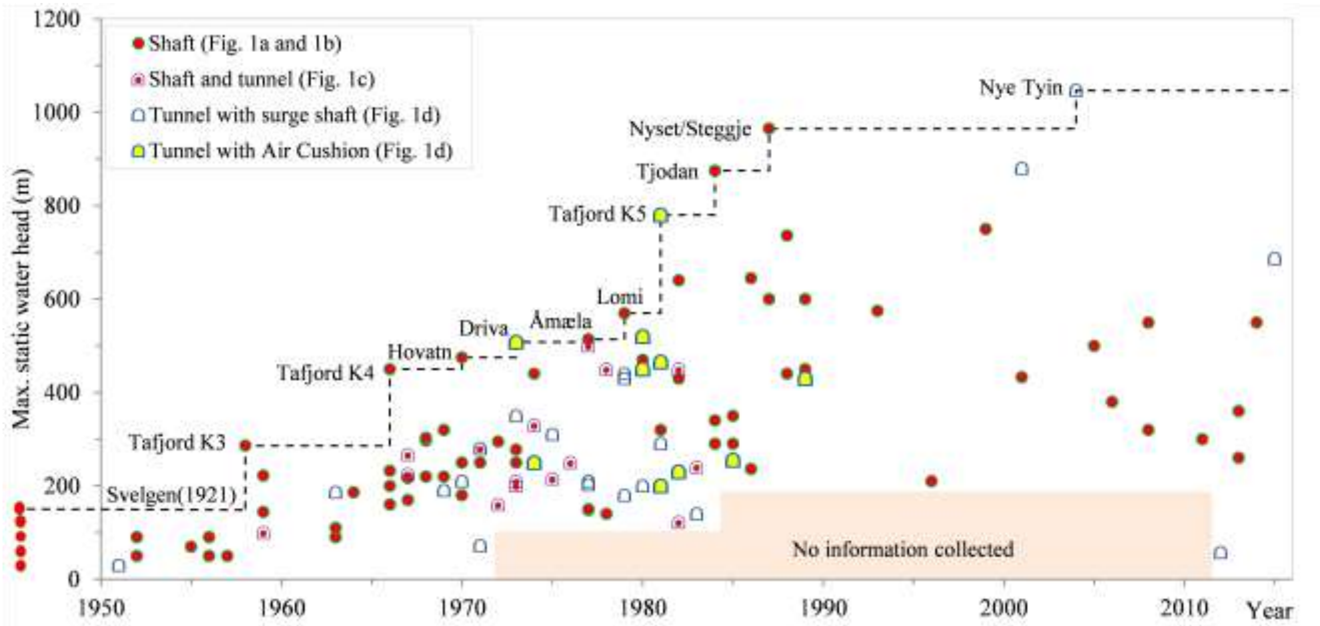

Figure 2. The static head variation of Norwegian unlined pressure tunnels and shafts over time. The figure is an updated version from Broch (2013) (Panthi and Basnet, 2016)

Most of the unlined pressure tunnels and shafts have been and are being successfully operated with no long-term instability problems excluding few exceptions, which were the basis for the development of design principles and criteria. Even though, all unlined high-pressure tunnels and shafts follow the developed design principles and criteria, there are some cases of failures even in modern time where further investigations were needed with substantial mitigation measures applied after the first water filling. Some of the major failure cases of tunnels and shafts with rock type and construction completion year are presented in Table 1.

Table 1: Failure of unlined pressure shafts and tunnels in Norway (Broch, 1982; Selmer-Olsen, 1985; Solli, 2018)

Project	Year	Waterhead (m)	Rock types	Cross-section Area (m^2)	Failure condition
Herlandsfoss	1919	136	Mica-schist	8.0 (Tunnel)	Hydraulic fracturing
Skar	1920	129	Gneiss-granite	Tunnel	Completely failed
Svelgen	1921	152	Sandstone	4.5 (Shaft)	Minor leakage
Byrte	1968	303	Granite Gneiss	6.0 (Shaft)	Hydraulic jacking
Åskåra	1970	210	Sandstone	9.0 (Tunnel)	Hydraulic jacking
Bjerka	1971	72	Gneiss	10.0 (Tunnel)	Leakage
Holsbru	2012	63	Dark Gneiss	18.0 (Tunnel)	Leakage
Bjørnstokk	2017	264	Granodiorite/granite	Tunnel and shaft	Hydraulic fracturing

As shown in Table 1 the first failure case was at Herlandfoss where the unlined pressure tunnel was partly failed, and considerable leakage occurred, and steel lining was further extended as a final solution. At Skar the waterway system was mostly failed due to very low rock cover. At Svelgen, the leakage was observed during the first filling of the pressure shaft. At Bryte the unlined pressure shaft failed due to hydraulic jacking through unfavorably oriented fracture system and faults. Similar was the case at the unlined pressure tunnel of Åskåra hydropower project. At Bjerka, leakage occurred through the pressure tunnel. A recent case of leakage through the pressure tunnel is at Holsbru hydropower project, which came in operation in 2012. The recent case of hydraulic fracturing was at Bjørnstokk, which came in operation in 2017. Most of these cases experienced failure at first water filling and the remedial measures were taken to bring these projects to operation.

3. BASIC DESIGN PRINCIPALS

The design of underground structures for the hydropower projects should be made in such a way that the design provides cost effective, long-term stable and sustainable solution. This can be achieved by considering rock mass as the part of a structural element that counteracts any load or pressure exerted by either unloaded rock mass or hydrostatic water head acting during operation (Edvardsson and Broch, 2002). In addition, combination of tunnel rock support consisting of rock bolts and sprayed concrete applied during construction to achieve safe working environment should be considered as part of the permanent support. It is, however, emphasized here that the sprayed concrete (shotcrete) is a permeable material and hence does not restrict water to penetrate to the rock mass (Panthi and Basnet, 2017). Thus, any design should make sure that there is no possibility of hydraulic fracturing/jacking that may cause water leakage out from the waterway system and constructed powerhouse and transformer caverns are long-term stable. Any design considerations should be based on the results from comprehensive engineering geological investigations. The aim of the design should be to avoid stability and long-term functionality of the underground structure in consideration (Panthi and Broch, 2022).

3.1. Placement of unlined pressure tunnels and shafts

The success history of the implementation and operation of unlined pressure tunnels and shafts in Norway is very good example of the capacity of rock mass that is capable of self- supporting. As shown in Figure 2, the unlined pressure tunnels and shafts built in Norway have varying static heads with maximum water head of 1047 m at Nye Tyin hydropower project. Over 99 percent of unlined pressure tunnels and shafts have been successfully operated with no noticeable long-term instability problems until the de-regulation of power market that took place in early 1990s. The Norwegian experience of development of unlined pressure tunnels and shafts gave good basis for location design of waterway system of hydropower plants and are famously recognized by the world as Norwegian Confinement Criteria (NCC). Equation 1 and Equation 2 are the two criteria that are related to vertical and lateral rock covers (Figure 3-left). The understanding is that both vertical and lateral rock covers should confine the pressure given by the static water head against hydraulic fracturing at any location of the pressure tunnel and shaft (Panthi and Broch, 2022).

$$h > \frac{P_w}{\gamma_r \times \cos\alpha} \qquad (1)$$

$$L > \frac{P_w}{\gamma_r \times \cos\beta} \qquad (2)$$

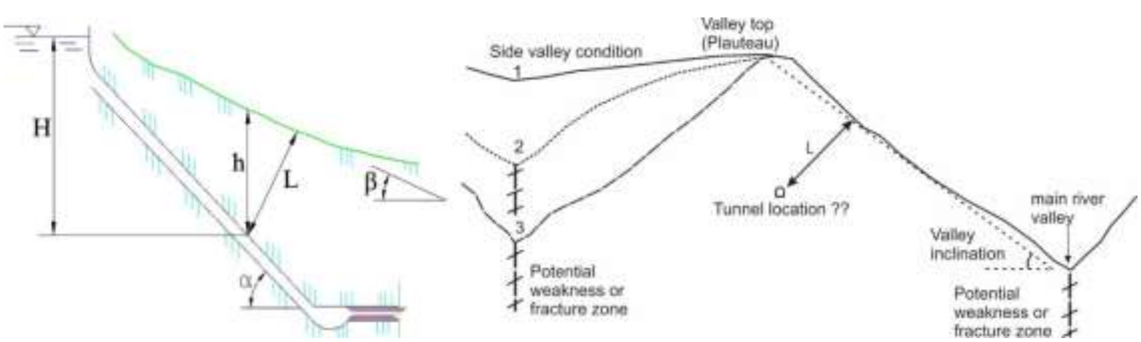

Figure 3. Idealized topography with geometrical parameters used in Norwegian confinement criteria (left) and different topographic conditions that may prevail in a hydropower scheme (right).

In Equation 1 and 2 and Figure 3, *h* is the vertical rock cover, H is the hydrostatic head acting in the tunnel or shaft, γ_w is the specific weight of water, γ_r is the specific weight of the rock, and α is the inclination of shaft / tunnel with respect to horizontal plane, L is the shortest distance from valley side slope topography to the tunnel location and β is the angle of valley side slope with respect to horizontal plane.

In general, the start of highest static pressure point and remaining upward (towards intake) alignment of an unlined headrace system assessed using Equation 1 and Equation 2 provide good result against hydraulic fracturing (jacking) for a topography representing almost no existence of secondary valley (side valley condition 1 in Figure 3-right). However, if the topography consists of more than one deep valleys like shown in Figure 3-right, the location assessment made using these two equations may not provide needed safety margin against hydraulic failure. Therefore, it is important to assess the magnitude of minimum principal stress (σ_3) along the pressurized headrace system which should always be more than the hydrostatic water head (Equation 3).

$$\sigma_3 > P_w \qquad (3)$$

The confinement criteria developed in Norway are mainly for tunnels and shafts that are mostly unlined excluding areas with weakness zones lined with in-situ concrete. Similarly, these criteria are equally relevant for tunnels lined with sprayed concrete (shotcrete) since sprayed concrete is a permeable support and almost equal water pressure will act on the rock mass as that on the sprayed concrete.

In addition, in relatively unjointed and massive rock mass as in Norway, it is important that the pressure tunnels and shafts should be placed in such a way that minimum instability challenges associated to induced stresses are met. The use of proper assessments methods is therefore essential for a meaningful instability assessment of rock burst / rock spalling condition in tunnels. Figure 4 should be used as preliminary basis to locate pressure tunnels and shafts so that rock spalling or rock burst (strain burst) along the alignment are minimized.

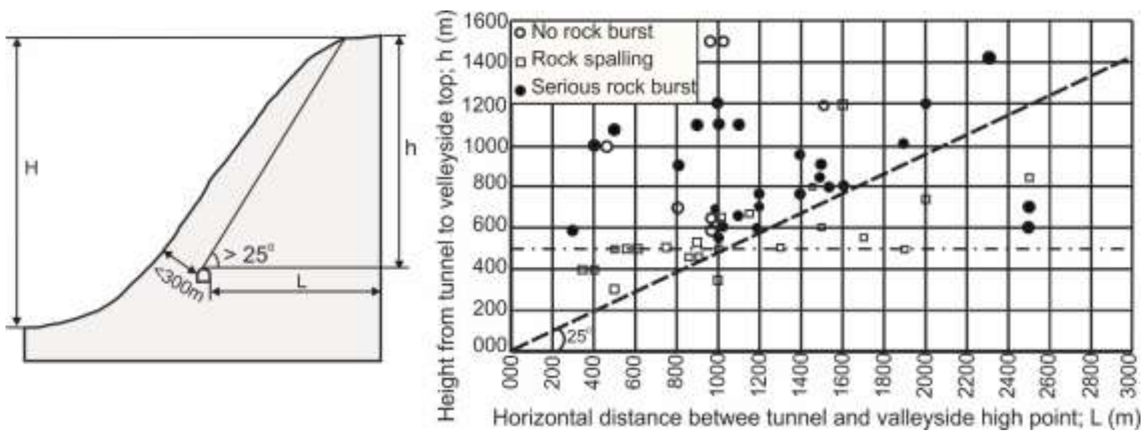

Figure 4. Location of tunnels and shafts with respect to topographic conditions (left), and a plot of rock burst / spalling in relation to height (h) from tunnel to top of valley-side and horizontal distance from tunnel to the top of valley side (L) (Panthi, 2018).

As indicated in Figure 4, most of the tunnels that had vertical height (h) between tunnel and plateau less than 500 meters and angle between tunnel location and plateau less than 25 degrees did not experienced rock burst / rock spalling. The tunnels that had exceeded this threshold were met stability challenges associated to rock burst / rock spalling. However, exceptions are made for the vertical shafts, the white circles located above the separation line in Figure 4-right.

3.2. Leakage assessment from unlined pressure tunnels and shafts

In addition to the placement design of the unlined headrace system, an assessment on the potential water leakage from the headrace system should be carried out. In general, the permeability of rock mass is governed by discontinuities and their engineering geological characteristics. Hence, among the most important aspect of unlined or shotcrete lined headrace system is to control water leakage while the system is in operation at full hydrostatic pressure so that the water leakage is within an acceptable limit boundary which should be less than 1.5 liters per minute per meter tunnel (Panthi, 2006). In an unlined or shotcrete lined pressure tunnel, water gives pressure (Pw) to the rock mass equivalent to the hydrostatic water head (H) as indicated in Figure 5.

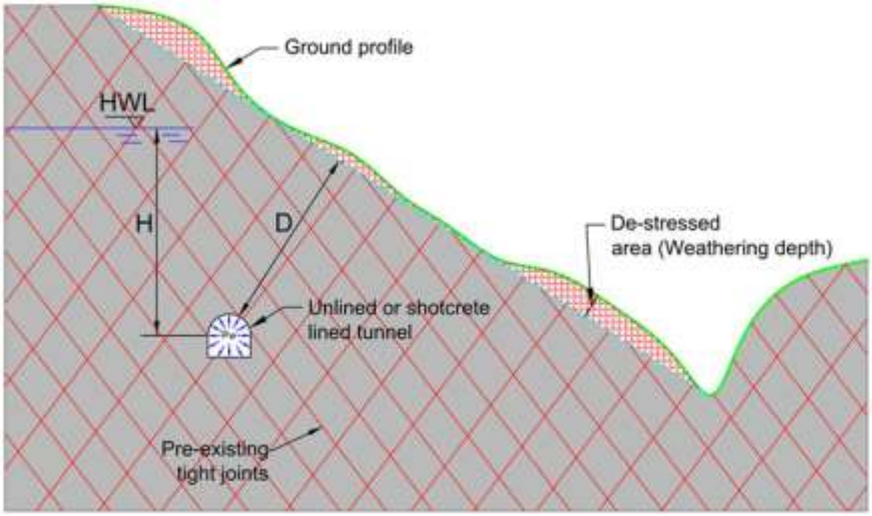

Figure 5. Typical topographic condition surrounding an unlined pressure tunnel / shaft (Panthi and Basnet, 2021).

As shown in Figure 5, due to presence of joints and discontinuities, the rock mass behaves differently when it is exposed to water pressure. The leakage potential through an unlined pressurized headrace system is therefore governed by degree of jointing in the rock mass and condition within different joint sets such as joint aperture, joint infilling conditions, spacing of the must unfavorable joint set and joint persistence. In addition, hydrostatic water head and shortest distance from the waterway to the topographic slope surface are very crucial to be assessed. Equation 4 proposed by Panthi (2006) may be used to estimate specific leakage (q_t) from an unlined or shotcrete lined pressurized headrace system. In Equation 4, H is the hydrostatic water head (Figure 4), J_n is joint set number, J_r is joint roughness number and J_a joint alteration number as described by Barton et al (1974) in the Q-system of rock mass classification. The joint permeability factor (f_a) given in Equation 4 can be estimated using Equation 5 as recommended by Panthi and Basnet (2021).

$$q_t = f_a \times H \times \frac{J_n \times J_r}{J_a} \qquad (4)$$

$$f_a = \mathcal{L} \times \frac{J_p}{D \times J_s} \qquad (5)$$

In Equations 4 and 5, f_a is a joint permeability factor with unit l/min/m^2 which may vary between 0.001 and 0.25 and is related to joint spacing (J_s) and joint persistence (J_p) measured in meters, shortest distance from tunnel to surface topography of the valley side slope (D) and $\mathcal{L}$ which is equivalent to 1 lugeon (1 l/min/m).

3.3. Shape and size of unlined pressure tunnels and shafts

The extent of frictional head-loss of a headrace tunnel or shaft depends on the shape and size. TBM excavated tunnels and shafts are circular in shape and have smooth wall surface and are hydraulically ideal in shape. However, it is not always feasible to use TBM as an excavation method for these tunnels and shafts since success of TBM application is largely dependent on the length of the tunnel and shaft to be excavated (Panthi, 2015). In general, drill and blast method of excavation is preferred construction method due to its flexibility in making quick engineering decisions if unforeseen geological conditions arise. However, the tunnels and shafts excavated using drill and blast method have undulated surface of varying smoothness due to overbreak caused by blasting and presence of fractured rock mass. In addition, shape and size of an unlined pressure tunnel / shaft will be determined mostly by construction requirements and easiness. The most practical tunnel shapes excavated using drill and blast method are inverted D or horseshoe shaped. The profile of excavated tunnels and shafts may either be unlined / shotcrete lined or concrete / steel lined depending on the rock mass and in-situ stress condition. The excavated surface of the tunnel walls will have undulation which depends on the quality of rock mass and proficiency of the contractor involved in the construction.

The optimum hydraulic shape of a water tunnel occurs when wall height of a tunnel is between 1 to 1.3 times the radius of the tunnel curvature above spring level. Rougher the surface, pronounced will be the flow resistance due to large undulations. Following Lysne et al (2003) and Basnet and Panthi (2018), frictional headloss (Equation 6 and 7) can be calculated using coefficient of resistance called hydraulic roughness represented by either friction factor (f) or manning coefficient (M_R) and calculated by Equation 8 and Equation 9 which largely dependent on both surface roughness (ε_R), the Reynolds number (R) and the hydraulic radius (R_h) of a tunnel / shaft which is a function of area (A) and perimeter (P) (Equation 10). In Norway, it is normal to keep water velocity in an unlined or shotcrete lined pressure tunnels between 1 to 2 m/sec.

$$H_f = \frac{f L v^2}{2g(4R_h)} \quad (6)$$

$$H_f = \frac{L v^2}{M^2 {R_h}^{4/3}} \quad (7)$$

$$\frac{1}{\sqrt{f}} = -2\log\left(\frac{\varepsilon_R}{14.8\, R_h} + \frac{2.51}{R\sqrt{f}}\right) \quad (8)$$

$$M_R = \frac{24}{{\varepsilon_R}^{1/5}} \quad (9)$$

$$R_h = \frac{A}{P} \quad (10)$$

In addition, singular losses that usually are formed entrance loss, trash rack loss, gate loss, bend loss, transition loss, niches loss, rock trap loss, exit loss etc. should be considered. For detail on calculation methods one can read Basnet and Panthi (2018). These singular losses cannot be avoided but could be minimized. It is therefore important to optimize the size of a tunnel taking consideration on the shape and size governing the frictional headloss and overall construction cost.

3.4. Shape and size of underground caverns

The size of an underground cavern is optimized based on the desired functional need. The shape of the cavern is designed as such that it achieves evenly distributed stresses along the whole periphery (roof and walls). The evenly distributed stress condition can be achieved by giving the cavern a simple shape as possible with an arched roof and with limited protruding corners. If a cavern roof is designed with a protruding corner which many do so to accommodate the space for crane beam, there is a chance that the cracks are developed in the corners between the transition of wall and arched roof. Such design may reduce stability considerably and the failure may extend further down to the cavern walls. It is emphasized here that the in-situ stress measurements should be carried out so that the magnitude and direction of the stresses are know. A comprehensive stability assessment should be carried out to ascertain that there is no serious stability problem that may cause serious damage to both walls and roof of the cavern.

4. OPERATION OF UNLINED PRESSURE TUNNELS AND SHAFTS IN HARD ROCKS

Norway has almost half of the reservoir capacity in Europe and thus has a great potential for providing the much-needed flexibility for the European power market in the future. After de-regulation of the power market in early 1990s, power price volatility has increased considerably which is intensifying in past 20 years. As a result, the operation of hydropower plants in Norway is becoming very dynamic. Operating the existing and new power plants with dynamic operational regime confronts with various technical challenges and operational risks. The Norwegian Research Centre for Hydropower Technology (HydroCen) is conducting research in several areas to assess such technical challenges and provide sustainable solutions to meet the future flexibility requirements in Norwegian hydropower system. The scope of research ranges from long-term stability of underground structures (especially the unlined pressure tunnels and shafts), electrical and mechanical systems, environmental impacts, and market conditions (Neupane et al, 2021). The assessment of the production data of some Norwegian hydropower plants (Figure 6) indicated that the dynamic operational regime looks dramatic in most of the hydropower plants which has direct influence on the long-term stability of unlined pressure tunnels and shafts.

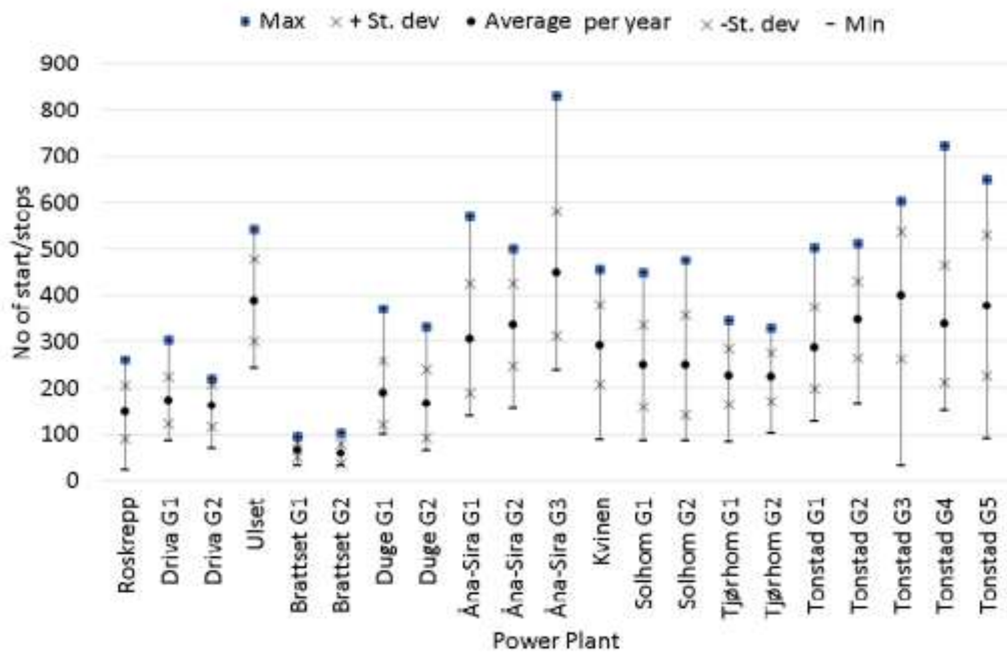

Figure 6. Statistical values of start/stops of some hydropower plants in Norway (Neupane et al, 2021).

As seen in Figure 6 the starts/stops (operational change) sequences of some hydropower plants show a clear distinction between hydropower plants with or without operational restrictions. Both average values and standard deviation are much smaller for hydropower plants with operational restrictions. The lowest number of starts/stops among all power plants is 65 per year per unit for Brattset. All other powerplants experience an average of 200 to 400 starts/stops sequences in annual average. Since over 95 percent of pressure tunnels and shafts of Norwegian hydropower plants are unlined, water is in direct contact with the rock mass and the pressure transients resulting from operational changes has direct impact on the discontinuities in the rock mass, which in long-term are causing block falls because of cyclic fatigue due to frequent pressure pulsations (Figure 7).

Figure 7. Examples of block falls and collapses witnessed in pressure tunnels and shafts of Norwegian HPP.

The analysis carried out by Neupane et al (2020) for two-year long real-time monitored data from the unlined headrace tunnel of Roskrepp hydropower plant in Southern Norway indicates that there occurs time lag between the water pressure in the tunnel and pore-water pressure in the rock mass deep into the tunnel wall (Figure 8).

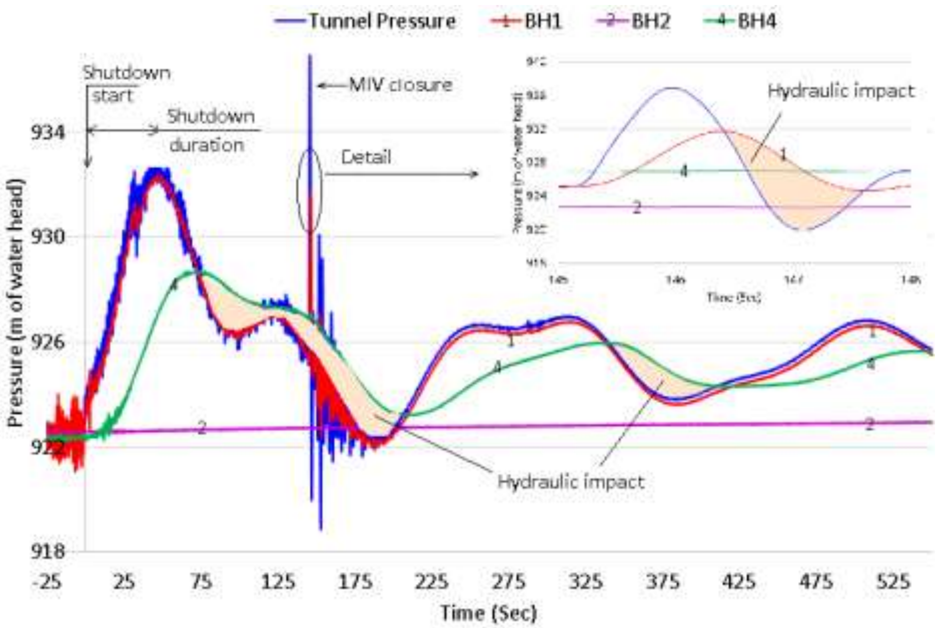

Figure 8. Tunnel pressure transient with pore pressure responses from boreholes (Neupane et al, 2021)

Figure 8 shows a pressure transient in the headrace tunnel and the rock mass pore pressure during a typical shutdown event at Roskrepp hydropower plant. The rock mass pore pressure measured in three boreholes, along with the hydraulic impact during the transient are shown in the figure. Both water hammer and mass oscillation are recorded by the pressure sensor because the measurement is done at a location between the turbine and the surge shaft. As seen in Figure 8, the boreholes which intersect the conductive joints in the rock mass i.e., BH1 and BH4 strongly respond to pressure transients whereas other boreholes are non-responsive indicating that there is no direct hydraulic contact. As one can see, BH1 registers a stronger response to pressure transients but there is very little time-lag during mass oscillation, resulting in very little to zero hydraulic impact during mass oscillation and significant hydraulic impact during water hammer. On the other hand, BH4 shows a clear time-lag during both mass oscillation and water hammer. But the amplitude of pore pressure in BH4 in response to the water hammer is smaller as compared to BH1. This difference in the response is due to different resistance to the flow through joints in the rock mass, which is a function of void geometry of joints and the length of flow path i.e., joint length between tunnel wall and its intersection points with individual boreholes. The distance between tunnel wall and boreholes (length for flow path) at BH1 and BH4 are 2.3 m and 8 m, respectively.

From a theoretical point of view, it can be said that the hydraulic impact on the joints in the rock mass depends on the magnitude of change of discharge during shutdown and the duration of shutdown event. These two parameters govern the nature of transient pressure pulses which travel into the joint wall surface in the rock mass causing additional forces. Another important parameter is the static pressure before transient which governs the resistance to flow through joints during transients. The joint hydraulic aperture is influenced by the effective stress across joints. During the operation of a power plant, the effective stress across the joints can vary depending on reservoir levels, which may change the initial hydraulic aperture before transients. Such changes of transient and changes in pore water pressure in the rock joints will cause a fatigue over the long period of the operation of hydropower plants causing a new crack in the rock mass leading to block failure as shown in Figure 7.

5. OPERATION OF PRESURE TUNNELS IN SWELLING ROCKS

It is important to note here that the rock mass in the periphery of hydropower water tunnels is unloaded and drained during tunnel construction and then the tunnel is exposed to cyclic wetting and drying processes during the operational lifetime of the project. If the pressure tunnels are aligned through weak and weathered rocks of sedimentary and volcanic origin such as flysch, volcanic sediments, andesites; and the pressure tunnel is shotcrete lined; there is a risk of collapse due to swelling of rocks (Figure 9). This is because, the interaction between rock mass and flowing waters through pressure tunnels may cause swelling of weak and weathered rocks of sedimentary and volcanic origin.

Figure 9. Collapsed tunnels passing through weak and weathered rocks of volcanic and sedimentary origin (left and center) and a cored highly weathered and weak flysch rock (right).

It is emphasized that the surrounding rock mass in pressure tunnels supported with shotcrete lining comes in direct contact with water which may lead to time-dependent deformation caused by both swelling and squeezing causing instability in tunnels as indicated in Figure 9. Hence, proper stability assessment and support measures are applied in pressure tunnels passing through swelling rocks. To do so, the swelling potential of intact rocks are first assessed by conducting mineralogical test to identify swelling clay minerals such as montmorillonite, anhydrite, zeolite etc. The next step will then be to carry out swelling pressure tests in intact rock samples in repeated cycles of drying and wetting (Selen et al, 2021). An example of such tests is shown in Figure 10.

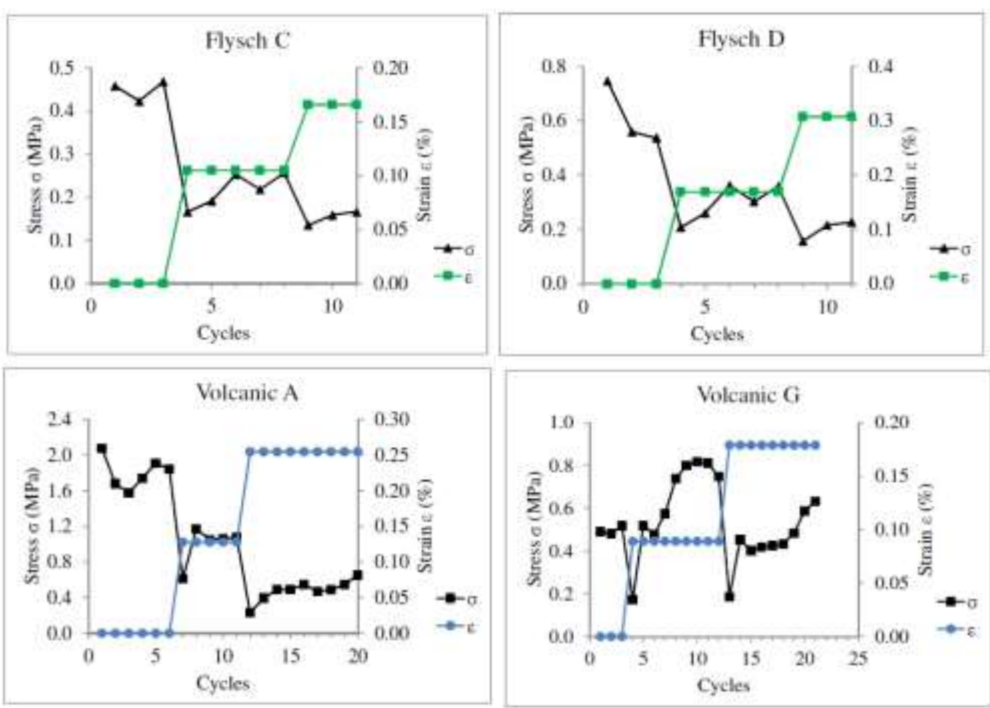

Figure 10. Cyclic swelling pressure development of intact rocks under controlled deformation in oedometer

It is noted here that extensive moisture fluctuations are special features of pressure tunnels of hydropower plants compared to tunnels built for infrastructure projects. The recent rend of the development of wind and solar power which is dependent on the wind intensity and day light conditions, respectively, the hydropower plants functions as energy balancing agents and are seldom operated to their base load. This changed scenario causes fluctuation in the operation regime of the power plants. To determine the effect of moisture fluctuations on the swelling behavior of weathered rocks surrounding pressure tunnels, repeated wetting and drying cycles of swelling tests should be performed on intact rock samples.

6. CONCLUSIONS

The experience gained from the construction and operation of Norwegian unlined pressure tunnels and shafts helped to develop design criterion and stability assessment principles focusing on engineering geology and rock mass quality. These design criteria and principals have got worldwide acceptance. As have been highlighted in this manuscript, the success of these criteria and principals depends on the engineering geological, geo-tectonic and topographic environment prevailing at selected locations where the hydropower plants to be built. As have also been demonstrated, recent operational trends of hydropower plants with more frequent start stop sequences have caused more dynamic load due to pore water fluctuation in the rock mass which is resulting to both long-term fatigue in hard rock mass and plastic deformation in weak and weathered rock mass of sedimentary and volcanic origin due to swelling of rock mass.

REFERENCES

Basnet, C. B., Panthi, K. K. 2018. Roughness Evaluation in Shotcrete-lined Water Tunnels with Invert Concrete based on Cases from Nepal. Journal of Rock Mechanics and Geotechnical Engineering, vol. 10, pp. 42-59.

Broch, E. 1982. The development of unlined pressure shafts and tunnels in Norway. ISRM International Symposium. International Society for Rock Mechanics.

Broch, E. 2013. Underground hydropower projects - Lessons learned in home country and from projects abroad. Norwegian Tunneling Society.

Edvardsson, S., Broch, E. 2002. Underground powerhouse and high-pressure tunnels. Hydropower Development Volume 14. Norwegian University of Science and Technology, 99p.

Neupane, B., Panthi, K. K., Vereide, K. 2020. Effect of Power Plant Operation on Pore Pressure in Jointed Rock Mass of an Unlined Hydropower Tunnel: An Experimental Study. Rock Mechanics and Rock Engineering, vol. 53, pp. 3073–3092.

Neupane, B., Vereide, K., Panthi, K. K. 2021. Operation of Norwegian hydropower plants and its effect on block fall events in unlined pressure tunnels and shafts. Water 2021, vol. 13 (1567), 20p.

Panthi, K. K. 2006. Analysis of engineering geological uncertainties related to tunneling in the Himalayan rock mass conditions. Norwegian University of Science and Technology. Doctoral thesis 2006: 41, 188p. ISBN 82-471-7825-7 and ISSN 1503-8181.

Panthi, K.K.. 2014. Norwegian Design Principle for High Pressure Tunnels and Shafts: Its Applicability in the Himalaya. Hydro Nepal: Journal of Water, Energy and Environment, Issue 14, pp. 36-40.

Panthi, K.K. 2015. Himalayan rock mass and possibility of limiting concrete lined pressure tunnel length in hydropower projects. Geosystem Engineering, vol. 18(1), pp. 45-50.

Panthi, K. K. 2018. Rock Burst Prediction Methods and Their Applicability. Chapter 11.2 - Rock burst: Mechanisms, Monitoring, Warning and Mitigation. Elsevier, 10 p.

Panthi, K. K., Basnet, C. B. 2017. Design review of the headrace system for the Upper Tamakoshi Project, Nepal. International Journal on Hydropower and Dams, vol. 24(1), pp. 60-67.

Panthi, K. K., Basnet, C. B. 2021. Fluid Flow and Leakage Assessment through an Unlined/Shotcrete Lined Pressure Tunnel: A Case from Nepal Himalaya. Rock Mechanics and Rock Engineering, vol. 54, pp. 1687–1705.

Panthi, K. K., Broch E. 2022. Underground Hydropower Plants. Comprehensive Renewable Energy, 2nd edition. Letcher, Trevor M. (eds.) Oxford, Elsevier, vol. 6, pp. 126–146.

Selen, L., Panthi, K. K., Vergara, M. , Mørk, M. 2021. Investigation on the Effect of Cyclic Moisture Change on Rock Swelling in Hydropower Water Tunnels. Rock Mechanics and Rock Engineering, vol. 54, pp. 463–476.

Selmer-Olsen, R. 1974. Underground openings filled with high-pressure water or air. Bulletin of the International Association of Engineering Geology, vol. 9(1), pp. 91-95.

Selmer-Olsen, R. 1985. Experience gained from Unlined High Pressure Tunnels and Shafts in Hydroelectric Power Stations in Norway. Norwegian Soil and Rock Engineering Association, Publication 3.

Solli, A. S. 2018. Evaluation on Hydraulic Splitting at Bjørnstok Hydropower Project. MSc. Thesis. Department of Geoscience and Petroleum, Norwegian University of Science and Petroleum (NTNU).

Vogt, J. H. L. 1922. Trykktunneler og geologi (Pressure tunnels and geology). Report no. 93. Norges Geol. Undersøkelse, Oslo, Norway.

Proceedings of the NROCK 2023
The IV Nordic Symposium on Rock Mechanics and Rock Engineering
ISBN 978-9935-9436-2-0
DOI 10.33112/nrock2023

The unrest on the Reykjanes Peninsula and eruption in Fagradalsfjall 2021 & 2022

Kristín Jónsdóttir, Icelandic Meteorological Office, Reykjavík, Iceland

The Reykjanes Peninsula is an oblique transform zone marked with adjacent volcanic systems intersected by strike-slip earthquake faults. For the first time since modern instrumentation was installed (last 30 years) a clear, rapid uplift signal was observed on the peninsula in January 2020, interpreted as a magmatic intrusion. This event was followed by several events of further unrest. Between January to July 2020 three intrusions were detected in the vicinity of Mt. Þorbjörn and from July to August 2020 another near Krýsuvík, all accompanied by increased seismic activity.

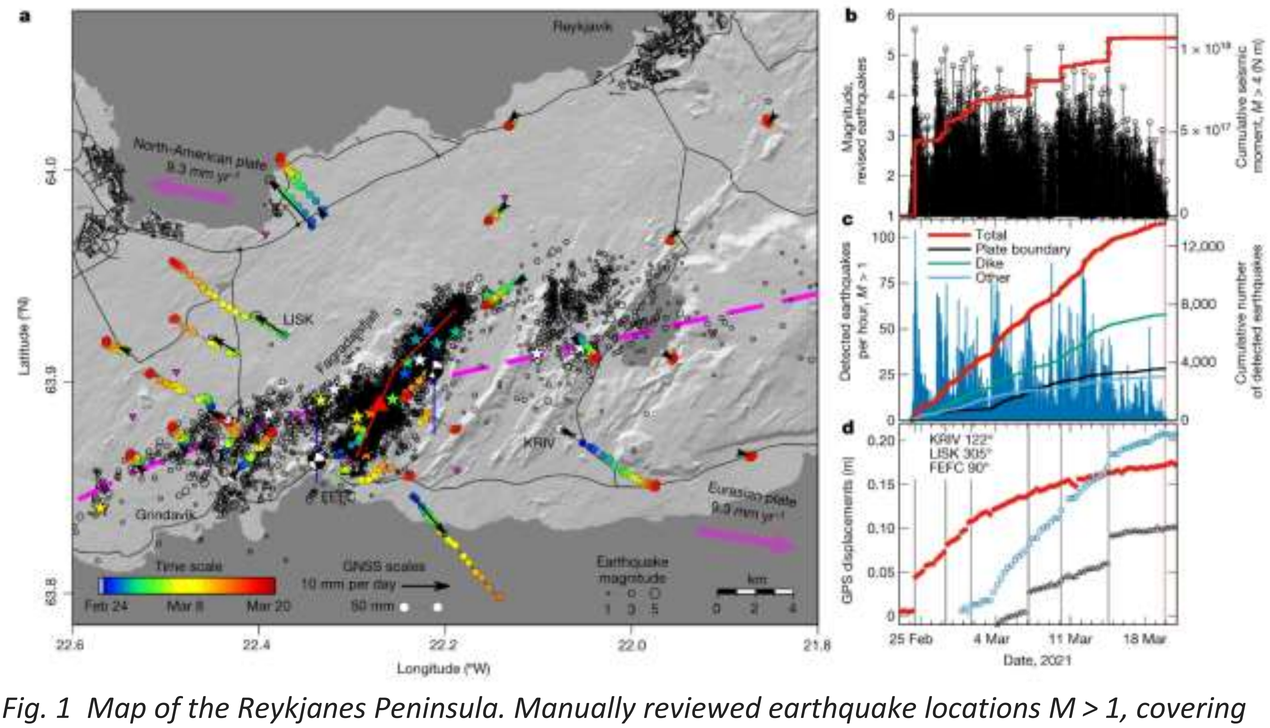

Fig. 1 Map of the Reykjanes Peninsula. Manually reviewed earthquake locations M > 1, covering the period from 24 February to 19 March 2021.

On the 24th of February 2021, a M5.7 earthquake was recorded NE of Fagradalsfjall and a dyke intrusion was detected beneath Fagradalsfjall a few days later. The intrusion continued until mid-March by which time the estimated length of the dyke was 9 km and the associated volume change 34 million cubic meters. This intrusive event triggered an unprecedented, roughly three-weeks long earthquake sequence, which extended over an area of some 350 km2 and counted over 50.000 earthquakes, of which 600 were above M3. It culminated in an effusive lava forming eruption which commenced on the 19th of March 2021 at 20.35 UTC. Lava was initially erupted from a ~100 m long fissure which opened in Geldingadalur valley in Fagradalsfjall. In the final days before the onset of the eruption, the seismicity as well as all deformation signals had dramatically decreased, at that time unexpected observables shortly before eruption onset.

This was the first eruption on the Reykjanes Peninsula in 800 years, and the first one in Fagradals-fjall in over 6000 years. The eruption was characterized by lava fountaining and the extrusion of basaltic lava flows, with an initial effusion rate of ~5 m3/s. The effusive eruption was accompanied by the release of magmatic gases. Activity remained stable until the 5th of April when two new fissures opened approximately 500 m north of the initial erupting craters. In total six fissures opened between the 5th and 13th of April. After the 27th of April, lava was erupted from one main vent (the fifth opening in temporal order) which in turn formed a crater that reaches ~120 m over the pre-eruption landscape. Lava was last seen spewing from the vent on September 18th.

Fig. 2 Icelandic Meteorological Office seismologist Kristín Jónsdóttir stands on solidified black basalt that glows red from erupting Fagradalsfjall behind her.

In total the eruption which started in the valley of Geldingadalir inside the Fagradalsfjall mountain massive produced a lava field covering about 4.9 km2 and created a total SO2 output of 0.9 Mt. The eruption progressed through different phases characterized by different emission sources, eruptive style, intensities, and associated hazards. However, in terms of intensity the eruption was small and arelatively easily accessible eruption, where the main hazards were in the near field to the thousands of visitors which had to be mindful of volcanic gasses, lava outbreaks and occasional minor lava bombs.   By joining forces in monitoring and utilizing the available expertise in different institutions, the Civil Protection, Icelandic Institute of Natural History, Institute of Earth Sciences of the University of Iceland, Iceland Geosurvey, the Environmental Agency, and the Icelandic Meteorological Office, which runs the 24/7 monitoring services, a good overview was established of the evolution of the eruption and its hazards.

Reference:
Fig. 1: Overview of seismicity and deformation.
From: Nature 609, 523–528 (2022). https://doi.org/10.1038/s41586-022-05083-4

Proceedings of the NROCK 2023
The IV Nordic Symposium on
Rock Mechanics and Rock Engineering
ISBN 978-9935-9436-2-0
DOI 10.33112/nrock2023.3

The potential for geothermal energy exploitation in Norwegian tunnels

Sondre Gjengedal (sondre.gjengedal@ngi.no)
Pål Drevland Jakobsen (pal.drevland.jakobsen@ngi.no)

The Norwegian Geotechnical Institute
Trondheim, Norway

ABSTRACT

Renewable thermal energy is a highly sought-after resource in many parts of the world, as a measure to reduce our reliance on fossil fuels and electric power as energy sources for space heating of buildings. Shallow geothermal energy is one of the preferred environmentally friendly thermal energy resources in Norway, where heat stored underground is utilized in conventional heat pump systems via 200-300 m deep boreholes. However, the underground space in our urban areas are under continuous development and puts increasing demand on both surface and sub-surface city planning. The public need for infrastructure tunnels, road or railway tunnels, is most often prioritized rather than development of geothermal systems. Tunnels can thus be a hurdle for the planning and further development of geothermal utilization in cities. In many European countries' tunnels are now increasingly considered as a source of thermal energy in their self. Large volumes of rock mass and groundwater are made available in tunnels and the tunnel can be "activated" for harnessing the heat energy within, so called *Energy tunnels*. The potential for utilizing geothermal energy from Norwegian tunnels via heat pump systems is now being investigated. The tunnels can be activated in several manners, where both passive closed loop systems or active open loop groundwater systems are the two main potential solutions. The applicability of incorporating these systems are here assessed for the Norwegian tunnel design and an initial view on the potential for utilizing our tunnel infrastructure is given. The potential thermal energy available in existing road and railway tunnels alone range in the several TWh scale if all tunnels are activated. The many thousands of kilometers of tunnels in Norway might thus become a future energy resource and a potential pathway to reach our climate goals and to increase the rate of energy transition to renewable energy sources.

KEYWORDS

Geothermal energy; Tunnels; Heating & Cooling Potential; Urban development

1. INTRODUCTION

The Norwegian energy mix in the building sector has traditionally been dominated by electricity generated by hydro power facilities, which for many decades have provided abundant, affordable and environmentally friendly energy. However, the current energy crisis and shortage of electricity and fossil gas in Europe has affected the global energy market and has sparked an increase in energy costs that has never been seen in Norway until now. The cost increase has triggered energy saving actions in all parts of society and we now see an increase in the rate of energy transition to renewables and alternative energy sources. Renewable thermal energy is a highly sought-after resource in all parts of the world, particularly as a measure to reduce our reliance on fossil fuels and electric power as energy sources for space heating of buildings and industrial processes. This is also the case for Norway and it is expected that the rate of geothermal utilization will see a swell in new development in the years to come.

Shallow geothermal energy is one of the preferred environmentally friendly thermal energy sources in Norway, where heat stored underground is utilized in conventional heat pump systems via 200-300 m deep boreholes, so called energy wells. This is deemed favorable because it is a local form of energy production that reduce the load on the power-grids and require less infrastructure development than the traditional high-voltage electricity system. Reduced need for electric power leads to reduced reliance on, and more independence from, economical and political situations that can affect the operational costs of a heating system. In the northern European countries, the need for heating is particularly apparent, but energy utilized for cooling applications and air/surface/process conditioning is increasingly relevant also here, especially for many new buildings in Norway due to the updated building code standards and regulations.

Both a buildings' heating and cooling demand can be realised with shallow geothermal energy systems, and particularly cooling is favorable due to the relatively low annual temperatures in the ground in Norway. A review study carried out in 2011 showed the important role that shallow geothermal energy can play in Norway's energy mix, where essentially all the heating and cooling required by Norway's building mass and industry can be covered by shallow geothermal systems, amounting to a saving of approximately 36.7 TWh of the electric energy annually (Ramstad, 2011). This saving on electric energy can then be made available for utilization in other sectors, which Statnett (the system operator of the Norwegian power system) project to have a significant increase in electric demand towards 2050. In short terms Statnett estimate that Norway's electric energy needs will increase by 24 TWh within 2027, resulting in a negative energy balance in four years. Thus, increased use of shallow geothermal energy now seems even more relevant than ever, especially given the increasing economic competitiveness of heat pump systems due to the high cost of electric and fossil energy on the European market. Today it is estimated that Norway has approximately 60 000 shallow geothermal systems in operation, producing 3.0 TWh of heat annually (Midttømme et al., 2020). The potential for further development is particularly apparent if these figures are compared to the 590 000 shallow geothermal systems in operation in Sweden, producing 17.1 TWh annually (Gehlin et al., 2020).

The underground space in the urban areas around the world are under continuous development and puts increasing demand on both surface and sub-surface city planning. One issue for conventional geothermal systems in urban cities arise when energy wells must compete with other underground infrastructure for the same underground space. The need of the public for infrastructure tunnels is most often prioritized over the geothermal systems of private contractors or building owners. These challenges are now increasingly being met by stakeholder and innovation & research communities by integrating energy systems directly into infrastructural components of buildings, the so-called *energy geostructures,* better known as *energy piles*, *energy walls*, *energy slabs* and so forth. While the thermal yield of such geostructures does not always match that of optimized conventional boreholes, the objective of using sub-surface structures is to potentially reduce the capital costs for shallow geothermal energy systems as well as adopting these systems into urban areas, where land availability is an issue.

Energy tunnels is one such integrated system where the tunnel itself is used for thermal energy production and heat and cold storage purposes. A variety of tunnel types can be employed for this purpose; road and railway tunnels, sewer systems, caves & mines, bomb shelters etc. The main difference of design and utilization rely primarily on how the thermal energy is accessed in these tunnels and at which temperature the heat can be extracted. Norway as a country has long tradition from tunnelling and use of our underground space, with more than 2100 tunnels and caverns nationwide, and today Norway still has a high tunnelling activity in our major urban cities (NFF, 2022). The potential for utilizing our tunnel infrastructure for energy purposes is thus a potential pathway to reach our climate goals and to increase the rate of energy transition to renewable energy sources.

2. ACTIVATION OF TUNNELS FOR ENERGY UTILIZATION

As with all shallow geothermal systems used for heating and cooling applications, tunnels can be activated for energy utilization via two different types of geothermal system designs, namely the *closed loop* system or the *open loop* system. In the closed loop design the tunnel is equipped with embedded heat exchanger elements (Figure 1), e.g. integrated HDPE pipes or steel plate heat exchangers, which circulates a heat carrier fluid within a tunnel piping network. The fluid within these pipes absorbs heat indirectly through these pipe walls and is able to perform also bellow freezing temperatures, as is typical for conventional borehole systems. The open loop design employs a pumping system that extract energy directly from water that is intruded into the tunnel, e.g. groundwater that enter via the fractures in the surrounding rock formation. The main criteria for employing the open loop system rely on the native water temperature within the tunnel, which must be above freezing levels. This inevitably vary depending on the location of the tunnel in question. One example of this variation is e.g. documented by Rybach (2010) whom has shown that in Switzerland the water temperature vary form 10 – 50 °C depending on the tunnel location, length and depth bellow the ground surface. In Norway the climate is colder than in Switzerland, which can pose a challenge for open loop system in situations where the water is close to freezing temperatures during the winter.

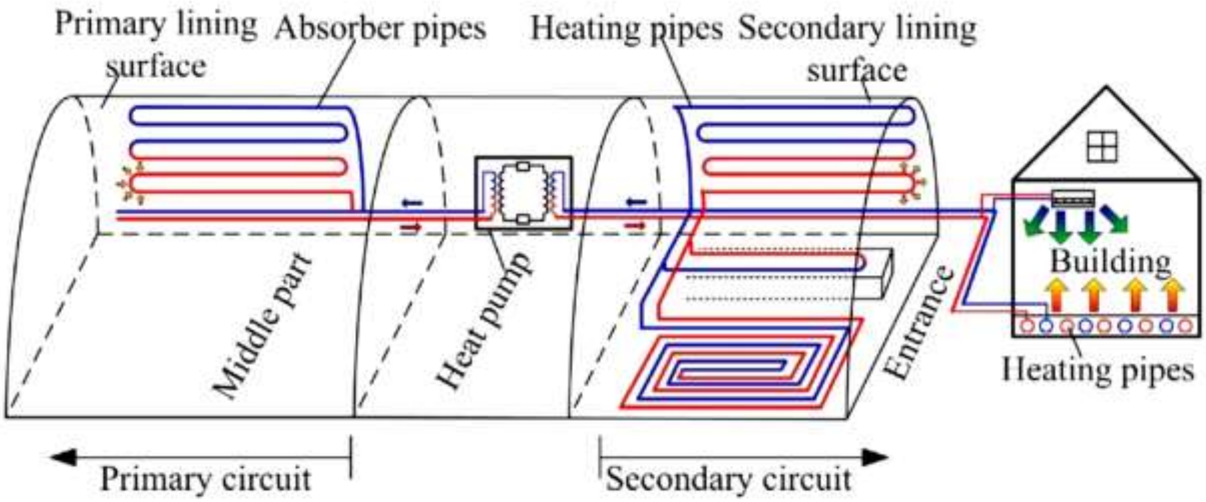

Figure 1: Principles for closed loop tunnel lining embedded heat exchangers (Zhang et al., 2014)

Different uses of the extracted and injected heat are mentioned in the litterateur, such as heating and cooling of subway stations or buildings near the tunnel (Nicholson et al., 2014; Barla et al., 2016; Stemmle et al.; 2022), heating the tunnel lining itself (Zhang et al., 2014), de-icing at the tunnel portals (Islam et al., 2006), road pavements, bridge decks and plattforms (Dupray et al., 2013; Bowers and Olgun, 2013). In Norway the potential for utilizing a tunnel in this manner is not widely recognized. Nevertheless, the concepts are employed in sewer tunnels in several of our largest cities. The VEAS-tunnel in the city of Oslo was equipped for this purpose already inn the 1980's where one of the tunnels in the sewer system is utilized as an open loop heat source for a local 30 MW district heating system, producing approximately 130 GWh annually for the surrounding customers. A closed loop sewer system is employed in the city of Stavanger where a 500-kW heat pump system produce 1,5 GWh of energy each year and provides heating and cooling to the town hall and associated buildings in the city center (Grønnestad, 2017).

The concept of utilizing road and railway tunnels as thermal energy sources was tested already in the early 2000's and world wide there are now reports of test pilot facilities in Japan (Islam et al., 2006), South Korea (Lee et al., 2012), China (Zhang et al., 2014), Germany (Schneider & Moormann; 2010), Austria (Markiewicz, 2004; Unterberger et al., 2004), Switzerland (Stemmle et al., 2022) and Italy (Barla et al., 2014; Insana, 2020;). Recently the concept has seen an increased interest among researchers and stake holders, as is evident by the increasing number of studies that investigate the thermal potential in different countries. Stemmel et al. (2022) has reviewed the current activity on activating road and rail tunnels in Europe and Asia and state that the most common configuration world wide, in view of number of tunnels, is the closed loop design with integrated pipe systems. However, the thermal potential in these installations are not elaborated and most installations seemingly only activate smaller sections of the tunnels, rather than complete and full-scale activation. The largest closed loop installation covers approximately 3 330 m^2 of the Reinstein tunnel B10 (Csesznák, Järschke & Wittke; 2016), where 6 720 meters of 25 mm PEX pipes are integrated into the tunnel wall lining (Figure 2).

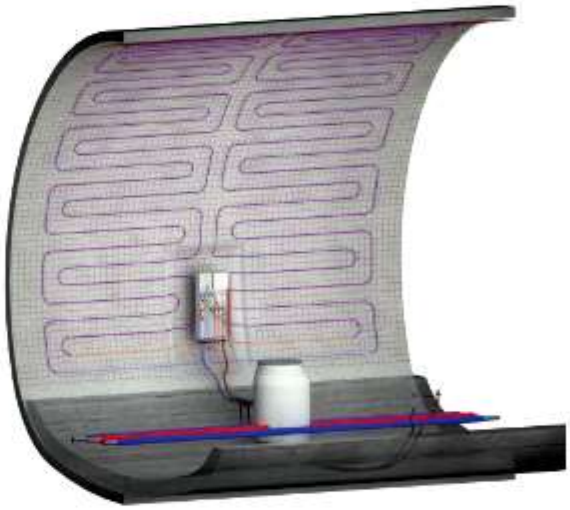

Figure 2: The PEX pipe installation principle in the Reinstein tunnel B10 (Csesznák, Järschke & Wittke, 2016).

The integration of closed loop piping systems in tunnels in a cost-effective manner is perhaps the biggest hurdle for tunnel activation in practice. Tunnel design and construction is mainly governed by other engineering aspects than energy optimization, which inevitably require the piping system to adapt to the construction method of choice. In many European countries the tunnels are designed to cope with soil and soft bedrock conditions, resulting in a tunnel design that rely heavily on concrete lining elements in the tunnel construction. The construction of precast concrete elements with integrated pipes is an advantage for tunnel boring machine (TBM) tunnelling, whereas drill & blast (D&B) tunnelling rely on onsite customisation. In this aspect the differences between countries in engineering tradition and construction customs plays a vital role.

The most straightforward and cheapest form of tunnel heat usage is reported by Rybach (2010) to be open loop systems that collect and transport inflowing waters via ducts to the tunnel portals (Figure 3). The determination of thermal potential of such open loop drainage water systems is quite intuitive, as the thermal power potential (P [kW]) scale proportionally with the amount of water drained (Q [L/s]) and the useful temperature drop (ΔT [°C]) available of the water, as shown in equation (1) (with C_P being the thermal capacity of water (kJ/l,°C)).

$$P = Q \cdot \Delta T \cdot C_P \qquad (1)$$

Rybach (2010) has investigated this thermal potential for 15 road and rail tunnels in Switzerland and report of potential production rates in the range of 150 kW – 11 693 kW thermal power per tunnel. The outflow rates of drainage water are the governing factor for these systems, where the flow rates reportedly vary from 6 – 300 l/s depending on the tunnel in question. The largest drainage rates are reported from the Gotthard road tunnel (120 l/s at 15 °C) and the Grenchenberg Railway tunnel (300 l/s at 10 °C), where the drainage rates are virtually constant all year round. This stable drainage of water at constant temperatures render such open loop systems highly effective and reliant for geothermal exploitation and theoretically, if the thermal energy can be utilized all year round (8750 hours of operation), these two tunnels alone can annually produce energy in the range of 39,5 GWh – 102,3 GWh, respectively.

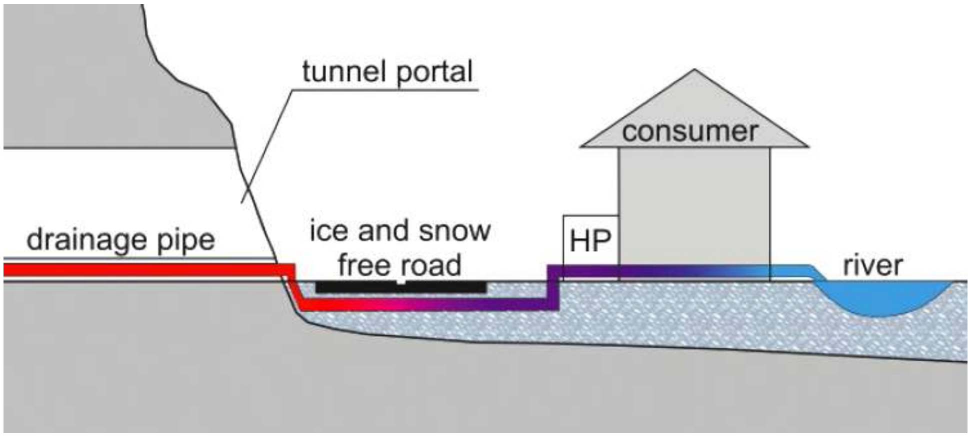

Figure 3: Principle for open loop system and typical examples for heat utilization (Stemmle et al. 2022)

3. NORWEGIAN TUNNELLING ACTIVITY & TUNNEL DESIGN

Historically the tunnelling activity in Norway was centered around the hydropower development in the early 70's towards the late 80's, which culminated in more than 4000 km of hydropower tunnels. The main activity today is related to large infrastructure projects in the major cities across the country, predominantly related to road and railway tunnels. Norway now has more than 1000 road tunnels and 750 railway tunnels totaling more than 3000 km of length (Grøv et al., 2004). The length of tunnel excavated in Norway the last 20 years is approximately 50 – 100 km annually (Figure 4), where roughly 65-70 % of the over-all tunneling volume corresponds to the construction of road and railway tunnels.

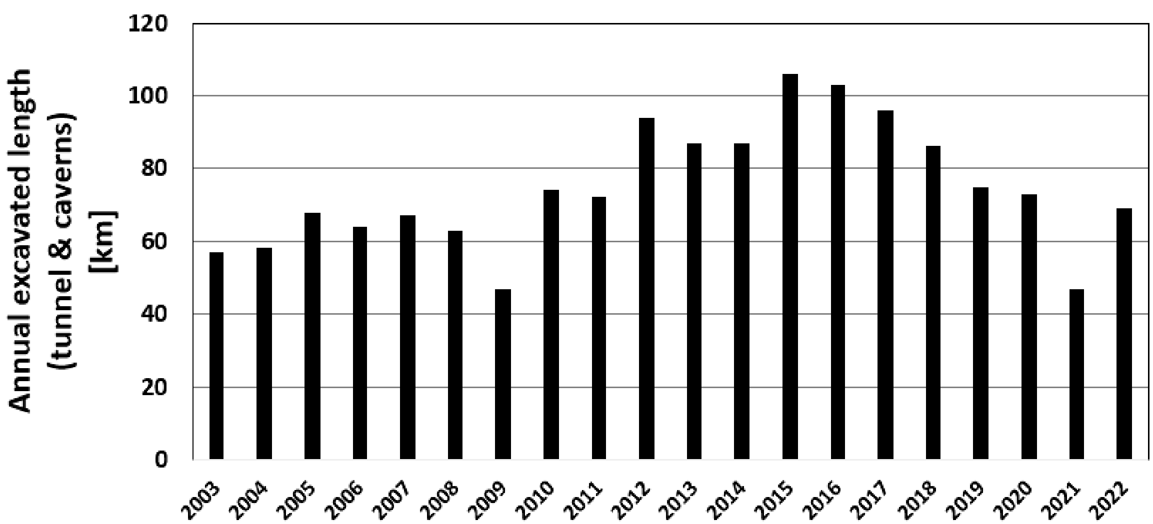

Figure 4: Tunnelling production in Norway (NFF, 2022)

The typical road and railway tunnel concepts are designed with a fully drained structure, where the mechanical stability of the tunnel is primarily supported by rock bolts and sprayed concrete. A water and frost protection system is usually installed as a separate independent freestanding structure via a membrane & insulated pre-cast concrete segment lining. The lining is customized depending on the frost load for the tunnel in question. Water is thus diverted from the carriage-way and guided towards drainage channels in the tunnel invert (Figure 5), which transport inflowing waters via ducts to the tunnel portals or to pumping stations.

Most modern road tunnels therefore have an open space behind this segment lining which is available for thermal activation via the closed loop design. The native rock temperature is found to govern the temperature within this open space, and the tunnel temperature within this envelope is rarely bellow zero degrees even though temperatures in the carriage-way might be much colder in tunnels in certain parts of the country during the winter months (Pedersen & Iversen, 2002). However, the temperature variation in Norwegian tunnels is highly dependent on a variety of factors that can impose limitations on the use of this open space for thermal systems. An optional application is to employ the closed loop system in the tunnel invert, where the drainage of water towards the ducts ensure a continuous replenishment of drainage water with native temperatures from the deeper parts of the rock mass. The annual temperature variation in this part of road and railway tunnels has not been investigated in Norway so far.

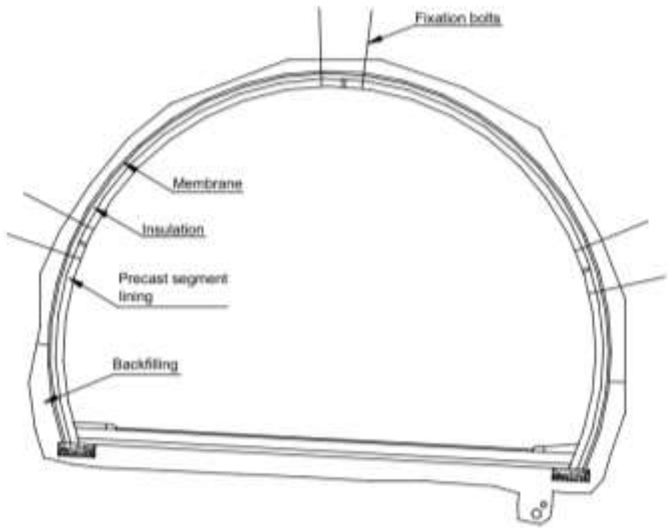

Figure 5: Design principle of pre-cast concrete segment lining for water and frost control (Grøv et al., 2004)

The most straightforward and cheapest form of tunnel heat usage in the Norwegian tunnel design is obviously the same system that is reported by Rybach (2010). The open loop systems that collect and transport inflowing waters via ducts to the tunnel portals is applicable in all tunnels, as the majority of tunnels today have installed drainage systems regardless of the potential for heat usage. The water is now simply diverted to drains and rivers outside of the tunnels. The main limiting factor will be the rate of drainage from the tunnel and whether this rate is continuous or variable throughout the year. Leakage limitations are routinely specified for construction of new road and railway tunnels in Norway, but the actual inflows are not readily available in tunnel statistics. However, inflow limitations are typically set in the range of 5 – 40 l/min per 100-meter tunnel length for most tunnel projects. Strict limitations are particularly given in urban areas to ensure limited risk of subsidence and resulting damage on surface structures. It is therefore possible to evaluate the potential of open loop system with these limitations as guide.

Subsea tunnels are particularly good candidates for open loop systems because all subsea tunnels are equipped with pumping stations at the base of the tunnel for removal of sea water. Unlike conventional tunnels, the subsea tunnels have a continuous inflow of water all year from the sea. Installing compact heat exchanger systems in these pumping systems should therefore not present itself with large additional costs for tunnel activation.

4. POTENTIAL OF GEOTHERMAL EXPLOITATION IN NORWAY

The potential for geothermal exploitation of tunnels in Norway is perhaps best evaluated by comparison with the current market activity and development of conventional borehole heat pump systems. The average size for a "large" borehole heat pump installation in Norway today typically comprise of ca. 10 boreholes of 250 meters drilled depth, totaling about 2,5 km of 40 mm HDPE ground heat exchanger length for these installations (Midttømme et al., 2020). Upon direct comparison with the average tunneling activity in Norway for the past two decades it is evident that the current construction rate of 50-100 km of new tunnels annually is equivalent to 20 – 40 such large borehole heat pump installations being installed, should only one single length of 40 mm HDPE heat exchanger pipe be installed in the invert of these tunnels. In period 2011-2019 Midttømme et al. (2020) report that there are 20 – 100 large borehole heat pump systems, with four or more boreholes, being installed each year in Norway. It is therefore evident that the current tunneling activity is proportional with the over-all large-scale geothermal development in Norway, in view of tunnel length alone.

New tunnels can however be customized in the design phase of projects to include multiple loops of heat exchanger pipes per meter tunnel, to potentially cover larger volumes of rock mass. It is essentially the tunnel size and length that limit the design size, which is perhaps difficult to compare directly to conventional bore hole systems. A conventional borehole heat exchanger is typically installed in a 140 mm wide borehole. Norway's largest geothermal system to date is the 20 GWh system in Ahus hospital in Oslo with 228 such boreholes, each 200-meter deep. These boreholes combined cover a rock surface area equal to 20 000 m^2, which essentially is the contact points towards the rock mass and the effective heat exchanger area of the system. By comparison with the typical T10,5 road tunnel size in Norway, this contact area only adds up to the circumference area of a 600-meter long road tunnel. The potential for installing comparable quantities of heat exchanger pipes in tunnels is thus seemingly not the main issue even for relatively short tunnels. It is therefore rather a question on whether the tunnel is sufficiently adjacent to a building in need of this thermal energy that will determine whether a tunnel should be activated for energy use or not.

To make use of the water in the drainage system is a promising solution in existing Norwegian tunnels due to the relatively low cost of Installing compact heat exchanger systems in existing tunnels. The potential for geothermal exploitation in this manner does primarily rely on the rate of water drainage from the tunnel in question. In practice this type of system would perform best if a given flow quantity of water is guaranteed all year round. In view of the typical inflow limitations of 5 – 40 l/min per 100-meter tunnel length it is apparent that the geothermal potential might vary significantly for each tunnel case and favors long tunnels that guide all available water to the same portal area for disposal. One possible way to evaluate the potential for this system might be to evaluate all 3000 km of road and railway tunnels in Norway in view of these limits via Eq. (1) under the assumption that the useful temperature drop available of the water is $\Delta T = 3°C$. The possible range of geothermal potential will then fall within the range 31 MW – 250 MW of thermal power and 270 – 2 180 GWh of energy for open loop tunnel systems in Norway. Still the question is whether the tunnel portals are sufficiently adjacent to a building in need of this thermal energy.

Further evaluation of these energy tunnel concepts is under way in Norway. One possible and promising tunnel case for further evaluation is the newly built 19 km long Follobanen Railway tunnel in Oslo, which has water drainage towards the center of Oslo. Here there is a pressing need for this energy and the length of the tunnel alone is so long that, even with the strictest inflow limitations, the tunnel still might provide more than 16 l/s of water towards the city and thus potentially provide more than 200 kW of thermal power.

5. CONCLUSIONS

The application and utilization of geothermal tunnel energy is a promising technology that can fit into the Norwegian tunnel design well without the need for substantial alterations of the main design methodology. The technology has a huge potential in Norwegian urban areas in view of current tunnel activity and tunnel design. Preliminary evaluation in this paper suggest that the potential thermal energy available in existing road and railway tunnels alone range in the several TWh scale if all tunnels are activated. The main question is whether the tunnels are sufficiently adjacent to a building in need of this thermal energy. Further evaluation of these energy tunnel concepts is under way in Norway.

REFERENCES

Barla, M., Perino, A. (2014). *Geothermal heat from the Turin metro south extension tunnels*. In: World Tunnel Congress 2014, Iguassu Falls, Brazil, May 9-15, pp. 1-8.

Barla, M., Di Donna, A., Perino, A. (2016). *Application of energy tunnels to an urban environment*. Geothermics 61, pp. 104–113.

Bowers, G.A., Olgun, C.G. (2013). *Systèmes géothermiques de dégivrage des tabliers de ponts basés sur les fondations énergétiques*. In: Laloui, L., Di Donna, A. (Eds.), Géostructures énergétiques, ISTE Ltd. and John Wiley & Sons Inc, pp. 239-256

Csesznák, A., Järschke, R., Wittke, M., (2016). *B 10 Rosenstein Tunnel – Designing a geothermal energy system in a spa protection area*. Geomechanics and Tunneling, Ernst & Sohn GmbH, Vol (9 - 5), pp. 458 – 466.

Dupray, F., Mimouni, T., Laloui, L. (2013). *Alternative uses of heat-exchanger geostructures*. In: Laloui, L., Di Donna, A. (Eds.), Energy Geostructures: Innovation in Underground Engineering, ISTE Ltd. and John Wiley & Sons Inc, pp. 119-138.

Gehlin.a S., Andersson, O., Rosberg J-E., (2020). *Country update for Sweden 2020*. Proceedings World Geothermal Congress 2020+1. Reykjavik, Iceland.

Grønnestad, K. S., (2017) *Reduserer CO2-utslipp og varmer bygninger med byens kloakk*. Teknisk ukeblad. (www.TU.no). Accessed Online 30.01.2023

Grøv, E., Kveldsvik, V., Løset, F., Myrvang, A., Blindheim, O. T., Rygh, J. A., et al., (2004). *Norwegian Tunnelling*, Norwegian Tunnelling Society, Publication no. 14. pp. 81.

Insana, A., Barla, M. (2020). *Experimental and numerical investigations on the energy performance of a thermo-active tunnel*. Renewable Energy 152, pp. 781-792.

Islam, S., Fukuhara, T., Watanabe, H., Nakamura, A. (2006). *Horizontal U-Tube road heating system using tunnel ground heat*. Journal of Snow Engineering of Japan 22(3), pp. 229-234.

Lee, C., Park, S., Won, J., Jeoung, J., Sohn, B., Choi, H. (2012). *Evaluation of thermal performance of energy textile installed in Tunnel*. Renewable Energy 42, pp. 11-22.

Markiewicz, R. (2004). *Numerische und Experimentelle Untersuchungen zur Nutzung von geothermischer Energie Mittels erdberührter Bauteile und Neuentwicklungen für den Tunnelbau*. Doctoral Thesis. Institute for Soil Mechanics and Geotechnical Eng., Technical Univ. of Vienna, Germany.

Midttømme, K., Alonso, M. A., Krafft, C. G., Kvalsvik, K. H., Ramstad, R. K., Stene, J., (2020) *Geothermal energy use in Noway, country update for 2015-2019*. Proceedings World Geothermal Congress 2020+1. Reykjavik, Iceland.

NFF, (2022). *Tunnelstatistikken 2022*. Norsk Forening for Fjellsprengningsteknikk (www.NFF.no). Accessed Online 30.01.2023

Nicholson, D.P., Chen, Q., De Silva, M., Winter, A., Winterling, R. (2014). *The design of thermal tunnel energy segments for Crossrail, UK*. Engineering Sustainability 167 (3), pp. 118–134.

Pedersen, K. B., Iversen, E., (2002). *Frostmengde I vegtunneler*. Statens Vegvesen, Vegteknisk Avdeling – Intern rapport nr. 2301. pp. 22

Ramstad, K.R., (2011). *Grunnvarme I Norge – kartlegging av økonomisk potensial*. NVE rapport 5/2011

Rybach, L., (2010). *Geothermal Use of Warm Tunnel Waters – Principles and Examples from Switzerland*. GRC Transactions, Vol 34, pp. 949 – 952.

Stemmle, R., Menberg, K., Rybach, L., Blum, P., (2022). *Tunnel geothermics – A review*. Geomechanics and Tunneling, Ernst & Sohn GmbH, Vol (15 - 1), pp. 104 – 111.

Schneider, M., Moormann, C. (2010). *GeoTU6 – a geothermal Research Project for Tunnels*. Tunnel 29, pp.14-21.

Unterberger, W., Hofinger, H, Grünstäudl, T. Adam, D., Markiewicz, R. (2004). *Utilization of Tunnels as Source of Ground Heat and Cooling – Practical Applications in Austria*. In: Proceedings of the ISRM International Symposium 3rd ARMS, Kyoto, 2004, pp. 421–426.

Zhang, G., Xia, C., Yang, Y., Sun, M., Zou, Y. (2014). *Experimental study on the thermal performance of tunnel lining ground heat exchangers*. Energy and Buildings 77, pp. 149-157.

Proceedings of the NROCK 2023
The IV Nordic Symposium on
Rock Mechanics and Rock Engineering
ISBN 978-9935-9436-2-0
DOI 10.33112/nrock2023.4

SINTEF-TRIPOD in Underground Design – An Important Rock Engineering Tool

Nghia Quoc Trinh (nghia.trinh@sintef.no)

Nghia Quoc Trinh
SINTEF, Trondheim, Norway
Eivind Grøv
SINTEF, Trondheim, Norway

ABSTRACT

Many rock engineering projects today may face rock mechanics challenges such as particularly complicated geometry or excavation plan, and complicated geological conditions. There may be no similar existing experience to lean on. Thus, empirical methods have limitations and uncertainties in such cases. Therefore, SINTEF has developed a reliable rock engineering tool to deal with the challenges. The tool is a combination of Investigation, Numerical modelling, and Monitoring. We use the term “SINTEF-TRIPOD” for the methodology. This paper presents the application of the SINTEF-TRIPOD for few important infrastructure projects in Oslo, which are Follo Line metro project and a water supply project.

KEYWORDS

Metro tunnel; Water supply cavern; Investigation; Numerical model; Monitoring.

INTRODUCTION

SINTEF has developed a toolbox to deal with rock engineering challenges in underground caverns and tunnels. This is given the name “SINTEF-TRIPOD”, and it is a combination of three components "Investigation tools – Numerical modelling – Monitoring". The SINTEF-TRIPOD has been developed initially based on SINTEF's experience in the mining industry, and it is now applying also in infrastructure projects.

The first component of the toolbox is "Investigation". Our investigation tools are including stress measurement, laboratory tests, and geological mapping. Stress measurements are carried out before and during construction phase of the project. The measurements include both 2-D and 3-D in relevant locations close to the concerned area. Laboratory tests for obtaining intact rock mechanics properties are carried out in connection with the stress measurements. Geological mapping is carried out to obtain the rock mass characteristics and conditions of the site. The investigations provide input parameters for numerical modelling. Based on the input data, a more reliable numerical model can be established to provide information for further evaluation and decision-making. To increase the reliability of the model even further, it is then followed, verified, and improved along the way by communicating with monitoring equipment. Early verification can be done with available information at early stage, such as existing conditions, current excavation status. Any discrepancy between the model and in-situ observation or monitoring data must be studied carefully to detect the pitfalls and possible improvement. A working model applied by SINTEF combines stress measurement, laboratory, numerical modelling, and monitoring as typical shown in Figure 1.

This paper presents application of the SINTEF-TRIPOD for two infrastructure projects as shown in Figure 2 in Oslo, Norway. The first project is Follo Line – a metro project connecting Oslo central station to Ski. The second project is a New Water Supply Oslo.

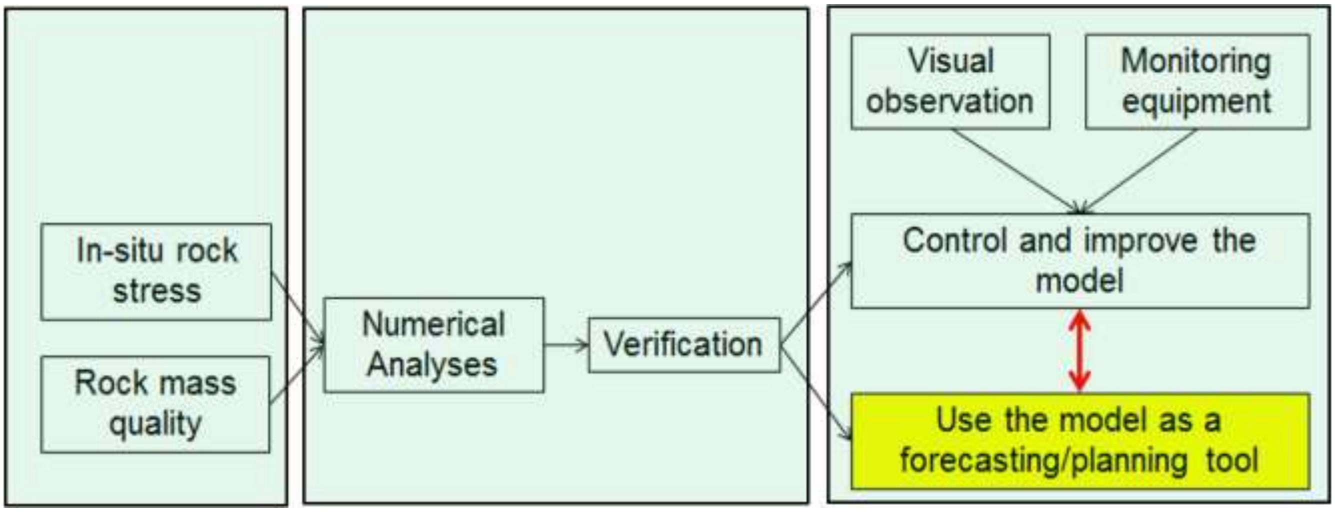

Figure 1. Recommended working model for combining measurement, laboratory, numerical modelling, and monitoring (Trinh et al., 2016) – Three green boxes represent three components of the SINTEF-TRIPOD.

1. FOLLO LINE PROJECT

1.1. Project Information

BaneNOR (Norwegian National Rail Administration) has decided to construct the Follo Line Project with new railway tunnels connecting Oslo and Ski. The excavation period commenced in 2015, and it is scheduled for operation in early 2023. In 2015, the estimated cost of the project was 25 billion Norwegian kroner (NOK) (Kruse, 2017). The location and layout of the Follo Line project and the junction is shown in Figure 2.

The project comprises a 22 km long twin-tube-tunnel to be excavated mainly with tunnel boring machines (TBM, D = 9.96 m), but also by drill & blast and drill & split (D = 9.5 m). The drill & blast and drill & split tunnel section was in the first part of the Follo Line tunnels, near Oslo Central Station, and where the Follo Line tunnels go below the Ekeberg tunnels. Vertical distance between Follo Line tunnels and Ekeberg tunnels in this junction was just less than 4 m, as shown in Figure 2. This made the construction of the intersection to be very challenging. In addition, the Ekeberg tunnels have high traffic as part of European highway No.18 and No.6. Thus, the construction of the Follo Line tunnels in this intersection is performed with the following requirements from The Norwegian Public Roads Administration (SVV):

- No negative effect on the stability of the Ekeberg tunnels.
- No stopping of traffic in the Ekeberg tunnels during the construction of the Follo Line tunnels. Thus, the stability of the existing tunnels must be ensured at all time.
- Any risk of instability in the existing tunnels must be detected beforehand to make necessary precaution actions.

Since 2014, SINTEF has assisted Bane NOR in dealing with the rock mechanics challenges and safety requirements for the construction of the mentioned intersection in this project. To meet the requirements from SVV and to study the stability of the existing Ekeberg road tunnels and the Alna river tunnel in connection with the construction of the Follo Line tunnels, SINTEF uses a comprehensive approach, which is a combination of three components: Investigation – Numerical modelling – Monitoring, forming a rock mechanic tool for the project.

1.2. Investigations

Detailed description of the geological conditions and different surface and sub-surface investigations had been presented in Holmøy et al. (2015). This paper briefly presents the in-situ rock stresses measurements and rock mass properties.

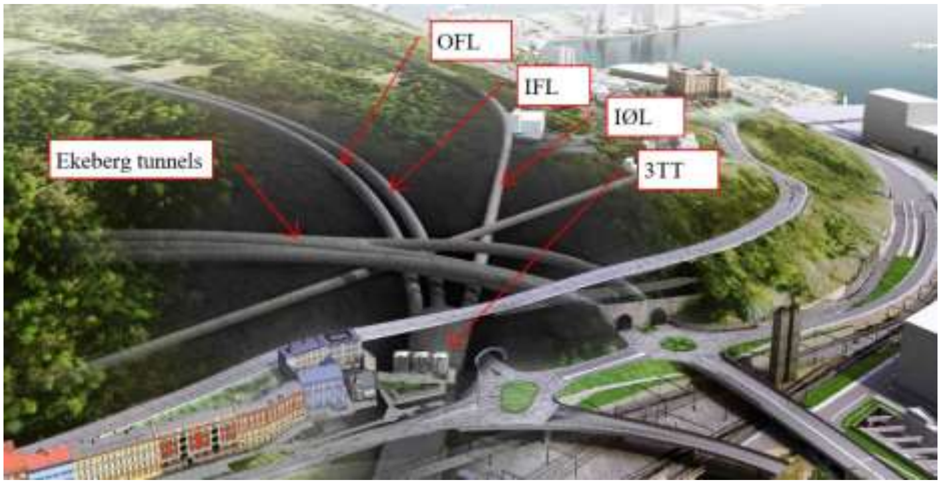

Figure 2. Junction between Ekeberg tunnels (existing) and the Follo Line tunnels with the following names: Inbound Østfold Line (IØL), Inbound Follo Line (IFL), Outbound Follo Line (OFL), 3-Tracks Tunnels (3TT) (BaneNOR, 2021).

In pre-excavation stage, SINTEF carried out stress measurements in 2011 and 2012. During excavation of the Inbound Østfold Line (IØL), in 2016 when the tunnelling face was at chainage 1890, an additional 3D stress measurement was carried out to obtain the in-situ stress condition at the site. The measuring method was over-coring method, as described in Trinh et al. 2016. The measurements in 2011, 2012, and 2016 were 3D- and 2D-stress measurements. Results from the 3D-stress measurements are given in Table 1.

The in-situ stress level measured in 2016 was much higher than the measurements in 2011, sigma 1 was twice and sigma 3 was 5 times higher than the measurements in 2011. This may be explained by a local weakness zone or maybe caverns/tunnels or the existing Alna river tunnel not too far away from the location of 2016 measurements. Comprehensive calibrations of the numerical model with result of stress measurements in 2011 and 2016 were done during planning and early construction stages of the Follo Line project. It was found that all the numerical model results with input from 2016 measurement gave far higher values than the results obtained from 2D stress measurements measured in the existing infrastructure, whilst with input from 2011 measurement, the numerical model results fitted quite well. Thus, it was decided that the results from the stress measurement in 2011 can be used as a representative in-situ stress for input in the numerical model for this project. In-situ stress for the model was estimated based on the measurement in 2011. At elevation zero, the sigma in east-west direction was 10 MPa, north-south 6 MPa, vertical 4.5 MPa, and the stress had gravitational gradient.

Table 1. Results from 3D-stress measurements carried out by SINTEF.

Year of measurement	Measured Stress 3D overcoring	Magnitude (MPa)	Dip direction (degrees)	Dip (degrees)
2011	Sigma 1	9.9 ± 1.9	N248.4	24° SW
	Sigma 2	7.5 ± 1.9	N145.0	27° SE
	Sigma 3	1.9 ± 2.8	N14.0	61° SE
2016	Sigma 1	21.6 ± 2.1	N338	35° SW
	Sigma 2	17.3 ± 3	N224	27° SE
	Sigma 3	10.9 ± 0.9	N104	61° SE

During early establishment of the model and simulation, the inputs for rock mass properties has been estimated based on mapping and laboratory tests. Results of this model were verified with the registered data obtained from monitoring equipment (stress change and displacement in connection with the tunnelling progress). Through certain construction progress, a very comprehensive calibration and testing of the model with collected data from monitoring equipment were carried out. This work was done with weekly excavation reports and monitoring data. Result of this calibration was that the rock mass properties used in the initial analyses were updated. The updated inputs of the rock mass properties for the 3D numerical model are rock mass Young's modulus (Em)= 10 GPa, poisson ration is 0.15, internal friction angle = 55 degrees, and cohesion is 2 MPa.

1.3. Numerical model

Based on the scanning of the existing tunnels and the drawings of the planned Follo Line tunnels, a 3D numerical model was established. FLAC3D (Itasca, 2021) code was used to model a 3D picture of the crossing of these tunnels. Geometry of the Ekeberg and Follo Line tunnel system is presented in Figure 3. When constructing the geometry for the simulations, the excavation method and sequence were modelled as per a specific process according to the contractor's plan.

The excavation method was conventional "drill and blast" in the area outside the crossing. Whilst near or under the existing tunnels, the excavation method "drill and split" was applied to minimise damage to the rock mass around the tunnel. In the "drill and blast" sections, a normal pull length of 5 m for each blasting round was used. In the "drill and split" section, a pull length of 2.5 m for each splitting round was used. Thus, in the model geometry, the Follo Line tunnels were divided into every 5 m and 2.5 m in the "drill and blast" and "drill and split" area, respectively. By doing this, every excavation step was simulated to obtain the whole development of stress distribution and displacement from the starting of the construction process.
Simulation process in this project is as follow:

- Simulation 1: No excavation in the model. This simulation was dedicated to obtain the original in-situ stress condition within the site boundary.
- Simulation 2: All existing tunnels were excavated to model the existing condition, before the construction of the Follo Line tunnels. This simulation was done to obtain the existing stress situation and deformation and verify with the observation and 2D measurements in the existing tunnels. This step was considered as an early verification of the model.
- Simulation 3: This was the most complicated simulation for the project, where all the planned excavation steps and sequences were strictly followed: 63 simulation steps for the excavation of the Inbound Østfold Line, 58 simulation steps for the Inbound Follo Line (IFL) and Outbound Follo Line (OFL), 65 simulations steps for the "Three tracks" tunnel.

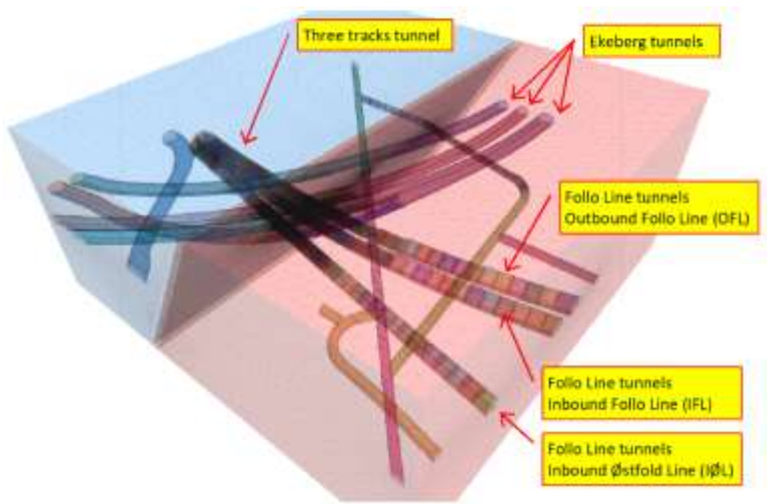

Figure 3. Geometry of the 3D numerical model for the intersection between Follo Line tunnels and Ekeberg tunnels.

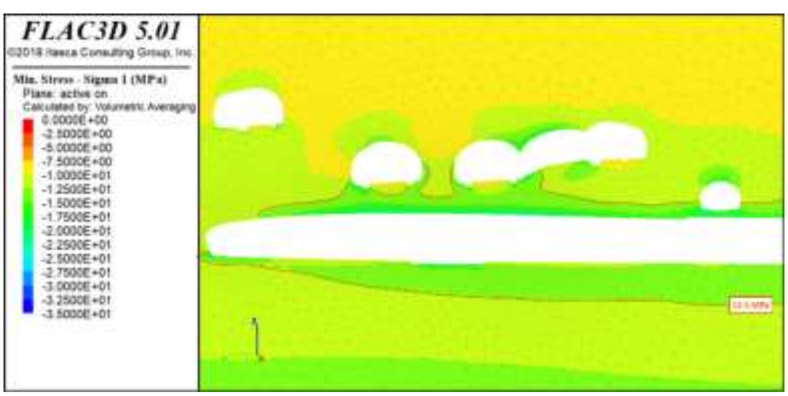

Figure 4. Distribution of sigma 1 at final excavation stage – Vertical section along IFL (negative value means compression).

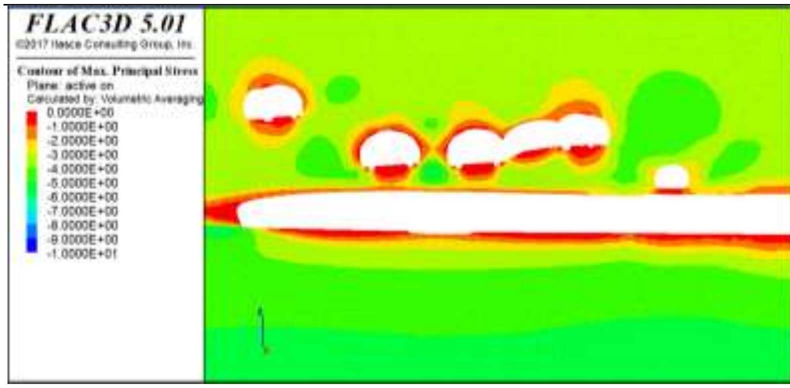

Figure 5. Distribution of sigma 3 at final excavation stage – Vertical section along IFL (negative value means compression).

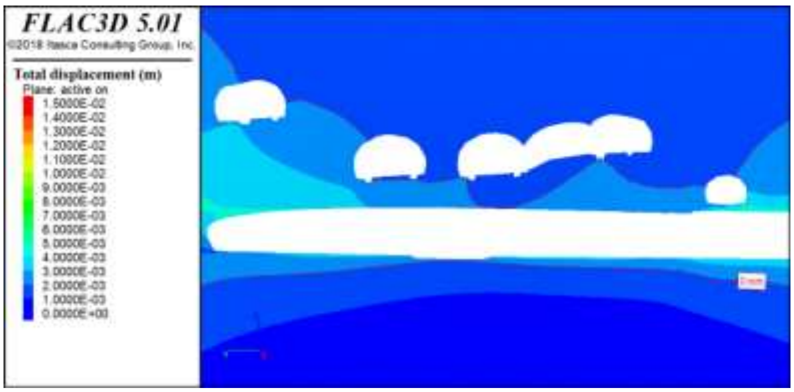

Figure 6. Distribution of displacement at final excavation stage – Vertical section along IFL.

Some results of the 3D-model are shown in Figures 4 to 6. According to the figures, the following comments were made:

- The maximum stress component (sigma 1) around the tunnel was estimated to increase slightly from about 12 MPa (in-situ original condition) to about 17.5 MPa. In the critical area (the horizontal rock pillar between Follo Line tunnels and Ekeberg tunnels), the model estimated the same amount of stress increase.
- The minimum stress component (sigma 3) around the tunnel decreases from about 5 MPa (in-situ original condition) to about 2.5 MPa. The reduction is approximately 2.5 MPa.
- The tunnel excavation results in a displacement of about 2 to 3 mm around the tunnel. Below the existing Alna river tunnel, the model showed that displacement in the new tunnel is from 4 mm to 6 mm. It is thus expected that the maximum displacement in the junction will be 4 to 6 mm after completion of the construction of Follo Line tunnels.
- Before excavation of the Follo Line tunnels, the model result showed yield elements in the floor of the Ekeberg tunnels; whilst after excavation of the Follo Line tunnels, the model results showed slightly more yield elements in the horizontal pillar.
- In general, the model results showed that there is a certain impact from the excavation of the Follo Line tunnels on the Ekeberg tunnels. However, the amount of change was estimated to be modest (stress change of about 5 MPa, and the displacement change of 2 to 6 mm depending on excavation stage). Model results gave an impression of overall stable condition for both tunnel systems.
- A monitoring system consists of extensometers and long-term-door-stopper monitoring (LTDM) were installed at key locations for better control of the stability situation. The monitoring system will be presented in the next chapters.

1.4. Monitoring of stress and displacement

In this project, it was very important to catch the stress and displacement development in very early stage, well before any instability problem may appear. The purposes to get early information were:

- Early information can be used to calibrate the numerical model, improving the model during the early construction so that the model becomes a reliable tool for testing the critical excavation stages – excavation close to or directly below the Ekeberg tunnels.

- The stress redistribution and displacement development in the rock mass can be followed from the beginning, so that any unexpected development can be detected in a good time for further study and actions.
- Early registered data from monitoring equipment can be used with the corresponding rock mass behaviour observed during the construction to design and test the warning system well before the construction progress to the critical area – under the Ekeberg tunnels.

Description of the monitoring program and warning system can be found in Trinh et al. (2016 and 2021). The locations of the monitoring system are presented in Figure 7.

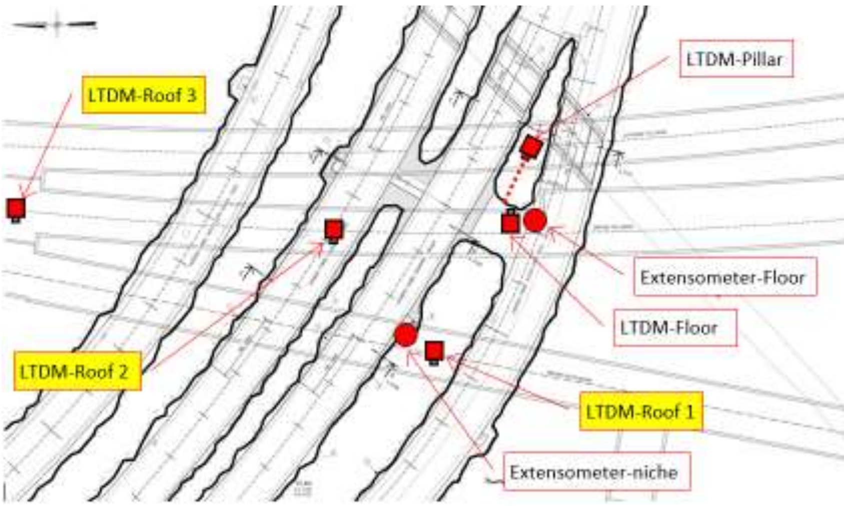

Figure 7. Locations of monitoring equipment for monitor the stress and displacement (Trinh et al. 2021).

Data from monitoring equipment was used to control the quality of the numerical model, to make the model becoming a reliable forecasting tool. Results from the numerical model were compared with the stress data from the monitoring devices, the data from two critical LTDMs ("LTDM-Pillar" and "LTDM-Floor") are presented in Figures 8 and 9. These two LTDMs were installed to monitor the stress evolution in the existing Ekeberg tunnels as a result of the excavation of the Follo Line tunnels. The LTDMs were installed at the most critical locations, where the Follo Line tunnels were at their closest to the Ekeberg tunnels – less than 4 m vertical distance. Both LTDMs were installed in May 2015, when the excavation of the Follo Line tunnels was still a very long distance away (more than 150 m) and, therefore, having practically no influence on the Ekeberg tunnels. Early installation of the LTDMs provided a good possibility of obtaining, from the start, the evolution of induced stress in the Ekeberg tunnels as the excavation of the Follo Line tunnels approached. Any abnormal change or evolution of stresses during the excavation progression could be detected early enough to implement appropriate precautionary measures, if necessary. The early monitoring data were also used for model verification.

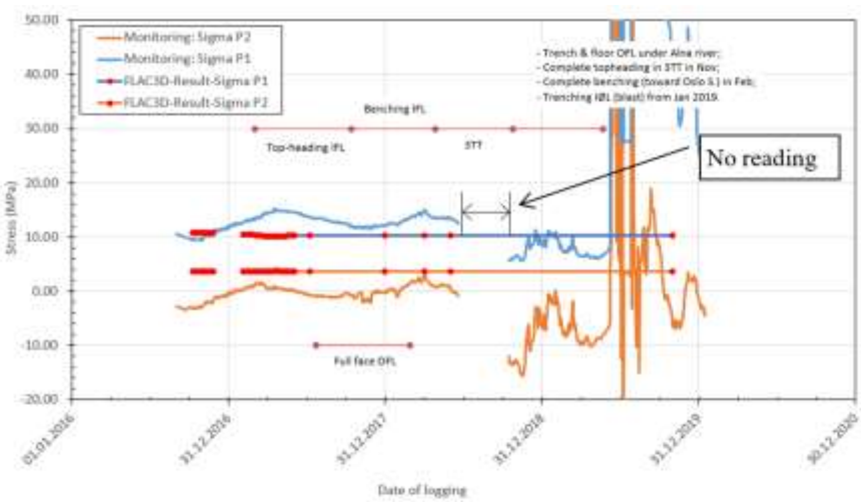

Figure 8. Comparison of stress from monitoring (LTDM-Pillar) versus numerical model.

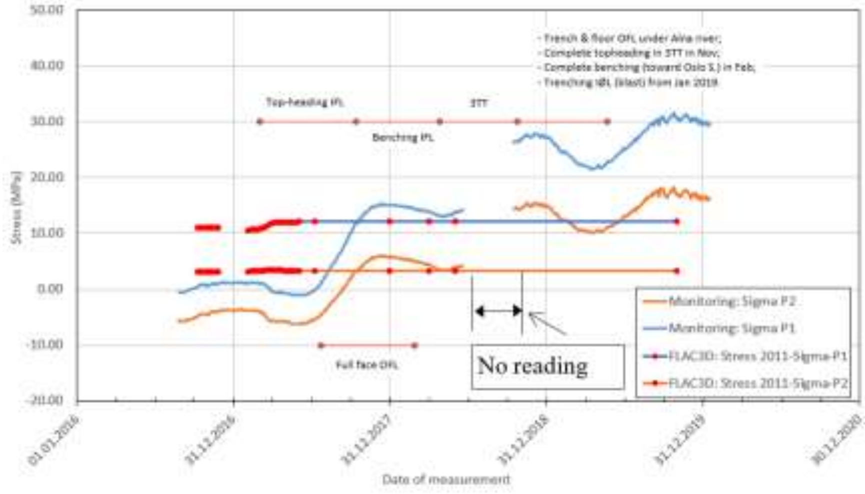

Figure 9. Comparison of stress from monitoring (LTDM-Floor) versus numerical model.

The results from the numerical model and the recorded data at the "LTDM-Pillar" shows that they fit relatively well as shown in Figure 9. The model results versus the monitoring data for the "LTDM-Floor" are presented in Figure 10. As can be seen from the figure, the model results did not fit well before September 2017. After September 2017, the stress in this location quickly increased, and the model results fitted better with the monitoring data. A possible explanation for this could be joint movement and better rock contact to increase the stress evolution. After the "no reading" period, data from the LTDMs became unreliable as pointed out in Trinh et al. (2021).

Displacement result from the numerical model was compared with the data from "Extensometer-Floor", as shown in Figure 10. It can be seen that the model result fit well with the monitoring data. During the critical excavation stage (fourth quarter 2017 to first quarter 2018), the model can predict the displacement with only less than 0.5 mm discrepancy. After critical period, the monitored data was deviated from numerical result due to additional blasting work and may be some drifting of the extensometer. More detailed information for stress and displacement comparison can be found in Trinh et al. (2021).

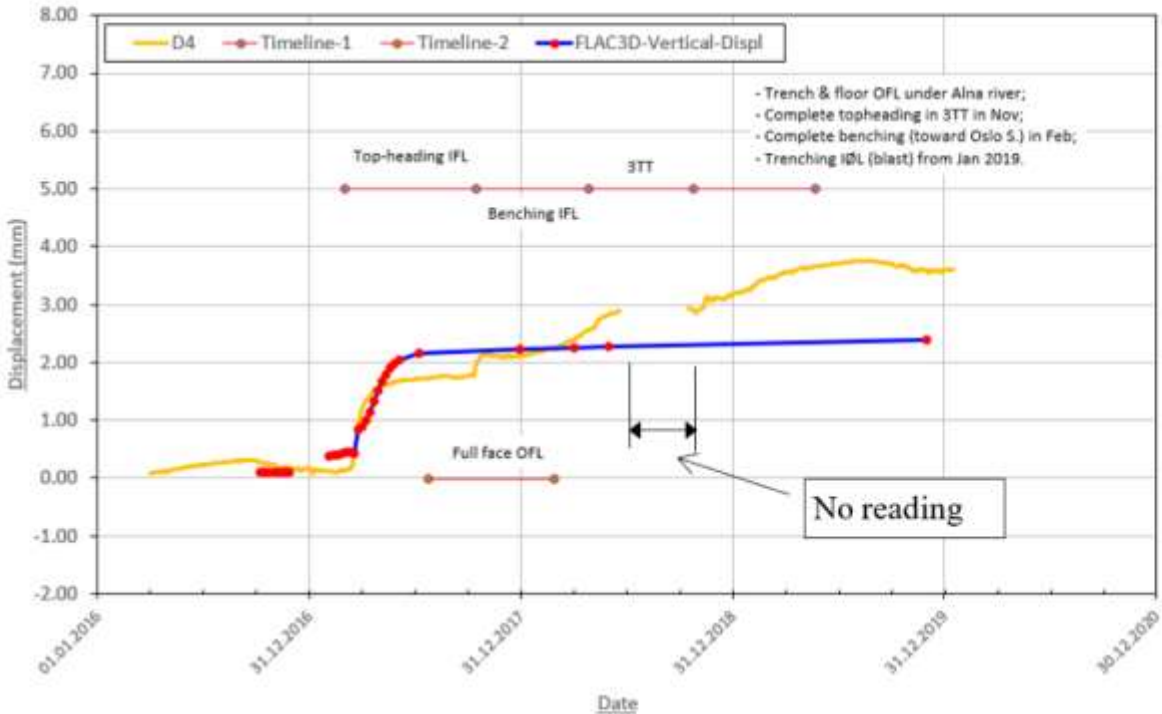

Figure 10. Comparison of displacement from monitoring versus numerical model.

2. NEW WATER SUPLY PROJECT

Oslo is the fastest growing city in Europe. The prognosis indicate that the population growth will continue. Today 90% of the water supply to Oslo is from a limited source named Maridalsvannet and its water treatment plant at Oset. This makes the city very vulnerable to incidents that strikes either the source or the treatment plant. The municipality of Oslo is therefore in the process of building a secondary water supply. According to the plan, by 1st January 2028 the new water supply to Oslo will be ready. The new water treatment plant is located at Huseby. The treatment plant consists of six large caverns with cross sections varying between 20m x 24m to 26m x 43 m. In addition, an assembly chamber for a TBM is being excavated within this underground complex. The treatment plant consists of three different levels and is a complicated system of caverns and connecting tunnels. The volume is approximately 1 million m3 which is all excavated in a relatively small area (Mørck et al., 2022).

Based on initial geological investigation and design, it was expected that the geological conditions were not very favourable in this underground treatment plant. The plan was to use heavy rock support with arches of lattice girders in combination with rock bolts and sprayed concrete. As a reference, similar but smaller and less complicated caverns nearby were built using the same rock support concept. There was also identified several weakness zones, adding the reason for the need of the designed lattice arches.

VAV found it necessary to follow-up the effect the excavation of such a large volume on such a small area could have on the stress conditions in the rock mass and the potential deformations in the caverns. In collaboration with the contractor Skanska, SINTEF was engaged to model the development of the stress redistribution and displacement before starting the actual excavation. The same SINTEF-TRIPOD procedure was applied in this project as in the Follo Line project. The simulation campaign is as follows:

- Investigation: Simulates the situation in-situ at the starting point of the project, before the tunneling and blasting work starts.
- Numerical model: Comprehensive 3D numerical model was established using FLAC3D program. Several simulations were carried out in certain order with clear objectives for each simulation steps. This to follow the planning and construction closely, helping the project team in making correct decision.
- Monitoring: Stress and displacement are monitored continuously, and the measured values are compared to the modelled values. The model is updated and calibrated with the observations made in the surveillance program. This gives us a strong basis for deciding and verifying the rock support. So far, the measurements have confirmed that the rock support is sufficient for both local and global rock stability.

The comprehensive simulations and the monitoring gave the project owner's side team the confidence to downsize the rock support in the caverns. The caverns are now supported by 20 cm thick sprayed concrete applied in two layers and rock bolts (L= 5-6 m, phi=22mm, C/C = 1.75) applied between the two rounds of sprayed concrete. Examples of simulation result are presented in Figures 11 to 14. Based on the results from the numerical model, a list of areas have been identified for frequent visual inspection throughout the excavating process. So far, fracturing of sprayed concrete has been found, which could be due to overloading, but may also be shrinkage. No or very little spalling of sprayed concrete have been found.

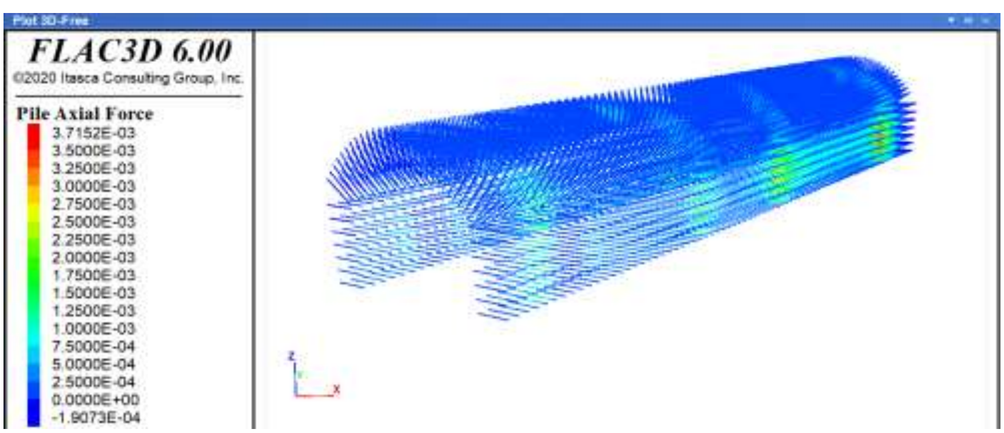

Figure 11. Axial force in the systematic bolts. The result indicated that maximum axial load on bolts is 0.37 ton, whilst the capacity of the bolts is design to be more than 30 tons.

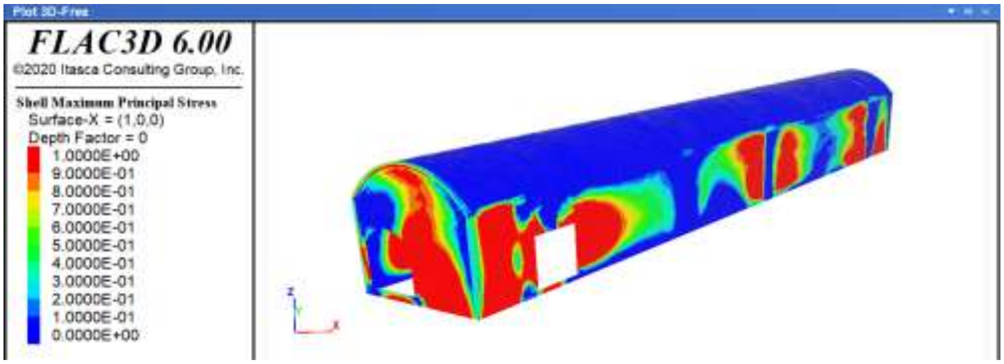

Figure 12. Minor principal stress (due to mathematical convention in FLAC3D this is named as "maximum principal stress") in sprayed concrete. Red areas indicate tensile stress is larger than tensile strength of the sprayed concrete.

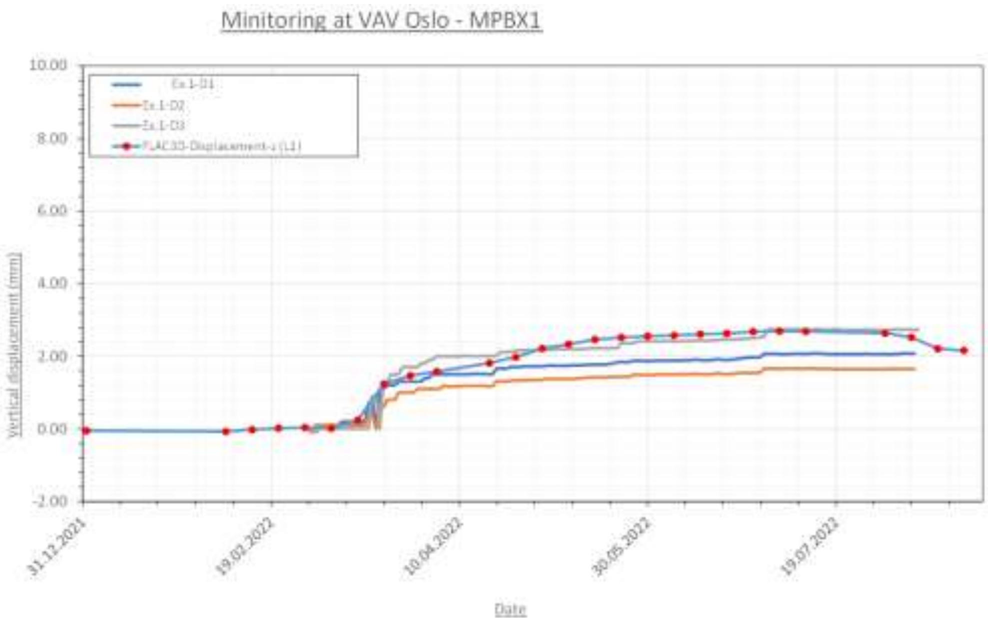

Figure 13. Deformations modeled versus recorded deformations in extensometer MPBX1. FLAC3D result was for the anchor point closest to the cavern (Ex.1-D3).

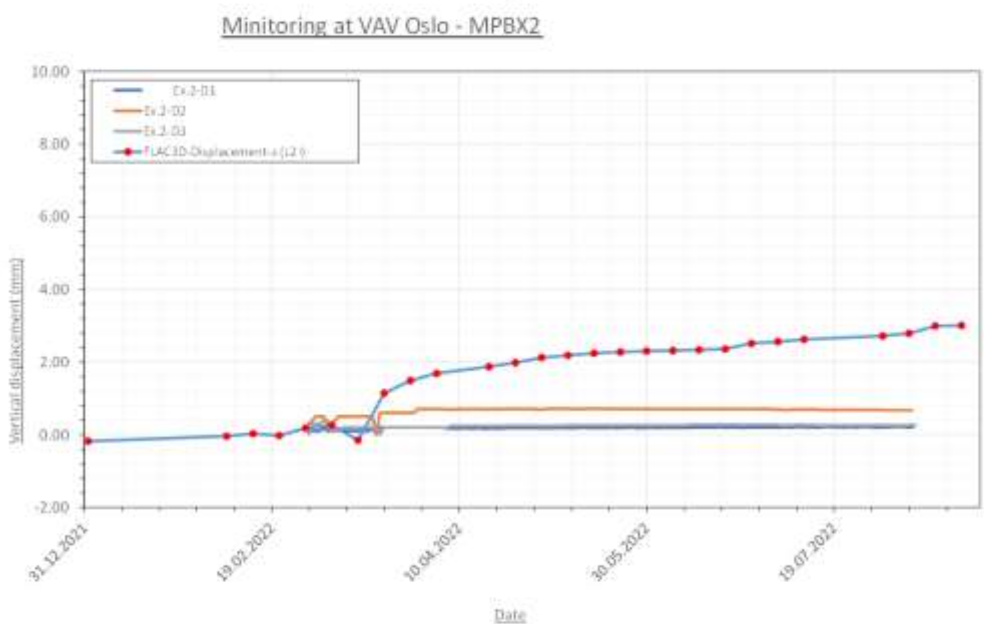

Figure 14. Deformations modeled versus recorded deformations in extensometer MPBX2.

3. CONCLUDING REMARKS

The Follo Line project was successfully excavated in 2019. Experience from the construction was that the entire rock mechanics procedure (the SINTEF-TRIPOD) was working smoothly providing reliable information for evaluation of the safety situation for both new and existing tunnels. With help from other components, the 3D numerical model established for the Ekeberg and Follo Line junction demonstrated that it is a reliable tool for planning and construction of such complicated crossings.

The application of the SINTEF-TRIPOD to the New Water Supply project provided vital inputs to optimise the rock support for the underground complex. Project cost saving from the optimisation process was estimated to be more than 100 million Norwegian krone. It is also expected lot of time saving from construction work with the reduction of the rock support.

The described rock mechanic toolbox (the SINTEF-TRIPOD) in this paper can be divided into three components, which are:

- Investigations: Stress measurements 2-D and 3-D, laboratory tests, and geological mapping. The investigations provide input parameters for the numerical model.
- Numerical model: Comprehensive numerical model (two- and/or three-dimension) was established for stability analyses of the project. The numerical model should be able to include as much as possible the geometrical details such as existing and future tunnels, and the construction sequence was simulated carefully. The obtained results were used for model calibration in the existing tunnels and evaluation of the overall stability related to the construction of the new tunnels.
- Monitoring: A monitoring program was established to monitor the displacement and stress change at the junction during the construction of the Follo Line tunnels. The monitoring program was established for stability monitoring and the data was also used for model calibration.

With successfully application in these projects, it is believed that the SINTEF-TRIPOD toolbox with combination of three components (Investigation, Numerical model, and Monitoring) are important pillars for dealing with any challenged rock engineering project.

REFERENCES

Kruse HC 2017 Bane NOR presentation in "Supplier Meeting 2 February 2017". (https://www.banenor.no/contentassets/c0667e70caf7487f999232196f66cd2d/4.-follo-line-project---hans-christian-kruse_en.pdf). Access on 06 August 2020.

BaneNOR Homepage 2021 (https://www.banenor.no/Prosjekter/prosjekter/follobanen/om-follobaneprosjektet/innhold/2018/bane-nor-lyser-ut-fire-nye-kontrakter-i-follobanen/). Last accessed 2021/03/10.

Holmøy K.H., Trinh Q.N., Backer L., 2015 3D-numerisk analyse, Follobanen/Ekebergtunnelene FJELLSPRENGNINGSTEKNIKK, BERGMEKANIKK CONFERENCE 2015, S Engen ed pp 26.1–12 (Tekna, Oslo, Norway).

Trinh Q. N., Holmøy H. K., Larsen T., and Myrvang A. 2016 Continued rock stress and displacement measurements 6combined with numerical modeling as an active, realistic rock engineering tool. RS2016 Symposium, 7th International Symposium on In-Situ Rock Stress, Johansson, E., Raasakka, V. ed (RIL, Tampere, Finland) pp. 181–93.

Itasca Homepage 2021 (https://www.itascacg.com/software/downloads/flac3d-5-01-update. Last accessed 2021/05/25).

Trinh Q. N., Holmøy, K. H. and Sagen H. W. (2021) Challenging Infrastructure Project Assisted by Monitoring and Numerical Modelling as the Follo Line Tunnels were Excavated Below Existing Tunnels. Journal of Rock Mech Rock Eng 54, pp 1671–85.

Mørck I., Thorsen S., Grøv E., Trinh Q.N. 2022 New water supply oslo – caverns for the new water supply: rock support, stress and strain development. FJELLSPRENGNINGSTEKNIKK, BERGMEKANIKK CONFERENCE 2022, S Engen ed pp 39.1–21 (Tekna, Oslo, Norway).

Proceedings of the NROCK 2023
The IV Nordic Symposium on
Rock Mechanics and Rock Engineering
ISBN 978-9935-9436-2-0
DOI 10.33112/nrock2023.5

An investigation of key parameters involved in fault activation mechanisms in CO_2 storage

Ali Mortazavi/Corresponding author (ali.mortazavi@nu.edu.kz), Dilnaz Zhumakanova

School of Mining & Geosciences, Nazarbayev University, 53 Kabanbay Batyr Ave., Astana, Kazakhstan,

ABSTRACT

The objective of this research work is to conduct a comprehensive study of fault activation mechanisms and delve into the mechanisms involved in fault reactivation processes in CO_2 storage. Faults constitute a major component of geological formations and change the rock mass system's mechanical behavior significantly, in particular at large scales. The focus of this research is to conduct an analysis of key caprock geomechanical design parameters and compare the significance of each parameter. In this study, the well-documented studies on caprock integrity analysis and fault activation were reviewed and evaluated. The key geomechanical design parameters associated with CO_2 storage were identified and discussed. Accordingly, a procedure for weighting these parameters was developed based on the Fuzzy Analytic Hierarchy Process (FAHP) and used in the comparison of the selected parameters. Based on the developed weighting scheme, the fault friction angle has the highest significance in caprock behavior followed by rock mass permeability and regional in-situ stress ratio. The obtained results are in harmony with practical observations and published research works. With further verification, the proposed approach can be used in the selection of key geomechanical design data required for CO_2 storage site analysis and design.

KEYWORDS

CO_2 Storage, Fault activation mechanisms, Numerical modelling, weighting procedures

1. INTRODUCTION

To safely store Carbone dioxide, it is vital to ensure the integrity of the caprock during the CO_2 injection process and production within a reservoir. A change in fluid pressure and temperature within a geological reservoir/formation affects the regional in-situ stress within the reservoir and surrounding rock. Accordingly, the potential hazards associated with CO_2 storage are a reactivation of major pre-existing discontinuities and faults and the creation of new fractures within the caprock zone, which may breach the hydraulic integrity of the storage site. Faults constitute a major component of storage site caprock and change the rock mass system's mechanical behavior significantly, in particular at large scales. The hydraulic integrity of the reservoir rock mass will be assessed by investigating potentials for shear fracturing, tensile fracturing, and fault and pre-existing discontinuity reactivation. Faults and major discontinuities exist in almost all rock masses. In particular, when we deal with rock mass at large scales as we face in CO_2 storage, faults play a significant role in the deformational behavior of the rock mass and dominate the overall behavior of the rock system. Characterization and determination of fault's strength properties have always been a challenge in rock engineering. From a mechanical stress field point of view faults themselves, affect the in-situ stress regime significantly locally and change the stress field differently depending on the faulting mechanism, shear zone thickness, dip, dip direction, strike length, and depth.

An accurate representation of fault geometry and characterization of fault behavior and fault properties is a major component of geomechanics modeling of CO_2 storage projects.

2. GEOMECHANICAL INVESTIGATIONS OF FAULT ACTIVATION MECHNISMS

Rutqvist et al. (2013) presented a review of modeling studies on fault reactivations and induced seismicity during underground CO_2 injection. The modeling exercises were of coupled mechanical-fluid flow type and included quantitate analysis of fault weakening and rupture as well as seismic activities. These model simulations showed that the critical factors affecting seismicity due to CO_2 injection are the local in situ stress field, fault orientation and size, fault strength, and injection pressure. They numerically simulated the activation potential of a 1km long fault and showed that the magnitude of produced seismic event would likely be less than about 3.6, even if the entire 1 km fault would be activated. The study demonstrated that fault reactivation, even associated with relatively small seismic or aseismic events, could potentially increase CO_2 seepage out of the intended storage complex and therefore reduce the effectiveness of a CO_2 storage operation.
Urpi et al. (2016) conducted a dynamic analysis of CO_2-injection-induced fault rupture with slip-rate dependent friction coefficient. An idealized CO_2 injection scenario was simulated employing the FLAC-3D code coupled with the TOUGH2 code. The mechanical stress field was coupled to multiphase fluid flow to evaluate the stress and pressure perturbations induced by fluid injection and the response of a nearby normal fault. The FLAC-3D interface element was used to simulate the frictional behavior of the fault in a coupled hydro-mechanical manner, capable of computing the poro-elastic stresses acting on the fault plane and the pressure field perturbed by the fluid injection. Different scenarios of injection rate and fault rheologies were simulated to demonstrate the deformation process on fault. The study showed that rupture on the fault plane occurs at the bottom of the reservoir which is in harmony with analytical solutions. These results show that the magnitude values are heavily influenced by the initial drop in friction angle and it takes only 1 µm of fault slip until the rate-dependency kicks in. Therefore, an initial shear strength drop is necessary to nucleate dynamic shear slip on the fault. It was concluded that a different injected fluid can perturb the pressure and stress distribution differently. This study showed that the considered fault rheology can significantly affect the modeling results.
Jeanne et al. (2017) investigated the effects of the distribution and evolution of the coefficient of friction along a fault and the seismic activity associated with a hypothetical CO_2 sequestration operation. They postulated that the pressure buildup inside the storage formation can induce slip along pre-existing faults and create seismic events felt by the population. The role of variations in friction coefficient and friction law on fault stability was evaluated. A hypothetical industrial-scale carbon sequestration project in the Southern San Joaquin Basin, USA was simulated numerically. They concluded that the variation in fault friction coefficient has a significant effect on seismic activity ranging from 1.88 to 5.88 in event magnitude. Moreover, the fault friction coefficient causes stress build-up on the fault surface before rupture, and the presence of an argillaceous caprock can prevent the development of large-magnitude seismic events.
Zappone et al. (2020) discussed the results of an experiment on the injection and storage of carbon dioxide (CO_2), the purpose of which was to study the integrity of sealing faults and caprock. The experiment was conducted in a deep saline aquifer of the Northern Carnic Alps in Italy and was analyzed in Mont-Terri underground laboratory. Due to the fact that the Opalinus clay formation is one of the good analogs of the rock for storing CO2 at depth, CO_2-saturated salt water was pumped into the upper part of a 3-meter fault in this clay. It was found that CO2 did not migrate through the sealing defects, indicating that the defects effectively sealed the CO_2 in the injection zone. However, the injection of CO_2 affected the integrity and permeability of the caprock with the formation of new cracks. The conducted experiments show that sealing faults can be effective in preventing CO_2 migration in deep saline aquifers. Overall, the study provides valuable information about the challenges associated with the safe storage of CO_2 in deep saline aquifers.
Guglielmi et al. (2021) conducted field-scale fault reactivation experiments by fluid injection. The effect of liquid injection on the reactivation of faults in caprock, which acts as a sealing layer of rock preventing the leakage of liquids like natural gas and carbon dioxide (CO_2), was investigated. The focus of this study was CO_2 absorption in geological formations. It was found that liquid injection can cause fault reactivation but the leakage due to this is not significant. Also, the results of the study suggest that the reactivation of the fault may be aseismic, that is, it cannot cause seismic activity. They concluded that aseismic movement that dominates fault activation suggests that measurements of seismicity can hardly be used to track loss of caprock integrity.

3. KEY GEOMECHANICAL PARAMETERS AFFECTING FAULT ACTIVATION

Storage of CO_2 in geological information is associated with high risks. It is well established that the investigation of geomechanical parameters at the design stage of CO_2 storage sites provides the reservoir rock mass characteristics, which are associated with some risks in the design. The inherent uncertainties that exist in geomechanical data pose significant risks in the geomechanical design of CO_2 storage sites. From a realistic design and risk assessment point of view, it is essential to determine a suitable weighting strategy for risk-prone design parameters. The goal of this research is to develop a realistic weighting procedure to assess and compare various geomechanical parameters that are important in the design of CO_2 storage sites.

In this study, seven key geomechanical parameters used in the geomechanical analysis of CO_2 storage sites were selected, and a weighting procedure was developed using the Fuzzy Analytic Hierarchy Process (FAHP) method. The developed weighting methodology is presented in detail in Mortazavi and Kuzembayev (2022) and was employed here to demonstrate the significance of various parameters associated with CO_2 storage. The selected parameters were chosen based on a thorough literature review of geomechanical analyses conducted on CO_2 storage sites (Rutqvista et al., 2013; White et al., 2014; Urpi et al., 2016; Jeanne et al., 2017; Zappone et al., 2020; Guglielmi et al., 2021). The obtained preliminary results show that FAHP is a reliable method for weighting geomechanical parameters and can be used as a guide in the selection of key design parameters associated with CO_2 storage in geological information. An overview of the employed methodology is presented in the next sections.

3.1. FAHP-based weighting procedure

The Fuzzy Analytical Hierarchy Process (FAHP) method proposed by Buckley (1985) forms the basis of the proposed weighting methodology. The Fuzzy Analytical Hierarchy Process (FAHP) is a multi-criteria decision-making (MCDM) method based on the hierarchical structure analysis and systematic determination of the criteria weights using the fuzzy set theory. The criteria weight depends on linguistic evaluation provided by experts according to their experience and knowledge. A weighting process based on fuzzy logic is a more appropriate approach to overcome uncertainties; in some cases, decision-makers are more confident in giving a judgment range than fixed values. FAHP is used in a wide range of fields, such as risk assessment, energy, business, engineering, and others (Mardani et al., 2015). Considering the significant uncertainties faced in geological and geomechanical information, it is critical to have a weighting procedure to determine the significance of various parameters and assign the available budget in a more realistic way to determine the data required for the final design. It should be realized that there are a variety of methods developed based on the FAHP method. In this study, the geometric mean method using the triangular membership function was used. The geometric mean method was first developed by Buckley (1985) to extend the AHP to the situation of using linguistic variables. In this method, a unique fuzzy number is determined for the weight of the selected parameters, and the method is managed more easily mathematically. Moreover, the method is more suitable for cases in which there is a lack of sufficient data and a high scatter in the available data. The theoretical basis of the method is outlined in Buckley (1985) and further elaborated in Mortazavi and Kuzembayev (2022).

3.2. Selection of key geomechanical parameters involved in CO_2 storage

The Caprock geomechanical parameters are key components of underground CO_2 storage site design that affect the safety and success of the storage operation significantly. Complexities associated with in-situ rock properties at large scale, the existence of major geological structures such as faults, the coupling of hydro-mechanical stress fields involved, and complicated boundary conditions associated with CO_2 storage sites make this process very complicated, and conventional design methods may lead to significant errors. Moreover, the accuracy of design data plays a key role in the success of the design process. Accordingly, a specific group of physical and mechanical characteristics is measured in the laboratory or by in situ testing to determine the Caprock design parameters.

A set of key host rock mass physical, mechanical, in-situ, and strength parameters was selected for the analysis presented here. These parameters were selected based on the top literature published on CO_2 storage geomechanical design outlined in section 3. Accordingly, the following geomechanical parameters that are used in caprock integrity analysis of CO_2 storage sites, were selected for the evaluation and application of the proposed weighting procedure.

Table 1. Key geomechanical parameters involved in caprock integrity analysis

Parameter	Definition
P1	Fault friction angle
P2	Rock mass deformation modulus
P3	Rock mass permeability
P4	In-situ horizontal to vertical stress ratio (S_h/S_v)
P5	Fault cohesion
P6	Rock mass porosity
P7	Rock mass density

3.3. Weighting of the selected parameters involved in CO_2 storage

In the FAHP methods, fuzzy pairwise comparison matrices were constructed by using linguistic evaluations with respect to the decision-makers' judgments. The typical linguistic variables for pairwise comparison of each criterion are shown in Table 2.

Table 2. Linguistic Variables for Pairwise Comparison of Each Criterion

Linguistic Variables	Triangular Fuzzy Scale	Triangular Fuzzy Reciprocal Scale
Equally strong	(1, 1, 1)	(1, 1, 1)
Moderately strong	(2, 3, 4)	(1/4, 1/3, 1/2)
Strong	(4, 5, 6)	(1/6, 1/5, 1/4)
Very string	(6, 7, 8)	(1/8, 1/7, 1/6)
Extremely strong	(9, 9, 9)	(1/9, 1/9, 1/9)
	(1, 2, 3)	(1/3, 1/2, 1)
	(3, 4, 5)	(1/5, 1/4, 1/3)
Intermediate values	(5, 6, 7)	(1/7, 1/6, 1/5)
	(7, 8, 9)	(1/9, 1/8, 1/7)

In the proposed method by Buckley (1985), in step one a fuzzy pairwise comparison matrix, $\widetilde{D} = [\widetilde{a}_{ij}]$, is constructed based on the significance of selected parameters. Then, the fuzzy geometric mean value, $\tilde{r}_i$, is computed for each parameter *i* as;

$$\tilde{r}_i = (\tilde{a}_{i1} \times \tilde{a}_{i2} \times \ldots \times \tilde{a}_{in})^{1/n} \qquad (1)$$

The fuzzy weight $\widetilde{w}_i$ for each parameter *i* is calculated as;

$$\widetilde{w}_i = \tilde{r}_i \times (\tilde{r}_1 + \tilde{r}_2 + \cdots + \tilde{r}_n)^{-1} \quad (2)$$

where $\tilde{r}_k = (l_k, m_k, u_k)$ and $(\tilde{r}_k)^{-1} = \left(\frac{1}{u_k}, \frac{1}{m_k}, \frac{1}{l_k}\right)$

In the last step, the fuzzy weights are defuzzified by any difuzzification method. In this study, the Center of Area (CoA) method was used. Implementing the above procedure the weighting of the selected parameters was determined. The obtained results are presented in Tables 3 to 6.

Table 3. The pairwise comparison matrix

Parameters	P1	P2	P3	P4	P5	P6	P7
P1	1	4	2	3	4	5	7
P2	0.25	1	0.20	0.25	4	5	5
P3	0.50	5	1	3	5	6	6
P4	0.33	4	0.33	1	4	5	5
P5	0.25	0.25	0.20	0.25	1	2	3
P6	0.20	0.20	0.17	0.20	0.5	1	2
P7	0.14	0.20	0.17	0.20	0.33	0.50	1
Sum	2.68	14.65	4.07	7.90	18.83	24.50	29.00

Table 4. The calculated pairwise comparison matrix for geomechanical parameters involved in CO_2 storage

P's	P1			P2			P3			P4			P5			P6			P7		
P1	1	1	1	3	4	5	1	2	3	2	3	4	3	4	5	4	5	6	6	7	8
P2	0.20	0.25	0.33	1	1	1	0.20	0.25	0.33	0.20	0.25	0.33	0.20	0.25	0.33	0.20	0.25	0.33	0.20	0.25	0.33
P3	0.33	0.50	1	0.33	0.5	1	1	1	1	0.33	0.50	1.00	0.33	0.50	1.00	0.33	0.50	1.00	0.33	0.50	1.00
P4	0.25	0.33	0.50	0.25	0.33	0.50	0.25	0.33	0.50	1	1	1	0.25	0.33	0.50	0.25	0.33	0.50	0.25	0.33	0.50
P5	0.20	0.25	0.33	0.20	0.25	0.33	0.20	0.25	0.33	0.20	0.25	0.33	1	1	1	0.20	0.25	0.33	0.20	0.25	0.33
P6	0.17	0.20	0.25	0.17	0.20	0.25	0.17	0.20	0.25	0.17	0.20	0.25	0.17	0.20	0.25	1	1	1	0.17	0.20	0.25
P7	0.13	0.14	0.17	0.13	0.14	0.17	0.13	0.14	0.17	0.13	0.14	0.17	0.13	0.14	0.17	0.13	0.14	0.17	1	1	1

Based on the criteria given by Buckley (1985), the determined fuzzy pairwise comparison is consistent. Accordingly, the calculated geometric mean $\tilde{r}_i$ values and fuzzy weights $\widetilde{w}_i$ are calculated and presented in Table 5.

Table 5. The defuzzified and normalized weights determined for key parameters associated with CO_2 storage

Parameters		$\widetilde{w}_i$		$\widetilde{w}_{ave}$	Norm	Weight (%)
P1	0.35	0.62	0.99	0.65	0.59	59.41
P2	0.04	0.06	0.10	0.06	0.06	5.90
P3	0.06	0.11	0.25	0.14	0.13	12.64
P4	0.04	0.08	0.14	0.09	0.08	7.88
P5	0.04	0.06	0.10	0.06	0.06	5.90
P6	0.03	0.05	0.08	0.05	0.05	4.77
P7	0.02	0.04	0.05	0.04	0.04	3.51
Sum				1.10	1.0	100

The final sorted weights determined for the key geomechanical parameters used as an input in the design of underground CO_2 storage sites are summarized in Table 6.

Table 6. The final sorted weights determined for key parameters associated with CO_2 storage

Parameters	Weight (%)
Faults friction angle (P1)	59.41
Rock mass permeability (P3)	12.64
In-situ stress ratio (S_h/S_v) (P4)	7.88
Rock deformation modulus (P2)	5.90
Fault cohesion (P5)	5.90
Rock mass porosity (P6)	4.77
Rock mass density (P7)	3.51

4. CONCLUSIONS

With regard to the data-limited nature of the geomechanics design problem and the uncertainties associated with design data, it is vital to have a methodology to distinguish the significance of design parameters. In this study, the application of FAHP to the evaluation of key geomechanical design data of CO_2 storage sites was demonstrated and a weighting scheme was developed. Among the seven parameters that play role in the overall caprock, which has fault structures, the fault friction angle has the highest significance followed by rock mass permeability and in-situ stress ratio. The predicted weightings were determined based on expert opinions compiled from the top scientific papers published in highly ranked journals. The obtained results may be subjective to the expert opinions but are in harmony with mechanistic analyses conducted on geomechanical design aspects of CO_2 storage. If a more comprehensive survey of expert opinion is carried out at an international level and used as an input to the developed weighting procedure, then the obtained results would be more reliable and can be used as an aid in the design of new CO_2 storage sites. A comprehensive questionnaire of key geomechanical parameters involved in CO2 storage is under preparation. It is intended to send this questionnaire to at least 100 top international experts involved in CO2 storage. This is work in progress and will provide valuable data for the study.

5. ACKNOWLEDGEMENTS

The authors gratefully acknowledge the funding provided by Chevron/Nazarbayev University Research Collaboration Program as part of the FY2022-Chevron/NU RCP research project.

REFERENCES

Guglielmi, Y., Nussbaum, C., Cappa, F., De Barros, L., Rutqvist, J., & Birkholzer, J. (2021). *Field-scale fault reactivation experiments by fluid injection highlight aseismic leakage in caprock analogs: Implications for CO_2 sequestration*, International Journal of Greenhouse Gas Control, 111, 103471, https://doi.org/10.1016/j.ijggc.2021.103471

Mardani, A., Jusoh, A., Zavadskas, E.K., (2014). *Fuzzy multiple criteria decision-making techniques and applications–Two decades review from 1994 to 2014*, Expert Syst. Appl. 2015, 42, 4126–4148

Mortazavi A., Kuzembayev N., (2022). *Development of a Weighting Procedure for Geomechanical Risk Assessment*, Energies, 15, 6517. https://doi.org/10.3390/en15186517

Rutqvista, J., Cappa, F., Mazzoldia, A., Rinaldia, A., (2013). *Geomechanical modeling of fault responses and the potential for notable seismic events during underground CO_2 injection*, Energy Procedia, 37, 4774 – 4784

Urpia, L., Rinaldia, A., Rutqvist, J., Cappa, F., Spiers, C.J., (2016). *Dynamic simulation of CO_2-injection-induced fault rupture with slip-rate dependent friction coefficien*t, Geomechanics for Energy and the Environment, 7, 47–65

Zappone, A., Rinaldi, A.P., Grab, M., Wenning, Q., Roques, C., Madonna, C., etal., (2020), *Fault sealing and caprock integrity for CO_2 storage: an in-situ injection experiment*, Journal of Geophysical Research. Solid Earth Disscussion, https://doi.org/10.3929/ethz-b-000461768.

Whitea, J.W., Chiaramontea, L., Ezzedineb, S., Foxalla, W., Haoa, Y., Ramireza, A., et al., (2014). *Geomechanical behavior of the reservoir and caprock system at the In Salah CO2 storage project*, Earth, Atmospheric, and Planetary Sciences, 111 (24) 8747-8752, https://doi.org/10.1073/pnas.1316465111

Proceedings of the NROCK 2023
The IV Nordic Symposium on
Rock Mechanics and Rock Engineering
ISBN 978-9935-9436-2-0
DOI 10.33112/nrock2023.6

Infrastructure Restriction Volumes for Future Mining at the LKAB Malmberget Mine

Jonny Sjöberg (jonny@itasca.se)

Theofanis Rentzelos, Mikael Svartsjaern, Jonny Sjöberg, Mattias Sjölander
Itasca Consultants AB, Luleå, Sweden

Linda Jonsson, Albin Andersson
Luossavaara-Kiirunavaara Aktiebolag (LKAB), Malmberget, Sweden

ABSTRACT

Large-scale sublevel cave mining unavoidably results in the rock mass around the orebodies being affected by caving and stress redistribution. Knowledge about the extent of areas that will not allow safe placement of infrastructure is essential for the planning process for deeper mining. This paper presents a case study from the LKAB Malmberget iron ore mine in which "infrastructure restriction volumes" were developed for guidance of where mining infrastructure such as ramps, shafts, etc., should not be located for future mining at depth. The methodology used involved simulating historic and future production in a mine-scale numerical model, containing relevant geology but no infrastructure. The mine-scale model simulates caving and material flow together with mechanical (stress and deformation) calculations in a coupled process. Stresses were extracted from the mine-scale model and applied to local models, built based on case areas with observed and documented damages from the mine. The local models were constructed with detailed geology and explicit infrastructure. Several criteria for predicting damage were tested and compared with mapping data from multiple locations in the mine. The most suitable criterion for prediction of damage that corresponds to infrastructure function being compromised was the Strength-Stress Ratio (SSR), which describes the "margin capacity" of the rock mass. This criterion was then applied to the mine-scale model to create restriction volumes for each year of mining down to a depth of 1900 m, corresponding to the depletion of currently known orebodies in the mine. The restriction volumes consider static (aseismic) loading only. Development of infrastructure inside the restriction volumes should be avoided or minimized, but in cases where developing infrastructure inside the restriction volumes is necessary, this should be done in a way allowing for future rehabilitation. For current infrastructure located inside the restriction volumes rehabilitation or alternative infrastructure plans should be developed.

KEYWORDS

Sublevel caving; numerical modelling, global-local modelling; strength-stress ratio

1. INTRODUCTION

Large-scale sublevel cave (SLC) mining is a cost-efficient bulk mining method, allowing a high degree of mechanization. Constant improvements over the years have resulted in high productivity and (comparably) low costs, making it possible to mine iron ore underground at large (currently up to 1000 m) depth. However, SLC mining inevitably results in the rock mass volume around the orebodies being significantly affected by caving and stress redistribution. For planned continued mining towards depth it is important to gain knowledge about the extent of regions that will not allow safe placement of mine infrastructure, such as ramps, shafts, etc.

This paper presents a case study for the LKAB Malmberget iron ore mine in which "infrastructure restriction volumes" were developed for guidance of where mining infrastructure should preferably not be located for future mining at depth.

The Malmberget iron ore mine is owned and operated by the Luossavaara-Kiirunavaara Aktiebolag (LKAB) mining company. The mine is situated in the municipality of Malmberget in northern Sweden, some 70 km north of the Arctic Circle and 1200 km north of Stockholm. The mine comprises 20 orebodies of varying size, shape and orientation, over an area of 8 km^2. Annual production is around 16 million metric tons (Mton) of crude ore with mining currently ongoing between the 475 and 1123 m mining levels, corresponding to approximately 400–900 m below ground surface. The ore is transported by front loaders to ore passes at the production levels, and then through the ore passes to chutes at the main haulage level. From these, the ore is transported by trucks to underground crushers, and subsequently by conveyor belt and skip to the concentrator plant on the ground surface, (see also Figure 1). The current main haulage level is located at the 1250 m level, denoted M1250.

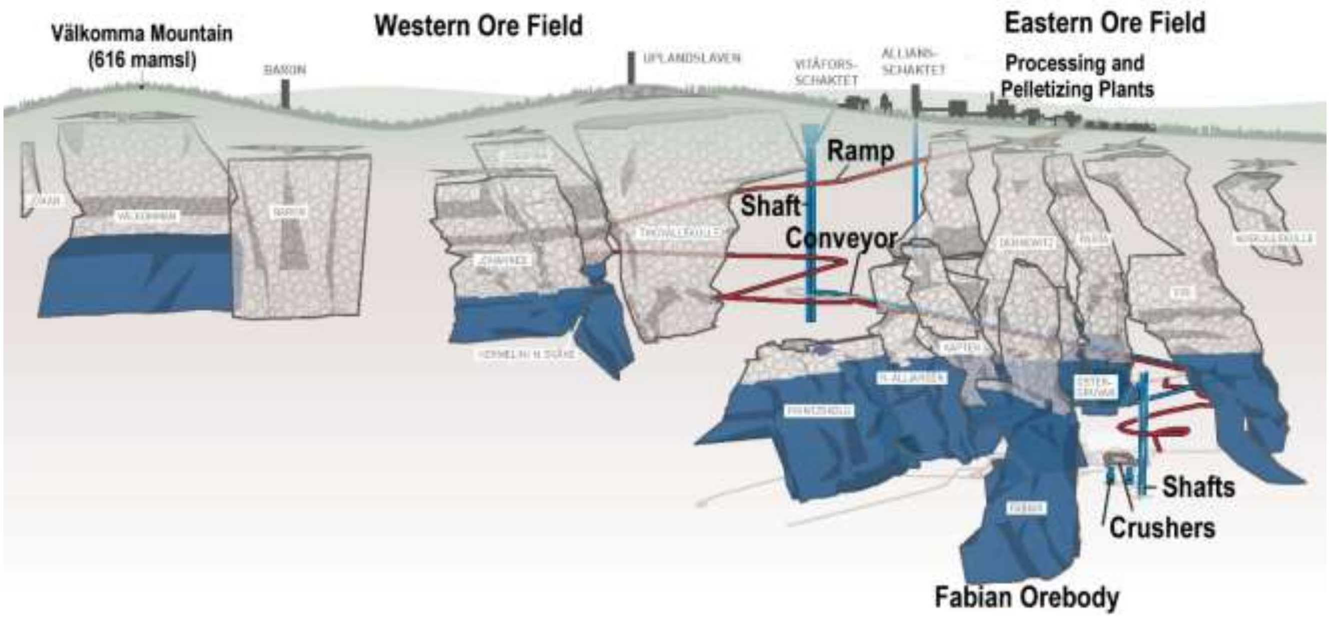

Figure 1. Schematic figure showing major orebodies and mine infrastructure at the Malmberget mine. Grey areas are mined ore and blue areas are unmined ore, view towards north.

2. METHODOLOGY

2.1. Approach

The methodology used involved simulating historic and future production in a mine-scale (global) numerical model, containing relevant geology but no infrastructure. The mine-scale model simulates caving and material flow together with mechanical (stress and deformation) calculations in a coupled process, see e.g., Sjölander et al. (2022).

Local models were then built based on case areas with observed and documented damages from the mine. The local models were constructed with detailed geology, explicit infrastructure, and with the option to include surface support. The stress states for relevant years (noted time of damage occurrence) were retrieved from the mine-scale model and superimposed on the local model. The infrastructure in the local model was then excavated and the areas containing damage observations were evaluated with respect to stresses from the mine-scale model, drift convergence, support loads, and secondary stresses to define criteria identifying conditions likely to lead to infrastructure damage. The criteria developed using one local model were then applied to a second local model from a different location. If the criterion holds true the definition can be carried through to the mine-scale model for prognosis, if not, then the criterion is scrapped.

The methodology is seemingly straight-forward but does necessitate iteration between the mine-scale and the local models. The criteria must be based on data available in the mine-scale model used to do prognosis, but must also be proven to be associated with numerical damage indicators in the local models. The observed damage from the field cases must be contained in the parts of the local model where the numerical results indicate that damage is plausible. This step was essential to verify that (i) the damage is controlled by static loading (aseismic), and (ii) the resolution of the mine-scale model is acceptable for adequate stress differences to occur on local scale during mining.

Following this, the criteria that can be successfully applied over the different local models were then applied in the mine-scale model. The criteria were used to create restriction volumes for each year of mining down to a depth of 1900 m, corresponding to the depletion of currently known orebodies in the mine. The "target" level of damage indicated by the criteria will mimic the level of damage contained in the calibration cases, i.e., the level of damage in the field observations will determine the level of potential damage related to the restriction volumes.

2.2. Damage Observations

Several observed and documented damages in mine infrastructure were provided by LKAB and used for purpose of developing a damage criterion. The documented cases contained a selection of damages on the infrastructure along with their location, a brief description, photos, and the date that they were mapped. Only specific cases were used for the development of criteria that could predict higher-risk areas for the location of future infrastructure. The exclusion of certain cases was based on the type and location of a certain damage or failure. Specifically, cases located in the proximity of production areas were not considered suitable for the development of criteria that was later to be applicable to areas where permanent mining infrastructure is going to be located. Additionally, damages on the rock support that could not be associated to rock movements were excluded. An example of documented damages is shown in Figure 2.

Two sets of damage observations were used – one with minor damages, e.g., cracking of shotcrete, minor rockfalls and minor damage to installed reinforcement, and one with more severe damages resulting in infrastructure function being compromised. Calibration of the developed criterion against the second category of data enhanced its precision in identifying areas where permanent infrastructure development could potentially result from rock failures of similar severity.

Figure 2. Example of damage observations in the LKAB Malmberget mine.

2.3. Numerical Models

2.3.1. Mine-Scale Model

All analyses in this project were conducted using the three-dimensional finite difference code *FLAC3D* (Itasca, 2019), using a *FLAC3D-CAVESIM* coupling aimed at simulating the progression of caving, see also Hebert & Sharrock (2018). All orebodies in the Malmberget Mine were included in the mine-scale model and six large-scale structures were also included in the model, based on the structural-geological model and an assessment of what the most critical and important structures were from a caving influence perspective with respect to the studied infrastructure (Figure 3). The *FLAC3D* model was built using an "oct-tree" mesh in which the mesh is composed of hexahedral zones arranged in a structured cubic pattern. This applies to the whole model except in the area around the large-scale structures, where the mesh is made up of an irregular hexahedral mesh to follow the fluctuation of the large-scale structure. The outer dimensions of the model were set to 9675 x 9535 x 3480 m. The cubic pattern of the hexahedral elements has a size of 12 m in the near vicinity of the orebodies and the structures, and then gradually increases in size out to the outer-most part of the model where the element size is 96 m. All structures were modeled as continuous discrete planes without any thickness.

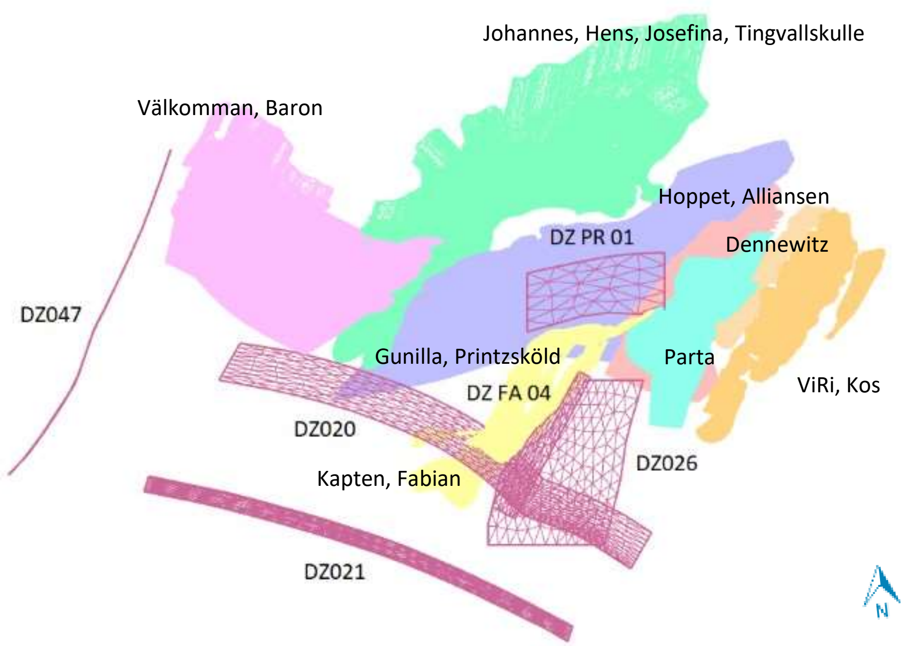

Figure 3. Plan (projected) view showing orebodies and large-scale structures in the numerical mine-scale model of the Malmberget Mine.

The rock mass was simulated with the *IMASS* (Itasca Constitutive Model for Advanced Strain Softening) material model (Ghazvinian et al., 2020), and the large-scale structures were modeled with the Mohr-Coulomb plastic model. Material properties were defined through calibration of the model versus caving, surface cratering and surface deformation, and are described in Sjölander et al. (2022). The initial stress state used in the model was based on Perman et al. (2016), who determined the initial stress field in the Malmberget Mine by calibrating a three-dimensional numerical stress analysis model with the results of stress measurements.

Mining in the numerical model can be divided into four parts: (1) mining with shrinkage stoping at the beginning of the twentieth century, (2) mining with sub-level caving before 1995, (3) mining with sub-level caving between the years 1995 and 2019, and (4) future mining with sub-level caving until year 2070 and the mining level 1888 m. For the first part, the ore is extracted the conventional way for numerical analyses in *FLAC3D* and for the three latter parts, the ore is extracted using a ring-by-ring principle in *CAVESIM*. For future production, a draw schedule was obtained from LKAB with an assumed annual production increase of 25 % (to 20 million metric tonnes annually by year 2025 and until year 2037). Each ring was individually extracted in *CAVESIM* with the coupling to *FLAC3D* being activated every year of equivalent production for each orebody.

2.3.2. Local Models

Two different local models were created for two selected areas with observed infrastructure damage in the mine, with one example shown in Figure 4. The models were constructed as a hybrid mesh with tetrahedral elements surrounding the infrastructure. Blasted and caved rock volumes were modelled as "caved rock" and correspond to the planned production and the predicted rock caving as they developed in the *FLAC3D-CAVESIM* global model each year. Areas with documented damages to the infrastructure were identified as locations of "higher interest" and a higher resolution zoning was applied to them to increase the precision of the results. The zones at these locations have a maximum edge length of 0.5 m. The maximum edge length of the zones increases gradually further away from these locations with a maximum value of 2.0 m.

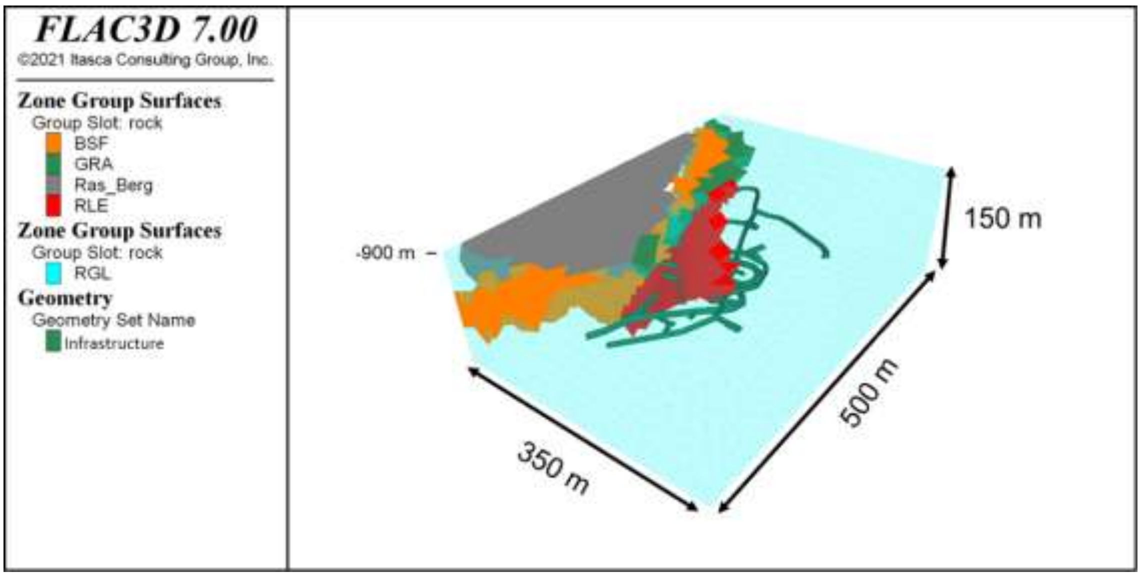

Figure 4. Example of local model.

3. CRITERIA FOR INFRASTRUCTURE DAMAGE

3.1. Development of Criteria

A series of criteria were developed and tested to find a criterion or a combination of criteria that could best explain the documented damages to the infrastructure and subsequently be used for the identification of other risk areas. The following criteria were tested:

- Stresses from the mine-scale model including principal stresses (σ_1, σ_3), differential stress (σ_1- σ_3), and change in differential stress ($\Delta(\sigma_1$- $\sigma_3)$);
- Stresses in shotcrete in local models;
- Deformations in local models;
- Depth of yielding in local models;
- Stress in areas with large deformations in local models; and
- Stress-Strength Ratio (SSR) for the mine-scale model.

The first two (stresses from the mine-scale model, and stresses in shotcrete in local models) showed none or poor correlation with observed infrastructure damages. None of these criteria could thus be used to replicate the field observations.

The third criterion tested assessed the correlation between the deformations in the local model and the reported damages to the infrastructure. The criterion was tested for all three deformation components (x, y, z) as well as for the displacement magnitude and the differential displacements between mining years, using the local-scale models. The magnitude of displacements provided a fair correlation with the field observations as many of the documented damages on the permanent infrastructure were included in the areas identified as medium or high risk i.e., areas that experience larger deformations. This relation suggests that the stress field retrieved from the global model is the main cause of the damages and therefore it can be used directly for the prediction of other risk areas without the need of constructing additional local models. This criterion, however, also indicates several "false positives" i.e., areas that are classified as medium or high risk but have no documented damages.

To reduce the instances of "false positives" various criteria were tested in combination with the deformations in the local model. One such criterion was the ratio of the maximum yielding depth to the tunnel height, which was used to ensure compatibility across the entire infrastructure. This criterion demonstrated a strong correlation with deformations, as areas classified as medium or high risk consistently had a larger yielding depth to tunnel height ratio. However, the combination of these two criteria did not help reduce the "false positive" cases.

The strong correlation between areas with larger deformations and the location of the field observations led to the conclusion that the initial stress field as this is retrieved from the global model is, together with the infrastructure geometry, a main driver of the damage development. Therefore, the development of a stress related criterion appears to be the best method to identify and predict areas with higher potential for infrastructure damage. Further examination of stresses in areas with large deformations revealed that the calculated major principal stress did not correlate well with observed damages. For the differential stress, a weak correlation between areas classified as medium/high risk and areas with high differential stresses was found. Moreover, the incremental change of the major principal stresses since the excavation of a specific drift was studied. In general, this showed a good correlation between areas that previously had been identified as medium/high risk by the large deformation criterion and areas that experience an even increase in the major principal stress of 3–5%. However, this could not be extended to all local models, thus indicating that there are other differences between the studied areas that were not accounted for.

The next parameter examined was the Strength-Stress Ratio (*SSR*), which quantifies the "margin capacity" of the rock mass, i.e., an *SSR*=1.0 implies that stresses and strengths are equal, while a higher SSR means that the strength is higher than the current acting stress on an element. SSR is calculated using the Mohr circle, starting with the actual stress state, σ_1 and σ_3, at a point (a zone) in the model, see Figure 5.

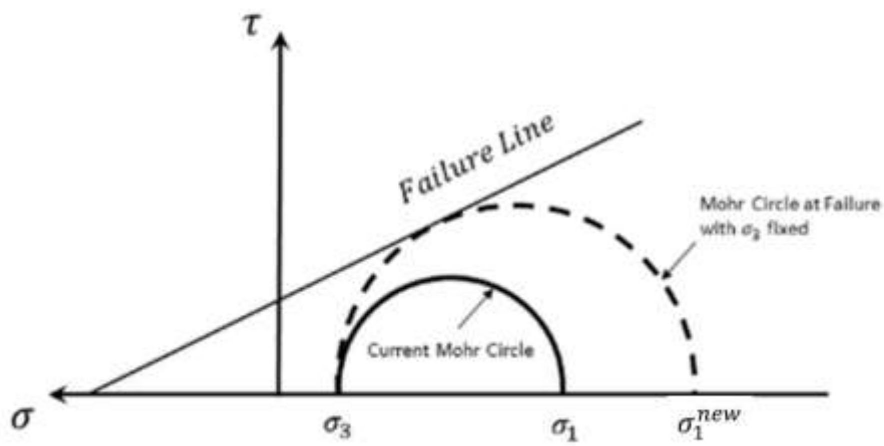

Figure 5. Schematic figure showing the definition and calculation of SSR.

The minor principal stress, σ_3, is fixed and the Mohr circle enlarged until it is tangent to the failure line, with a new major principal stress, σ_1^{new}, thus determined. The Strength-Stress Ratio is then defined as:

$$\mathrm{SSR} = \left|\frac{\sigma_1^{\mathrm{new}} - \sigma_3}{\sigma_1 - \sigma_3}\right|. \qquad (1)$$

The SSR criterion thus accounts for both the acting stresses and the variation of strength in the different geological units in the rock mass. An upper limit of SSR ≤ 10 is used in *FLAC3D*. If the current stress state is in tensile failure, then SSR is set to 0.

The value of *SSR* is calculated for every zone of the numerical model using the current major and minor principal stresses retrieved from the global model and the corresponding strength of the rock at the particular zone considering the current stress confinement. *SSR* as a prediction parameter was tested for the two local models used. The results showed a good correlation between the field observations; in particular, it was observed that the majority of the damages under examination were taking place in areas where SSR had a value of 2.5 or less, with only a small deviation of 10–20 m (Figure 6).

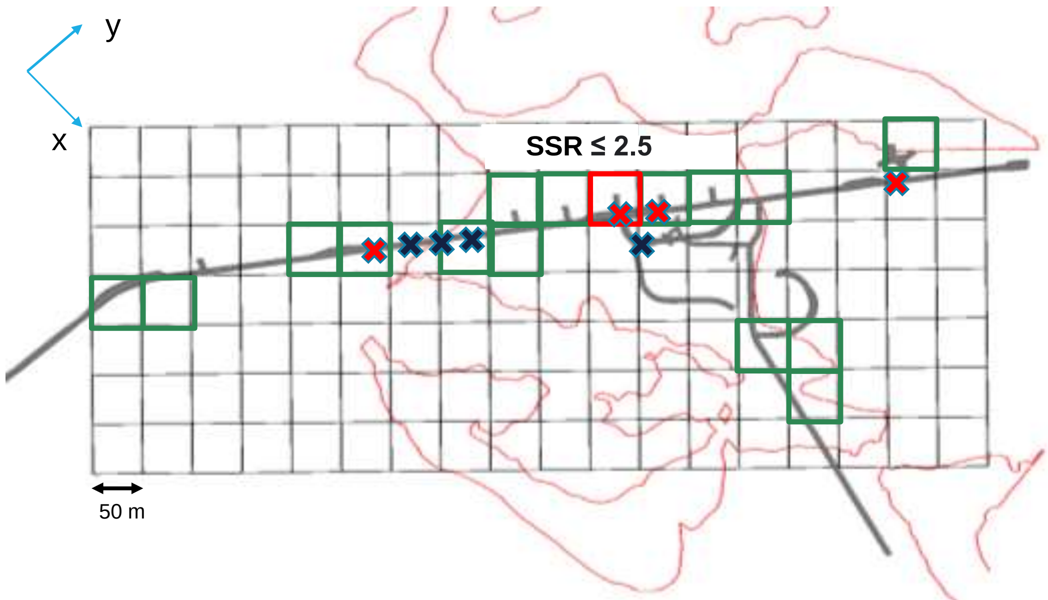

Figure 6. Example of application of the large deformation results on top of the Strength-Stress Ratio plot for a local model and year 2019, with red crosses showing the location of the observed infrastructure damages and dark blue crosses showing past damages (previous years).

3.2. Application and Calibration

As described above, the *SSR* criterion emerged as the most suitable fit to the field observations being able to replicate the location of damages on the permanent infrastructure with sufficient precision in both local models. Therefore, it was deemed as a robust criterion that can be applied globally to define higher-risk areas where the development of future infrastructure should be avoided or minimized. The *SSR* criterion can be applied directly to the mine-scale model, resulting in the identification of all the zones with a *SSR* value equal to or lower than the cut-off value selected (SSR=2.5). The restriction volume obtained is the product of the merging of those zones into one unified volume. The number of zones with an *SSR* value equal to or lower than the cut-off value, and subsequently the overall restriction volume varies annually, depending on the caving process and stress redistribution occurring during mining at deeper levels.

However, when developing the resulting volumes for SSR=2.5, very large volumes result for deeper mining, as illustrated in Figure 7. Since the damages used for the development of the criterion were exclusively minor damages on the infrastructure, the value of 2.5 was considered overly conservative and the rock volumes produced by its application too large for the purposes of this work. To enhance the precision of the produced "restriction volumes" further calibration of the selected criterion was undertaken using the additional data with more severe observed damages. The refined calibration validated that the preliminary value of 2.5 was too conservative and that a new lower value should be used to increase the precision of the criterion. Hence, a series of different *SSR* values were tested against all the calibration data. Example results are shown in Figure 8. The majority of the locations with severe damages in the calibration data were located in areas with an *SSR* value of 1.5 or less, within a spatial deviation of around 10–20 m.

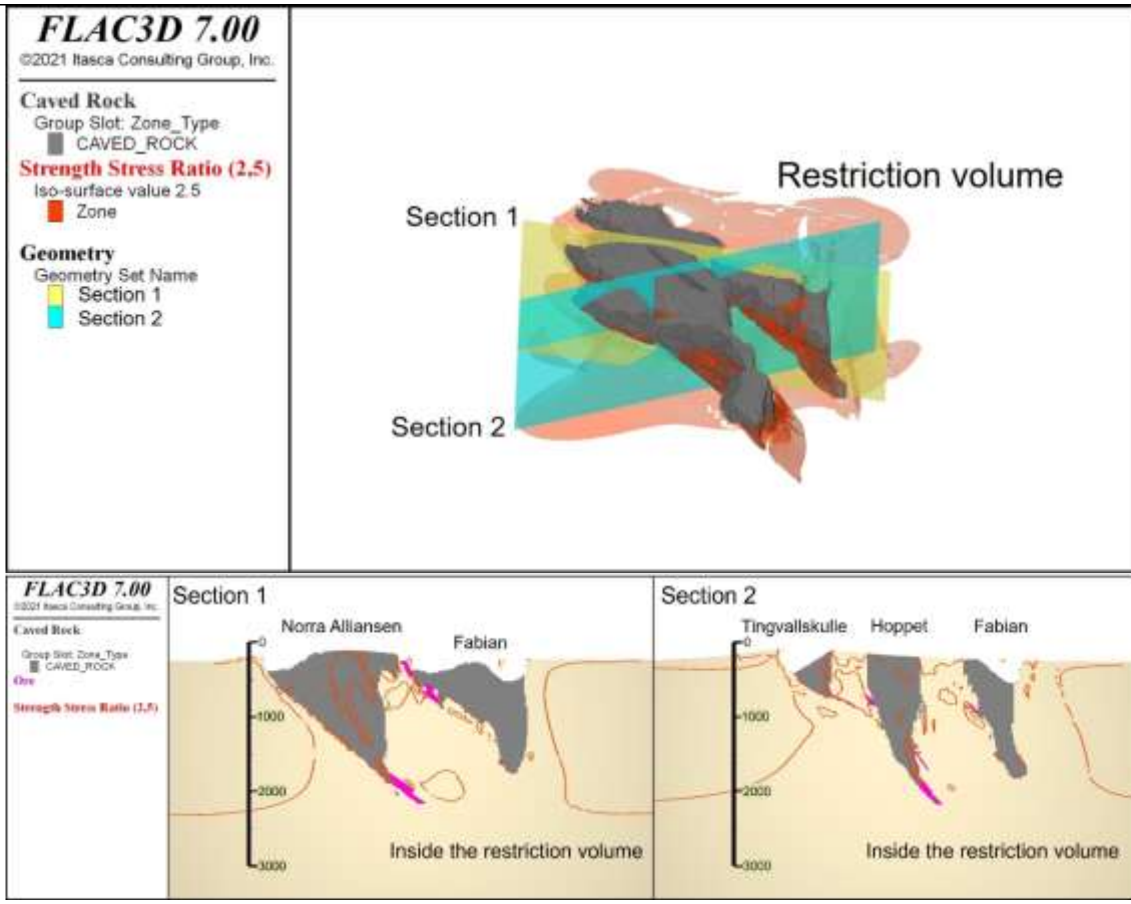

Figure 7. Development of "infrastructure restriction volumes" shown in 3D view (top) and selected cross-section views (bottom) for the year 2070 and SSR value of 2.5.

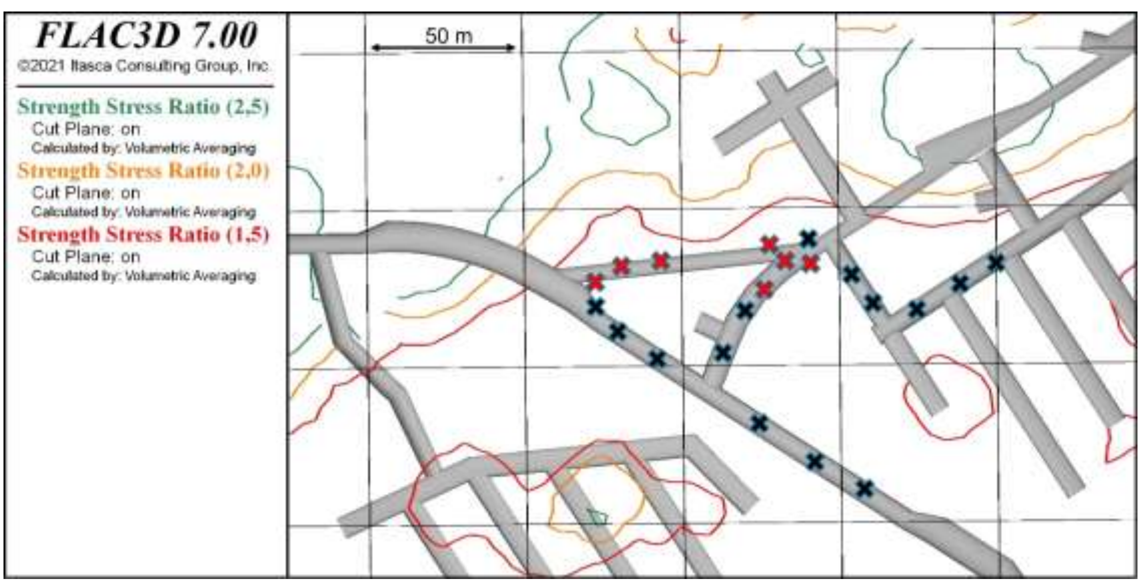

Figure 8. Example of testing of different SSR values for a selected area in the mine with infrastructure damage for year 2021, with red crosses showing the location of the observed infrastructure damages and dark blue crosses showing past damages (previous years).

4. INFRASTRUCTURE RESTRICTION VOLUMES

4.1. Final Restriction Volumes

The final application of the criterion resulted in considerably smaller restriction volumes, which were more precise in targeting areas with higher potential to develop stability problems, similar to those used for the calibration. The revised restriction volumes for year 2070 can be viewed in 3D and in the two selected sections in Figure 9. Developing infrastructure within the restriction volumes, or in areas that will later be included in the volumes, should be done with ability of rehabilitation in mind. For infrastructure that have already been developed in areas that will be included in the restriction volumes during the expected service time, rehabilitation plans should be created.

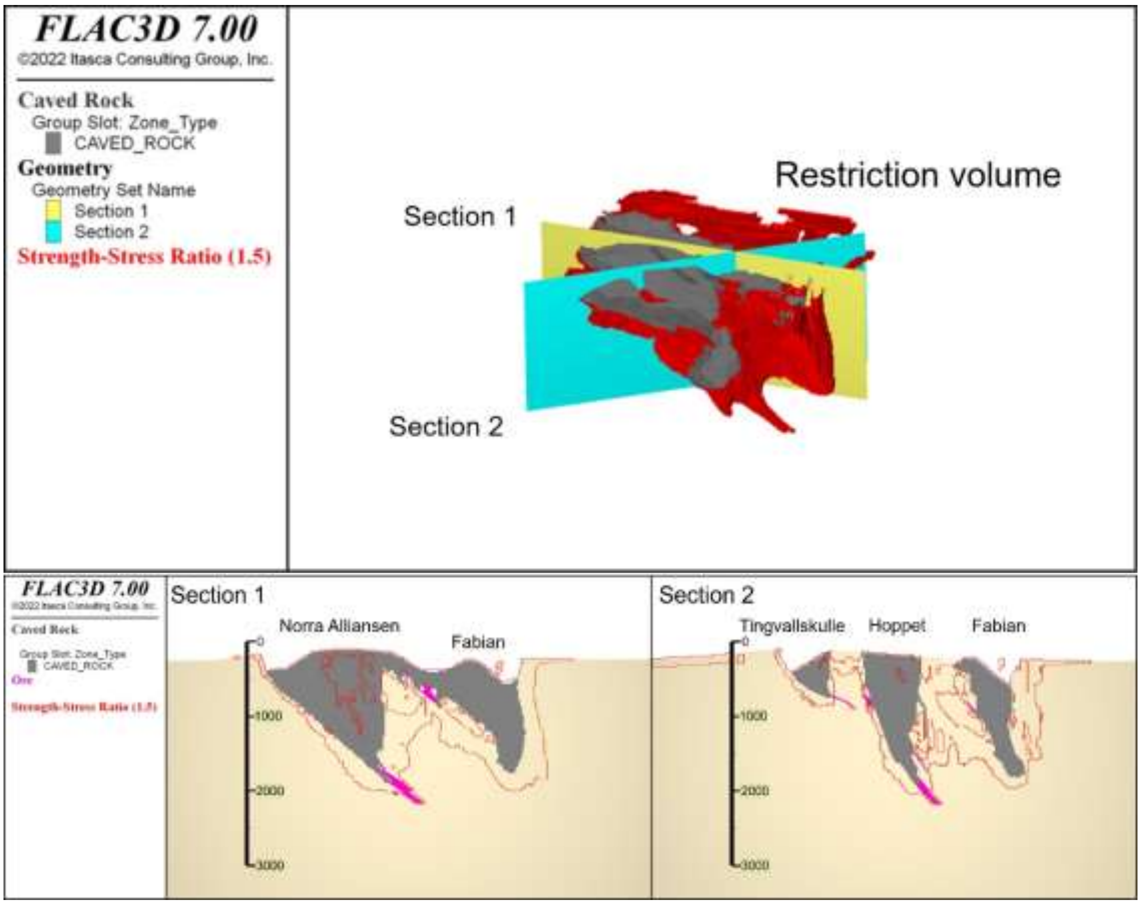

Figure 9. Development of "infrastructure restriction volumes" shown in 3D view (top) and selected cross-section views (bottom) for the year 2070 and SSR value of 1.5.

The infrastructure restriction volumes represent volumes of the rock mass within which the potential for damages to the infrastructure, similar to the damage in the calibration cases, is increased. The damage potential within the volume is uniform, meaning that damage is not more likely to occur deeper into the volume compared to close to the boundary. In general, however, the closer the position is to the orebody the more likely it is to be damaged. However, there are exceptions to this rule; developing in rock already yielded might be more beneficial than developing through rock that is expected to yield after development, thus, the lack of gradient in the volumes.

4.2. Discussion

The criteria for the development of the volumes were based on pre-existing damage (observed failures and fall-outs) observed in the mine. Only specific damages were used while others had to be excluded since they either could not be associated to failure mechanisms related to rock movements or were situated in proximity to production areas. Apart from the damage mapping, the geological model can be a source of uncertainty. The current geological model starts at 250 m depth and extends to some distance from the orebodies, thus lacking information near the surface and farther from the orebodies. The material parameters used for the different rock types were defined through previous calibration (Sjölander et al., 2022), and do not account for possible variations of the material properties within the same rock unit volume.

The infrastructure restriction volumes have been developed in relation to specific mining years. The mining years are based on the conceptual 20 Mton annual production plan. Deviations from this mining plan might affect the reliability of the restriction volumes, in particular when mining levels in different order or using a different mining method. Finally, the restriction volumes are based on static (aseismic) loading. The volumes have not been correlated to seismic risks and any attempts to cross-reference the restriction volumes to seismicity should be performed with great care.

5. CONCLUSIONS AND RECOMMENDATIONS

Based on the results of this study, the following conclusions can be drawn:

– The infrastructure restriction volumes represent rock mass volumes with higher potential of occurrence of damages corresponding to infrastructure function being compromised.
– Development of infrastructure inside the restriction volumes should be avoided or minimized. In case of developing infrastructure inside the restriction volumes, this should be done in a way allowing for future rehabilitation. For current infrastructure lying inside the restriction volumes rehabilitation or alternative infrastructure plans should be developed.
– The reliability of the restriction volumes can be affected in case of a revision of the conceptual mining plan or change of the mining method. A complementary analysis and a potential update of the restriction volumes is required in these cases.
– The yearly development of the restriction volumes should be considered during the mine design process to account for areas of volume contractions.
– The general methodology applied is judged to be suitable also for non-mining applications, provided that suitable observations are available for calibrating the criteria.

6. ACKNOWLEDGEMENTS

The work presented in this paper was funded by LKAB, which is gratefully acknowledged along with the permission to publish and present this paper.

REFERENCES

Ghazvinian, E., Garza-Cruz, T., Bouzeran, L., Fuenzalida, M., Cheng, Z., Cancino, C. and Pierce, M. (2020). *Theory and Implementation of the Itasca Constitutive Model for Advanced Strain Softening (IMASS)*. Proceedings of the Eight International Conference & Exhibition on Mass Mining (MASSMIN 2020), R. Castro, F. Báez & K. Suzuki (eds), pp 451–461.

Hebert, Y. and Sharrock, G. (2018). *Three-dimensional simulation of cave initiation, propagation and surface subsidence using a coupled finite difference–cellular automata solution*. Proceedings of the Fourth International Symposium on Block and Sublevel Caving, Y. Potvin & J. Jakubec (eds), Australian Centre for Geomechanics, Perth, pp. 151-166, https://doi.org/10.36487/ACG_rep/1815_09_Hebert

Itasca (2019). *FLAC3D* (Fast Lagrangian Analysis of Continua 3D) Version 7.0, Itasca Consulting Group, Inc, Minneapolis, USA.

Perman, F., Wettainen, T., Gonzalo, C. and Sjöberg, J. (2016). *Three-dimensional modeling and stress calibration for a complex mining geometry*. Proceedings RS2016, 7th International Symposium on In-Situ Rock Stress (Tampere, Finland, May 10-12, 2016), ISBN 978-951-758-606-1, pp. 127–138.

Sjölander, M., Jonsson, L., Figueiredo, B., Sjöberg, J. and Ersholm, F. (2022). *Analysis of caving and ground deformations in Malmberget using a coupled CAVESIM-FLAC3D*. Proceedings Caving 2022 (Adelaide, August 30 – Sept 1, 2022), Potvin, Y. (ed.). Perth: Australian Centre for Geomechanics, doi:10.36487/ACG_repo/2205_53.

Proceedings of the NROCK 2023
The IV Nordic Symposium on
Rock Mechanics and Rock Engineering
ISBN 978-9935-9436-2-0
DOI 10.33112/nrock2023.7

Quantitative numerical assessment of blast-induced wall damage

Marie-Hélène Fillion (mfillion@laurentian.ca)

O. Karimi
Laurentian University, Sudbury, Canada
M.-H. Fillion
Québec Ministry of Transportation, Québec, Canada
Laurentian University, Sudbury, Canada
P. Dirige
Workplace Safety North, Sudbury, Canada
Laurentian University, Sudbury, Canada

ABSTRACT

One of the cost-effective methods used for rock breakage in mining is drilling and blasting. In open pit mining, blast-induced damage can reduce the level of stability of benches and pit slopes, which is a concern for the safety of mine personnel. Rock fracturing and fragmentation by blasting is the result of the coalescence of existing and new fractures (created by the blast) in the rock mass. The stress waves affect the rock mass in a few milliseconds while the effects of gas pressure last in the scale of hundreds of milliseconds and have a greater effect on rock fragmentation. The presence of in-situ fractures can have a significant impact on the extent of blast-induced damage beyond the intended area of the blast. These fractures are generally preferential paths of least resistance for the explosive energy. It is therefore necessary to account for the effect of the in-situ fracture network to reliably characterize fracture development and blast-induced damage. Discrete fracture networks (DFN) are representations of joint systems and can estimate the distribution of in-situ fractures within a rock mass. The combined finite (FEM)/discrete (DEM) element method (or FDEM) is a useful tool to simulate the complex rock blasting process. FEM is used for calculating stress distribution and displacements before fracturing (static phase) and, once the fracture process begins, DEM is used for simulating the fractured medium (large displacement phase). The principal objective of this paper is to develop a DFN-based numerical FDEM model to assess the influence of gas pressure on blast-induced damage using a propagating boundary condition, which simulate the effect of gas pressure on a growing network of fractures. A two-holes open pit bench blast was simulated in 2D environment. In this simulation, gas pressure was applied on a propagating boundary (boundary of developed fractures). The numerical model is simulated based on rock and blast properties obtained from an operating open pit mine. The level of blast-induced damage was quantified based on the area of the blast damage zone and the intensity of blast-induced fractures. The results show that the propagating boundary condition provides a realistic simulation of blast holes interaction and blast-induced fracture development.

KEYWORDS

Blast-induced damage; Wall damage; Discrete Fracture Network; Combined finite/discrete element method; Fracture intensity.

INTRODUCTION

In open pit mine operations, drilling and blasting is a widely used method for rock breakage. The desired outcome for blast design could be fragment size, muck-pile shape, direction of displacement, minimizing fly rocks, and/or minimizing damage to final walls (Hall, 2015; International Society of Explosives Engineers, 2011). Insufficient knowledge of the rock properties and in-situ joints characteristics can cause delays and safety concerns in an open pit mine operation due to inadequate rock fragmentation, fly rocks and wall damage.

Wall damage is the extension of cracks and creation of new fractures beyond the intended area of fragmentation, and this can result in instabilities and hazardous environment. This could lead to loss of production, slope failures, damage to equipment and staff injuries (Silva et al., 2019). The blasting outcomes, such as blast-induced damage, are difficult to predict due to the complexity of the blasting process (Mitelman & Elmo, 2014). A good knowledge of the structural features (e.g., in-situ fractures networks) and reliable numerical simulations of the blasting process can aid in overcoming these challenges. Moreover, since the blasting process starts from a static phase to a large displacement phase, modeling should include both continuum and discontinuum models for better representation of the blasting process (Han et al., 2020).

1. DISCRETE FRACTURE NETWORKS

The rock mass consists of one or more rock types and natural fractures. Blast-induced rock fragmentation and wall damage are influenced by these fractures. The fractures act as planes of weakness allowing for the explosive energy to dissipate. Moreover, the in-situ fractures provide venting paths for the explosion gases. Therefore, the fractures should be represented in the blasting simulations. Discrete Fracture Networks (DFN) are 3D representations of joint systems that can estimate the distribution of in-situ block sizes based on field measurements of the fracture properties, i.e., fracture orientation (dip and dip direction) and intensity; and using statistical distributions. The P_{ij} system (Table 1) was introduced by the DFN community as a straightforward way to characterize DFN models in terms of scales and dimensions. The index *i* stands for dimension of sample and the index *j* represents dimension of measurement (Elmo et al., 2014b; Rogers et al., 2009). P32 (fracture area per unit volume) is the preferred measure of the fracture intensity since it represents a non-directional intrinsic measure of fracture intensity (Elmo et al, 2014a). A DFN-based analysis relies on quantifiable joints properties and provides realistic fracture networks with the key advantage of preserving the real joint properties during the modelling process.

Table 1. The Pij system of fracture intensity (Rogers et al., 2009).

		Dimension of Measurement				
		0	1	2	3	
Dimension of Sample	1	P10 No of fractures per unit length of borehole	P11 Length of fractures per unit length			Linear Measures
	2	P20 No of fractures per unit area	P21 Length of fractures per unit area	P22 Area of fractures per area		Areal Measures
	3	P30 No of fractures per unit volume		P32 Area of fractures per unit volume	P33 Volume of fractures per unit volume	Volumetric Measures
Term		Density		Intensity	Porosity	

The DFN model used in this paper was generated using Fracman (Golder Associates, 2020). Table 2 presents the orientation properties (dip and dip direction) of three fracture sets obtained from an open pit mine operated by Iamgold. The P32 value for the input data was calculated based on P21 (length of fractures per unit area) value (Elmo et al., 2014a). Then, using input parameters such as the dispersion of the orientation cluster (Fisher's constant K) and the volumetric fracture intensity P32 (Table 3), the DFN model in the dimensions of 54m long (X axis) × 24m wide (Y axis) × 20m deep (Z axis) was generated (Figure 1a). The length and width of the model were chosen to match the size of the numerical modeling geometry, which represents an open pit bench blast. The bench geometry was extended in length and in width to prevent unrealistic damage when stress waves reach the side and bottom boundaries. Fractures are generated as circular planes and the DFN volume is large enough to reliably represent these fractures. Since the blasting simulation is in 2D environment, a 2D longitudinal section of the 3D DFN model was extracted to represent the intersecting fractures within the rock mass (Figure 1b). These fractures were imported as an input to the developed FDEM model for the blasting scenario.

The orientation data were verified against the input orientation data using DIPS (Rocscience Inc., 2021). Figure 2a presents the stereonet of the input fracture orientation data and Figure 2b illustrates the orientation of the DFN generated fractures. Table 4 compares the input fracture orientation data with the orientation of the DFN generated fractures and their percentage of variation. According to the joint properties database, a variation of +/- 10 degrees in dip direction was observed in surveyed fracture set J1. This fracture set is subvertical which leads to higher variation in dip direction for the DFN generated fractures. Therefore, a more significant variation (14.7%) in dip direction obtained from the DFN model was observed. Based on the percentage of variation, the significant variation in dip for fracture set J10 (25.0%) is considered acceptable because it is due to a low dip value and the actual variation is one degree. Most of the orientation values fall under 5% variation.

Table 2. Fracture sets properties.

Parameters	Value per Fracture Set		
	J1	J2	J10
Dip (°)	85	41	4
Dip Direction (°)	95	269	96

Table 3. Input data for DFN model generation.

Parameters	Value
Fisher's K	60
P32 (1/m)	0.52

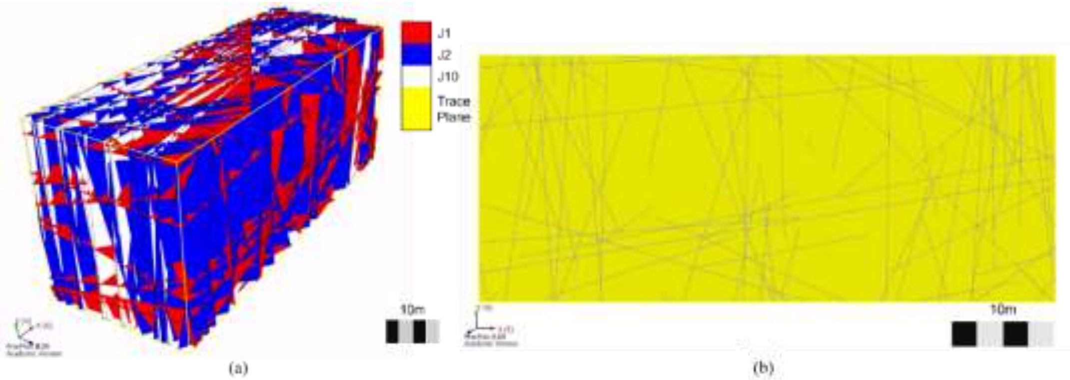

Figure 1. DFN model in Fracman (Golder Associates, 2020): (a) 3D DFN model, (b) 2D longitudinal section.

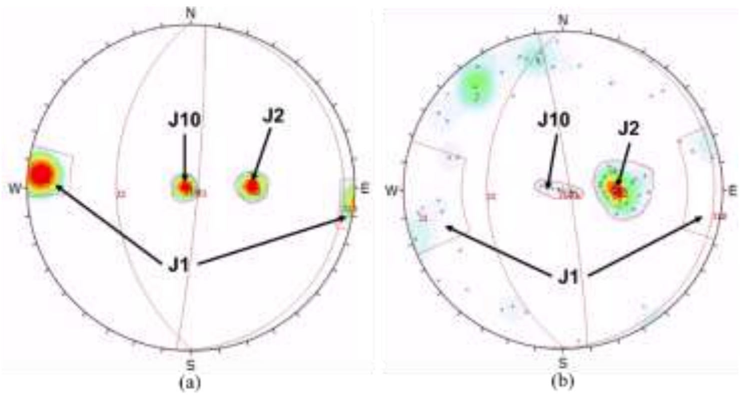

Figure 2. Orientation comparison using DIPS (Rocscience Inc., 2021): (a) Stereonet with input fractures' orientation, (b) Stereonet with DFN generated fractures.

Table 4. Fracture orientation comparison.

	Input Orientation		DFN Generated Orientation		Variation (%)	
Fracture Sets	Dip (°)	Dip Direction (°)	Dip (°)	Dip Direction (°)	Dip	Dip Direction
J1	85	95	84	81	1.2	14.7
J2	41	269	39	269	4.9	0.0
J10	4	96	3	98	25.0	2.1

2. BENCH BLAST NUMERICAL SIMULATION

This paper focuses on the wall damage assessment in terms of blast-induced fracture intensity using a propagating boundary condition to implement the effect of gas pressure within existing and blast-induced fractures. The simulation includes DFN-generated fractures to represent the role of in-situ fractures in the development and propagation path of blast-induced fractures. The bench blast scenario was simulated in 2D environment. The numerical model was developed based on blast design properties obtained from an open pit mine operated by Iamgold. The DFN model described in Section 1 was used as the input for the simulated scenario. Section 2.1. describes the numerical tool used for simulating the blasting scenario. Section 2.2 details the bench and blast design geometries. Section 2.3 provides the input parameters and material properties used in this analysis. Section 2.4. presents the detonation and gas pressures formulation and how these pressures were applied to the blastholes as pressure boundaries. Finally, Section 2.5. presents the blast damage assessment method.

2.1. Combined Finite/Discrete Element Method (FDEM)

The numerical simulation of the rock mass could be categorized depending on its behavior: continuous or discontinuous approaches (Elmo et al., 2013; Hamdi et al., 2014). For the continuum mechanical problems, the FEM is widely used for simulating large domains or fracture propagation (Hazay & Munjiza, 2016; Jing, 2003). The discrete element method (DEM) is the most used method for discontinuum problems such as fluid flow in fractured medium or large displacements caused by blasting (Hazay & Munjiza, 2016; Zhang, 2016).

Once rock blasting is initiated, the rock mass receives a dynamic load, which results in fracture development, rock fragmentation and muckpile formation. The fragmentation process consists of the detonation of explosives (detonation pressure), creating stress waves in the rock mass to initiate expansion and opening of existing fractures, and new cracks formation. Cracks expand and propagate because of the expansion of explosive gases (gas pressure) and the coalescence of the fractures forms rock fragments. When the fragmented rocks are being ejected because of the gas expansion, the movement is large enough and cannot be modeled with continuum approaches. Neither FEM-only or DEM-only approaches are adequate for simulating rock fragmentation by blasting.

The combined finite-discrete element method (FDEM), which was proposed by Munjiza et al. (1995) and Munjiza (2004), is an advantageous method that combines the finite and discrete element methods (Sun et al., 2016). This method can be used for numerical modeling of the processes that transition from continuum to discontinuum media by incorporating the contact detection interface analysis, as well as fracture creation and propagation (Hazay & Munjiza, 2016; Sun et al., 2016). For modeling the blasting process, FEM is used for calculating stress distributions and displacements in rock before fracture development. Once the fracture process begins, DEM is used for the fractured medium (Zhang, 2016).

2.2. Simulated Blasting Model

To represent blasthole interaction during the blasting process, a two-blastholes open pit bench blast was modeled using Irazu 2D (Geomechanica Inc., 2022). The 2D simulation is faster to simulate in terms of computational time. The scenario simulated for this paper use the DFN model described in Section 1 as an input to the FDEM simulation, as well as rock, blast design and explosive properties which are discussed in Section 2.3. The geometry of the simulated scenario is presented in Figure 3.

There are various studies in the literature regarding the numerical simulation of stress waves only or peak explosive pressure on boundaries of blastholes and their effects on fracture initiation and propagation (Wang et al., 2018). However, due to the complexity of the blasting process, there is limited information about the role of in-situ fractures and gas pressure in the propagating path of blast-induced fractures (Wang et al., 2018). In this simulation, the detonation and gas pressures are applied to the blastholes' boundaries as separate pressure boundaries and the propagating boundary condition developed by Geomechanica Inc. is used to represent the gas pressure within the blast-induced fractures.

The side boundaries of the rock domain are free to move in the vertical (Y) direction, i.e., towards the free surface representing the top of the bench. The bench face is free to move in the vertical (Y) and horizontal (X) direction and the bottom boundary is fixed to its location to represent confined ground. These constraints are used to prevent from generating any unrealistic displacement values near these boundaries. The mesh size progressively increases from 10cm (surrounding the blastholes) to 2m (at the rock boundaries). This progressive increase in mesh size allows for a higher resolution in areas experiencing large magnitudes of stresses and displacements, while lowering the computation time at a larger distance from the blastholes. The horizontal and vertical lengths are exaggerated to remove the effect of unrealistic extra damage near the model boundaries.

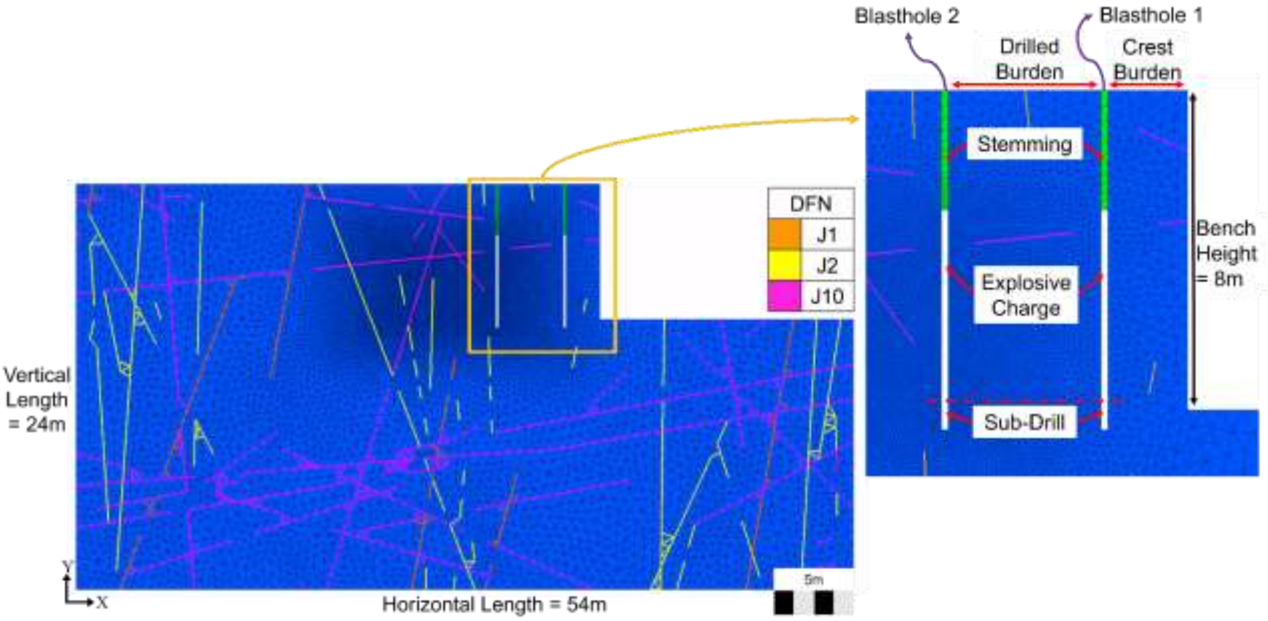

Figure 3. Geometry of the simulated model.

2.3. Material and Blast Design Properties

The rock properties, blast design parameters and explosive properties used in the simulation were obtained from an operating open pit mine. The bench is excavated in a hard rock formation. The required properties for a FDEM simulation are presented in Table 5. The fracture energies for Mode I and II were calculated based on the formulations presented by Whittaker et al. (1992). Table 6 presents the blast design parameters used in developing the numerical model geometry illustrated in Figure 3. The mine site uses a bulk explosive (mixture of ANFO and emulsion also known as heavy ANFO) which is manufactured on site (Table 7). The bulk explosive is considered fully coupled. Finally, the fractures in the DFN model are considered broken which defines them as pure frictional discontinuity surfaces (Geomechanica Inc., 2022). Table 8 presents the values assigned to the DFN model imported to the blasting simulation. The friction coefficient is the tangent of equivalent internal friction angle which was obtained from the mine's geotechnical database.

Table 5. Rock properties for FDEM simulation.

Parameters	Value	Symbol
Density (kg/m^3)	2700	ρ
Young's Modulus (GPa)	60	E
Poisson's Ratio	0.25	υ
Cohesion (MPa)	22	C
Tensile Strength (MPa)	11	f_t
Friction Coefficient	0.47	f_r
Friction Energy Mode I (N/m)	31	G_I
Friction Energy Mode II (N/m)	310	G_{II}
Constitutive Law	Plane strain	

Table 6. Blast design parameters.

Parameters	Value
Crest burden (m)	2
Drilled burden (m)	4
Stemming Length (m)	3
Charge Length (m)	5
Subdrill (m)	0.5
Blasthole diameter (mm)	165
Bench height (m)	8
Inter-Row delay (ms)	142

Table 7. Explosive properties.

Parameters	Value
Explosive Type	Heavy ANFO
Density (kg/m^3)	1200
Velocity of detonation (VOD) (m/s)	5000

Table 8. Fracture properties for DFN.

Parameters	Value
Fracture type	Broken
Friction Coefficient	0.73

2.4. Blasting Pressure Boundary Formulation

The formulation for the maximum detonation pressure within a borehole used in this paper was presented by Hajibagherpour et al. (2020) (Eq. 1).

$$P_d = \frac{4.18\times10^{-7}\times\rho_e\times VOD^2}{1+0.8\rho_e}\times({}^{d_c}/{}_{d_h})^{2.4} \quad (1)$$

Where P_d is the detonation pressure (Pa), VOD is velocity of the detonation (m/s), ρ_e is explosive density (g/cm^3), d_c is explosive diameter (mm), and d_h is blasthole diameter (mm). Since the explosives are considered fully coupled (d_c/d_h=1), Eq. 1 could be written as Eq. 2:

$$P_d = \frac{4.18\times10^{-7}\times\rho_e\times VOD^2}{1+0.8\rho_e} \quad (2)$$

A pressure-time curve is required to apply the detonation pressure with regards to time steps for FDEM analysis. Eq. 3 presents the formulation to determine pressure as a time function (Hajibagherpour et al, 2020).

$$P_t = 4P(e^{-\frac{\beta t}{\sqrt{2}}} - e^{-\sqrt{2}\beta t}) \quad (3)$$

Where P_t is the time history of the dynamic load imposed on blasthole boundary (Pa), *P* is the maximum detonation/borehole pressure (Pa), β is damping factor (1/s), and *t* is time (s). β is calculated using Eq. 4 (Hajibagherpour et al, 2020).

$$\beta = -\sqrt{2}\frac{\ln(1/2)}{t_r} \quad (4)$$

Where t_r is the rise time (time of peak pressure). This parameter is calculated by maximum velocity in different media and length of the media (Hajibagherpour et al, 2020). Lu et al. (2012) presented Eq. 5 to calculate the rise time:

$$t_r = \frac{L_e}{VOD} \quad (5)$$

Where L_e is the length of the column charge (m).

The peak gas pressure (borehole pressure) generated after a blast could be calculated using Eq. 6 (Zou, 2017):

$$P_b = 0.12 f_c^n \rho_e VOD^2 \quad (6)$$

Where P_b is borehole pressure (Pa), *VOD* is velocity of detonation (m/s), ρ_e is the density of explosive, f_c is coupling factor (ratio of the volume of the explosive to the volume of the blasthole excluding the stemming column), and *n* is coupling factor exponent (value between 1.2 and 1.3 for dry holes and 0.9 for holes filled with water). For a fully coupled explosive, f_c=1 and Eq. 6 could be written as Eq. 7:

$$P_b = 0.12\rho_e VOD^2 \quad (7)$$

Using the available explosive properties (Table 7), the peak detonation pressure is 6.73GPa and the peak gas pressure is 3.36GPa. Using Equations 3 and 4, the detonation and gas pressure-time curves for both blastholes were calculated. Figure 4 depicts the blasting curves applied to both blastholes. Blasthole 2 has the same pressure-time curves with an addition of 142ms delay timing which represents the inter-row delay.

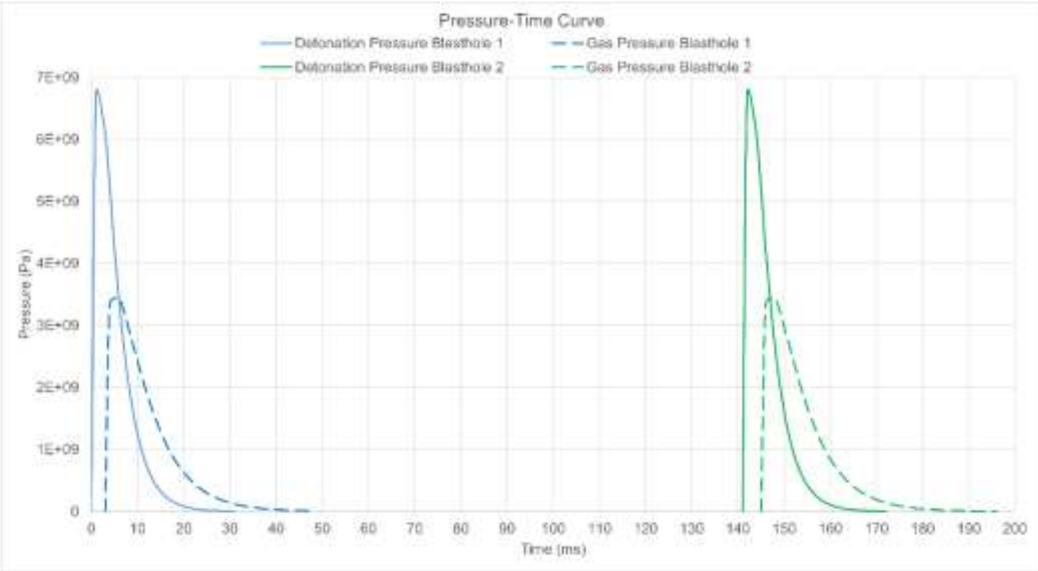

Figure 4. Detonation and gas pressure-time curves.

2.5. Damage Intensity Formulation

To assess and compare the intensity of blast-induced damage in the final wall area, the damage intensity index, D_i, presented by Lupogo et al. (2014) was used. The damage intensity index is defined in Equation 8. Since the focus of this research is to determine the damage intensity in the final wall, D_i was assessed for the back wall area (blast damage zone).

$$D_i = {}^{Yielded\ area}/_{Total\ area} \tag{8}$$

where *Total Area* is the area of the blast damage zone (red and yellow boundaries in Figure 5), and *Yielded Area* is the summation of fractured elements areas in the desired section (Figure 6). The yielded elements are the elements that are neighboring a fracture initiated or propagated during the blast.

Two domains for the total area were considered for the model: (1) Domain 1 (red boundary) which includes heavily damaged, partially damaged, and lightly damaged rock mass, and (2) Domain 2 (yellow boundary) which encompasses heavily damaged and partially damaged rock mass. Domain 1 covers 55m^2 and Domain 2 has a total area of 22m^2.

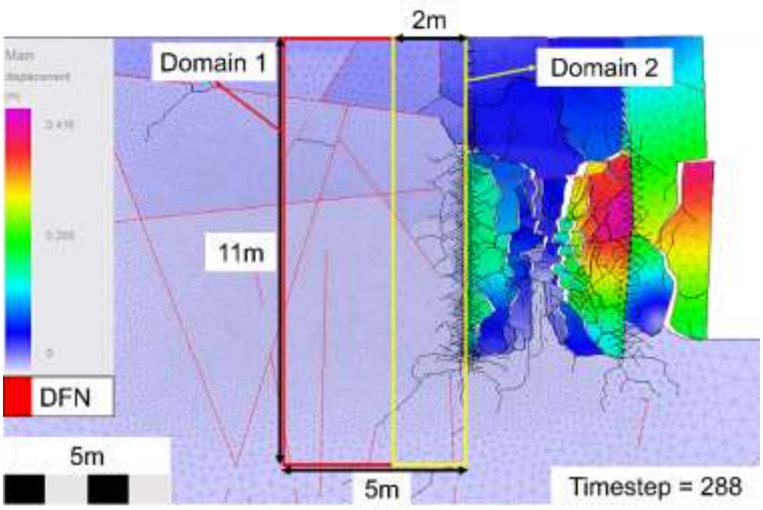

Figure 5. Total Areas selected for the blasting simulations (Domain 1 in red and Domain 2 in yellow).

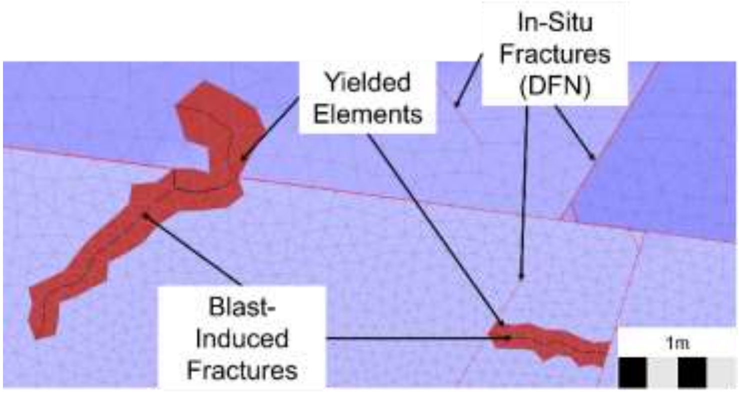

Figure 6. Example of yielded elements (highlighted in red).

3. SIMULATION RESULTS AND BLAST DAMAGE ASSESSMENT

The simulation was conducted using Irazu 2D, a FDEM software developed by Geomechanica Inc. (2022). Section 3.1. presents the simulation results for a propagating boundary condition applied to the boundaries of the blastholes and of the blast-induced fractures to represent gas expansion during the blasting process. In Section 3.2. the damage intensity of the bench wall is assessed.

3.1. Blast Simulation with Propagating pressure boundary

The pressure-time curves for detonation and gas pressures, as depicted by Figure 4, were applied as boundary conditions in this numerical simulation. Figure 7 illustrates the results obtained at three different timesteps during the blasting process. First, the detonation pressure is applied to the external boundary of the two blastholes. Figure 7a shows the fractures generated shortly after blast initiation, when the detonation pressure damages the surrounding rock and generate the initial fractures, transversally to the blasthole boundary. Shortly after blast initiation, the gas pressure is applied on the boundary of blast-induced fractures using the propagating boundary condition developed by Geomechanica Inc. (2022). With this condition, gas flow is considered adiabatic since the gases expand rapidly within the fractures with no heat loss (Zhang, 2016). The pressure is applied on the fractures' boundary until the fractures reach to the radius of the pressure front and/or the pressure reaches zero by the timesteps defined (see Figure 4). Figure 7b illustrates the propagation of blast-induced fractures and the coalescence of these fractures with the closest in-situ fractures represented by the DFN (red fractures in Figure 7). Figure 7b also represents the coalescence of blast-induced fractures between the two blastholes, as well as the timestep for which fractures reach the free face, with the associated increase in displacement. Then, as a result of fracture propagation and gas expansion, rock fragments are formed, and significant displacements are observed (Figure 7c). At the timestep of Figure 7c, venting of the explosion gases has occurred, and no additional damage is observed in the final wall area (i.e., left side of blasthole 2). Since the focus of this paper is wall damage intensity, the numerical simulation is stopped after reaching the large displacement stage shown in Figure 7c.

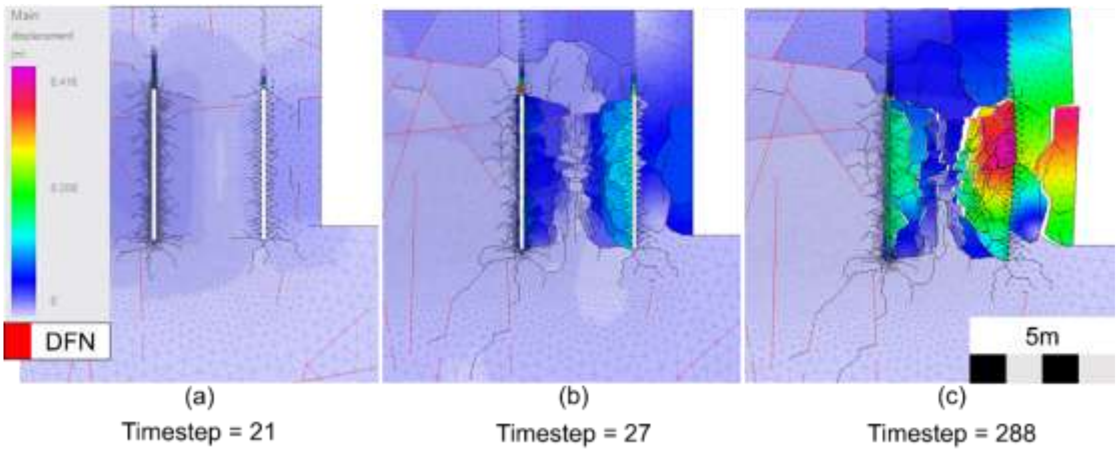

Figure 7. Blasting simulation using a propagating boundary condition: (a) Fracture initiation, (b) Fractures reach the free face, and (c) Rock fragmentation and displacement.

3.2. Damage Intensity Assessment

The damage intensity index D_i was calculated using Equation 8 for domains 1 and 2, as illustrated in Figure 5. Table 10 presents the damage intensity values calculated from the results of the blast damage simulation. The D_i value comparison between domains 1 and 2, shows that the damage intensity for domain 2 is slightly higher than domain 1. This was expected because domain 2 covers a smaller area and includes a heavily damaged zone in the vicinity of blasthole 2 and a partially damaged zone, as the distance from blasthole 2 increases. As illustrated in Figure 7b and 7c, the fractured rock is mostly focused on half of the drilled burden distance, i.e., in a one-meter distance from blasthole 2.

Table 10. Damage intensity values for domains 1 and 2.

Scenario	Damage Intensity (D_i)	
	Domain 1 (red)	Domain 2 (yellow)
Blast with Propagating Boundary Condition	0.012	0.015

Due to the formulation used for blast damage assessment (Eq. 8), D_i is influenced by the area selected for blast damage assessment and by the resolution (i.e., mesh size) used for the numerical simulation of the blasting process. When comparing multiple blast design scenarios with the suggested blast damage assessment method for blast optimization, the same area and resolution should be used to represent the blast damage zone.

4. CONCLUSION

Blast-induced damage should be minimized to ensure safety for mine personnel and equipment. The results of the blasting simulation demonstrated that in-situ fractures influence the propagation path of blast-induced fractures. Consequently, this will influence the dissipation of explosive energy and explosion gas venting during the blasting process. A sufficient knowledge of in-situ fracture network is needed for reliably assessing the outcome of a blast design. Discrete fracture network (DFN) modelling is a useful tool to represent the characteristics of the fracture network (in-situ fracture orientation and intensity) in numerical simulations of the blasting process, in order to evaluate how these fractures can influence fracture propagation and blast-induced damage. A reliable estimate of the volumetric fracture intensity (P32) is necessary to generate a DFN model representative of the field conditions. The P32 value (area of fractures per unit volume) cannot be measured in the field and is therefore estimated from P10 (number of fractures per unit length of borehole) and/or P21 (length of fractures per unit area). A limited dataset is often one of the limitations in geologically governed simulations. Sufficient and good quality structural data (dip, dip direction, spacing, persistence, etc.) are necessary to generate a representative DFN model.

The results of this study demonstrated that the combined finite-discrete element method (FDEM) is a capable tool to simulate the static and dynamic phases of the blasting process. Despite the advantage of reducing the computational time, a two-dimensional FDEM blasting simulation is limited because it cannot represent the interaction between blastholes on the same row. Blast-induced fracture propagation and fragmentation are three-dimensional processes, and this can have an impact on the resulting wall damage assessment. Moreover, the rock properties should be a primary consideration in blast simulation because, as opposed to blast design parameters (burden, spacing, timing sequence, etc.), rock properties are site-specific and cannot be controlled. A sufficient level of confidence in the rock properties (strength, elastic properties, density, etc.) used for FDEM simulation is then necessary for a reliable wall damage assessment. According to the blasting simulation presented in this paper, the propagating boundary condition used to represent the effect of the gas pressure allowed for a realistic simulation of fracture development, blasthole interaction and formation of rock fragments. The proposed blast damage assessment method can be used to evaluate different blasting scenarios for minimizing wall damage, while reducing the costs of conducting multiple test blasts.

5. ACKNOWLEDGEMENTS

The authors acknowledge the support of the Natural Sciences and Engineering Research Council (NSERC) and Iamgold Corporation for research funding, WSP-Golder for access to the DFN software Fracman, and Geomechanica Inc. for access to the FDEM software Irazu.

REFERENCES

Elmo, D., Liu, Y., & Rogers, S. (2014a). Principles of discrete fracture network modelling for geotechnical applications. In: Proceedings of the First International DFNE Conference, 19-23 October, Vancouver, British Columbia, Canada. 8 p.

Elmo, D., Rogers, S., Stead, D., & Eberhardt, E. (2014b). Discrete Fracture Network approach to

characterise rock mass fragmentation and implications for geomechanical upscaling. Mining Technology, 123(3), 149–161. https://doi.org/10.1179/1743286314Y.0000000064
Elmo, D., Stead, D., Eberhardt, E., & Vyazmensky, A. (2013). Applications of Finite/Discrete Element Modeling to Rock Engineering Problems. International Journal of Geomechanics, 13(5), 565–580. https://doi.org/10.1061/(ASCE)GM.1943-5622.0000238
Geomechanica, Inc. (2022). Irazu 2D Geomechanical Simulation Software (Computer Software). V.5.1. Theory Manual. Geomechanica Inc., Toronto, ON, Canada. 123 p.
Golder Associates. (2020). FracMan: DFN software suite [Computer software]. Golder Associates, Toronto, ON, Canada. Retrieved from http://www.golder.com/fracman/.
Hajibagherpour, A., Mansouri, H., & Bahaaddini, M. (2020). Numerical modeling of the fractured zones around a blasthole. Computers and Geotechnics, 123, 103535. https://doi.org/10.1016/j.compgeo.2020.103535
Hall, A. (2015). Predicting Blast-Induced Damage for Open Pit Mines Using Numerical Modeling Software and Field Observations (M. A. Sc. Thesis). Laurentian University, Sudbury, Ontario, Canada. https://zone.biblio.laurentian.ca/handle/10219/2930
Hamdi, P., Stead, D., & Elmo, D. (2014). Damage characterization during laboratory strength testing: A 3D-finite-discrete element approach. Computers and Geotechnics, 60, 33–46. https://doi.org/10.1016/j.compgeo.2014.03.011
Han, H., Fukuda, D., Liu, H., Salmi, E., Sellers, E., Liu, T., & Chan, A. (2020). Combined finite-discrete element modelling of rock fracture and fragmentation induced by contour blasting during tunnelling with high horizontal in-situ stress. International Journal of Rock Mechanics and Mining Sciences, 127, 104214. https://doi.org/10.1016/j.ijrmms.2020.104214
Hazay, M., & Munjiza, A. (2016). Introduction to the Combined Finite-Discrete Element Method. In Computational Modeling of Masonry Structures Using the Discrete Element Method, Sarhosis V., Bagi K., Lemos J. & Milani G. (Ed.). IGI Global.: pp. 123-145. doi: 10.4018/978-1-5225-0231-9.ch006
International Society of Explosives Engineers. (2011). ISEE blasters' handbook. (18th ed.). Cleveland, Ohio: International Society of Explosives Engineers.
Jing, L. (2003). A review of techniques, advances and outstanding issues in numerical modelling for rock mechanics and rock engineering. International Journal of Rock Mechanics and Mining Sciences, 40(3), 283–353. https://doi.org/10.1016/S1365-1609(03)00013-3
Lu, W., Yang, J., Yan, P., Chen, M., Zhou, C., Luo, Y., & Jin, L. (2012). Dynamic response of rock mass induced by the transient release of in-situ stress. International Journal of Rock Mechanics and Mining Sciences, 53, 129-141. https://doi.org/10.1016/j.ijrmms.2012.05.001
Lupogo, K., Tuckey, Z., Stead, D., & Elmo, D. (2014). Blast damage in rock slopes: potential applications of discrete fracture network engineering. In Proceedings of the 1st International Discrete Fracture Network Engineering Conference, Vancouver, Canada. p (Vol. 14).
Mitelman, A., & Elmo, D. (2014). Modelling of blast-induced damage in tunnels using a hybrid finite-discrete numerical approach. Journal of Rock Mechanics and Geotechnical Engineering, 6(6), 565–573. https://doi.org/10.1016/j.jrmge.2014.09.002
Munjiza, A. (2004). The combined finite-discrete element method. John Wiley & Sons Ltd., Chichester, UK. doi: 10.1002/0470020180.
Munjiza, A., Owen, D. R. J., & Bicanic, N. (1995). A combined finite-discrete element method in transient dynamics of fracturing solids. Engineering Computations, 12(2), 145–174. https://doi.org/10.1108/02644409510799532
Rocscience Inc. (2021). DIPS Tutorial (version 8) (Computer Software). Available from https://www.rocscience.com/software/dips
Rogers, S., Elmo, D., Beddoes, R., & Dershowitz, W. (2009). Mine scale DFN modelling and rapid upscaling in geomechanical simulations of large open pits. In: Proceedings of the International Symposium on 'Rock Slope Stability in Open Pit Mining and Civil Engineering', November 2009, Santiago, Chile: 11 p.
Silva, J., Worsey, T., & Lusk, B. (2019). Practical assessment of rock damage due to blasting. International Journal of Mining Science and Technology, 29(3), 379-385. https://doi.org/10.1016/j.ijmst.2018.11.003
Sun, G., Sui, T., & Korsunsky, A. (2016). Review of the hybrid finite-discrete element method (FDEM). In: Proceedings of the World Congress on Engineering, 29 June - 1 July 2016, London, U.K., 5 p.
Wang, Y., Wang, S., Zhao, Y., Guo, P., Liu, Y., & Cao, P. (2018). Blast induced crack propagation and damage accumulation in rock mass containing initial damage. Shock and Vibration, 2018. https://doi.org/10.1155/2018/3848620
Whittaker, B.N., Singh, R.N., Sun, G., (1992). Rock Fracture Mechanics: Principles, Design, and Applications (p. 570). Amsterdam: Elsevier.
Zhang, Z.-X. (2016). Rock fracture and blasting: Theory and applications. Elsevier Inc., Cambridge, MA, USA.
Zou, D. (2017). Theory and technology of rock excavation for civil engineering (p. 699). Springer, Singapore.

Proceedings of the NROCK 2023
The IV Nordic Symposium on
Rock Mechanics and Rock Engineering
ISBN 978-9935-9436-2-0
DOI 10.33112/nrock2023.8

Numerical Analysis of the Sensitivity of Joint Parameters to the Cross-cut in Response of Dynamic Loading

Senzia Warema (senzia.warema@ltu.se)

Senzia Warema[1,2] (corresponding primary author)
1.Rejlers Sverige AB,Sweden
2.Luleå University of Technology,Luleå,Sweden

Shahin Shirzadegan[3]
3.Ramboll Sverige AB,Sweden.

Erling Nordlund[2]

Changping Yi[2]

Flavio Lanaro[1]

ABSTRACT

Rock masses are far from being continuum and consist essentially of intact rock and discontinuities such as joints. Presences of discontinuities affects the propagation of the stress wave in rock mass. In this paper the impact of joints properties and features on the dynamic response of underground cross-cuts to seismic loading induced during dynamic large-scale field test in Kiirunavaara mine, was numerically investigated. The numerical methods used comprise the finite element code LS-DYNA and the 2D Universal Distinct Element Code (UDEC). The LS-DYNA model simulated the blasting and acquired the crushed zone and the vibration velocities around the crushed boundary. The vibration velocities from LS-DYNA were then used as an input velocity in the UDEC model. The studies of parameters such as joint normal and shear stiffness, joint spacing and joint orientation were conducted. The vibration responses at the wall of the underground cross-cut from UDEC were analyzed and compared to observed field test results. The results show that the normal stiffness has large effects on the peak particle velocity (PPV) while the shear stiffness contributes less influence. However, changes on joint space and orientation affect the PPV at the wall of the cross-cut. The joint stiffness explains the quality of the joint to transmit the stress wave while the joint spacing, joint orientation describe the blocky in burden which explain number of times the stress wave will be reflected before reaching cross-cut wall. The analysis can be useful during designing of the blast, burden as well as cross-cut support.

KEYWORDS

underground cross-cut; joints; numerical modeling; dynamic response

1. INTRODUCTION

The rock is divided in two categories: intact rock and rock mass, the latter is characterized by existence of discontinuities such as joints, faults, and other features. Sometimes rockmass can be subjected to dynamic events as earthquake or induced seismicity such as blasting, excavation at high depth etc. The disturbance induced by the dynamic events propagates in rock mass in the form of stress waves. The presences of the discontinuities affect the propagation of stress waves through the rock mass. Therefore, prediction and evaluation of wave attenuation or amplification across the jointed rock mass are vital components upon designing. These components are vital upon designing dimensions and orientations of underground cross-cuts, appropriate rock supports, time span as well as uses of the cross-cut. However, stress waves across the discontinuities (joints) experience complex phenomena that include multiple reflections, transmissions, refraction, superposition as well as absorption. Mechanical and spatial properties of the joints are vital factors that affect the wave propagation in the joints. The harm side of the stress wave propagation as rockburst in deep mines, collapse surface and sub-surface structures as well as damaged caused by it, has attracted researchers to study the wave propagation in jointed rock in different aspects, from theoretical, experimental and numerical point of view.

Perino et al. (2010) and Chai et al. (2017) performed theoretical studies that considered one joint set with parallel joints through rock mass model. The incident wave applied in one end and the reflected wave at the other end of the model. The number of the parallel joints altered, as was the space between the joints. Both models showed that the wave amplitude decreases as the number of joint increases. The increase in joint number increases delay time (phase), also the amplitude increases with the increase of the normal stiffness. The analytical study and quantification of stress wave propagation in the jointed rock mass widely use Displacement Discontinuity Model (DDM) (Schoenberg 1980, Pyrak-Nolte 1996). In that model stress is considered continues while displacement is discontinuous. In the other hand Ma and An (2008) performed numerical simulation of blast-induced rock fracturing where a finite element model was used to study the wave propagation through jointed model, in their model the orientation of the joint was changed and the focus were the type of damage that might be caused by the wave reflection on free surface. Huang et al. (2015) used the PFC2D code to simulate the propagation of stress wave in the filled joints since unfilled joints are not so common in presence. The fill material in joints including weathered clay, sand, silt etc, either saturated or unsaturated, has impact in mechanical properties of the joints. The simulation considered that the filled material has no tensile strength and therefore the reflected tensile wave will stop passing through and complex multiple reflections occur in layer of filled material. The work of Zhang et al. (2013) simulated the blasting as induced wave propagation in the jointed rock and its effects on the test site walls of tunnel. The numerical model used the coupling of LS-DYNA and UDEC, the former was used to simulate the blasting, and the latter was used to simulate the wave propagation in the jointed rock. UDEC coupled with 2D-AUTODYN model used by Chen and Zhao (1998) to study wave attenuation in blasted dry jointed rock mass. The modelling results showed that the presence of the joints in the rock mass causes rapid attenuation of the waves.
Numerical modeling must establish origin of joint. The joint origin may influence the wave propagation as it may affect the number of joints in given joints spacing. Therefore, this study took into consideration joint origins, joint stiffness, orientation and joint spacing.
Shirzadegan (2020) reported the large-scale dynamic field tests conducted in Kirunavaara mine in Sweden after reported cases of rockburst. The tests aimed to assess the capacity of rock support systems subjected to dynamic loading. Blasting was used to generate the seismic waves. The tests were also studied using numerical analyses (Shirzadegan, 2020). A combination of UDEC and LS-DYNA was used in the analyses. However, it was concluded that lack of certainty of mechanical and spatial values of joints. In this study the numerical modelling was carried out to investigate the sensitivity of joint parameters in wave propagation, severity of its damage in test wall performed based on large scale dynamic test 6 conducted in Kiirunavaara mine (Shirzadegan et al.,2016b). The LS-DYNA was used to simulate blasting and the UDEC was used to model the dynamic response of the test wall.

2. FIELD TEST AND NUMERICAL MODELING

2.1 FIELD TEST

The large-scale field tests were carried out in the Kirunavaara mine. The mine is located in the northern Sweden. The orebody strikes about North-South and dips 60° to the East. The orebody is estimated to be 4 km long with an average width of 80 m. The orebody lies between trachyo-andesite and rhyolite. The main mining method is large-scale sublevel caving (Malmgren, 2005). The tests were conducted in the northernmost part of the Kiirunavaara mine, block 9 and mining level 741 m. Seven tests were conducted (Shirzadegan et al.; 2016a and 2016b) in cross-cuts 93, 95, 100 and 103.

In Tests 1 – 5, the distance between the blasthole and the test wall was 2.8 – 3.9 m. Based on the results from these tests and numerical analysis by Zhang et al. (2013), the distance was increased to 8.1 – 8.7 m in Tests 6 and 7. In Tests 6 and 7 the blastholes were drilled in the middle of the pillar between cross-cut 100 and 103.
The holes were charged with NSP711 explosive, and the length of the charge was 10 m. The blastholes were not stemmed to reduce the effect of gas pressure. Shirzadegan et al.(2016b) mapped sixty five (65) joints in the site area. The mineralization and geology of the site are illustrated in Fig. 1

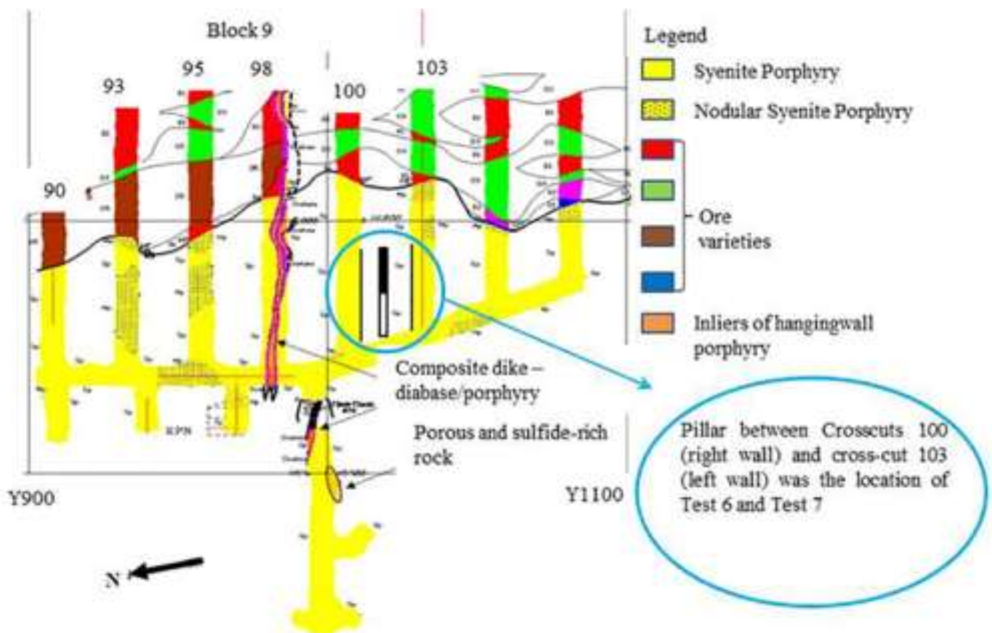

Figure 1: Location of the test site (Shirzadegan et al. 2016b).

2.2 NUMERICAL MODELING

According to Zhang et al. (2013) the explosion cannot be simulated using UDEC as the detonation creates a crushed zone around the blasthole that causes enormous energy absorption. Therefore, LS-DYNA was used to simulate the detonation stage of the blast. The NSP 711 explosive used in the field test is modelled with an explosive material model in LS-DYNA and with the Jones-Wilkins-Lee (JWL) equation of state (EoS) (Lee et al. 1968) as Equation (1):

$$p = A_1\left(1-\frac{w}{R_1 V}\right)e^{-R_1 V} + B_1\left(1-\frac{w}{R_2 V}\right)e^{-R_2 V} + \frac{wE}{V} \qquad (1)$$

where:

p = the pressure;
A1, B1, R1, R2 and ω = constants
V = the specific volume
E = the internal energy.

A1, B1, and E have units of pressure while R1, R2, and w are unitless. The parameters of NSP 711 explosive were calibrated by Helte et al. (2006) and are listed in Table 1. In Table 1, ρe is the density of the explosive used, D is the velocity of detonation of the explosive, PCJ is the Chapman-Jouguet pressure of the explosive and Ee is the initial internal energy of the explosive.

Table 1.Properties of NSP 711 Explosive

ρ_e (kg/m^3)	*D* (m/s)	P_{CJ} (GPa)	A_1 (GPa)	B_1 (GPa)	R_1	R_2	*w*	E_e (kJ/cc)
1500	7680	21.15	759.9	12.56	5.1	1.5	0.29	7.05

A Crushed Zone Boundary (CZB) with a diameter of 1.1 m was obtained by the LS‑DYNA analysis and used as an internal boundary in UDEC. At the CZB the velocity-time history calculated by LS-DYNA was applied as an

internal boundary condition in UDEC. The particle velocity applied at the CZB and the UDEC model are shown in Fig 2a. The UDEC model is used to simulate the stress wave propagation in the jointed rock mass.
The UDEC model of Test 6 was 80m x 80 m was built. The diameter of crushed zone boundary (CZB) was 1.1 m. The blastholes were drilled in the pillar between cross-cuts 100 and 103. Cross-cuts were 7 m wide and 5.2 m high.
History points in the model of cross-cut 100 were located on the test wall, 1.5 m above the floor (bottom), 2.2 m above the floor (middle) and 3.5 m above the floor (upper) in Fig.2a. Plastic deformation, wave propagation and running time considerations led to the zone size 0.2 m. The external boundaries of the model were located as far as about four times the dimension of the cross-cut and were set as non-reflecting (viscous) boundaries to address reflected waves. Fig 2a represents two joint sets UDEC model structure.
In this UDEC model the in-situ stresses used were based on the work by Malmgren and Sjöberg (2006) that considered mine-scale of the Kirunavaara mine. The adopted stresses are -16.48MPa and -11.28MPa in x and y directions, respectively. Since this paper reports a sensitivity study a base case was defined, see Table 2. One parameter at a time was varied while the other parameters were held constant and equal to the base case values. The input parameters for the mechanical properties of intact rock and mechanical properties of joints used in the Base Case are listed in Table 2 and Table 3 (Malmgren and Nordlund, 2006, 2008 and Brandshaug, 2009).

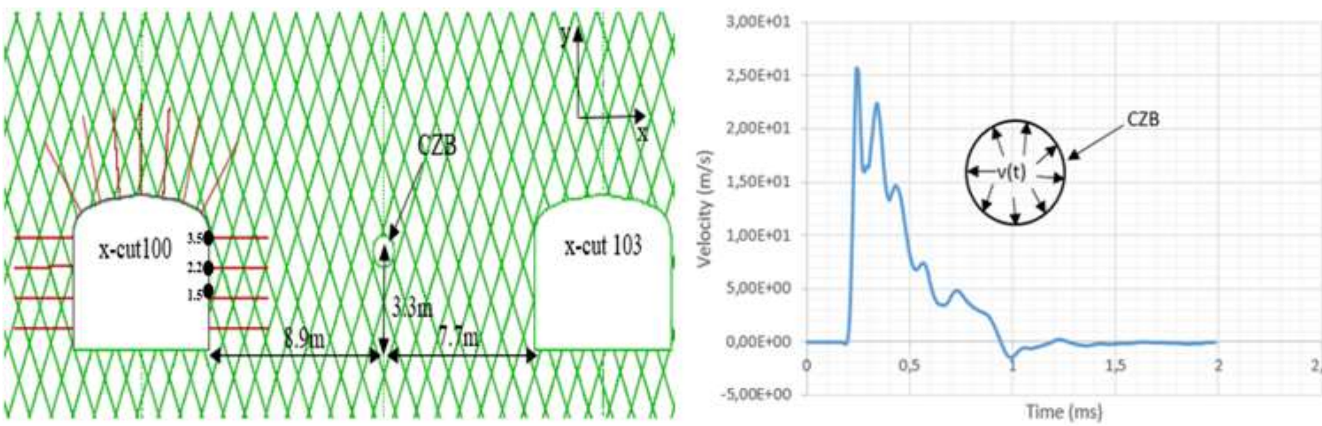

Figure 2: a)UDEC Model layout, b) Vibration velocity around the Crushed Zone Boundary

Table 2: Strength Properties of Intact Rock.

Density (Kg/m^3)	Elastic Modulus (GPa)	Bulk modulus (GPa)	Shear modulus (GPa)	Cohesion (MPa)	Friction angle (o)	Tensile strength (MPa)	Poisson's ratio
2800	70	50.7	27.6	31	61	16.5	0.27

Table 3: Parametric values of the joint.

Parametric properties	Parametric values	Base case
Normal Stiffness (GPa/m)	40, 50,70,90,110,150,200,250	110
Shear Stiffness (GPa/m)	3, 6, 9, 11, 15, 20,30	9
Joint space (m)	1, 2, 3	1
Orientation of joint set ID 1 (º) ID 2 (º)	 100,115,130 51, 66, 81	 115 66
Joint Origin (m)	-1,-1 0,0 1,1	0,0
Cohesion (MPa)	N.A	0.5
Tensile Strength (MPa)	N.A	0.5
Friction angle (º)	N.A	35

3. RESULT AND DISCUSSION

This work aimed to numerically study the effects of joint mechanical and spatial behaviour on wave propagation based on large-scale field test. Histories points defined at the wall to monitor responses of the rock mass. The results are in displacement and peak particle velocity.

3.1 Effect of Joint Stiffness

The normal stiffness is the slope of the linear elastic normal stress versus normal displacement curve recorded during normal compressive loading of a joint. The shear stiffness is the slope of the linear elastic part of the shear stress versus shear displacement curve recorded during shear loading.

Joint stiffness together with the other factors such as the poison ratio of the joint, angle and type of incident waves are the factors that control the magnitude of waves the transmitted, refracted and/or reflected at the joint.

The result showed that the PPV recorded by the history point in the model at the bottom (lowest point) are the highest and the history at the upper history point are the lowest. Furthermore, an increase of the normal stiffness led to an increase of PPV, but the increase of shear stiffness led to a decrease of the recorded PPV (Fig3). The simulation were made when joint stiffness changes while other joint parameters like spacing and orientation kept constant at the base case values.

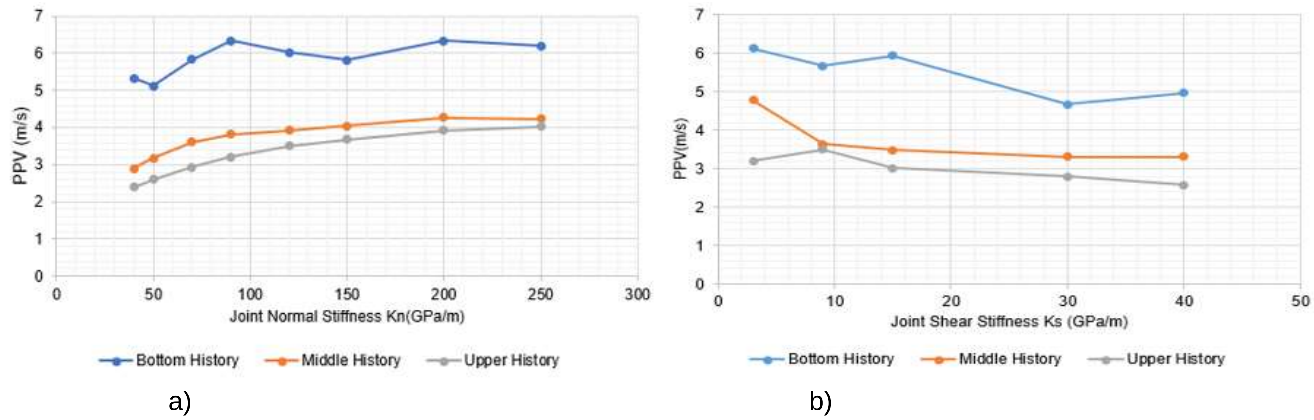

Figure 3: PPV of history points due to changes in a) Joint normal stiffness b) Joint shear stiffness.

The displacement-time histories with different stiffness are shown in Figure 4. For some of the stiffness values the displacements show a peak, but for other stiffness values the displacements keep on increasing during the whole simulation time. The displacement in the upper point shows an undulation with time, which is not the case for the other two history points.

The displacement of the tested cross-cut wall increased as the normal stiffness increased. Models with low normal stiffness reached the peak faster than those with high normal stiffness. After peak, the displacement remained more or less the same until the end of the simulation (Fig.4a). When the shear stiffness increases to displacement increases, low shear stiffness model records larger displacement at the surface of the drift cross-cut than models with high shear stiffness (Fig.4b). The same trends as for velocity, the displacement at the bottom histories records large displacement and upper history small displacement.

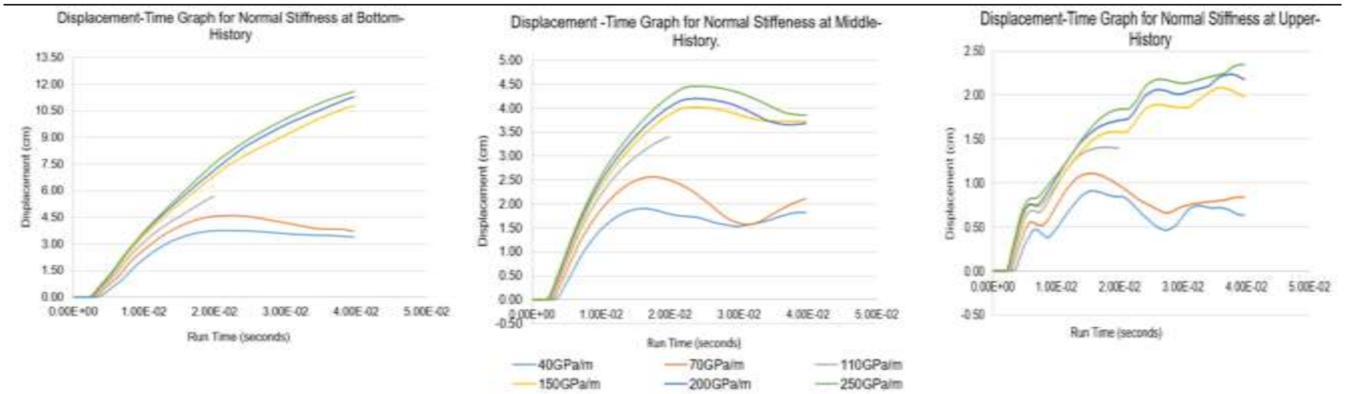

a)

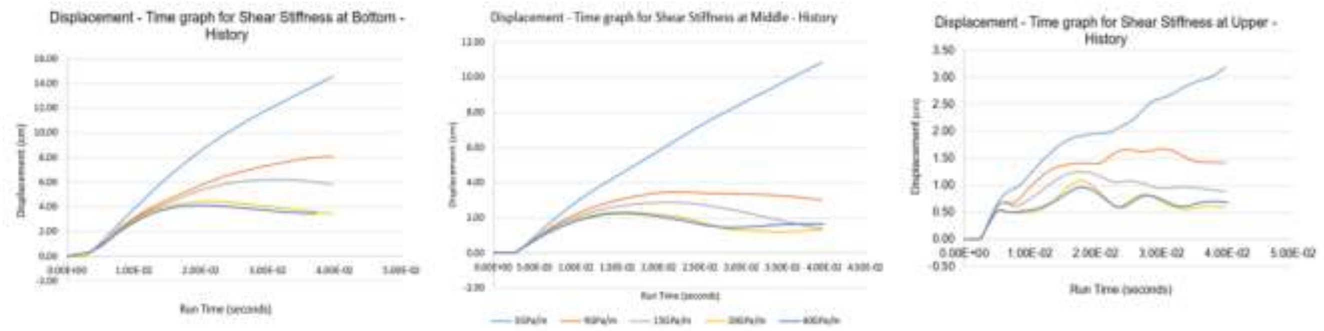

b)

Figure 4: Displacement – run time at histories points. a) Normal stiffness changes b) Shear stiffness changes

Velocity and displacement were increases as the joint normal stiffness increases but decreases as the joint shear stiffness increases. Modeling of stress wave propagation across joints shows that filtering of wave is less if the joint normal stiffness is high and vice-versa. This is because the normal stiffness of the joint determines to what extent the joint will open when incident stress wave crosses over. Pyrak-Nolte(1996) and Zhao(2014) shows that the transmission coefficient increases with increasing normal stiffness of the joint, however studies by Gu et al(1996) and Li(2013) showed that it is only possible if the incident wave is p-wave. The results of simulations are based on the P- incident wave that originate from CZB agree with Gu et al (1996) and Li (2013).

3.2 Effect of Joint Space.

The effect of joint spaces on the stress wave propagation was observed by monitoring ppv at the history points defined in the wall of the cross-cut. The results show that the PPV were higher for small joint spacings (1 m). The PPV decreased with increasing up to spacing to 3 m. When the spacing increases more. i.e., > 3 m, the PPV increases (Fig 5).
In these simulations joint spacing were changing but joint orientation and joint stiffness were kept constant to the base case values.

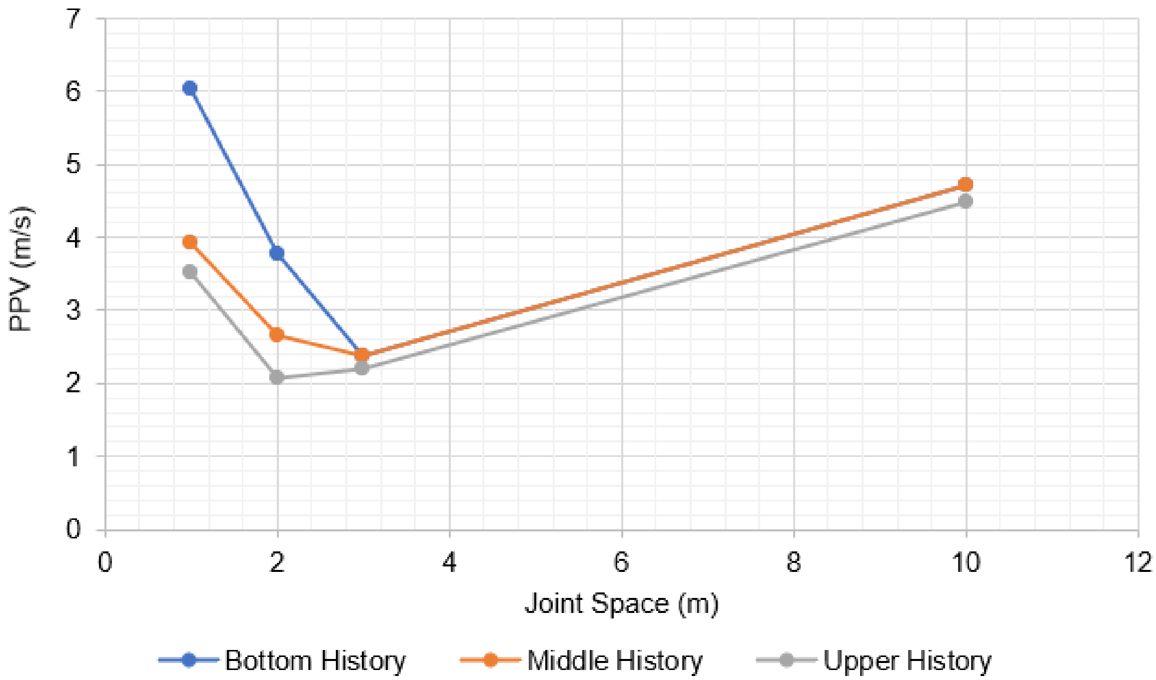

Figure 5: Velocity at the cross-cut wall with different Joint spaces

Tensile yield with different joint spacing is shown in Figure 6. For small joint spacing (1-2 m), the whole wall and the shoulder (for 1 m spacing) have yielded in tension. For the case of 3 m spacing, yielding has only occurred at mid height very loacal also with respect to depth from the surface. For the case of 1 m spacing there is almost no yielding in the centre of the burden. In the case of 2 m – 3 m, yielding has occurred in the middle of the burden, but these zones are located around the discontinuities in the burden. For the cases of 10 m and 14 m joint spacing, tensile yielding occurred in in the whole wall with several meters depth. Tensile "fractures" develop from the wall towards the CZB. For the joint spacing 10 m more "random" zones in the middle of the burden than in the case of 14 m spacing. When the spacing is 14 m the yielding is concetrated to the tensile "fractures". For the intact rock yielding has occurred from the wall to a depth of several meters. The tensile "fractures" has propagated the whole way from the wall to the CZB (or vice versa). A conical volume of rock defined by the tensile "fractures" has developed.

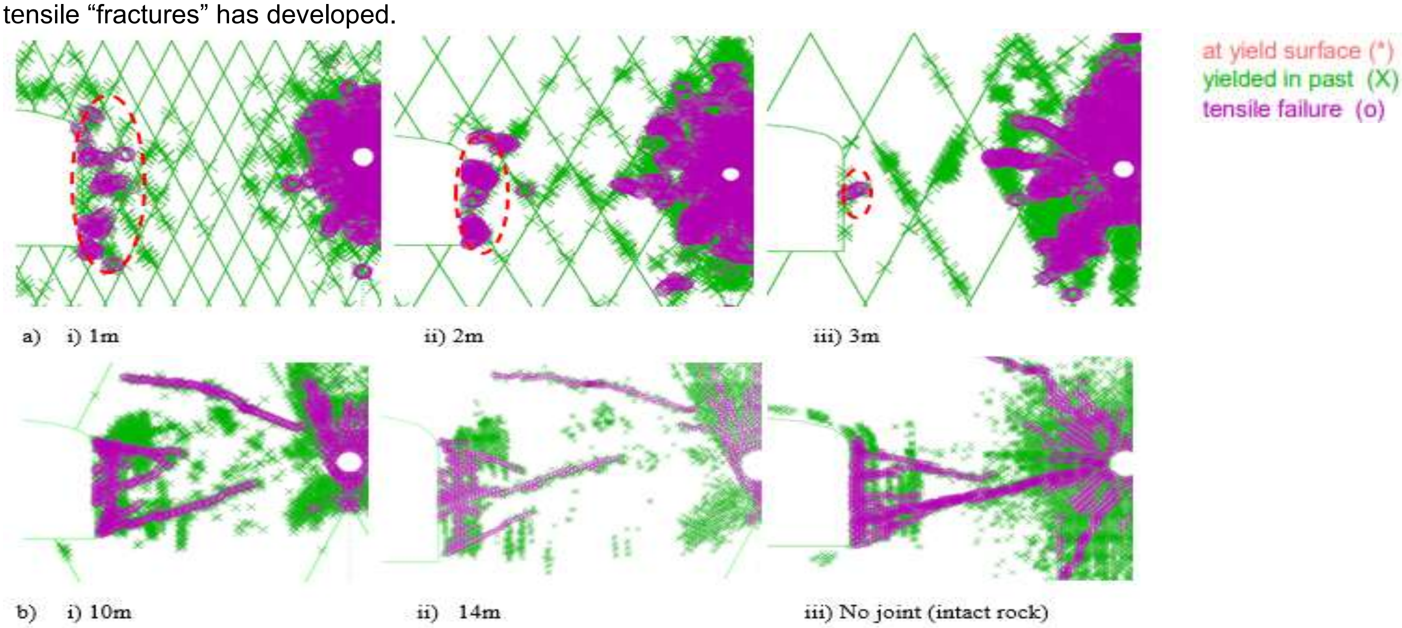

Figure 6: Tensile yield at different joint spaces. a) Joint spaces within the burden depth. b) Joint spaces large than the burden depth

Small joint spacing may result in many parallel joints within a small volume. This may lead to superposition of waves as result of multiple reflection. Part of the wave may be trapped between the joints resulting in attenuation of the wave or resonance (high amplitude). Zhu (2011) showed that in some cases the magnitude of wave transmission is increasing with increasing joint number which means small joint space in given domain. The wave propagation at joint space bigger than depth of burden (> 8.9m) crosses over single joint before reaching the cross-cut wall, this single joint is the result of locating the origin of the joint at the center (0,0) of the UDEC model during building up.
Heavily jointed as results of small joint space cause the rock to act as the intact rock hence thick depth of tensile failure.

3.3 Effect of Joint Orientation.

Four different models were analysed to investigate the effect of joint orientation. The orientation of one joint set varied while the orientation of the other joint set was kept constant. The orientation of the joint with varying orientation, was changed by 15(°) at a time. Parameters other than joint orientation were kept constant to base case values.
Joint set 1 (JS1) and set 2 (JS2) for the base case are oriented to 115 and 66 degrees respectively. The orientation of joint sets J1 and J2 are presented in Table 4. The values in the blue line in the table 4 were kept constant while the counter-value in grey were changing.

Table 4: Orientation of J1 & J2 that used in simulation.

J1	100	115	120	115	115	115
J2	66	66	66	51	66	81

The orientation of joint sets JS1 and JS2 makes more or less same angle to the incident wave except that are dipping in different directions (Fig.7). The changes of JS1 to 100˚ and 130˚ made about 80˚ and 50˚ to incident wave direction.

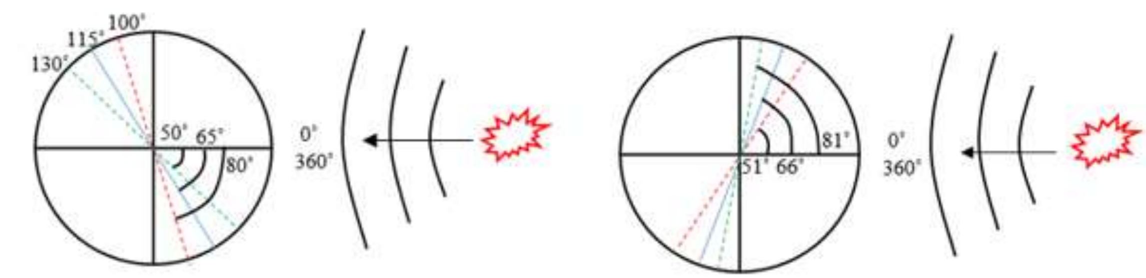

a) J1 b) J2

Figure 7: Direction and orientation of joint sets. a) J1 b) J2

The relationship between the PPV and the dip angle of both joint sets is shown in Figure 8. Figure 8(a) shows the case of 100˚ produces the high PPV compared to the other cases at all history points. For joint set 2, the case of 66˚ gives the high PPV compared to the other cases, see Figure 8(b). The possible reason is due to multiple transmissions and reflections of waves

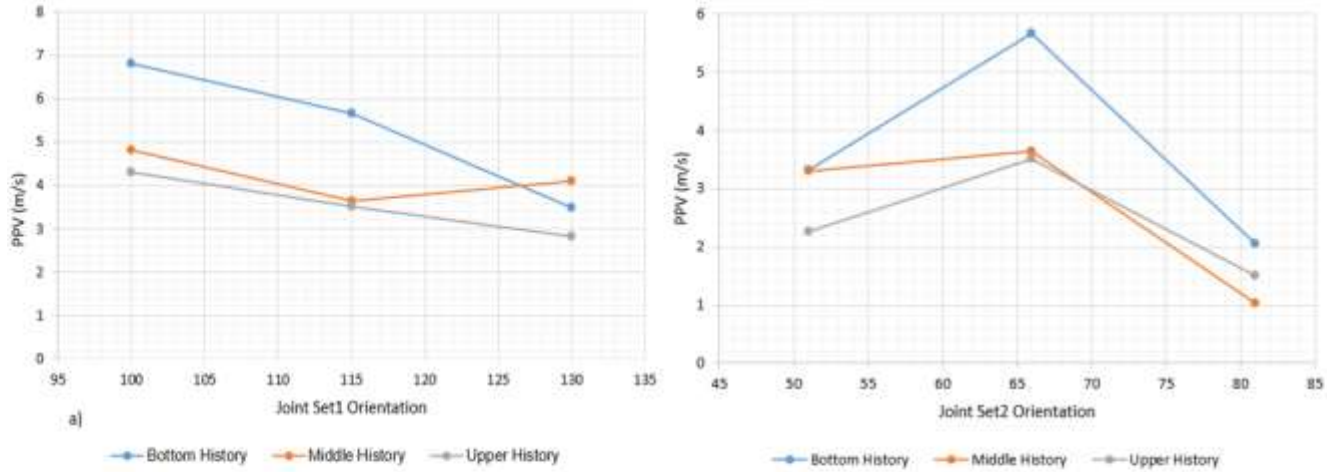

Figure 8: Velocity changes with Joint orientation changes, a) Joint set 1 b) Joint set 2

The depth of tensile yielding intensity around the tunnel wall corresponding to ppv recorded. Joint set 1 with 100˚ orientation has higher records of ppv and deep tensile yielding. The J2 orientation angles of 51 and 82 has low ppv records as well as shallow depth of tensile yielding in the cross-cut wall (Fig.9).

The orientation of the joint play vital roles in propagation of waves in the rockmass, the orientation of the joint determines at what angle the incident wave get to the joint medium. The extreme cases of transmission and reflection of the wave occurring when joint is perpendicular or parallel to the incident wave direction. Gu et al.(1996) analytical solution found that p-incident waves perpendicular to joint will result with very low rate of transmission and high rate of reflection of waves.

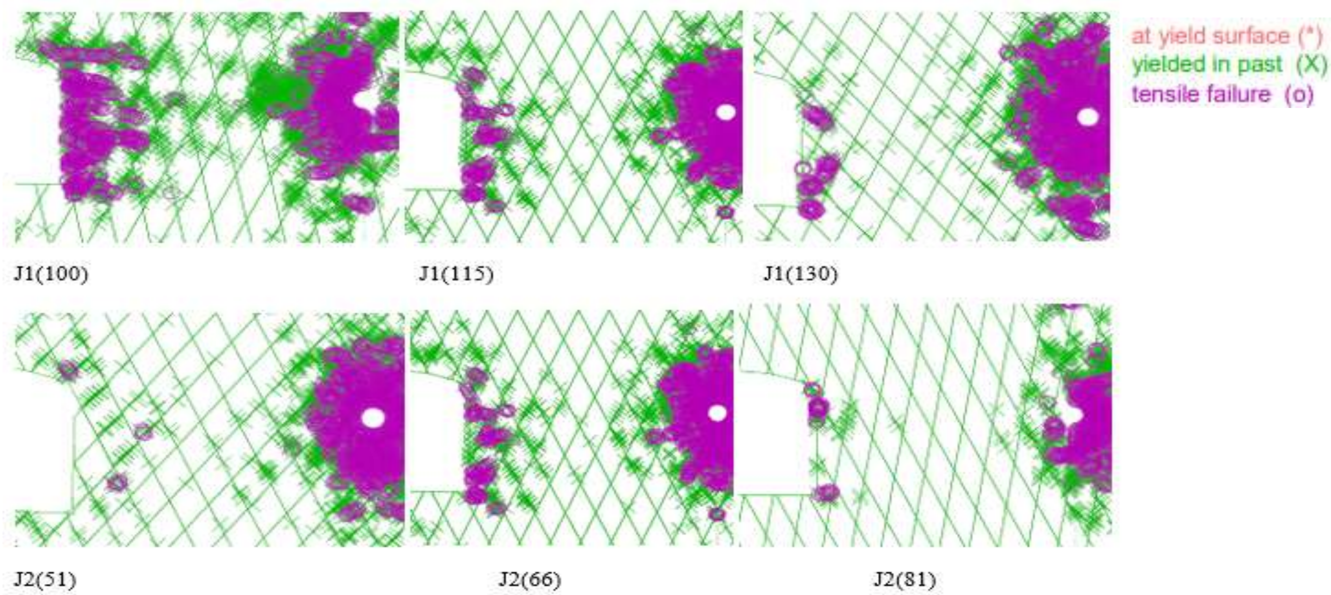

Figure 9: Tensile yielding around the cross-cut wall

3.4 Effect of Joint Origin

One of the joint parameters that has to be assigned a value in a UDEC model is the joint origin. It defines the coordinates of the point at which the first joint in a set starts. This means that depending on the joint origin, the joint will intersect the wall or not. If it intersects the wall, the position of the intersection affects the behaviour. One setup of joint origins of two joint sets can result in a wedge or not, it will also affect the deformation pattern

of the wall (see Figure 10). In this case, the joint origins changed by shifted in either direction while other joint parameters kept constant to the base case values.
If the joint origin coordinate is (0,0), see Figure 10. If the joint origin is moved 1m to the left and one meter down (-1,-1), two wedges are formed without any kinematic constraints and can therefore be ejected if the reflected wave at the wall creates tensile stresses that exceeds the strength of the joints. For the case when the origin was moved from (0,0) with 1 m to the right and 1 m up a wedge is formed at the bottom of the wall.
The PPV at the surface of the wall shows that the model with joint origin at the center (base case; 0,0) has the highest PPV. In the two other cases shows lower PPV than that of the base case. The PPV for (-1,-1) and (1,1) are similar. For the base case the bottom point is significantly higher than that of the joints with origin at (-1,-1) and (1,1).

Tensile yielding in the models shows different pattern with different joint origin. The joint origin at the center (0,0) has tensile yielding at the wall of the cross-cut. Tensile yielding with possible ejection at the bottom of the wall, occurs for the base case. However, in the models with origin origins at (-1,-1) and (1,1) show similar trends, i.e., there was no tensile failure at the wall of the cross-cut, but tensile yielding occurred inside the burden(Fig.10b).

The low PPV and tensile yielding in the cross-cut wall for the models with joint origin (-1,-1) and (1,1), respectively, could be due to the two scenarios. Firstly, the obstruction at the blasthole. The waves from the source were not evenly distributed around the blasthole, even though the surrounding area is in the damage zone. The obstruction somehow increases the attenuation of incident waves and hence low ppv and low tensile yielding at cross-cut wall. Secondly, joint origin shifting changed the location of joint intersection to the cross-cut, changed distance of first joint close to blasthole and formation of wedges. The changes of joints interaction to cross-cut wall not only affects the resonance phenomena as a result of multiple transmission and reflection but also it affects stress regime around the cross-cut wall.

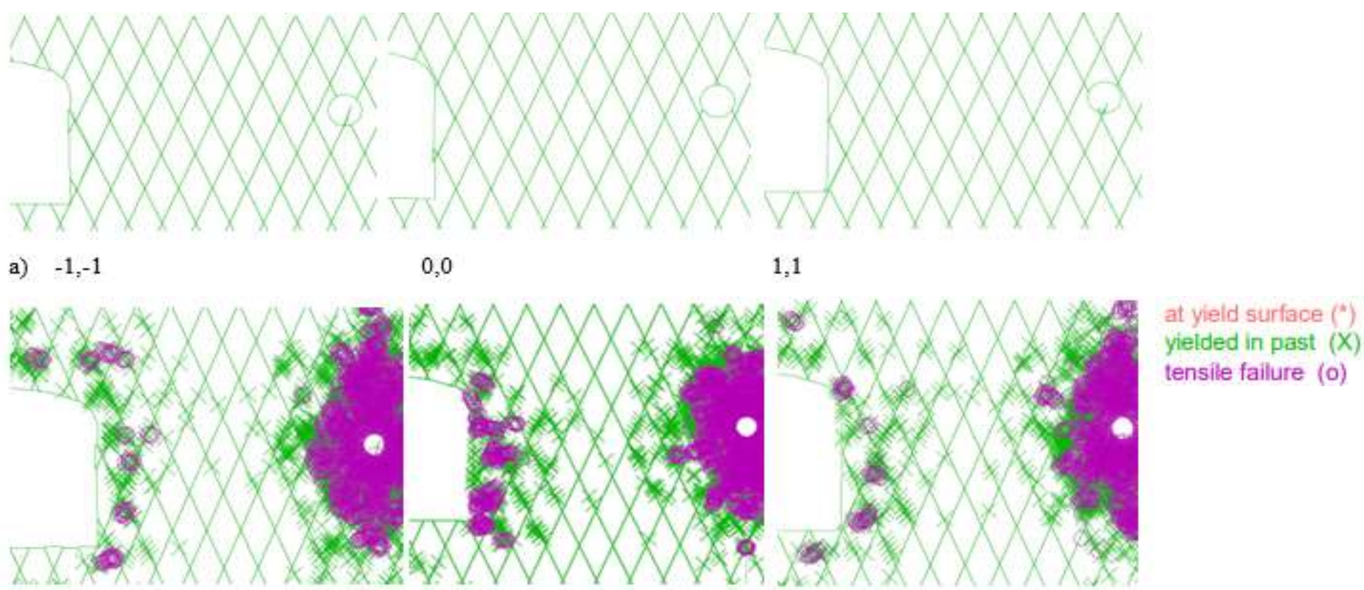

Figure 10: The model joints and tensile yielding.

Figure 11: The velocity records at the surface of the wall

4. CONCLUSION

This work uses coupling of numerical models to simulate the influences of mechanical and spatial properties of joint on wave propagation and stability of the cross-cut. It has drawn the following conclusions

- Joint stiffness: The PPV shows an asymptotic behavior with increasing joint stiffness (both normal and shear stiffness). This clear for the middle and upper history points. The PPV in the bottom point shows a similar behavior, but the curve does not flatten out as for the other points. The PPV looks different for the bottom point, and does not reach an asymptote. It undulates around a PPV value of around 6 m/s. The PPV for the middle and upper points are similar, with a higher PPV for the middle point.
- ***Joint spacing:*** The PPV in all points at the wall show a similar behavior. The PPV in the bottom and middle points decreases when the spacing increases from 1 m. For an increase in spacing from 1 – 3 m, the PPV increases. The PPV for 10 m is almost the same for all points at the wall. The PPV recorded at the bottom of the wall shows the largest change with joint spacing of all the three points.
- ***Joint orientation:***
    - Joint set J1: At the bottom and the upper position the PPV decreases monotonically with increasing orientation. However, the PPV at the middle of the wall has a minimum at 115°.
    - Joint set J2; At all of the points the PPV has a maximum at 6 m/s, its minimum for 81° and the intermediate value for 51°.
- ***Joint origin***: The PPV has its maximum for joint origin (0,0). The PPV for the points (-1,-1) and (1,1) are similar.

It should be noted that the parameters in this study that are independent are the normal and shear stiffness and the spacing and the joint orientation. The joint spacing and the joint origin are coupled. For larger spacings the result will be very sensitive to where the joints starts. See for example Figure 6. The location where the joint intersects the boundary affect the behavior of the rock mass.

5. REFERENCES

Barton N.R. 1972. A model study of rock-joint deformation. International Journal of Rock Mechanics and Mining Science: Volume 9, pages 579-602.

Brandshaug. T .2009. An Initial Evaluation of Effects of Seismic Motion on footwall Drift at LKAB's Kirunavaara mine. GT09-4001-1 LKAB Kirunavaara mine.

Chai S.B, Li J. C., Rong L. F., Li N. N.. 2017. Theoretical study for induced seismic wave propagation across rock masses during underground exploitation. Geomech. Geophys. Geo-energ. Geo-resour.3:95–105

Chen S.G, Zhao. J. 1998. A study of UDEC Modelling for blast wave propagation in jointed Rock Masses International Journal of Rock Mechanics & Mining Sciences 35,: 93-99

Chen Yu, 2014; Experimental study and stress analysis of rock bolt anchorage performance; Journal of Rock Mechanics and Geotechnical Engineering Volume 6, Issue 5, Pages 428-437
Gu B, R. Sufirez-Rivera, Kurt T. Nihei, and Larry R. Myer, 1996; Incidence of plane waves upon a fracture; JOURNAL OF GEOPHYSICAL RESEARCH, VOL. 101, NO. Bll, PAGES 25,337-25,346
Huang X.L, Qi S.W, Williams A, ZoY u, Zheng B.W. 2015. Numerical simulation of stress wave propagating through filled joints by particle model. Int. Journal of Solids Struct. 69:23–33
Ma G.W, An X.M. 2008. Numerical simulation of blasting-induced rock fracturing. Inter. Journal of Rock Mech. and Mini. Science. 45:966-975.
Malmgren .L, Sjöberg J. .2006. Bergmekaniska analyser för ny huvudnivå I KUJ (1365) Utredning nr 06-797 LKAB Sweden
Malmgren L 2005 Interaction between shotcrete and rock— experimental and numerical study. Doctoral thesis, Luleå University of Technology
Malmgren, L. and Nordlund E.. 2006. Behavior of shotcrete supported rock wedges subjected to blast-induced vibration. International Journal of Rock Mechanics & Mining Sciences, 43: 4,593–615.
Malmgren, L. and Nordlund E.. 2008. Interaction of shotcrete with rock and rock bolts—A numerical study, International Journal of Rock Mechanics & Mining Sciences, 45: 4,538–553.
Malmgren. L .2007. Strength, ductility and stiffness of fiber-reinforced shotcrete. Magazine of Concrete Research 59(4):287-296
Perino A, Zhu J. B., Li J. C., Barla G., Zhao J.. 2010. Theoretical Methods for Wave Propagation across Jointed Rock Masses, Journal of Rock Mech. Rock Eng. (2010) 43:799–809 DOI 10.1007/s00603-010-0114-5
PYRAK-NOLTE L.J .1996. The Seismic Response of Fractures and the Interrelations among Fracture Properties. Inter. J. Rock Mech. Min. Science. & Geomechanics. 73 (8) 787-802.
Pyrank-Nolte L.J, Myer L.R, Cook N.G.W, 1990. Anisotropy in seismic velocities and amplitudes from multiple parallel fractures. Journal of Geophysical research: Vol 95 Issue B7: pages 11345- 11358
Shirzadegan S. Nordlund E., Zhang P. 2016. Large Scale Dynamic Testing of Rock Support System at Kiirunavaara Underground Mine. Rock Mech. and Rock Eng. 49: 2773 - 2794.
Shirzadegan S. Nordlund E., Zhang P. 2016. Large scale dynamic testing of rock support at Kiirunavaara – Improved test design. Tunneling and Underground Space Technology 59: 183-19
Wang Z, Konietzky H. 2009. Modelling of blast-induced fractures in jointed rock masses. Engineering Fracture Mechanics 76 :1945–1955
Zhang P, G. Swan, E. Nordlund. 2015. 1D numerical simulation of velocity amplification of P-waves travelling through fractured rock near a free surface. The Journal of Southern Africa Institute of Mining and Metallurgy. 115:1121-1126
Zhang P, Yi CP, Nordlund E., Shirzadegan S., Nyberg U., Malmgren L., Nordqvist A.. 2013. Numerical back analysis of simulated rockburst field tests by using coupled numerical technique. In: Potvin Y (eds) Proceeding of seventh international symposium on ground support in mining and underground construction, Australian centre for Geomechanics, Perth, pp. 565-585
Zhao G. 2014. Modeling stress wave propagation in rocks by distinct lattice spring model. Journal of Rock Mechanics and Geotechnical Engineering 6 (4) 348 – 355
Zhao X.B, Zhu J.B, Zhao J, Cai J.G , 2011; Study of wave attenuation across parallel fractures using propagator matrix method; International Journal for Numerical and Analytical Methods in Geomechanics, https://doi.org/10.1002/nag.1050
Zhu J. 2011. Theoretical and numerical analyses of wave propagation in jointed rock masses. 10.5075/epfl-thesis-5130.

Proceedings of the NROCK 2023
The IV Nordic Symposium on
Rock Mechanics and Rock Engineering
ISBN 978-9935-9436-2-0
DOI 10.33112/nrock2023.9

Statistical insights arising from point load testing of Danian limestone

Francesco Petrella (francesco.petrella@arup.com)

Francesco Petrella
Ove Arup & Partners Danmark A/S, Copenhagen, Denmark
Anna Wudzka
Ove Arup & Partners Danmark A/S, Copenhagen, Denmark

ABSTRACT

The characterisation of the mechanical properties of the rocks can be carried out with conventional strength testing (e.g. unconfined compressive strength tests, tensile strength tests and triaxial tests) or with 'rapid' tests such as the point load test (PLT). Compared to the conventional tests the rapid tests are economical, quick and can also be carried out in situ; on the other hand, the results tend to be more scattered, correlations with the strength parameters depend on the rock type and the experience in using them in the design stage can be limited. This paper presents the results of PLTs carried out on Danian limestone and Maastrichtian chalk specimens, either as irregular lumps or as cylinders/disks, from multiple sites on Zealand in Denmark. The Danian limestone formations are weak sedimentary rocks with highly variable properties in terms of their strength, stiffness and in mass permeability. Their mechanical properties are governed by genesis, induration and the large variability of the fissuring and distribution of fissuring. By statistically analysing the results of the PLTs, it is possible to appreciate the impact that the height to equivalent diameter ratio has on the coefficient of variation for each induration class, which can therefore be used as guidance for specimen selection and/or preparation on site or in the laboratory.

KEYWORDS

Point load test; Danian limestone; weak rock characterization; height to equivalent diameter ratio

INTRODUCTION

The point load test (PLT) is an index test allowing for strength classification of rocks through measurement of the point load strength index $I_{s(50)}$, which can be correlated with the unconfined compressive strength, tensile strength and other properties of the rock. The PLT is a simple, fast and cost-effective way of obtaining information on the rock strength compared with other strength testing methods. In addition, PLTs may be performed both in situ and in the laboratory on different shapes and sizes of rock specimen and therefore may be preferable method of checking strength properties of rock. However, it is the understanding of the authors that these are seldom used for testing of Danian limestone. The results from PLTs are more variable compared with the results of the unconfined compressive strength tests, or triaxial tests on the rock: this is due to the variation of the size of tested specimen and the method of standardisation of the test result for the specimen size (Thuro & Plinninger, 2001).

The analysis presented below is based on a series of PLTs performed mainly on irregular rock lumps taken from the Danian limestone and Maastrichtian chalk cores tested in the laboratory and focuses on impact of the specimen size on the PLT results. The analysed sample of the PLT data excludes tests done on specimens of mixed indurations and with silicified parts or flint. Outliers defined as the $I_{s(50)}$ values higher than mean $I_{s(50)}$ value plus three standard deviations or lower than mean $I_{s(50)}$ value minus three standard deviations are also eliminated from the sample. In the following, the terms 'data set' and 'sample' are used interchangeably. Approximately 480 results of point load tests on limestone and chalk from two different sites on Zealand are presented below; only 20% of these were performed as axial tests while the others were performed as irregular lump tests.

Danian limestone and Maastrichtian chalk are weak sedimentary rocks; in Denmark their hardness is described by the degree of induration by geologists (Larsen et al., 1995). The degree of induration provides a very general indication of the rock strength.

1. ROCK CHARACTERIZATION BASED ON POINT LOAD TESTING

1.1. Danian limestone and Maastrichtian chalk

The Danian limestones are subdivided into Copenhagen and Bryozoan limestone. Copenhagen limestone overlies Bryozoan limestone, which is underlain by Maastrichtian chalk. These weak rocks were formed from calcareous materials deposited in a marine environment and are horizontally bedded. While the Danian limestone is characterised by variable induration, the Maastrichtian chalk consists mainly of white chalk, which is only slightly indurated.

Local geological practice describes both Danian limestones and Maastrichtian chalk by the degree of induration, providing indirect information on the strength and compressibility of the rock material. The degree of induration is a semi-quantitative parameter subdivided in a five degree-scale as shown in Table 1 together with the corresponding ISRM rock grade as well as the indicative strength defined as compressive strength σ_c and point load strength index $I_{s(50)}$. The strength of the rock increases with increasing degree of induration as well as rock density.

For the purpose of this analysis, tests on specimens of Danian limestone and Maastrichtian chalk were grouped on the basis of the degree of induration.

Table 1. Degree of induration according to Danish practice (Larsen et al., 1995) with corresponding indicative compressive strength σ_c and point load index $I_{s(50)}$ based on Hansen & Foged (2002).

Induration	Term	Description	ISRM Rock Grade	σ_c, (MPa)	$I_{s(50)}$, (MPa)
H1	Unlithified	The material can be easily formed by hand. Grainy material will fall apart when dry.	R0	0.25-1	-
H2	Slightly indurated	The material can easily by cut with a knife and can be scratched with a fingernail. Individual grains can be picked out with the fingers when the material is grainy.	R1	1-5	0.1-1
H3	Indurated	The material can be cut with a knife but cannot be scratched with a fingernail. Individual grains can be picked out with a knife when the material is grainy.	R2	5-25	1-4
H4	Strongly indurated	The material can be scratched with a knife. Individual grains do not come out with a knife. Fractures will follow grain surfaces.	R3, R4	25-100	2-5
H5	Very strongly indurated	The material cannot be scratched with a knife. Cracks and fracture surfaces will go through individual grains in grainy materials.	R5, R6	100-500	4-10

Figure 1 to Figure 3 present the variation of the moisture content and bulk density of the limestone and chalk with the degree of induration and the strength expressed as $I_{s(50)}$. High moisture content and low bulk density characterise the weaker H2 material, while the strongly indurated materials have lower moisture content and higher bulk density. As it may be observed from Figure 1 to Figure 3, the data overlap as limestone material with the same moisture content or bulk density may have different induration and strength. Only the data presented in Figure 1 from H2 indurated material mostly follows the indicative range of the point load index $I_{s(50)}$ provided by Hansen & Foged (2002). As it can be appreciated from Figure 2 and Figure 3 within the tested H3 and H4 indurated material there are results with the lower $I_{s(50)}$ than the lower range provided in Table 1. This maybe due to the geologist's subjectiveness of the evaluation of the degree of induration or by the scatter of the point load test results in addition to the inherent variability of ground properties.

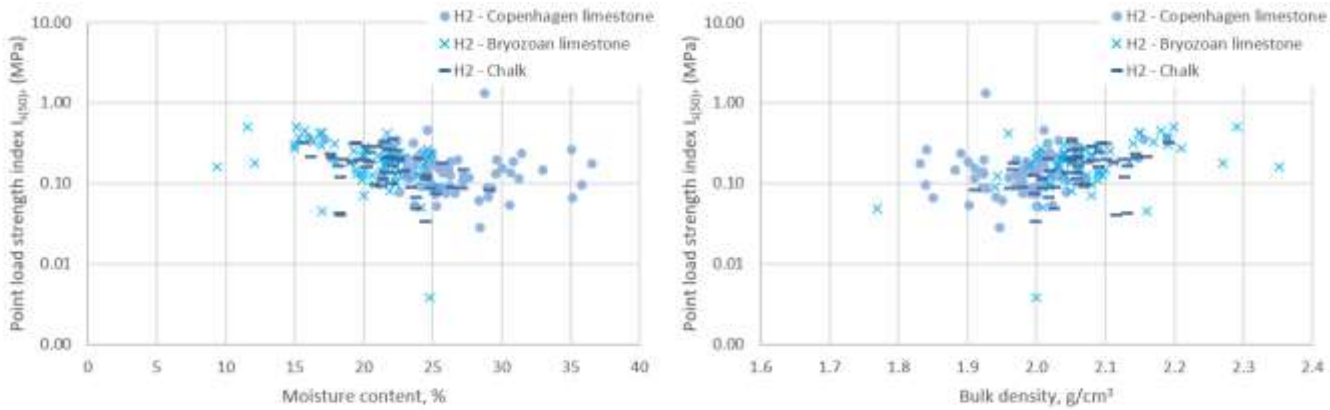

Figure 1. Normalised Point Load Strength Index $I_{s(50)}$ vs moisture content and bulk density for H2 indurated material.

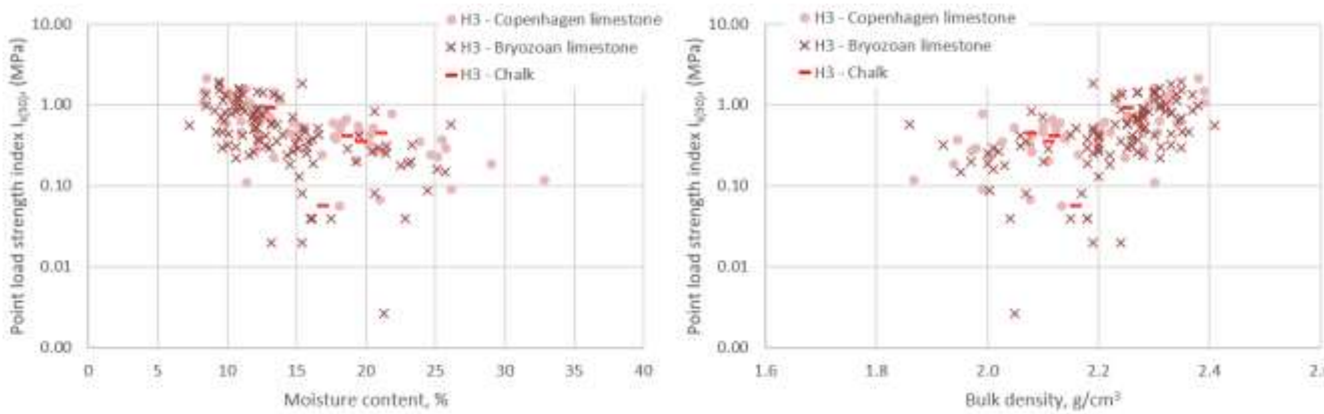

Figure 2. Normalised Point Load Strength Index $I_{s(50)}$ vs moisture content and bulk density for H3 indurated material.

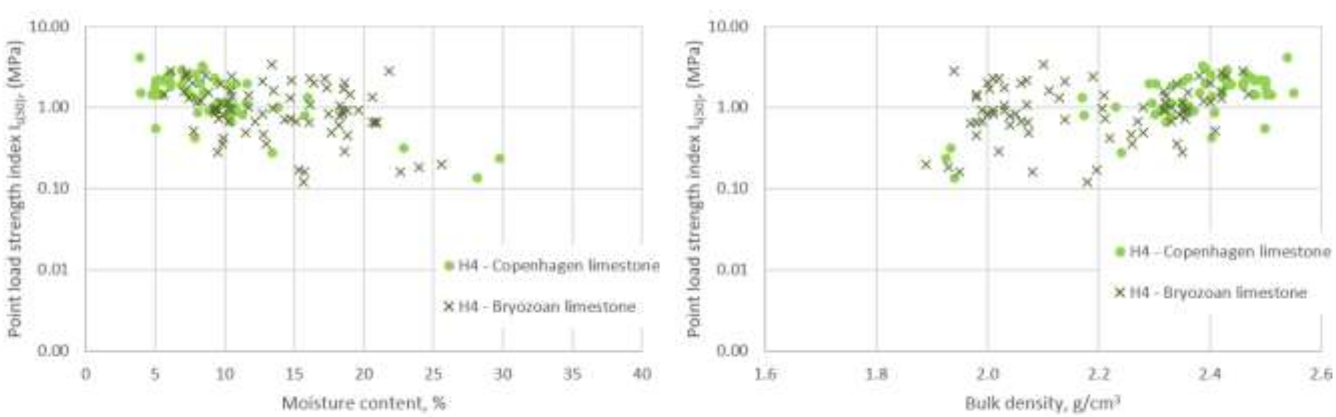

Figure 3. Normalised Point Load Strength Index $I_{s(50)}$ vs moisture content and bulk density for H4 indurated material.

1.2. Point load testing

The PLT provides an indirect measure of the uniaxial strength of rock and can be performed on site, as well as in the laboratory on specimens of different shapes. While the test was originally introduced by Protodyaknov (1960), the first comprehensive coverage of PLT is normally attributed to Broch and Franklin (1972), whose contribution was the basis for the first ISRM suggested methods on this test. A description of the test procedure and the definition of the specimen dimensions are provided by the ISRM (1985). The data presented in this analysis was obtained in the laboratory mainly from irregular lump tests; for 20% of specimen axial tests were carried out.

The ISRM (1985) provides suggestions for specimen dimensions for different types of tests (see Figure 4). For axial and irregular lump tests the required ratio between the distance between the conical platen contact points D, referred to in the following as 'specimen height', and the lowest specimen height to width ratio is between 0.3 and 1.0, and preferably close to 1.0. The equivalent core diameter D_e has been calculated in accordance to ISRM (1985):

$$D_e = \sqrt{\frac{4 \times W \times D}{\pi}} \qquad (1)$$

where all the symbols are defined in Figure 4.

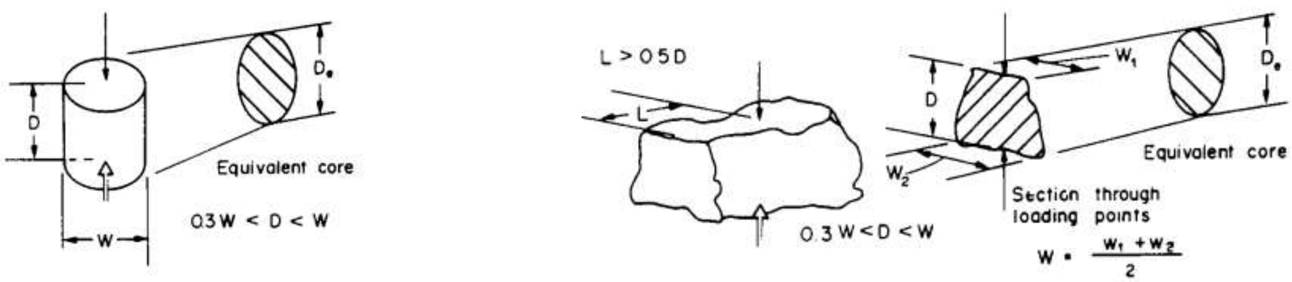

Figure 4. Specimen shape requirements for the axial test (left) and the irregular lump test (left) (ISRM, 1985).

The point load strength index is defined as the value of the point load strength that would have been measured by a diametral test with D=50mm (ISRM, 1985):

$$I_{s(50)} = \frac{P}{D_e^2} \times \left(\frac{D_e}{50}\right)^{0.45} \qquad (2)$$

where P is the failure load required to break the specimen, while D_e is defined in Figure 4. The first part of the equation is defined as uncorrected point load strength I_s, while the second part is the size correction factor. The $I_{s(50)}$ normalises point load test results with respect to the specimen shape and size.

1.3. Data set summary, limitations and aim of this study

The aim of this analysis is to assess the impact of the specimen size defined as ratio between D and the equivalent core diameter D_e on variability of the $I_{s(50)}$ results in order to achieve more precise and accurate PLT results for limestone and chalk materials depending on their degree of induration. It therefore focuses on the possibility of decreasing the epistemic uncertainty in the $I_{s(50)}$ evaluation by choosing a specific specimen size for the test.

Specimens with silicified parts or flint parts were excluded to remove lithological heterogeneity of the limestone material; the outliers were also excluded from the analysis presented in section 2.2. Six tests were carried out on H5 material and the data were not analysed due to very small sample size. In addition, the $I_{s(50)}$ values obtained from sample size with less than ten tests were eliminated, as the ISRM (1985) suggests to carry at least ten tests per sample; for this analysis a sample is defined by degree of induration and D/D_e ratio. It is noted that too few tests were available for the D/D_e ratio >0.8 for them to be statistical meaningful, which is a limitation of the data set assessed herein.

Data on the test duration was not available to the authors and it is therefore not possible to assess whether any of the tests presented in the following fall outside the 10 to 60 seconds test duration recommended by the ISRM (1985) and would require that they be invalidated.

The size of the sample for the tests performed on H2, H3 and H4 is 174, 156 and 120, respectively.

2. ANALYSIS

The variation of $I_{s(50)}$ with the D/D_e ratio for the full data set of H2, H3 and H4 indurated materials is presented in Figure 5 to Figure 7. A marked scatter can be observed in Figure 5 to Figure 7; a similar observation for weak carbonate rocks was made by Abbs (1985). No clear trend is observed between the D/D_e ratio and $I_{s(50)}$ for tested geomaterials as is to be expected given the definition and aim of the point load strength index.

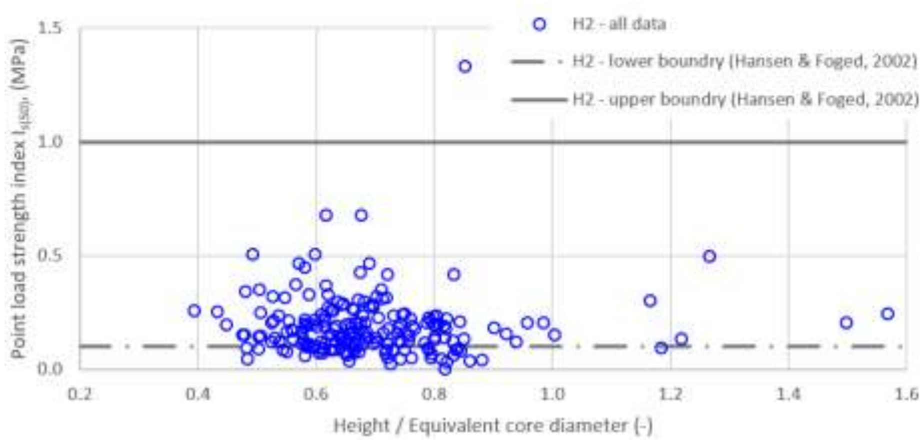

Figure 5. Point Load Strength Index $I_{s(50)}$ vs D/D_e for H2 indurated limestone and chalk.

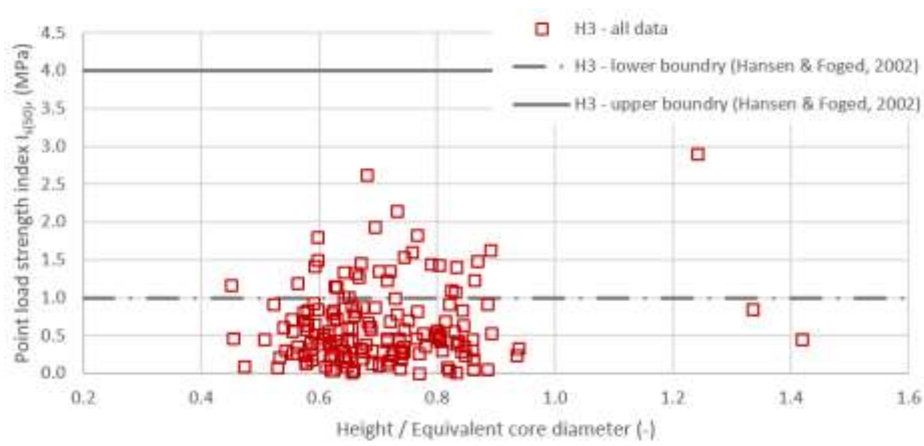

Figure 6. Point Load Strength Index $I_{s(50)}$ vs D/D_e for H3 indurated limestone and chalk.

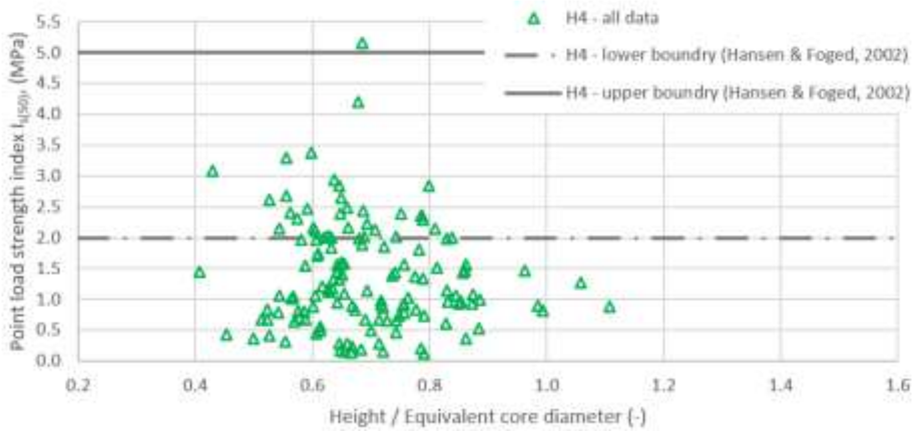

Figure 7. Point Load Strength Index $I_{s(50)}$ vs D/D_e for H4 indurated limestone.

2.1. Statistical distribution of the data

The statistical analysis of the point load strength index $I_{s(50)}$ distribution is initially performed by visualising the data set on histograms. Normal and lognormal distributions are considered, as these are the most commonly used data distributions for this type of analysis. A qualitative assessment of the frequency diagrams on the left hand side of Figure 8 may suggest that the lognormal distribution has the potential to represent the data set well; however, the variation of the $I_{s(50)}$ within each degree of induration does not seem to be symmetrical around the mean, neither for normal nor lognormal distribution: this would suggest an inherent uncertainty in terms of determining the variability of the $I_{s(50)}$ within a specific degree of induration and specimen size.

The inverse standard normal cumulative distribution function for different indurations of limestone and chalk is shown in Figure 9 to aid the determination of the data distribution. The $I_{s(50)}$ data for H2 indurated materials nearly plots on a straight line for both the normal and the lognormal distribution. Data sets for H3 and H4 indurations do not plot on a straight line for the normal distribution and seem to be better represented by a lognormal distribution.

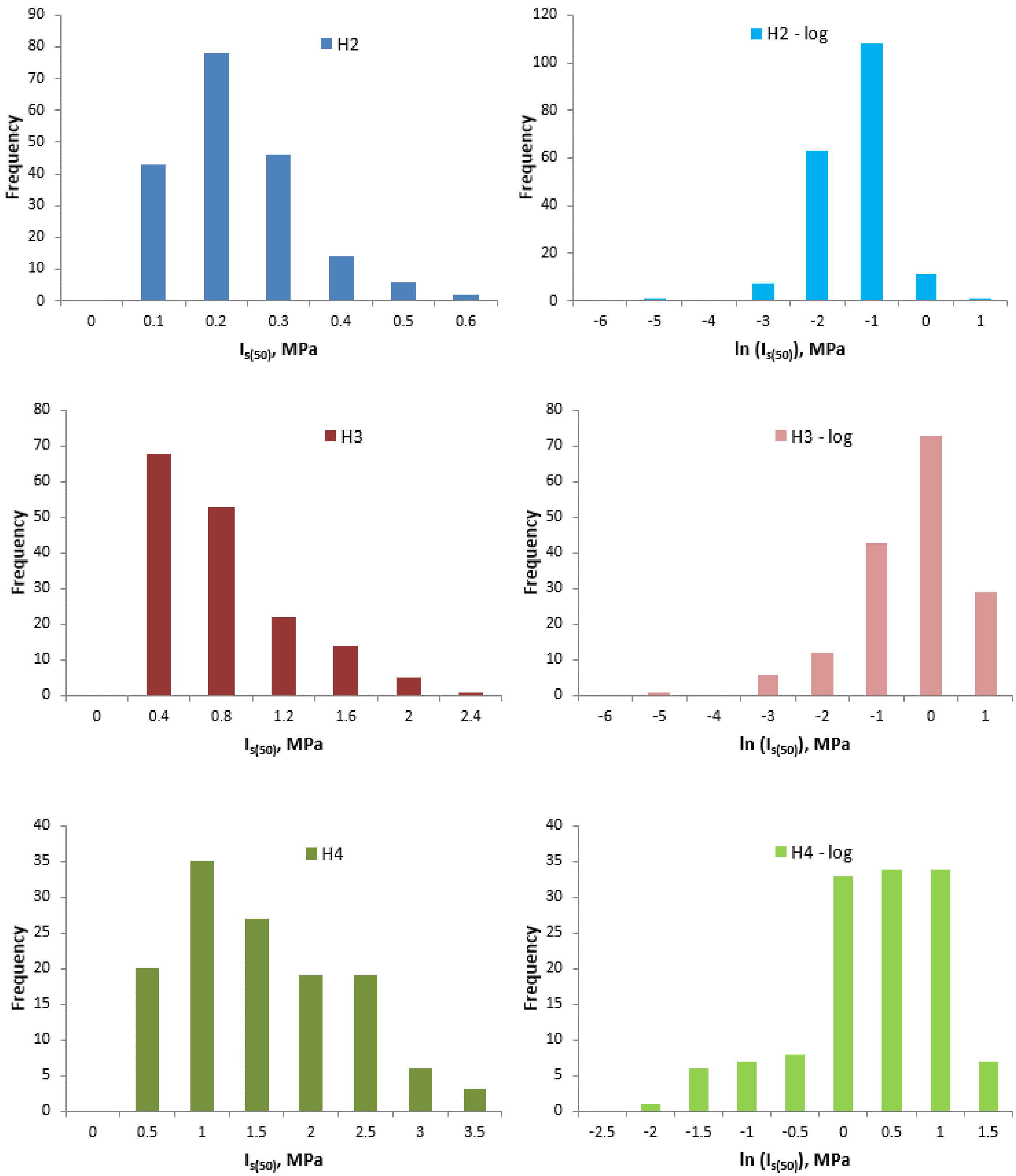

Figure 8. Histograms for different indurations of limestone and chalk to verify the distribution of the test data assuming normal (left) and lognormal (right) distributions.

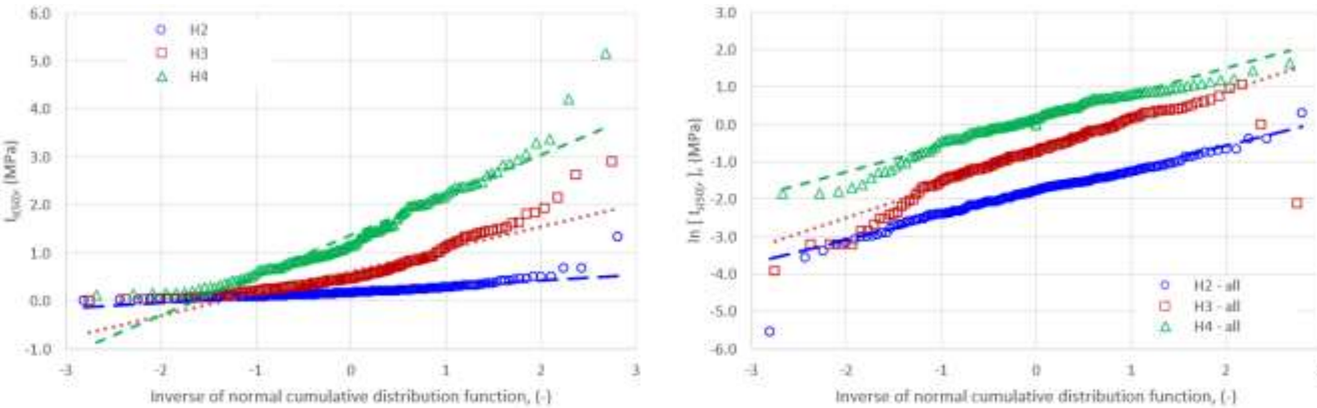

Figure 9. Inverse standard normal cumulative distribution function for different indurations of limestone and chalk to verify the distribution of the test data assuming normal (left) and lognormal (right) distributions.

2.2. Dependence of coefficient of variation on D/D_e ratio

The analysed tests were performed on specimens retrieved from different depths, however for the purpose of this analysis it is assumed that the weak rock strength represented by point load strength index $I_{s(50)}$ varies with the degree of induration and is independent from the sampling depth.

Usually, it is assumed that coefficient of variation (CoV) provides a measure of dispersion of the data which is independent of the mean value. The CoV is calculated for normal and lognormal distribution of the of the $I_{s(50)}$ data set excluding outliers defined test results values having more than ±3 standard deviations (three-sigma rule) from the mean value (Uzielli et al., 2007). In Figure 10 the CoV is plotted against the discrete mean values of D/D_e for different ranges of the degree of induration of limestone and chalk. The most numerous data set consists of specimens with D/D_e ratio in the range 0.6-0.7 for each degree of induration and is therefore expected to be less affected by the statistical estimation error.

The CoV calculated for the lognormal is generally higher than that of the normal distribution. Based on Figure 10 one could infer that for material with H3 and H4 induration the variability of $I_{s(50)}$ decreases vs D/D_e when this ratio is above 0.8, while this does not appear to be the case for H2 indurated material. Petrella (2001) found that the CoV reduces significantly within the D/D_e ratio range of 0.6 to 0.8 for various types of isotropic and anisotropic rocks, such as gneiss, granite and marble and that the curves have a downward concavity, which is only partly consistent with the data set assessed herein.

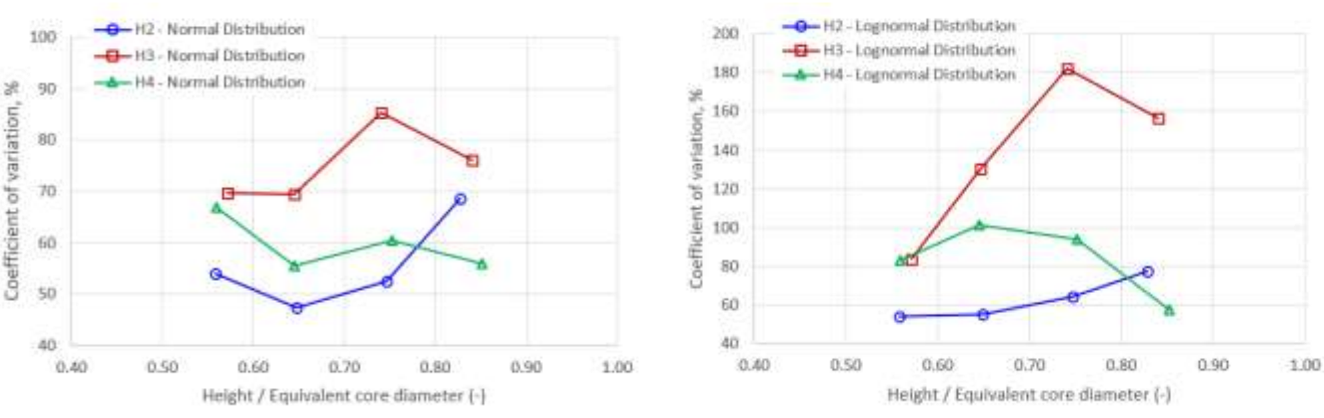

Figure 10. CoV vs D/D_e based on normal (left) and lognormal (right) distributions.

3. CONCLUSIONS

The results of circa five hundred point load tests carried out on specimens of Danian limestones and Maastrichtian chalk collected from two sites on the Danish island of Zealand were presented together with moisture content and bulk density. Notable limitations of the data set are the unavailability of tests for specimens with a D/D_e ratio >0.8 and missing information on the test duration.

It was found that the point load strength index values $I_{s(50)}$ obtained for H2, H3 and H4 indurated materials do not strictly follow the indicative $I_{s(50)}$ range values provided by Hansen & Foged (2002). Specifically, the results of 77% tests on strongly indurated (H4) specimens, 81% tests on indurated (H3) specimens and 20% on slightly indurated (H2) specimens fell outside the Danish literature ranges for Danian limestones.

The available data set does not allow to clearly attribute the scatter in the $I_{s(50)}$ values to the specimen size expressed by D/D_e ratio, although it would be expected to see a lower variability $I_{s(50)}$ when the specimen size is larger for the analysed degrees of induration of the tested limestone and chalk specimens. It shall be noted that the indicative ranges of compressive strength σ_c for the different degrees of induration are quite wide as the maximum value (high degree of induration) is 4 to 5 times larger than the lowest one (low degree of induration) as shown in Table 1. The scatter of the point load strength index $I_{s(50)}$ with the induration decreases with increasing induration. Therefore it is presumed that the variability in the $I_{s(50)}$ within the analysed test results is affected more by the aleatory uncertainty (Uzielli et al., 2007) of the data due to inherent heterogeneity of the limestone and chalk strength, than by the test specimen size.

4. ACKNOWLEDGEMENTS

The authors would like to thank Metroselskabet and Danish Road Directorate for granting permission to publish the information provided in this paper. The content of this paper shall not be considered endorsed by Metroskelskabet or the Danish Road Directorate. The authors are grateful to A. Cañavate Grimal for the insightful discussions on statistical analysis of the data and to Niels Savnik for his contribution to one of the data sets.

REFERENCES

Abbs, A.F. (1985). *The use of the point load index in weak carbonate rocks*. ASTM STP 883: 413–421.
Broch, E. & Franklin, J.A. (1972). *The Point-Load Strength Test*. International Journal of Rock Mechanics and Mining Sciences vol. 9: 669-697.
Hansen, H.K., & Foged, N.N. (2002). *Kalkens bjergmekaniske egenskaber*. In J. K. Frederiksen (Ed.), Ingeniørgeologiske forhold i København. Danish Geotechnical Society. dgf-Bulletin No. 19: 31-34.
ISRM (1985). *Suggested method for determining point load strength*. ISRM commission on testing methods. Working group on revision of the point load test method. Int. Journal Rock Mech. Min. Sci. & Geomech. Abstr, vol. 22: 51–60.
Larsen, G., Frederiksen, J., Villumsen, A., Fredericia, J., Graversen, P., Foged, et al. (1995). *A guide to engineering geological soil description*. dgf-Bulletin 1, Dansk Geoteknisk Forening.
Thuro K., Plinninger R.J. (2001). *Scale effects in rock strength properties. Part 2: Point load test and point load strength index. Rock Mechanics - A Challenge for Society*. Proceedings of the ISRM Regional Symposium Eurock 2001: 175-180.
Petrella, F. (2001). *Rapid tests for rock characterisation*. MSc Thesis. "La Sapienza" University of Rome (in Italian).
Protodyaknov, M.M. (1960). *New methods of determining mechanical properties of rock*. Proceedings of the International conference on strata control. Paris. Paper C2: 187-195.
Uzielli, M., Lacasse, S., Nadim, F., Phoon, K.K. (2007). *Soil variability analysis for geotechnical practice*. Characterisation and Engineering Properties of Natural Soils 3-4: 1653-1752.

Proceedings of the NROCK 2023
The IV Nordic Symposium on
Rock Mechanics and Rock Engineering
ISBN 978-9935-9436-2-0
DOI 10.33112/nrock2023.10

Back-calculation of in-situ stress condition based on the performed secondary stress measurements: Connected to the West Link Project, Sweden

Kriti Panthi (kritip@stud.ntnu.no)

Kriti Panthi
Norwegian University of Science and Technology, Trondheim, Norway
Roger Olsson, Øyvind Dammyr
Norwegian Geotechnical Institute, Oslo, Norway
Eric Hegardt
Swedish Transport Administration, Gothenburg, Sweden

ABSTRACT

A large underground cavern design at a shallow depth requires reliable estimation of in-situ stress conditions. Geological conditions, topography, and tectonic activity influence the magnitude of the in-situ stresses. The objective of this paper is to predict and evaluate the in-situ stress state before the excavation of two pilot tunnels in a railway access cavern. The access cavern, named Mellanplan, is a part of the Korsvägen section at the West Link Project in Gothenburg, Sweden. The first phase of the construction sequence at Mellanplan involved excavation of two pilot tunnels in the top heading, where a rock pillar remained in between the pilots. Before excavating the rock pillar, SINTEF Community performed secondary stress measurements from the roof of the two pilots, utilising the 2D doorstopper method. The results from these stress measurements are assessed and an interpretation of the stress field at Mellanplan is carried out. The concepts from the final rock stress model (FRSM) suggested by Stephansson and Zang (2012) are applied in the back-calculation of the initial stress state. A 3D numerical program, *RS3*, is applied for parameter stress analyses, where various stress inputs are evaluated. The results from stress analyses are validated with the induced stresses obtained from doorstopper measurements. The final rock stress model demonstrates the stress field at Mellanplan as $\sigma_H > \sigma_v > \sigma_h$. The findings in this study reveal that tectonic stress and residual stress have greater contribution towards the major horizontal stress component. Furthermore, σ_v and σ_h. are suggested as gravity induced stresses. Due to the complexity of stresses at shallow depths, there is a possibility of geological structures reducing the already low magnitude of σ_h.

KEYWORDS

Back-calculation; Estimation of in-situ stresses, Rock cavern; 3D modelling, Scandinavian geology

INTRODUCTION

Underground caverns are used for a variety of purposes in civil engineering, e.g., caverns for the installation of turbines, generators and transformers in hydropower projects, rock caverns for storage, underground sports facilities, and caverns for underground train stations. Large cavern spans combined with a small overburden are often more challenging than narrow caverns due to confinement issues and the requirement of securing an arching effect. Underground excavations near the ground surface tend to have arching deformations directed towards the free ground. In such cases, it is beneficial to have high horizontal stresses. The horizontal stresses that are at least equal to or greater than the vertical stress is favourable for the stability of caverns with large spans at shallow depths (Barton and Hansteen, 1978). Furthermore, a combination of large cavern spans and low overburden can result in stress-confinement reduction, which can contribute to structurally controlled failure. This form of instability issue involves gravity-driven processes leading to block falls from roof and sidewalls of underground openings. Alongside stress conditions, pre-existing geological structures have an important influence on the formation of wedges and block falls, and hence affect the stability of an underground opening (Martin et al., 2003).

Since cavern stability issues depend on stress conditions, the knowledge regarding in-situ stresses is important. The estimation of in-situ stress state can be based on elasticity theory, various stress measurement methods, monitoring or numerical modelling. In-situ stresses at a shallow depth are often complex and relatively less measured and reported. The reported stresses in the literature are generally at a depth greater than 50 m. The results from the stress measurements near the ground surface often have widespread data. According to Stephansson and Zang (2012), in addition to stress measurements, numerical modelling can contribute to the estimation of the variability of in-situ stresses.

This study is connected to the West Link (Västlänken), which is a railway infrastructure project, located in Gothenburg, Sweden. The project includes constructions of a six-kilometre underground tunnel and three new underground stations: Gothenburg Central Station, Haga and Korsvägen. The stress conditions at the shallow seated access cavern in Korsvägen, called Mellanplan (Figure 1), has been studied. Prior to the West Link, few rock stress measurements were conducted in the Gothenburg region. In order to estimate the in-situ stress state at the location, results from the secondary stress measurements conducted by SINTEF Community are utilised. The predicted in-situ stresses depict stress state before any excavation at Mellanplan.

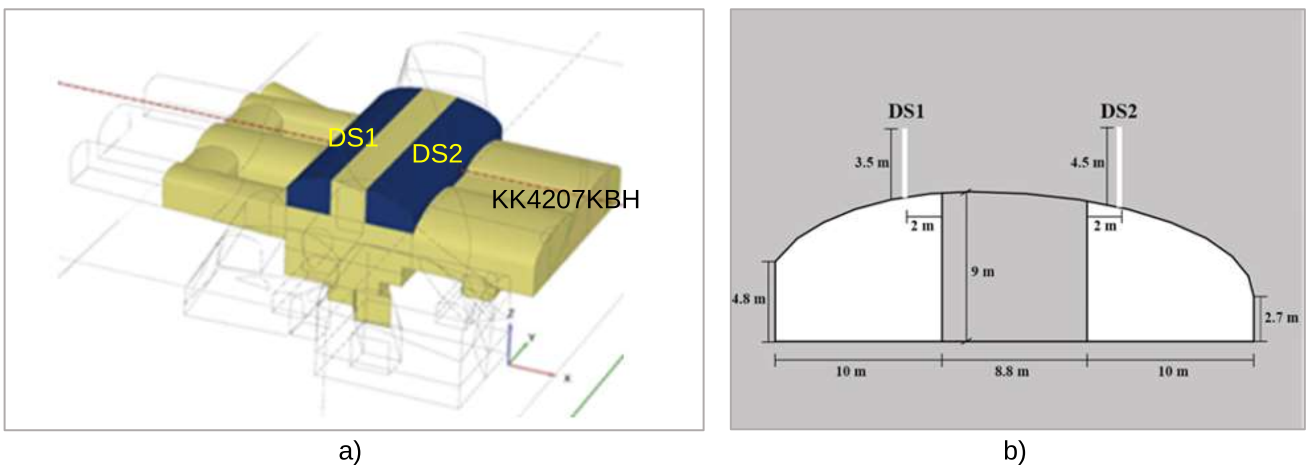

Figure 1. a) Overview of Mellanplan, where the blue volumes represent the excavated pilot tunnels in the top heading; b) Location of the two doorstopper measurements.

The construction of Mellanplan started in 2021, where the first step in the excavation sequence was the removal of two pilot tunnels at the top heading. The excavation method applied in this section is drill-and-blast. The next step in the construction sequence involves excavation of the rock pillar between the pilots. The benching under the top heading will be conducted in accordance with the excavation of track- and station tunnels (Trafikverket, 2016). During the study of the access cavern, only pilot tunnels at the top heading of Mellanplan were excavated. The length of both pilots is 50 m and are termed as East pilot and West pilot. The orientation of Mellanplan is N11W.

Before the excavation of the rock pillar, SINTEF Community performed secondary stress measurements on the roof of both East and West pilot in Mellanplan 28 m inwards from the south of Mellanplan, as shown in Figure 1. The measurements were carried out in April 2022, where the 2D Doorstopper method was utilised. Stress measurements were performed on vertical boreholes from the pilot roofs and are referred to as DS1 (West pilot) and DS2 (East pilot). The 2D stress measurement in DS1 was performed in a 3.5 m long vertical hole above the roof, and in DS2 the vertical hole length was 4.5 m. In DS1, measurements were registered between 0.6 m and 3.5 m hole depth. While in DS2, measurements were registered between 1.3 m and 4.1 m.

1. ROCK STRESS MODEL FOR MELLANPLAN

Formation of the final rock stress model (FRSM), suggested by Stephansson and Zang (2012), comprises of various steps, presented in Figure 2. The first step involves the best estimate stress model (BESM), which is developed by collecting and analysing the existing data on morphology, topography, geology, borehole and drill core.

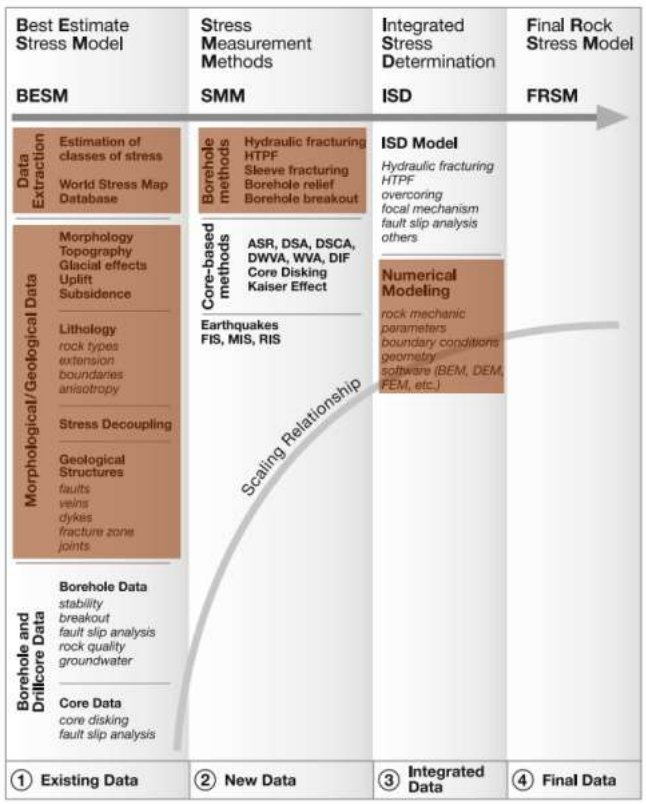

Figure 2. Establishment of the final stress model (FRSM) by combining best estimate model, new stress data and integrated stress determination. Brown highlights present data utilised for this paper. From: Stephansson and Zang (2012).

Generally, BESM should be established before conducting stress measurements, as its function is to guide the engineering geologists and geologists to select appropriate stress measurement techniques and assist in measurement planning. Since the stress measurements at Mellanplan were conducted prior to the BESM formulated for this study, the best estimate model in this case is valuable to predict factors influencing the stress field at Mellanplan. The second step in FRSM is the selection and performance of stress measurement method (SMM). In the West Link Project, 2D doorstopper method was selected as the measurement technique at Mellanplan. The stress measurements were conducted after the excavation of pilot tunnels, thus cannot be considered virgin stress measurement procedure. Nevertheless, the reported secondary stresses can be utilised to back-calculate the in-situ stress state. It should be stressed that the scope of the study presented in this paper involve the application of 2D doorstopper results for back-calculation. Hence, the results from previous stress measurements conducted nearby Mellanplan are not utilised directly for the back-calculation but are useful for the evaluation of the stress field at the location of the access cavern.

The final step in developing a rock stress model includes the integrated stress determination model (ISD). ISD model involves a combination of various stress measurement techniques to determine the in-situ stress conditions.

This is more beneficial than the conventional single measurement method as it increases the reliability of in-situ stress determination. As presented in Figure 2, ISD can also incorporate numerical modelling to predict rock stresses. The results from the conducted stress measurements should be used to validate the results from numerical modelling. Since only 2D measurements have been carried out at Mellanplan, the ISD is achieved in this case by combining the doorstopper results with numerical analysis. The stresses from doorstopper measurements are evaluated before utilising them to generate the best-fit in-situ stress model through 3D stress analyses and back-calculations.

2. GEOLOGY AND ROCK STRESSES

According to the Geological Survey of Sweden, SGU, the bedrock of Sweden consists of three principal components: 1) Precambrian crystalline rocks, 2) remains of a younger sedimentary rock cover from the Phanerozoic period and 3) Caledonides. Figure 3 displays that the tectonics in the area are dominated by slip-strike faults and thrust faults (BeFo, 2022; Heidbach et al., 2018). The majority of the weakness zones have a strike in the NW-SE directions. It should be noted that not all fault regimes and stress orientations from the World Stress Map database are presented in the figure below.

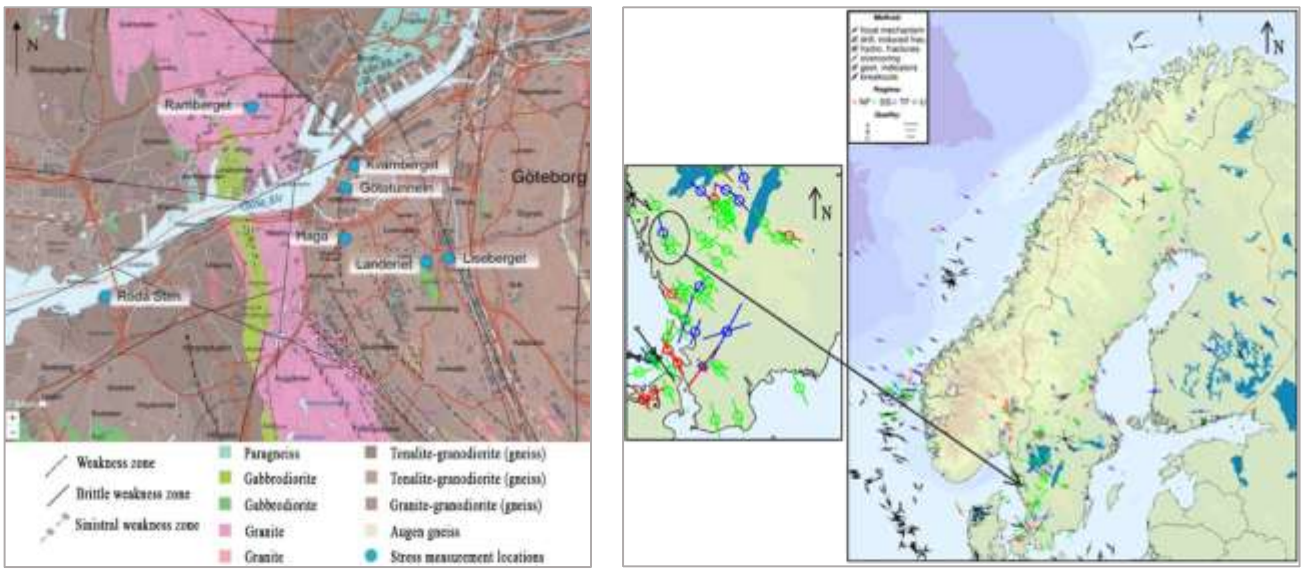

a) b)

Figure 3. a) Bedrock map of Gothenburg with weakness zones and locations of former stress measurement sites. Modified after: SGU (2022) and BeFo (2022); b) Horizontal stresses in Fennoscandian Shield and Gothenburg (circled). Various fault types are presented in the legend: green (Slip-strike) and blue (Thrust fault).

Based on the detailed tunnel mapping of the pilots, the main rock types in Mellanplan are granodiorite gneiss and metabasite. In addition, two major joint sets are registered, foliation joints and cross joints. The foliation joints have an average strike/dip of N149E/63°SW. Cross joints fall on the opposite direction of foliation joints with an average strike/dip value of N43W/30°NE. The foliation joints are dominating joints along the pilots in the top heading. The rock cover above the top heading crown of Mellanplan varies between 7 m to 15 m, where the mean rock surface level is estimated to be 11 m. The average soil thickness above the rock surface is predicted as 5.2 m.

The stress data from the Gothenburg region are based on the World Stress Map (Heidbach et al., 2018) and estimated rock stresses by Rock Engineering Research Foundation in Sweden (BeFo, 2022). In addition, results from previously conducted 3D overcoring stress measurements are utilised to formulate an estimation regarding the stress orientations. Figure 3 depicts orientations of major horizontal stresses, σ_H, in Scandinavia. The major horizontal stresses in the Fennoscandian Shield typically have orientations in NW-SE directions. According to the World Stress Map, this trend correlates with the horizontal stress conditions in the Gothenburg region.

In general, few rock stress measurements have been conducted in Gothenburg. Rock stress measurements are relatively costly and technically complex. Therefore, for the future underground projects, previously conducted stress measurements and documentations are important. Landeriet and Liseberget are locations near Mellanplan, where 3D overcoring stress measurements were performed in relation to the West Link Project. At both locations, the orientation of σ_H is estimated perpendicular or close to perpendicular to the access cavern (N80E ± N10E). While σ_h is predicted perpendicular to σ_H.

The results from stress measurements at Landeriert and Liseberg (borehole id: KK4207KBH and KK4222KBH) are depicted in Figure 4. The points in the graph present the measured in-situ minor and maximum horizontal stresses. Best-fit lines are derived from the measurements. The measured horizontal stresses at the overcoring sites differ from each other, since Liseberget is closer to a weakness zone (Figure 3). The results from the 3D overcoring measurements were complex due to widespread of data.

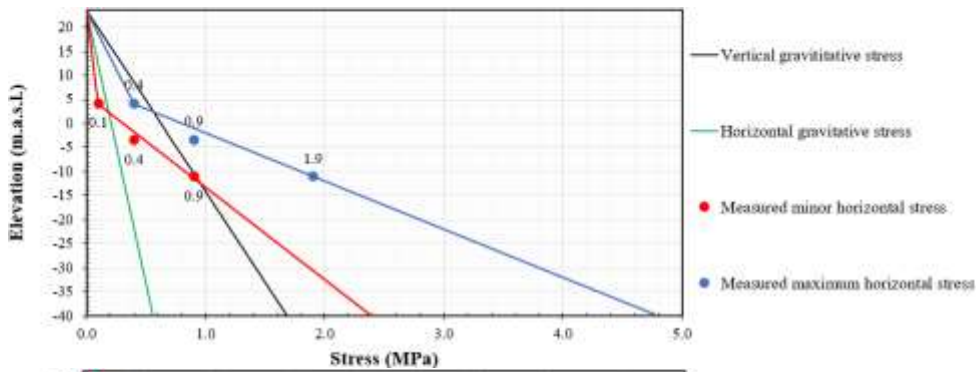

a)

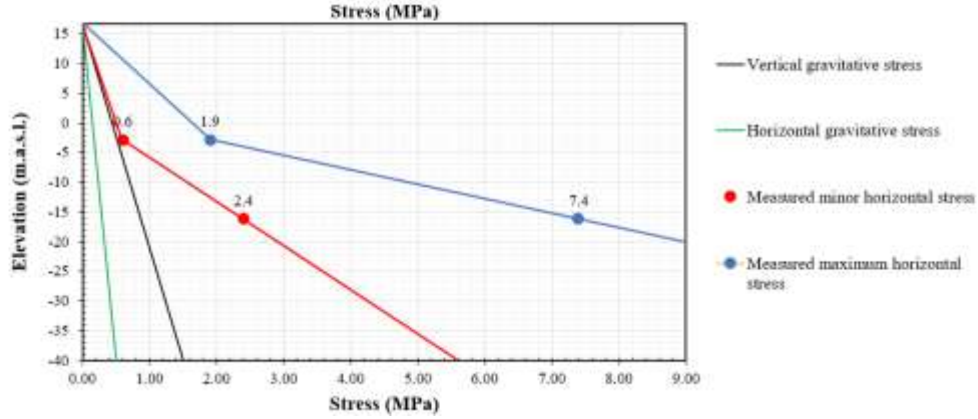

b)

Figure 4. a) In-situ horizontal stress measurements conducted at Landeriet, borehole KK4207KBH (location is shown in Figure 1 and 3). b) In-situ horizontal stress measurements conducted at Liseberget, borehole KK4222KBH (location is shown in Figure 3).

Rock Engineering Research Foundation in Sweden (BeFo) has interpreted the in-situ stress state in Gothenburg on the basis of the previously performed stress measurements. BeFo (2022) suggests the following stress state for Gothenburg. The notation for stress orientation of the major horizontal stress is presented as α_H in Table 1, while z presents depth and ρ is density of the rock.

Table 1. In-situ stress state in Gothenburg, estimated by BeFo (2022).

	σ_H [MPa]	σ_h [MPa]	σ_v [MPa]	α_H [°]
Minimum	0.077 z	0.007 z	0.021 z	N80E
Best estimated	0.104 z	0.016 z	ρgz	N130E
Maximum	0.171 z	0.037 z	0.032 z	N115E

3. DOORSTOPPER MEASUREMENTS

Assessment of the doorstopper measurements showed some uncertainties in relation to negative stress components and effect of anisotropy on stress measurements. Certain secondary horizontal stresses are calculated as negative stress components based on the doorstopper measurements. The absence of information regarding the occurrence of these negative stress components resulted in neglection of these data points for further estimation of the in-situ stress state at Mellanplan. Moreover, evaluation of the stress measurements showed that the doorstopper results from the East pilot are less likely to be affected by rock mass anisotropy than from the West pilot. The analysis of 2D doorstopper measurements is based on linear elasticity and assumes isotropic rock conditions. Therefore, it is considered reasonable to select East pilot for further estimation of in-situ stress field.

The horizontal stresses, reported by SINTEF Community, have magnitudes and orientations with respect to the north direction. The directions of the major horizontal stresses are given as angles from the north, with the minor horizontal stresses oriented perpendicular to σ_H. For the back-calculation of in-situ stresses from the 3D numerical program, *RS3*, the secondary stresses have to be resolved with respect to the orientation of Mellanplan. In the *RS3* models, the normal stress along Z axis (σ_{ZZ}) represents stresses due to the vertical overburden (z) of the rock mass. The 3D numerical models present induced horizontal stresses along the X and Y axes (σ_{XX} and σ_{YY}), where the length axis of the top heading is in the direction of the Y axis.

In order to compare σ_{XX} and σ_{YY} obtained from the *RS3* models with the measured secondary stresses, the latter is resolved to stresses in the X and Y directions of Mellanplan. Consider that measured σ_H makes an angle θ with the Y axis (length axis of Mellanplan) as illustrated in Figure 5, where the orientation of σ_h is perpendicular to σ_H. The horizontal stresses along the X and Y directions of Mellanplan, σ_{XX} and σ_{YY} are calculated by using σ_H and σ_h in Equations 1 and 2, suggested by Basnet and Panthi (2019). These equations consider the effect of horizontal shear stresses τ_{YX} and τ_{XY} (Figure 5). The equations below are derived for a linearly elastic model, where the material is anticipated to exhibit linear stress-strain behaviour.

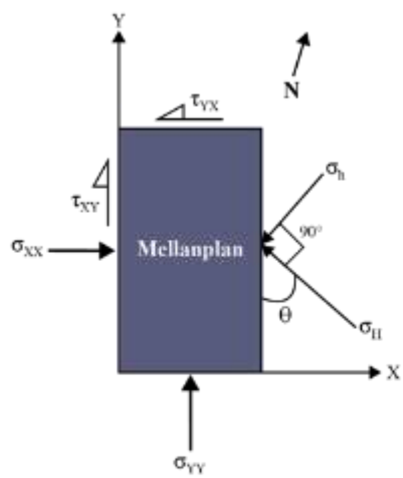

$$\sigma_{XX} = \sigma_H \cos^2\theta + \sigma_h \sin^2\theta \qquad (1)$$

$$\sigma_{YY} = \sigma_H \sin^2\theta + \sigma_h \cos^2\theta \qquad (2)$$

Figure 5. Resolved horizontal stresses, σ_{XX} and σ_{YY} at Mellanplan.

Table 2 introduces the calculated σ_{XX} and σ_{YY} at the East pilot, by applying Equations 1 and 2. For clarification, the resolved secondary stresses from the doorstopper will have the stress notifications: $\sigma_{XX(D)}$ and $\sigma_{YY(D)}$.

Table 2. Resolved secondary stresses $\sigma_{XX(D)}$ and $\sigma_{YY(D)}$ from the doorstopper at the East pilot. The angle between Mellanplan and σ_H is given as positive in the counterclockwise direction.

Hole depth [m]	σ_h [MPa]	σ_H [MPa]	α_H [°]	Angle between Mellanplan and σ_H	$\sigma_{XX(D)}$ [MPa]	$\sigma_{YY(D)}$ [MPa]
1.3	-1.1	0.2	N142E	27	-0.8	-0.1
2.5	-1	3.6	N22E	147	0.4	2.2
2.8	-0.4	3.6	N136E	33	0.8	2.4
3.2	-2.3	0.2	N132E	37	-1.4	-0.7
3.6	-0.3	1.5	N172E	-3	-0.3	1.5
4.1	0.4	3.7	N0E	169	0.5	3.6

Mean value of positive components	0.6	2.4
Std. deviation of positive components	0.2	0.9

Figure 6 presents the calculated values of $\sigma_{XX(D)}$ and $\sigma_{YY(D)}$ against hole depth at East Pilot as a scatter plot. The mean rock cover above the stress measurement site at the East pilot is approximately 12 m. While the borehole depth with stress measurements above the East pilot end at 4.1 m. The spread of stress data shown in the scatter plot below is as anticipated for stress conditions at shallow depths. The effect of weathering and geological structures on stresses is more likely to occur near surface grounds due to the open joints. Such complexity at shallow depths leads to scattering results, where the stress measurement does not provide a certain trend in data. Since, it is challenging to obtain similar scattering results in numerical modelling, an average interval for the entire borehole length is used to validate the results from the numerical analyses. In conclusion, the average intervals for $\sigma_{XX(D)}$ and $\sigma_{YY(D)}$ are determined by the mean values and standard deviations of the positive stress components as presented in Table 2 and Figure 6.

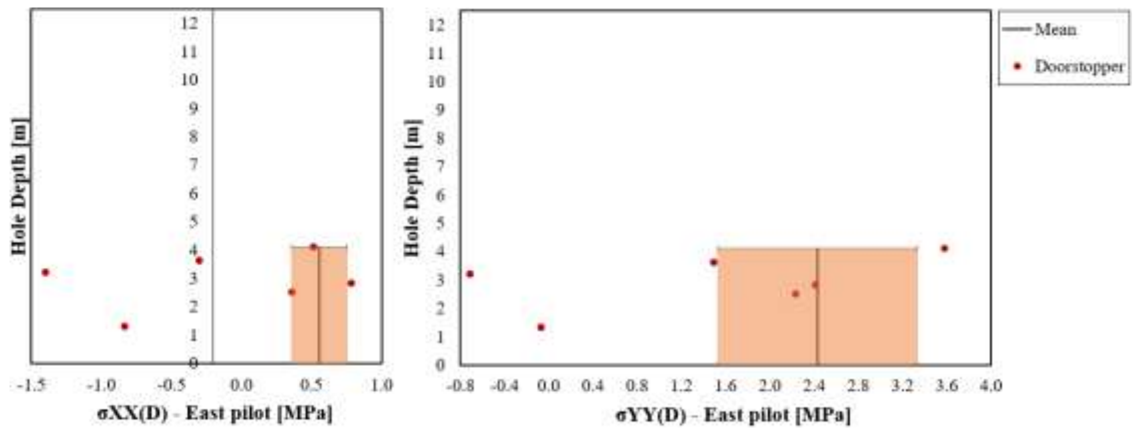

Figure 6. Resolved horizontal stresses, $\sigma_{XX(D)}$ and $\sigma_{YY(D)}$ at East pilot. The vertical line depicts the mean value of the positive stress components, while the marked area is the standard deviation.

4. NUMERICAL MODELLING

A 3D numerical program *RS3*, is applied for parametric stress analyses. The induced stress results from *RS3* are compared with the $\sigma_{XX(D)}$ and $\sigma_{YY(D)}$ and represents the development of the ISD. *RS3* is based on the finite element method (FEM), which describes the rock mass as a continuous medium. A continuous rock mass poses limitations regarding the representation of discontinuities. Although the rock mass displays some degree of anisotropy, the 3D models are generated as linear elastic where the rock mass is considered isotropic and homogeneous material on a large scale. This choice fits well since the calculated stresses from doorstopper measurements are based on linear elasticity and assume isotropic and homogeneous rock mass conditions. Figure 7 presents the model setup used in 3D modelling, where the red volume depicts the volumes removed in the excavation stage. Note that 40 metre long rock pillar remains between the pilots. Joint planes are not generated directly in the *RS3* models.

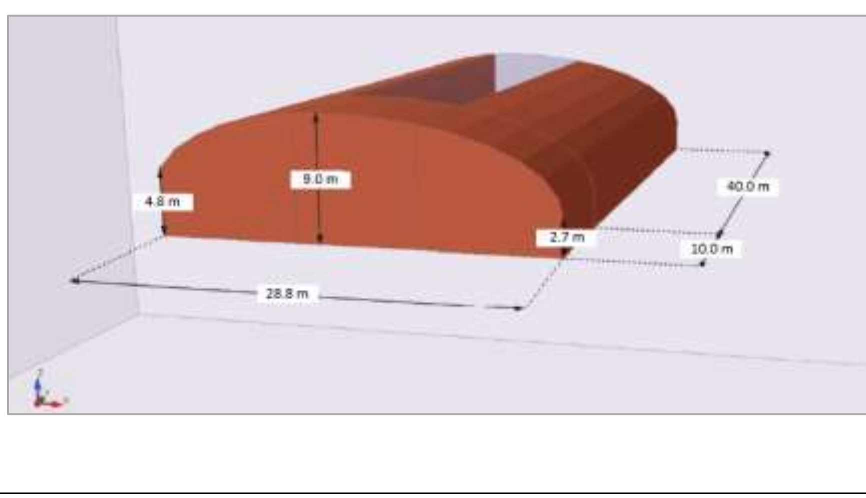

Figure 7. Model setup in RS3. The brown volumes are removed during the excavation stage.

The stress results from RS3 are obtained from a specific section at the top heading. The doorstopper measurement at the East pilot was conducted at 28 m inwards from the south of Mellanplan. Therefore, the query line for stress analyses in the RS3 models has been placed at the same location, as shown in Figure 8. Following the excavation stage, the secondary stress (σ_{XX} and σ_{YY}) results from the query line are plotted and compared with the stresses from the doorstopper measurements ($\sigma_{XX(D)}$ and $\sigma_{YY(D)}$).

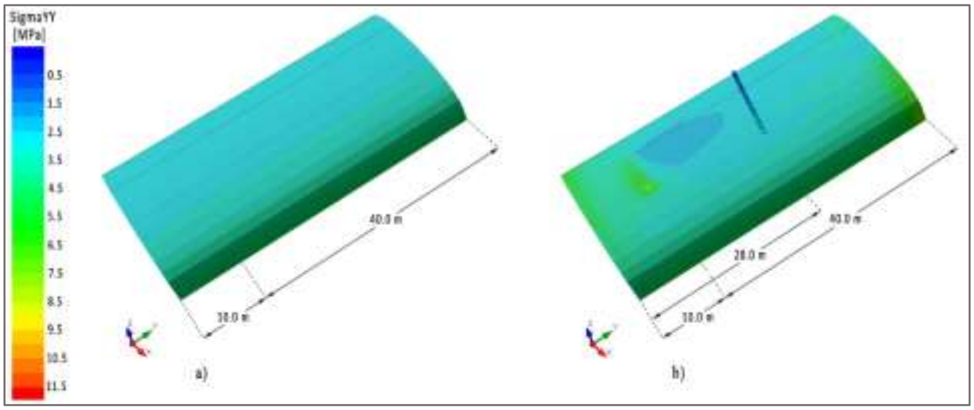

Figure 8. a) Initial stage and b) Excavation stage with query line on the roof. The figures display an example of σ_{YY} results on the tunnel contour.

Table 3 presents the rock mass properties as input parameters for granodiorite gneiss at Mellanplan. The rock mass parameters utilised for the numerical models are quantified and based on detailed pilot mappings, background material received from the West Link Project and laboratory investigations.

Table 3. Input parameters for rock mass in RS3.

Parameter	Unit	Value
Density	kg/m^3	2680
Poisson's ratio, v	-	0.25
Intact rock strength (UCS), σ_{ci}	MPa	140
Rock mass strength, σ_{cm}	MPa	20.6
Young's modulus, E_i	GPa	70
Deformation modulus, E_{rm}	GPa	44
GSI	-	65
Hoek-Brown constant, m_i	-	28
Disturbance factor	-	0

The back-calculation of in-situ stresses in this study is conducted by parametric analysis of stresses. The stress parameters such as K-values (horizontal to vertical stress ratio), stress orientations and locked-in stresses are the main stress input that can induce changes in the stress field. In-situ stresses as input in numerical modelling are given notations σ_H and σ_h, for major horizontal stress and minor horizontal stress, respectively. The vertical stress (σ_v) is considered equivalent to the vertical gravitational stress since it is a common estimation. The orientations of σ_H parallel or close parallel to Mellanplan (N160E-180E) are ignored as input in this study, considering they indicate a complete rotation of the stresses compared to stress directions derived from overcoring estimation. Even though the possibility of a complete stress rotation is plausible, it is considered unlikely and is therefore not investigated further.

For stress analyses, the rock properties and vertical stress (σ_v) are kept as constant parameters. With the purpose of determining representative in-situ stresses at Mellanplan, the stress data from 3D overcoring and stress estimation data provided by BeFo are initially applied as input in the numerical analyses. Following these methods, a trial and error approach with different stress magnitudes and orientations is carried out. The stress magnitudes are dependent on the K-values, where K_H values range from 0.33 to 14, and K_h values range from 0.33 to 3. Furthermore, the stress orientations are varied between N80E to N150E for the numerical trial. After the various numerical trials, the best method to determine the in-situ stress state at Mellanplan involved assumption of the minor horizontal stress, σ_h, as gravity induced stress only. While the major horizontal stress, σ_H, varies with different K_H values as input. K_H values represent ratio between the major horizontal stress (σ_H) and the gravitational vertical stress (σ_v). Due to the time and constraint, only the K_H values of 4, 6, 8, 10, 12 and 14 are selected as variable input parameters. The orientation of the major horizontal stress is presented as α_H in the results below.

The results demonstrating the best fits between the induced stresses from numerical analyses and the doorstopper measurements are obtained when σ_H has an orientation of N150E (Figure 9). Table 4 shows the input parameters used for the stress analyses in this direction. As the figure below indicates, the results achieved with a K_H value of 10 correlate best with the average stress interval for both $\sigma_{XX(D)}$ and $\sigma_{YY(D)}$. Throughout the doorstopper hole depth, up to 4.1 m, the induced stresses resulting from K_H = 10 lie within the standard deviations and are close to the mean stress value in correlation with measured stresses at East pilot.

Table 4. Input parameters for RS3 models providing results in Figure 13.

K_H	K_h	α_H
4, 6, 8, 10, 12, 14	0.33	N150E

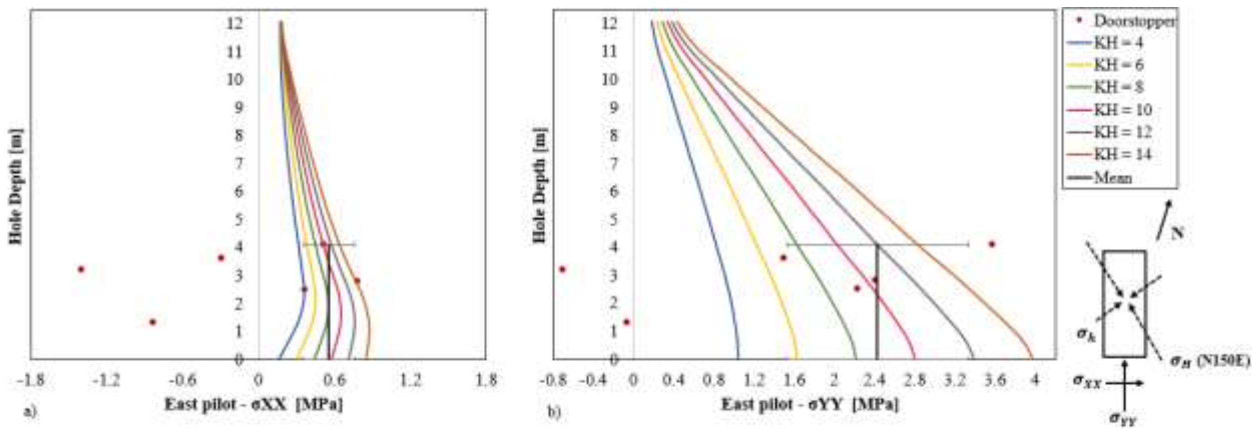

Figure 9. Secondary stresses from 3D models compared with scattered doorstopper stresses, when α_H is N150E.

The K_H values of 8 and 12 also provide secondary stresses within the average stress intervals throughout the entire borehole length. However, the best fit occurs when the input is K_H = 10. Therefore, a combination of K_H = 10 and K_h = 0.33 with major horizontal stress oriented in N150E is selected to be utilised to determine the best estimate in-situ stress state at the top heading location of Mellanplan.

5. IN-SITU STRESS STATE

The results from 3D modelling showed that the best fits between numerical and doorstopper stresses are achieved when the major horizontal stress has an orientation of N150E. Table 5 presents a range of input stress parameters that showed optimal results when secondary stresses from numerical analyses are compared with the doorstopper stresses.

Table 5. Input parameters in RS3 models that showed optimal results.

	K_H	K_h	α_H
Minimum	8	0.33	N150E
Best estimated	10	0.33	N150E
Maximum	12	0.33	N150E

Considering the vertical stress in Mellanplan is assumed to be gravitational, in-situ horizontal stresses, σ_H and σ_h, can be back-calculated. Based on the back-calculation, Figure 10 present the in-situ stresses at a shallow depth in Mellanplan. The rock stresses σ_h and σ_v are presented as gravity induced stresses, while σ_H is greater than the gravitational stress. The minimum and maximum estimation for σ_H is depicted as a stress range for the major horizontal stress in Figure 10. Although doorstopper measurement at the East pilot was conducted above the tunnel roof, the rock stresses presented in the figure below are extrapolated until the elevation at 0 masl. The back-calculated virgin stresses are assumed to be viable from an elevation of 0 masl. to 15.8 masl.

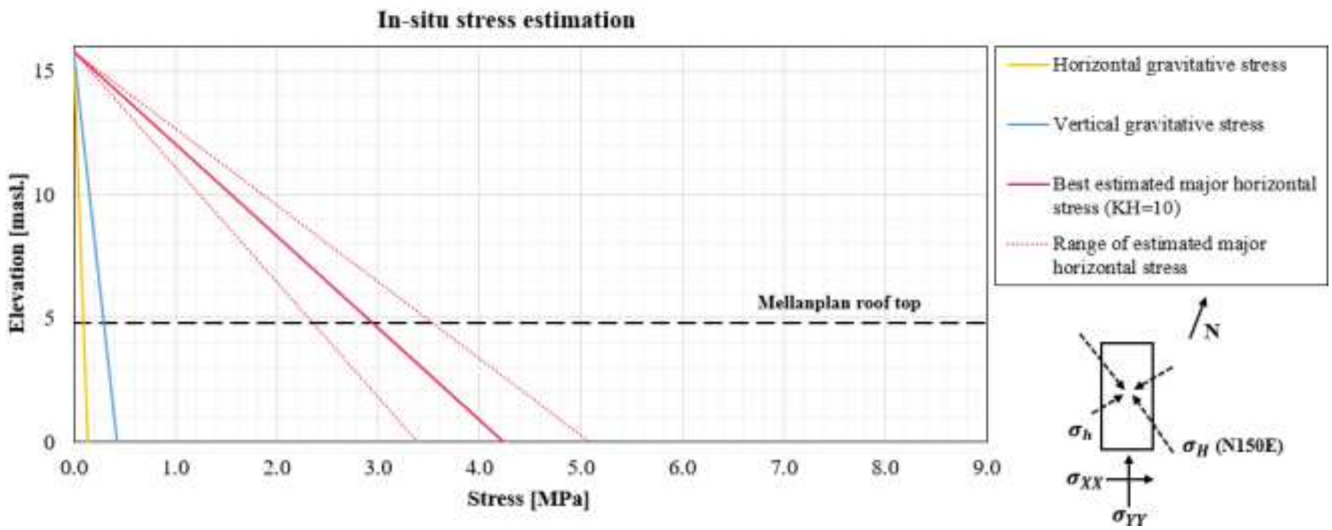

Figure 10. Final rock stress model with estimated in-situ stresses at a shallow depth in Mellanplan. The stress domain applies for elevation from 0 masl. to 15.8 masl.

6. CONCLUSIONS

The final rock stress model (FRSM) achieved in this study demonstrates the stress field at Mellanplan as $\sigma_H > \sigma_v > \sigma_h$. This stress state is only viable at a shallow depth, from 0 masl. to 15.8 masl. Such stress condition correlates with the suggested stress state by Martin et al. (2003) for Scandinavia. Nonetheless, this proposal also includes stress measurements at greater depths. The in-situ stresses at shallow depths can show complexity. Based on the best estimated stress model (BESM) and the results from numerical analyses, the major horizontal stress indicates to be highly influenced by the tectonic stress. It is likely to predict that the tectonic stress contributes greater to the major horizontal stress, than other stress components. Moreover, residual stress from periods with glaciation and deglaciation in Sweden, may also have greater influence on the major horizontal stress component. Due to the low overburden, the relatively low magnitude of minor horizontal stress is assumed as gravity-induced stress. However, weathering and geological structures may have reduced the already low magnitude of σ_h. The indications of low stress magnitudes, σ_h and σ_v, are also validated by the observed block falls from pilot roofs at Mellanplan.

The estimated orientation of σ_H differs from the predicted stress directions by overcoring measurements and BeFo. Geological structures may have attenuated the stress orientations slightly. As mentioned previously, there is a correlation between the strike of the faults and the orientation of σ_H. On the other hand, open joints can also influence stress distribution, which can be the cause of the rotation of stresses. The integrated stress determination (ISD) for the study involved combining the doorstopper results with numerical analyses. Further improvement of the final rock stress model can be accomplished, provided different stress measurement method is utilised at Mellanplan in the future, e.g., 3D overcoring or hydraulic fracturing tests. The results from two different measurement methods can increase the reliability in rock stress determination.

7. REFERENCES

Stephansson O, Zang A (2012) ISRM suggested methods for rock stress estimation—part 5: establishing a model for the in situ stress at a given site.” *Rock Mechanics and Rock Engineering*, 45, pp. 955-969.

Barton, N. and Hansteen, H. (1978) Large Underground Openings at Shallow Depth: Comparison of Deformation Magnitudes from Jointed Models and Linear Elastic F.E. Analyses. *Fjellsprengningsdagen - Bergmekanikkdagen*. Oslo, Norway: Norwegian Tunneling Society, pp. 20.1–20.30.

Basnet, C. B. and Panthi, K. K. (2019) Evaluation on the Minimum Principal Stress State and Potential Hydraulic Jacking from the Shotcrete Lined Pressure Tunnel: A Case from Nepal. *Rock Mechanics and Rock Engineering*, 52, pp. 2377–2399.

BeFo (2022) Evaluation and Interpretation of Initial Rock Stresses for Stockholm and Gothenburg. Tech. rep. BeFo - Rock Engineering Research Foundation.

Heidbach, O. et al. (2018) The World Stress Map Database Release 2016: Crustal Stress Pattern Across Scales. *Tectonophysics*, 744, pp. 484–498.

Martin, C., Kaiser, P., and Christiansson, R. (2003) Stress, Instability and Design of Underground Excavations. *International Journal of Rock Mechanics and Mining Sciences*, 40, pp. 1027-1047.

SGU (2022) Berggrund 1:50 000 - 1:250 000. URL: https://apps.sgu.se/kartvisare/kartvisareberg-50-250-tusen.html. (Accessed 10. November 2022).

Trafikverket (2016) Tekniskt PM Bergteknik Bilaga 2, Station Korsvägen. Tech. rep. E05-17-013-0700-1001, Version: B.

Proceedings of the NROCK 2023
The IV Nordic Symposium on
Rock Mechanics and Rock Engineering
ISBN 978-9935-9436-2-0
DOI 10.33112/nrock2023.11

Size Dependancy of Post-peak Stress-Strain Properties of Rocks

Abbas Taheri (abbas.taheri@queensu.ca)

A. Taheri
Queen's University, Kingston, Canada

J. Zhang
Formerly The University of Adelaide, Australia

ABSTRACT

Post-peak behavior of rock is significant to the stability of surface and underground rock excavations and the performance of drilling and excavation operations. Mechanical properties and damage characteristics of rocks are subjected to the measurement scale. The effect of size on sandstone's post-peak behavior and failure characteristics are investigated during monotonic uniaxial compressive loading. A series of tests were undertaken on sandstone samples with an aspect ratio of 2.5 and diameters of 19mm, 30mm, 42mm, and 63mm. The lateral strain-controlled loading method was adopted to capture the post-peak stress-strain characteristics. The three-dimensional digital image correlation (3D DIC) technique is utilized to investigate field strain patterns and local damage. The brittleness index was found to increase with an increase in diameter, indicating that the rock sample was damaged in a more brittle regime with a larger size. 3D DIC results demonstrated that in the pre-peak regime, the specimen deforms uniformly. In the pos-peak regime, however, the specimen shows localized behavior. This behavior is different for samples having different diameters. The overall post-peak was a combination of class I and class II behavior.

KEYWORDS

Sandstone; Post-peak; Brittleness; Digital Image Correlation, Damage

INTRODUCTION

Scale effect, which is defined by the influence of the absolute size (i.e., diameter) of cylinder samples when the aspect ratio is constant, may have considerable influence on rock properties. The effects of scale on rock strength have been investigated by several researchers (Bahaaddini et al. 2014; Darlington et al. 2011; Pan et al. 2009; Yoshinaka et al. 2008; Zhang et al. 2011). However, contradictory results are observed. Some scholars reported that scale effects do exist, and an increase in diameter leads to a reduction in rock strength (Cunha 1990; Jackson and Lau 1990). Other researchers observed no scale effects on rock strength (Thuro et al. 2001; Pells 2004). Masoumi et al. (2015) observed that the uniaxial compressive strength of Gosford sandstone first increased and then decreased in the diameter range of 19mm to 145mm. The studies mentioned above mainly focused on the strength of different rocks under scale effects. However, there are limited studies on the impact of scale on the post-peak stress-strain relations and the localized behavior of rocks after the peak stress point.

The complete stress-strain relation of rocks (i.e., the pre-peak and the post-peak behaviors) is considered a prominent tool in rock mechanics to describe strain energy evolution and for rock brittleness determination (Shirani Faradonbeh et al. 2021). The post-peak stress-strain curve of rock is detrimental to the stability of surface and underground rock excavations. For instance, rock post-failure behavior defines the energy released after failure, contributing to rock bursts in deep excavations. In addition, the rock complete stress-strain curve is significant in investigating the performance of drilling and excavation operations (Munoz et al. 2016c). Therefore, characterizing the post-peak behavior of rocks associated with localized behavior is critical to many rock Engineering applications (Munoz et al. 2016a).

Deformation localization is the intrinsic cause of rock failure and strain burst. Therefore, micro-cracking due to the applied load that leads to increased localized damage needs to be investigated thoroughly. This is mainly because the existing micro-cracks inside the rock create homogenous damage zone distributions in the rock mass. It would be interesting to investigate the effect of the scale of localized behavior of rock in the post-peak regime. To accurately investigate rock stress-strain behavior after the peak stress and localization behavior, in this study, a non-contact strain measurement method, i.e., three-dimensional digital image correlation (3D DIC), is utilized to investigate the post-peak stress-strain behavior and local damage of rock specimens with different diameters. This method makes 3D displacements and strains available at every point on the specimen's surface. The DIC method has been implemented to study the deformation of rock materials (Tung et al. 2013; Cheng et al. 2017; Munoz and Taheri 2017; Zhang et al. 2018; Zhou et al. 2019).

A series of uniaxial compression tests were carried out on sandstone specimens having different diameters, with an aspect ratio of 2.5. The lateral strain-controlled method was used to obtain the post-peak stress-strain behavior. Effects of scale on post-peak stress-strain characteristics were investigated. Strain energy development and brittleness index evolution under scale effects were presented. Finally, the 3D DIC method is utilized to study the field of axial and lateral strains during compression.

1. MATERIAL AND METHODS

1.1. Specimen preparation

Hawkesbury sandstone, a medium-strong sedimentary rock, is used as the testing material. Hawkesbury sandstone is an early Middle Triassic (Anisian) formation widely exposed in the Sydney Basin in Australia. The rock has an average uniaxial compressive strength (UCS) of 44 MPa and an average density of 2260 kg/m^3. All the rock samples were drilled from the same rock block and in a similar direction. Rock specimens with an aspect ratio (i.e., a length to diameter) of 2.5 and diameters of 19 mm, 30 mm, 42 mm, and 63 mm, are prepared. The diameter is more than 20 times larger than the grain size, satisfying the ISRM testing method recommendation (Fairhurst and Hudson 1999). The end surfaces and sides of rock specimens were prepared smooth and straight, as recommended by the ISRM.

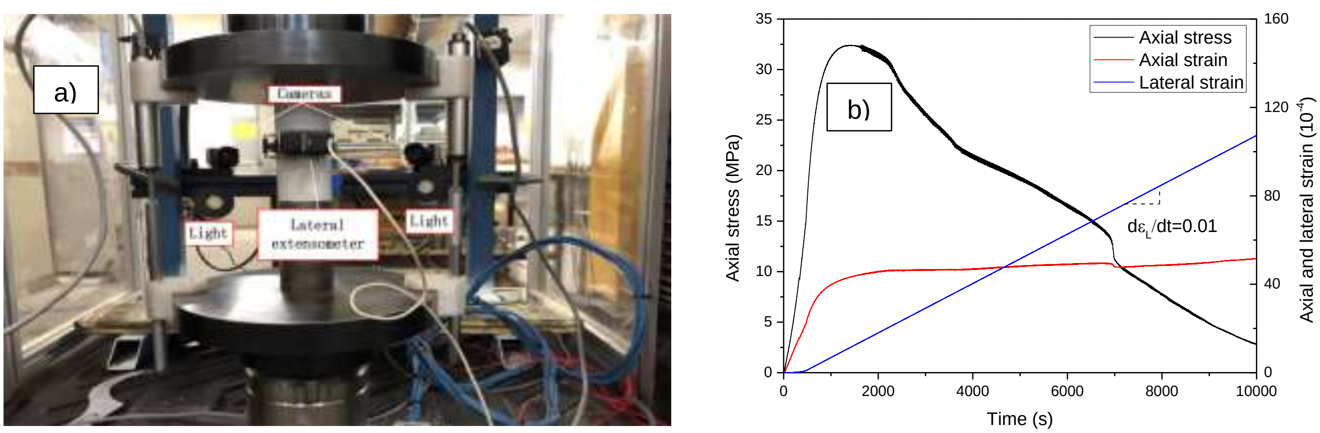

Figure 1. Experimental methodology; a) Test set-up; b) Time history of axial stress, axial and lateral strains in the lateral strain-controlled tests.

1.2. Uniaxial compression tests

Before the load tests, the rock specimens were instrumented by a lateral strain extensometer placed along the perimeter. To eliminate the end-edge friction effects, the lateral extensometer was mounted at the middle length of the specimens (see Figure 1a). During the compression test, the axial deformation of specimens was recorded by a pair of axial linear variable displacement transducers (LVDTs) attached on both the left and right sides of the specimen. A lighting system is used to shed additional light on the sample surface to capture the deformation of the sample using DIC cameras.

The rock specimens were loaded monotonically by a closed-loop servo-controlled hydraulic compressive machine (Type: Instron 1342 manufactured by Instron Inc.). The maximum loading capacity of the testing machine is 250kN. The lateral strain-controlled method loaded the rock specimens using the lateral strain extensometer. Figure 1b shows a typical test's time history of axial stress, axial strain, and lateral strain. As demonstrated in this figure, a constant lateral strain rate of 0.01×10^{-4}/s was used in the lateral strain-controlled tests.

1.3. Digital Image Correlation measurement

A detailed introduction of 3D Digital Image Correlation (DIC) application to uniaxial compression tests can be found in the first author's previous studies (i.e. Munoz et al. 2016a, b). Therefore, here, only a brief description is provided.

3D DIC is a non-contact optical method that measures surface deformation. A pair of high-resolution digital cameras (Type: Fujinon HF75SA-1, 1:1.8/75mm, 5 Megapixels resolution) was used to capture the images of the speckled surface of the sample. The speckle pattern on the rock samples should be created before the test. The sample surface was first sprayed with ordinary white paint and then spray-tarnished black paint. Then, each camera was calibrated using a 30mm standard target with uniformly spaced markers (see Figure 2a). During the loading test, the cameras captured images at a frame rate of an image per second during loading. The captured images were then processed by VIC-3D software to acquire the deformations and strain values (Sutton et al. 2009). To investigate the field strain patterns and local damage of rock samples, five virtual extensometers (i.e., DIC-E0, DIC-E1, DIC-E2, DIC-E3, and DIC-E4) were selected as presented in Figure 2b.

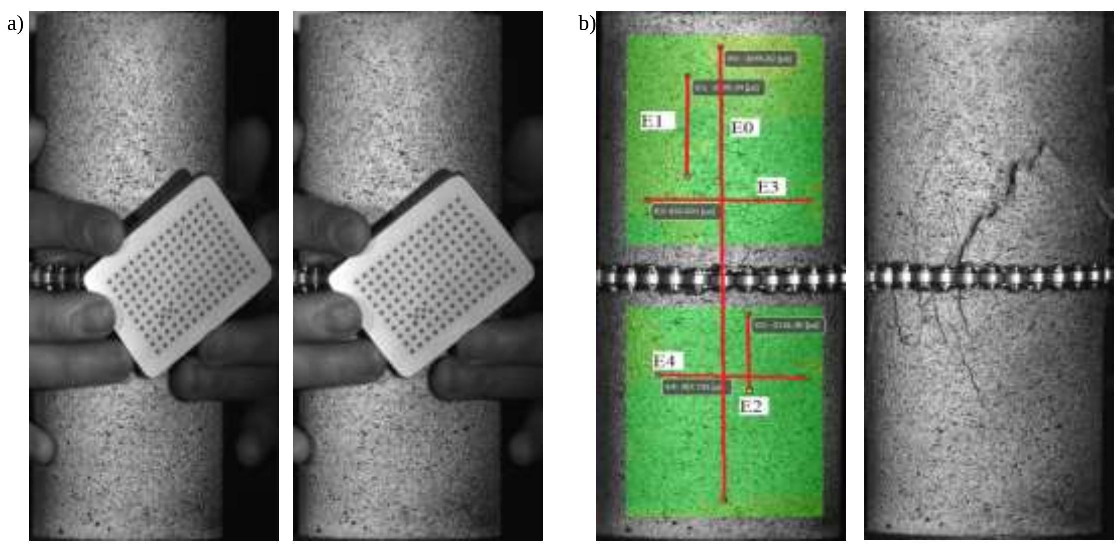

Figure 2. DIC measurement: a) Calibration procedure of the cameras' left and right pair imaging and b) location of virtual extensometers within the area of interest and rock failure during the test.

2. POST-PEAK STRESS-STRAIN CHARACTERISTICS

The stress-strain curves are normalized to investigate the dependency of scale effects on the post-peak behavior under uniaxial loading conditions, as shown in Figure 3. The normalized stress-strain curves were obtained by dividing the stresses and strains by peak stress and peak strain at failure.

The curves demonstrated in Figure 3, in general, show that in the post-peak regime, the stress-strain characteristics for samples with a diameter of 63mm showed a combination of class I and class II behavior based on the classification proposed by Wawersik and Fairhurst (1970). And the post-peak stress-strain curves almost overlapped with each other. The same phenomenon is also found in the samples with diameters of 42mm and 30mm. However, for the samples with a 19mm diameter, two showed a predominant class I behavior, and one had a dominant class II behavior.

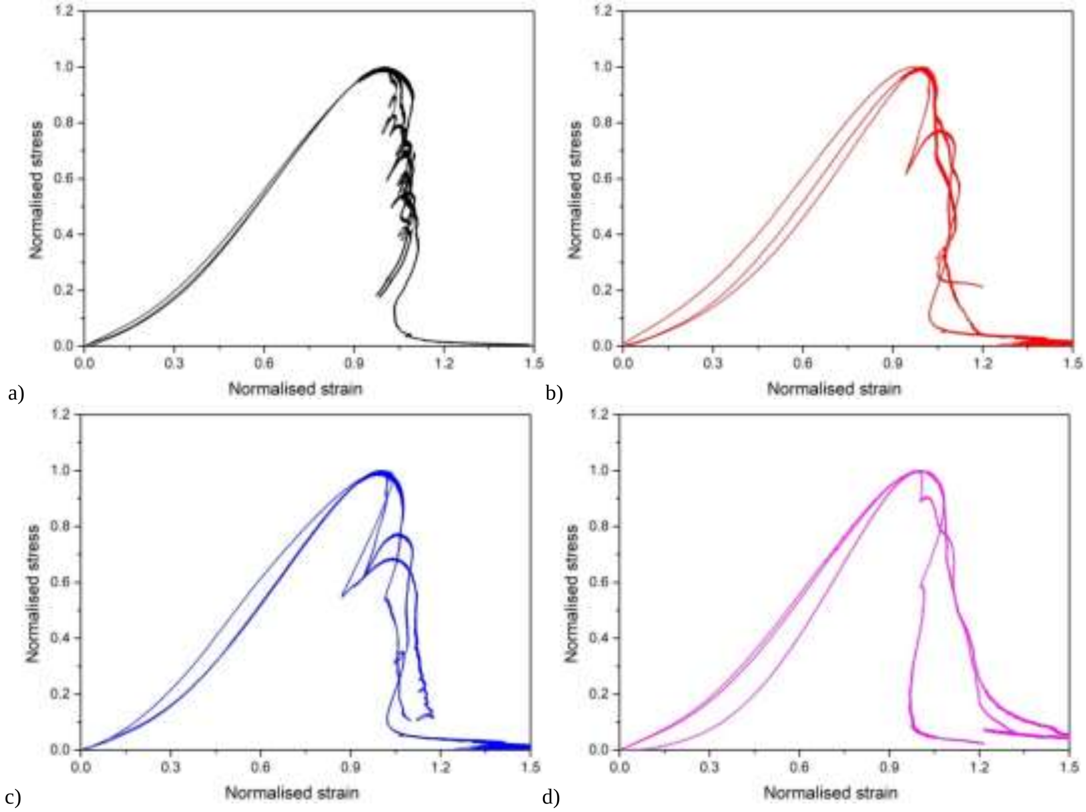

Figure 3, Normalized stress-strain relation of sandstone with different diameters: a) 63mm, b) 42mm, c) 30mm, and d) 19mm.

3. STRAIN ENERGY-BASED BRITTLENESS INDEX

Strain energy, or the amount of energy absorbed by a unit volume of rock under compression, is an important parameter to assess the rock's brittle behavior (Munoz et al. 2016b). The energy absorption capability is also essential when the rock is subjected to blast loads and impacts (Bažant et al. 2004). Variations of different strain energies in the experimental results are investigated to investigate the effect of sample size on the pre-peak and post-peak stress-strain behavior. Figure 4 and Equations 3a-c, demonstrate how pre-peak strain energy U_{pre}, peak strain energy U_{peak}, post-peak strain energy $U_{post,}$ and elastic strain energy U_e are derived. U_{pre} was estimated by the area under the stress-strain curve enclosed by loading the specimen up to the peak stress and then unloading it entirely. *E* is Young's modulus obtained by LVDTs. U_{post} as shown in Fig. 5a, is post-peak strain energy. A post-peak stress level of $1/3\sigma_f$ is recommended by Munoz et al. (2016a) to calculate U_{post}. U_e, which can be expressed by Equation 3a, is the strain energy consumed in the specimen when the failure point is reached (see Figure 4b). On the other hand, the peak strain energy U_{peak} and the total strain energy U_{total} can be expressed by Equations 3b and 3c as follow:

$$U_e = \frac{\sigma_f^2}{2E_{LVDT}} \quad (3a)$$

$$U_{peak} = U_{pre} + U_e \quad (3b)$$

$$U_{total} = U_{pre} + U_{post} \quad (3c)$$

Rock brittleness is an essential parameter to characterize the brittle fracture of rocks. Many brittleness indices were proposed by different scholars (Altindag 2008; Hajiabdolmajid and Kaiser 2003; Munoz et al. 2016b). In this study, three fracture energy-based brittleness indices proposed by the the first author (Munoz et al. 2016a) were adopted to describe the brittle fracture behavior under the scale effects. The brittleness indices were defined as follows:

$$B_1 = \frac{U_e}{U_{total}} \qquad (3d)$$

$$B_2 = \frac{U_e}{U_{post}} \qquad (3e)$$

$$B_3 = \frac{U_{peak}}{U_{total}} \qquad (3f)$$

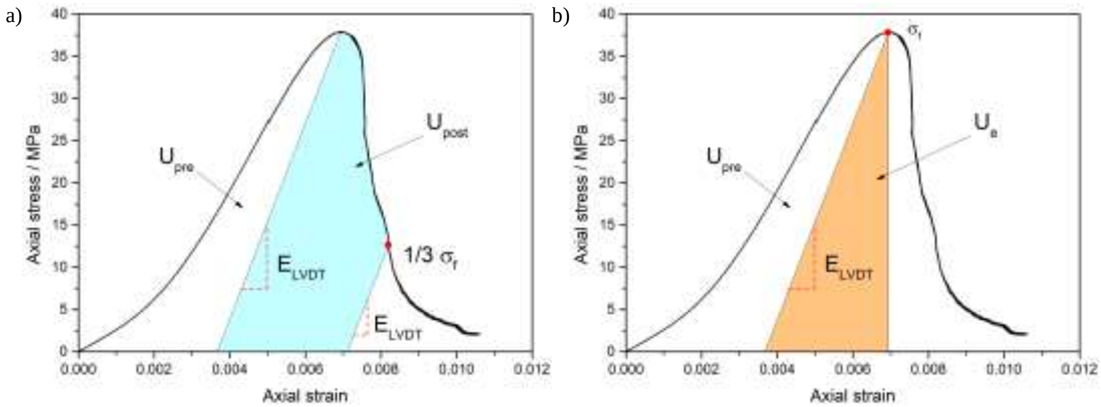

Figure 4, Strain energy of rock specimen under uniaxial compression: a) U_{pre} and U_{post}, and b) U_e

The three brittleness indices were calculated using the strain energy values and plotted in Figure 5. A higher brittleness index means the rock is more brittle. It can be seen from the figure that the three brittleness indices increased almost linearly with an increase in the sample diameter. This indicated that when the size of the rock sample is large, the rock exhibits more brittle behavior when subjected to uniaxial loading.

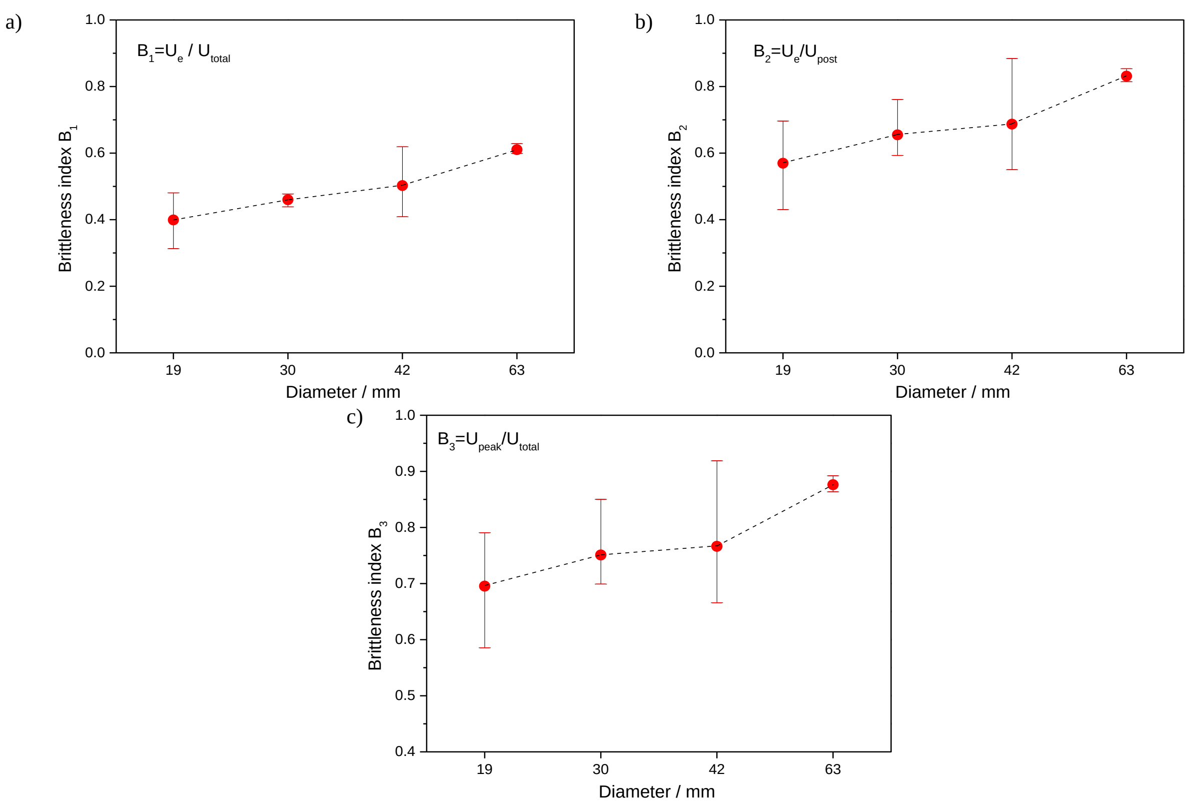

Figure 5, Scale effect on brittleness indices: a) B_1, b) B_2, and c) B_3

4. LOCALIZATION DURING UNIAXIAL LOADING

Eight stress levels (i.e., four in the pre-peak regime and four in the post-peak regime) were selected to show the field strain patterns of rock samples with different diameters. The four stress levels in the pre-peak regime are crack closure stress σ_{cc}, crack initiation stress σ_{ci}, crack damage stress σ_{cd} and peak stress σ_f which were identified from the volumetric strain-axial stress and crack volumetric strain-axial strain curves (Taheri et al. 2020). The four stress levels in the post-peak regime were $0.9\sigma_f$, $0.75\sigma_f$, $0.6\sigma_f$, and $0.4\sigma_f$.

Figure 6a shows the field of axial strain development of samples with a diameter of 42mm. The stress-strain curves obtained from LVDTs and virtual extensometers are compared. The virtual extensometers E0, E1, and E2, located vertically along the rock sample, are applied to measure the axial field strains. Due to the inherent bedding error in the axial strain results measured by the LVDT the virtual strain gauges show lower strain values in the pre-peak regime. In contrast, E3 and E4, located horizontally, are used to measure lateral field strains. The lateral strain values measured by these virtual extensometers are consistent in pre-peak and are slightly higher than the strain measured by the chain extensometer. The results obtained by the virtual extensometers indicate that in the pre-peak regime, the rock deformed uniformly. By comparing the color gradient of axial strain in the samples at different pre-peak stress levels in Figure 6b, i.e., most of the area of interest was found in two color patterns, it demonstrated the axial strain developed uniformly in pre-peak stage, which is consistent with the stress-strain curves measured by virtual extensometers.

As can be seen in Figure 6a, in the post-peak regime the virtual extensometers, the axial LVDT and the lateral chain extensometer follow the same trend until the strength is almost 23 MPa. After that the post-peak stress-strain curves of virtual extensometers, LVDT and chain extensometer are remarkably different. This is due to the development of the localization of strains (either axial, lateral) within the specimen. This results are consistent with the observation of field of axial strains demonstrated in Figure 6c. The results show that E2 and E4 are mainly located inside the localized damage zone and therefore the stress-strain behavior is class I strain softening. Whereas the other virtual extensometers are mostly outside of the localized damage zone and therefore demonstrate unloading and mostly a class II behavior. Axial LVDT and the chain extensometers demonstrate the overall post-peak behavior of the specimen. The overall failure behavior which is demonstrated by the external LVDT is a combination of class I and class II behavior.

Figures 7a-c presents the field of axial strains in the post-peak regime for specimens with diameters of 63mm, 30mm, and 19mm at the selected stress levels introduced before. As can be seen in these figures and Figure 6c, localization of strains around the shear bands have occurred at $\sigma=0.75\sigma_f$ for 63mm and 42mm samples and at $\sigma=0.6\sigma_f$ for 30mm specimen. 19mm specimen shows localization in the post-peak regime, however, no clear shear band is observable. This might be due to the small DIC measurement area when the sample size is considerably small. This demonstrates that the post-peak strain fields are significantly affected by the absolute size of the specimen.

a)

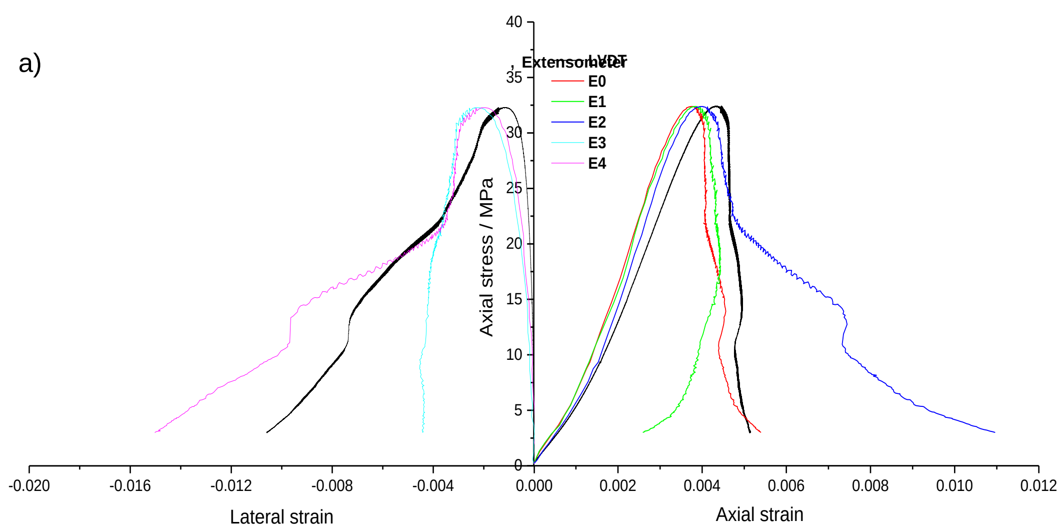

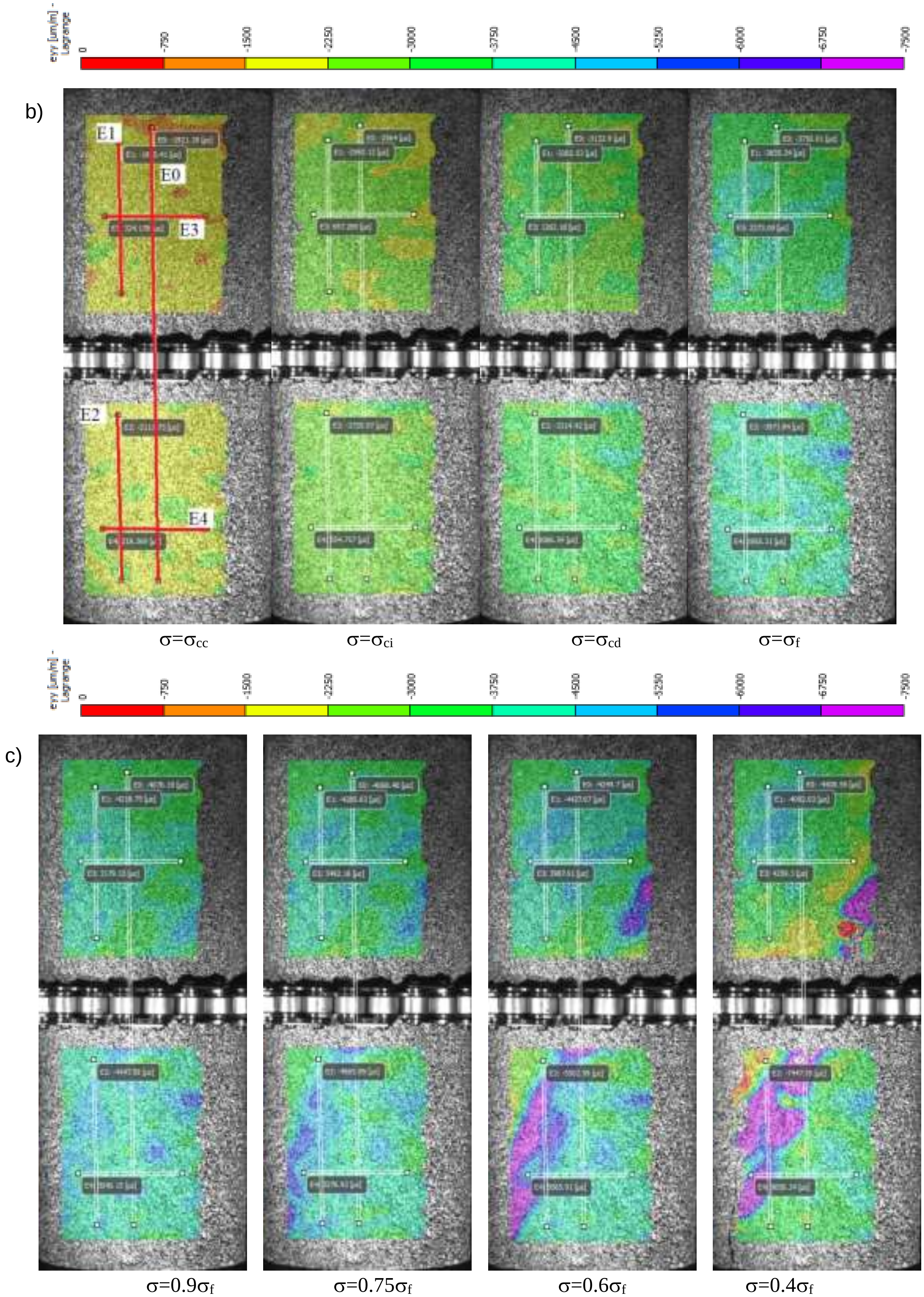

Figure 6, Stress-strain results of 42mm specimen: a) Stress-strain relation by axial LVDT, lateral extensometer, and virtual extensometers; b) Field of axial strains development in the pre-peak regime, and c) Field of axial strains development in the post-peak regime.

a)

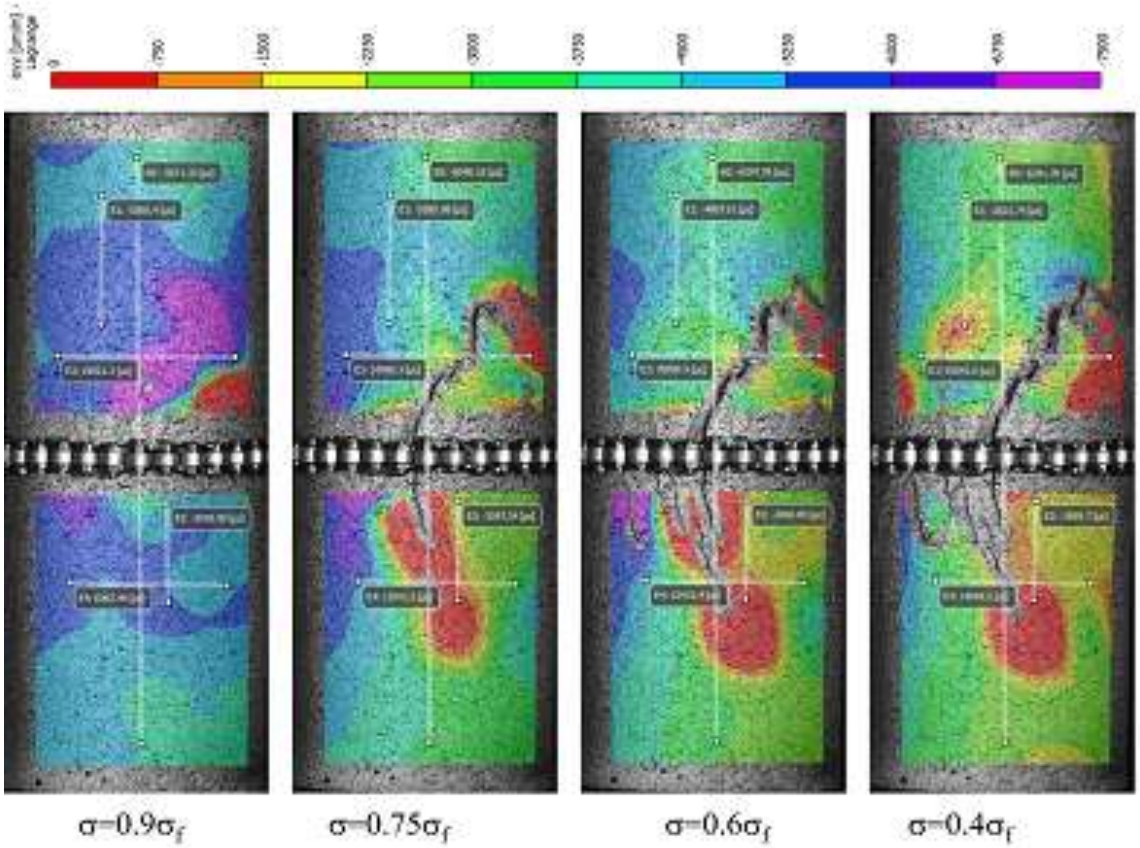

b)

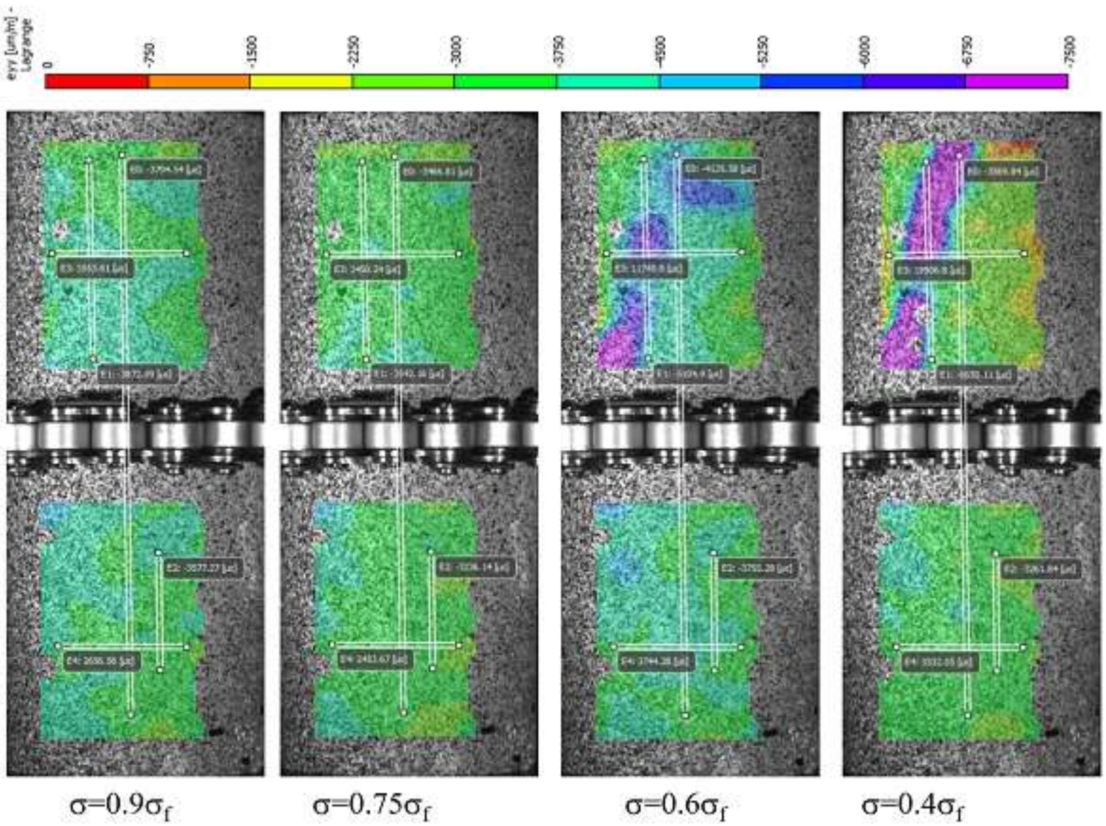

c)

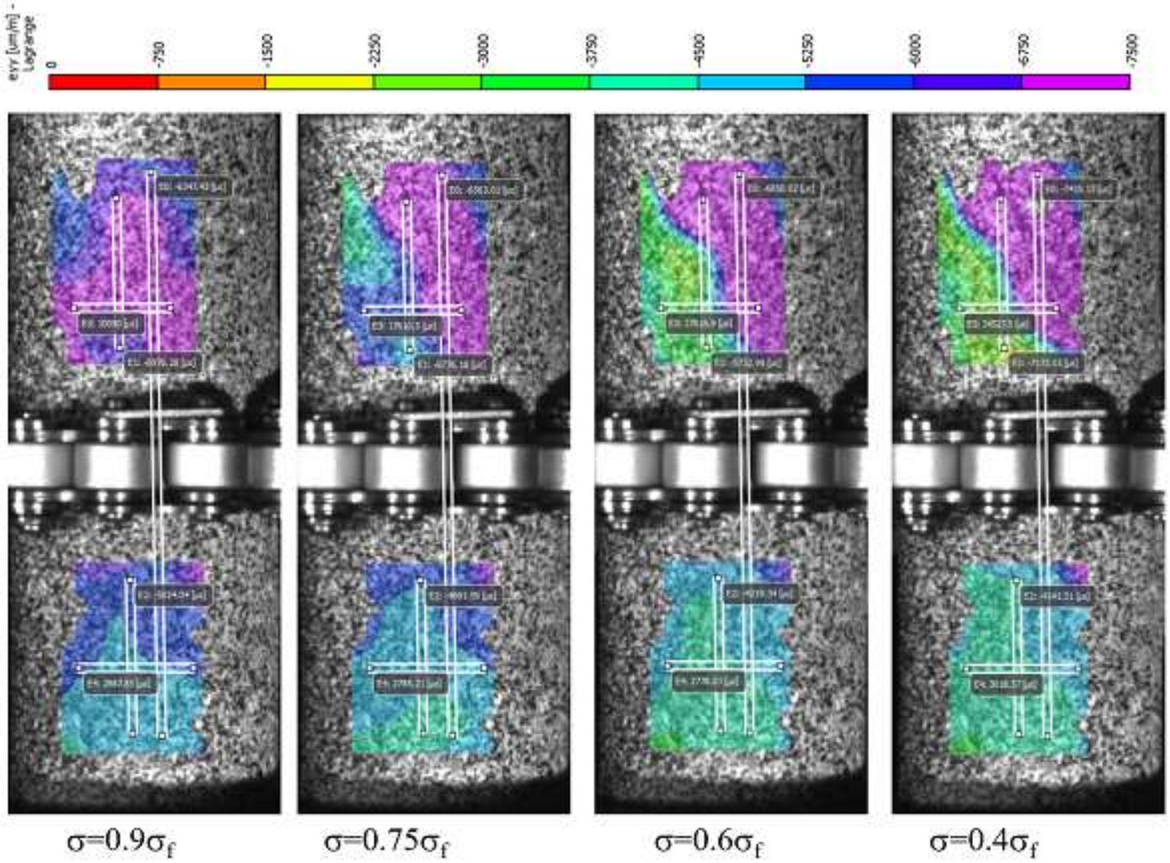

Figure 7. Field of axial strain developed in the post-peak regime for specimens: a) 63mm, b)30mm, and c)19mm.

5. CONCLUSIONS

Size effects on the mechanical properties, post-peak stress-strain behaviors, and field strain patterns were investigated under uniaxial compression. The lateral controlled method is adopted to capture the complete post-peak stress-strain relation of Hawkesbury sandstone. In addition, the three-dimensional digital image correlation (3D DIC) technique is used to examine the strain patterns and fracture characteristics. A series of tests were conducted on sandstone samples with a constant aspect ratio of 2.5 and different diameters. The following conclusions were drawn from this study:

1. The failure behavior of samples having different sizes is mainly a combination of class I and class II behavior.
2. By increasing the diameter of the rock sample, strain energy-based brittleness indices demonstrated that the rock exhibits more brittle behavior under uniaxial compression loading.
3. Rock in axial and lateral directions shows uniform deformation in the pre-peak regime, and strain localization occurs in the post-peak regime.
4. In general, the trend of the field of axial strain in the sample with different diameters was different. In the post-peak regime, localization around the shear bands occurs at 75% of peak strength for 63mm and 42mm samples and at 60% of peak strength for the 30mm specimen.19mm specimen did not show a clear shear band in 3D DIC measurements.

REFERENCES

Altindag, R. (2008). *Relationships between brittleness and specific energy in excavation mechanics*. International proceedings of 9th regional rock mechanics symposium, Izmir, Turkey, 437-451.

Bahaaddini, M., Hagan, P., Mitra, R. & Hebblewhite, B. (2014). Scale effect on the shear behaviour of rock joints based on a numerical study. *Engineering Geology*, 181, 212-223.

Bažant, Z.P., Barr, B., de Borst, R., Burtscher, S.L., Buyukozturk, O., Carol, I., Carpinteri, A., et al. (2004). Quasibrittle fracture scaling and size effect. *Materials and Structures*, 37, 547-568

Cheng, J.-L., Yang, S.-Q., Chen, K., Ma, D., Li, F.-Y. & Wang, L.-M. (2017). Uniaxial experimental study of the acoustic emission and deformation behavior of composite rock based on 3D digital image correlation (DIC). *Acta Mechanica Sinica*, 33, 999-1021.

Cunha, A.P. (1990). *Scale Effects in Rock Masses*: Proceedings of the First International Workshop on Scale Effects in Rock Masses, Loen, Norway, 7-8 June 1990. AA Balkema.

Darlington, W.J., Ranjith, P.G. & Choi, S. (2011). The effect of specimen size on strength and other properties in laboratory testing of rock and rock-like cementitious brittle materials. *Rock Mechanics and Rock Engineering*, 44, 513-529.

Fairhurst, C. & Hudson, J. (1999). Draft ISRM suggested method for the complete stress-strain curve for intact rock in uniaxial compression. *International Journal of Rock Mechanics and Mining Sciences*, 36, 279-289.

Hajiabdolmajid, V. & Kaiser, P. (2003). Brittleness of rock and stability assessment in hard rock tunneling. *Tunnelling and Underground Space Technology*, 18, 35-48.

Jackson, R. & Lau, J. (1990). *The effect of specimen size on the laboratory mechanical properties of the Lac du bonnet grey granite*. Procceeding of the first international workshop on scale effects in rock masses. Balkema (AA), 165-174.

Masoumi, H., Saydam, S. & Hagan, P.C. (2015). Unified size-effect law for intact rock. *International Journal of Geomechanics*, 16, 04015059.

Munoz, H. & Taheri, A. (2017). Specimen aspect ratio and progressive field strain development of sandstone under uniaxial compression by three-dimensional digital image correlation. *Journal of Rock Mechanics and Geotechnical Engineering*, 9, 599-610.

Munoz, H., Taheri, A. & Chanda, E. (2016a). Pre-peak and post-peak rock strain characteristics during uniaxial compression by 3D digital image correlation. *Rock Mechanics and Rock Engineering*, 49, 2541-2554.

Munoz, H., Taheri, A. & Chanda, E. (2016b). Fracture energy-based brittleness index evelopment and brittleness quantification by pre-peak strength parameters in rock uniaxial compression. *Rock Mechanics and Rock Engineering*, 49, 4587-4606.

Munoz, H., Taheri, A., Chanda, E. (2016c) Rock drilling performance evaluation by an energy dissipation based rock brittleness index. *Rock Mechanics and Rock Engineering*, 49: 3343–3355.

Pan, P.-Z., Feng, X.-T. & Hudson, J.A. (2009). Study of failure and scale effects in rocks under uniaxial compression using 3D cellular automata. *International Journal of Rock Mechanics and Mining Sciences*, 46, 674-685.

Pells, P. (2004). On the absence of size effects for substance strength of Hawkesbury Sandstone. *Australian Geomechanics*, 39, 79-83.

Shirani Faradonbeh, R. Taheri, A, Karakus M. (2021) Failure behaviour of a sandstone subjected to the systematic cyclic loading: Insights from the double-criteria damage-controlled test method. Rock Mechanics and Rock Engineering, 54, 5555–5575.

Sutton, M.A., Orteu, J.J. & Schreier, H. (2009). *Image correlation for shape, motion and deformation measurements: basic concepts, theory and applications*. Springer Science & Business Media.

Taheri, A., Zhang, Y., Munoz, H. (2020). Performance of rock crack stress thresholds determination criteria and investigating strength and confining pressure effects, *Construction and Building Materials*, 243, 118263.

Thuro, K., Plinninger, R., Zäh, S. & Schütz, S. (2001). *Scale effects in rock strength properties. Part 1: Unconfined compressive test and Brazilian test*. EUROCK 2001: Rock Mechanics-A Challenge for Society, 169-174.

Tung, S.-H., Weng, M.-C. & Shih, M.-H. (2013). Measuring the in situ deformation of retaining walls by the digital image correlation method. *Engineering Geology*, 166, 116-126,

Wawersik, W. & Fairhurst, C. (1970). A study of brittle rock fracture in laboratory compression experiments. *International Journal of Rock Mechanics and Mining Sciences & Geomechanics Abstracts*. 7, 561-564.

Yoshinaka, R., Osada, M., Park, H., Sasaki, T. & Sasaki, K. (2008). Practical determination of mechanical design parameters of intact rock considering scale effect. *Engineering Geology*, 96, 173-186.

Zhang, G., Xing, Y. & Wang, L. (2018). Comprehensive sandstone fracturing characterisation: Integration of fiber Bragg grating, digital imaging correlation and acoustic emission measurements. *Engineering Geology*, 246, 45-56,

Zhang, Q., Zhu, H., Zhang, L. & Ding, X. (2011). Study of scale effect on intact rock strength using particle flow modeling. *International Journal of Rock Mechanics and Mining Sciences*, 48, 1320-1328.

Zhou, X.-P., Wang, Y.-T., Zhang, J.-Z. & Liu, F.-N. (2019). Fracturing Behavior Study of Three-Flawed Specimens by Uniaxial Compression and 3D Digital Image Correlation: Sensitivity to Brittleness. *Rock Mechanics and Rock Engineering*, 52, 691-718.

Proceedings of the NROCK 2023
The IV Nordic Symposium on
Rock Mechanics and Rock Engineering
ISBN 978-9935-9436-2-0
DOI 10.33112/nrock2023.12

Full-scale pullout tests of rock anchors in limestone testing rock mass uplift failure

Bjarte Grindheim (Bjarte.grindheim@ntnu.no)

B. Grindheim, C. C. Li
Department of Geoscience and Petroleum, Norwegian University of Science and Technology (NTNU), Trondheim, Norway
A. H. Høien
Norwegian Public Roads Administration (NPRA), Bergen, Norway

ABSTRACT

Rock anchors is a high-capacity reinforcement measure used to stabilise large-scale infrastructure. In principle, they can fail in four ways: (1) rock mass uplift failure; (2) grout-rock interface failure; (3) tendon-grout interface failure; and (4) steel tendon tensile failure. Full-scale field uplift tests were performed in a limestone quarry. The tests were designed to test failure mode 1, rock mass uplift failure, aiming to estimate the uplift load-bearing capacity of the rock mass. The tests achieved a higher rock mass capacity than what was calculated with the "weight over overlying rock cone" method and using presumptive shear strength values along the assumed failure cone. The failure shape showed to be structurally dependent on the rock mass structure, and a uniform cone was not developed. Stress measurements showed an increase in the horizontal stress in the rock mass during the pulling of the anchor, which indicates the formation of a load arch in the rock mass. The results showed that the current design method is over conservative in a medium strong rock mass and there is a need for development in the design method for strong and unweathered rock masses.

KEYWORDS

Rock Anchor; rock mass failure; load bearing arch; failure surface; field test

INTRODUCTION

Rock anchors are high-capacity reinforcement measures used to support and stabilise large scale infrastructures (Hanna, 1982), such as dams, abutments of bridges, road cuts, slopes (Xanthakos, 1991), wind turbines (Yan et al., 2013; Shabanimashcool et al., 2018), and submerged structures (Mothersille and Littlejohn, 2012; Roesen and Trankjær, 2021). The forces from the structures are transferred to the competent ground through the rock anchors. The rock anchors transfer load through tension, the tensional load in the anchor is resisted by the shear strength of the surrounding ground (Hanna, 1982). The correct usage and design of rock anchors requires knowledge and understanding of their failure modes (Tayeh et al., 2019). Rock anchors can in principle fail in four ways, which are (1) rock mass uplift failure; (2) grout-rock bond or interface failure; (3) tendon-grout or interface failure; and (4) steel tendon tensile failure (Littlejohn and Bruce, 1977; Brown, 2015). The failure modes are illustrated in Figure 1. The weakest of the four failure modes determines the capacity of the anchoring system (Pease and Kulhawy, 1984; Kim and Cho, 2012).

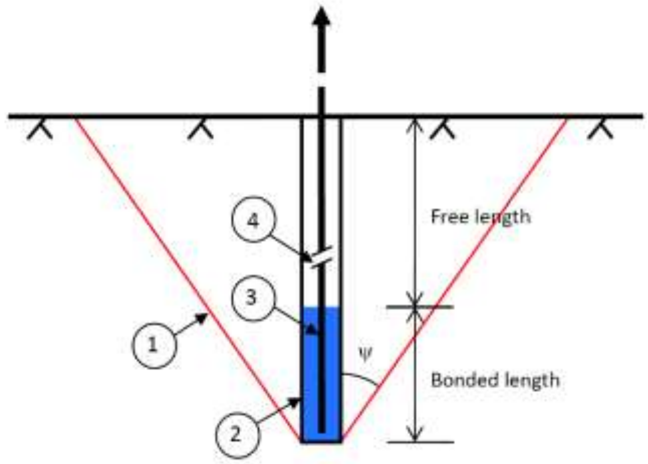

Figure 1. Four principal failure modes of a rock anchor from literature: (1) rock mass uplift failure; (2) grout-rock bond or interface failure; (3) tendon-grout bond or interface failure; and (4) steel tendon tensile failure.

The uplift capacity of the rock mass around a rock anchor is calculated based upon the dead weight of an inverted rock cone surrounding the anchor (Xanthakos, 1991) and/or the shear resistance of the rock mass along the cone with presumptive or back calculated shear strength values (Brown, 2015). The dead weight calculations alone are conservative as the shear and tensile strength of the rock mass is ignored (Xanthakos, 1991). Bruce (1976) showed that these estimations underestimated the rock mass capacity by one order of magnitude. There are very few documented cases of rock mass uplift failure (Xanthakos, 1991). The observed rock mass uplift failures in literature are from shallow anchoring depths (Brown, 2015), such as Bruce (1976), Ismael et al. (1979), Ismael (1982), Dados (1984), Weerasinghe and Littlejohn (1997), García-Wolfrum et al. (2007) and Thomas-Lepine (2012).

Brown (2015) listed several deficiencies with the current design method against failure mode 1. These deficiencies are mentioned in the following. The induced stresses in the overlying rock mass from the anchor is not considered. The effect of the anisotropy of the rock mass on the stresses and failure shape is not considered. The tests with rock mass uplift failure were done with shallow anchoring depths, which questions if this is representative for larger and longer anchors. The literature has shown how the rock mass structure affects the failure shape of shallow anchors, however for deeper anchors the rock mass structure might not be as controlling and the assumption of a 90º uplift cone might not be valid. The usage of presumptive and back calculated shear and tensile strength values based on a "theoretical" failure cone to calculate the rock mass capacity is questionable, as the variability of the strength parameters within the varying local rock mass structure is not considered as well as the progressive and complex nature of the rock mass failure. Bruce (1976) also questioned if rock mass failure occurs for anchors installed deeper than 2 m, since he only observed rock mass uplift failure in anchors installed at depths less than 2 m and the other failure modes occurred in the anchors installed deeper than 2 m.

Testing of full-scale rock anchors in real rock masses are important due to the uncertainties and deficiencies of the current design methods. The design method against rock mass uplift failure is considered as the least satisfactory and therefore it was investigated through full-scale uplift tests in a limestone quarry. The tests were highly instrumented to measure the stresses and localise the fracture plane. The novelty of the tests was to increase the understanding of the uplift failure of the rock mass through a thorough instrumentation scheme, which may be used to develop a more precise dimensioning method against rock mass uplift failure.

1. TEST ARRANGEMENT AND PROCEDURE

1.1. Test setup

The full-scale field tests were planned to investigate the uplift capacity of the rock mass surrounding rock anchors. Four anchors were installed in the limestone quarry of Verdalskalk AS in Tromsdalen, Norway. The anchors were 64 mm bar anchors with lengths 2.5 m and 3 m, the steel had a Young's modulus of 200 GPa and nominal tensile strength of 1000 MPa. They were installed with endplates in 140 mm boreholes. The anchoring depths of the anchors were 1 m and 1.5 m. On top of the anchors were a steel beam placed, the beam had a span of 3 m, which was decided based upon the anchoring depths and an apex angle of 90º from literature (Littlejohn and Bruce, 1977; Brown, 2015). A hydraulic jack was placed on top of the beam at the centre around the anchor before the test.

The test site was in a corner of an open pit quarry with a relatively flat surface and strong unweathered limestone. The rock mass was homogeneous with a uniaxial compressive strength (UCS) of 115 MPa, ranging from 106.7 to 121.4 MPa. Three joint sets were found and measured in the rock mass. All the joints were planar and rough. Close to the bench crest, there were signs of blast damage in the rock mass. Therefore, the holes were drilled with a minimum distance of 3 m to bench crest and a minimum spacing of 3 m in between the anchors. Around the two longest anchors, there were drilled holes with 102 mm diameter to a depth of 2.5 m for the instrumentation. All drilling was done pneumatically.

Concrete platforms had to be casted for the beam to be levelled on the surface. The formwork of the platforms was levelled by a leveller and then filled with rocks and grout. The grout was left to harden for four weeks until the tests. The anchors were lifted into the boreholes by an excavator and then grouted from the bottom and up with a water-cement ratio (W/C) of 0.42 with an average strength of 56.2 MPa after 28-days.

The instrumentation of the anchors varied in the tests. On all the anchors, the oil pressure was measured to calculate the anchor load and the vertical displacement of the anchor was measured by a thread extensometer (LVDT). The surface heaving of the rock mass was measured by six LVDTs fastened on an aluminium beam, which was placed under the steel beam, with the threads fastened to small bolts on the rock surface. The two longest anchors installed at 1.5 m depth, anchors A1.5m and B1.5m, were highly instrumented. There were installed load cells and extensometers in the rock mass around these anchors. Two observation holes at each anchor were drilled to map the jointing in the rock mass before and after the tests with acoustic and optic televiewer. Geophones were used to monitor the seismic signals from the rock mass when it fractured during the tests of the three anchors B1m, A1.5m and B1.5m. The P-wave velocity of the rock mass was estimated to be 2000 m/s.

1.2. Test procedure

The test arrangement of anchor A1.5m is shown in Figure 2. The beam was placed on two concrete platforms with the anchor in centre. A 3500-kN hydraulic jack was placed on top of the anchor and beam, the area in centre of the beam was fortified with a 5 cm thick steel plate. The hydraulic jack was pressurised from a gasoline driven hydraulic pump and a booster unit with capacity of 700 bar.

Figure 2. Test arrangement of anchor A1.5m. The steel beam is placed upon two concrete platforms with a hydraulic jack on top on the anchor. The LVDTs on the aluminium beam measured the surface heaving of the rock mass and the yellow geophones measured the microseismic activity during the test.

The load was applied on the anchors in two ways. The two shortest anchors, A1m and B1m, were loaded first in a continuous manner with a load rate from 5-7.5 kN/s until failure occurred. After failure, the displacement of the anchor was continued until the end of the jack stroke, and then the jack was repositioned, and the displacement was continued until the anchor load was low enough to be lifted by an excavator. The two longest anchors, A1.5m and B1.5m, were loaded stepwise and each load step was held for 5 minutes due to the borehole extensometer were only logged once every 5 minutes. The load steps had an average load rate of around 11.5 kN/s. The load in the system dropped if the pump was stopped, therefore the operator had to keep a little flow going to maintain the load at the desired level. All the pullout tests were performed in the period 15th and 16th June 2022.

After the tests were finished, the rock anchors were removed and the loose rocks around the location of the anchors were removed by an excavator. The failure surfaces were then cleaned and scanned with the lidar on an iPad.

2. RESULTS AND ANALYSIS

The test results are summarised in Table 1 for all the tests. The results from the test of anchor B1.5m is shown more in detail, but the results from the other tests were similar. The load and displacement curve of the anchor is shown in Figure 3. The load increased linearly in the beginning (i.e., elastic stage), then it started to bend (i.e., plastic stage) before reaching the peak load. After peak load, the load dropped gradually, the drops at 210 mm and 420 mm marks the end of the jack stroke. The rock mass surface heaving around anchor B1.5m is shown in Figure 4. The surface heaving of all the anchors was approximately 10% of the anchor displacement closest to the anchor until 200 mm displacement, then it increased to 15-20% of the anchor displacement for the remaining of the tests. The heaving decreased with distance from the anchor.

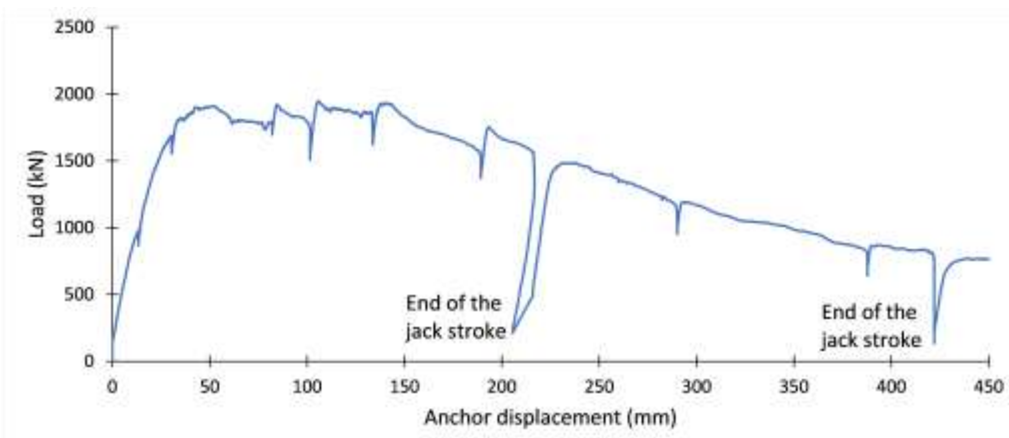

Figure 3. Load-vertical displacement curve of anchor B1.5m. The load drops at 210 mm and 420 mm displacement marks the end of the jack stroke.

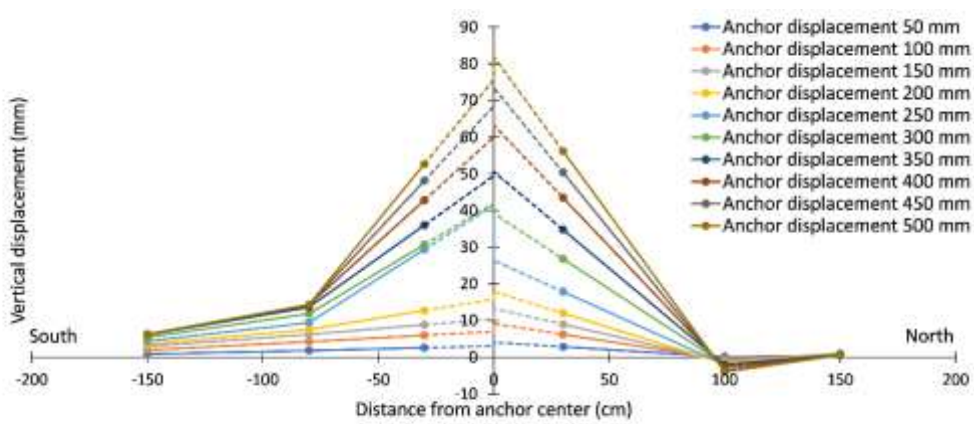

Figure 4. Rock mass surface heaving around anchor B1.5m at distance, where the dotted lines are extrapolations.

The horizontal stress and vertical displacement of the rock mass was measured around anchors A1.5m and B1.5m with load cells and borehole extensometers. These measurements for anchor B1.5m are presented in Figure 5. The horizontal stress in the rock mass increased in the elastic loading of the anchor and it became more unstable in the plastic and post peak stage of the loading, as seen in Figure 5(a) and Figure 5(b). The vertical displacement in the rock mass increased most in between 55-95 cm depth at 44 cm from the anchor (Figure 5(c)) and 45-85 cm at 103 cm from the anchor (Figure 5(d)).

The lidar scan of the failure surface combined with the location of the seismic events and profiles along the failure surface are shown in Figure 6. The seismic events are plotted in the north-east plane with all events on the surface, as depth measurements were unreliable since all the geophones were placed on the surface. The profile in the east-west direction was longer as two of the joint sets in the rock mass formed a wedge in that direction, the failure surfaces of all the tests had this asymmetrical shape with a wedge formed in that direction. The average apex angle was measured from the profiles (Figure 6(b)), for anchor B1.5m the apex angle was 132°. The results from all tests are summarised in Table 1.

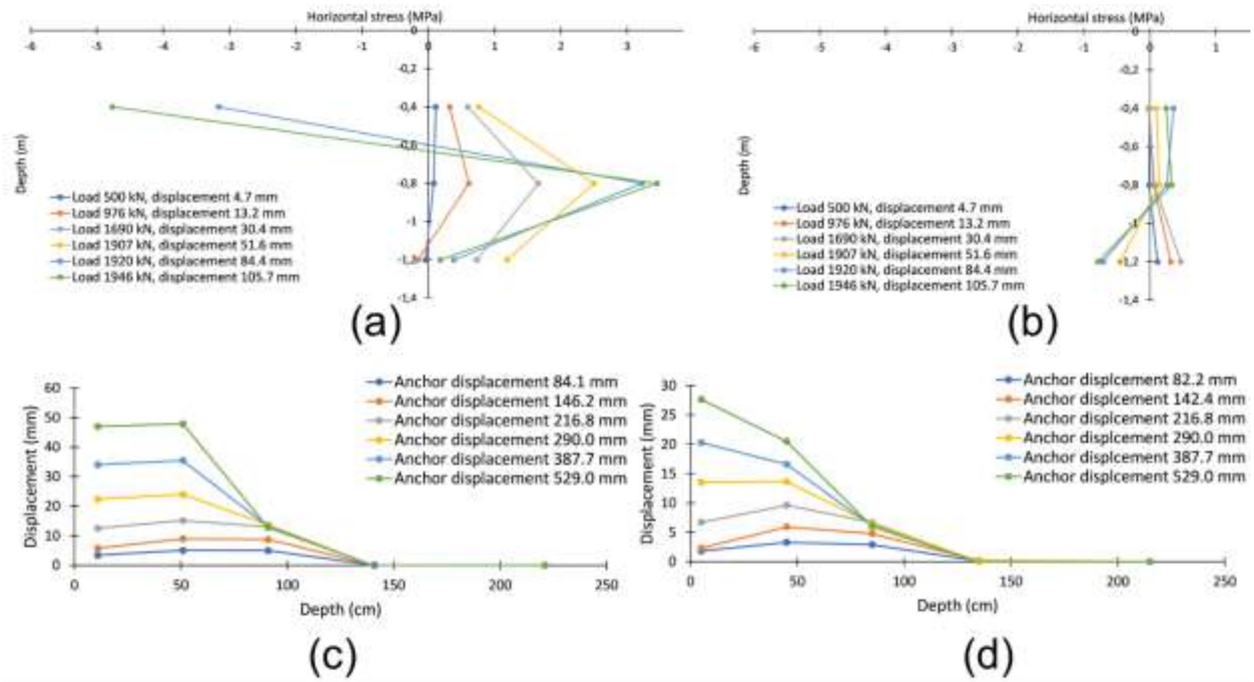

Figure 5. Horizontal stress measurements and borehole extensometer measurements around anchor B1.5m. (a) horizontal stress 41 cm west of the anchor; (b) horizontal stress 49 cm east of the anchor; (c) borehole extensometer measurements 44 cm southwest of the anchor; and (d) borehole extensometer measurement 103 cm southwest of anchor.

Table 1. Summary of test results from all tests.

Anchor no.	**A1m**	**B1m**	**A1.5m**	**B1.5m**
Bonded section (m)	0.9	0.9	1.4	1.4
Maximum uplift load (kN)	2461.6	2309.5	2422.6	1946.2
Anchor displacement at max load (mm)	66.7	59.6	71.8	105.7
Cone volume (m^3)	2.28	2.27	3.55	3.66
Apex angle (degrees)				
- *from extensometers*	-	-	105-170	105-170
- *from televiewer*	-	-	-	125
- *from profiles*	127	131	142	132

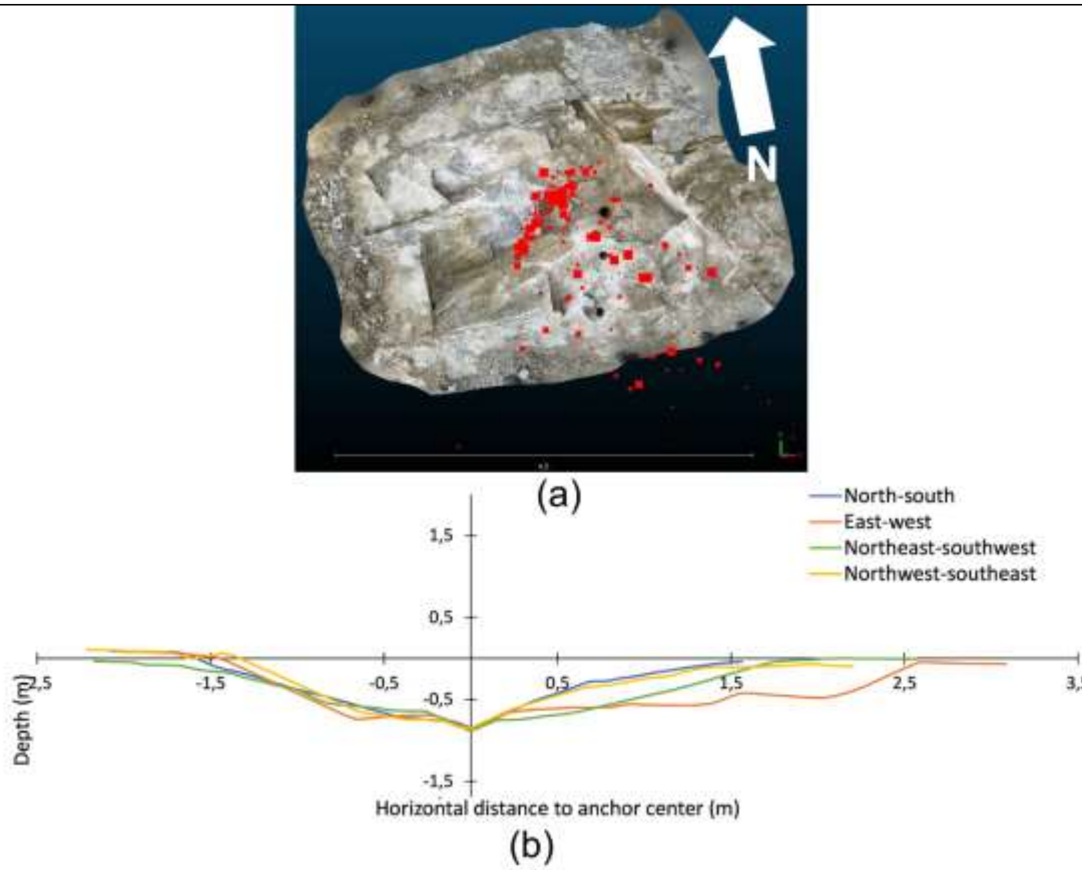

Figure 6. Lidar and seismic data: (a) Lidar scan of failure surface around anchor B1.5m with the location of the seismic events; (b) profiles of the failure surface. The relative size of the seismic events is shown by the size of the dots.

3. DISCUSSION

3.1. Failure shape and failure mode

In literature, the width and location of the apex angle varies, the location of the apex angle has been placed at the bottom or at the middle of the bonded section (Littlejohn and Bruce, 1977; Brown, 2015). These tests were designed with the assumption of a 90º apex angle placed at the bottom of the bonded section. Wyllie (1999) discussed the effect of joints on the shape of the failure cone, horizontal jointing would result in a wider apex angle while vertical jointing would result in a smaller apex angle. The measured apex angles in the four tests were ranging from 127-142º, which is greater than what is mentioned in most literature and standards. The commonly recommended apex angles to use are in between 60-90º, with 60º for weak rock masses and 90º for stronger rock masses. García-Wolfrum et al. (2007) showed on small intact rock samples that the apex angle is not constant, but smallest at the bottom and increasing towards the surface. The location of the apex angle in these tests varied in depth from 0.59-0.83 m below the surface, where non of them occurred at the bottom of the bonded section.

The failure mode seen in these tests was a combination of rock mass failure and bond failure between grout-rock. The deepest parts of the bonded length had interfacial bond failure between grout-rock. This was observed when the failure surface was cleaned, then the lowest part of the borehole was still intact in the rock mass as shown in Figure 7. Weerasinghe and Littlejohn (1997) also observed combination of rock mass failure and bond failure in weak mudstone. They suggested that the apex lies within the top 0.5 m of the fixed anchor, and that bond failure occurs below 0.5 m depth, which is a possible explanation for the observed failure in these tests since the depth of the failure was consistent between 0.59-0.83 m even though the bonded lengths varied between 0.9-1.4 m depth. Another explanation is due to the measured apex angles, since the angles were wider than what is shown in literature, then the area affected by the tests were wider than the length of the beam. This resulted in the beam confining the outer area of the affected rock mass, which increased the rock mass strength. Therefore, a combined failure occurred, with failure at the rock-grout interface in the lower part of the bonded section and in the rock mass in the upper part, as illustrated in Figure 8.

Figure 7. Intact borehole at the bottom of the failure crater after anchor B1.5m.

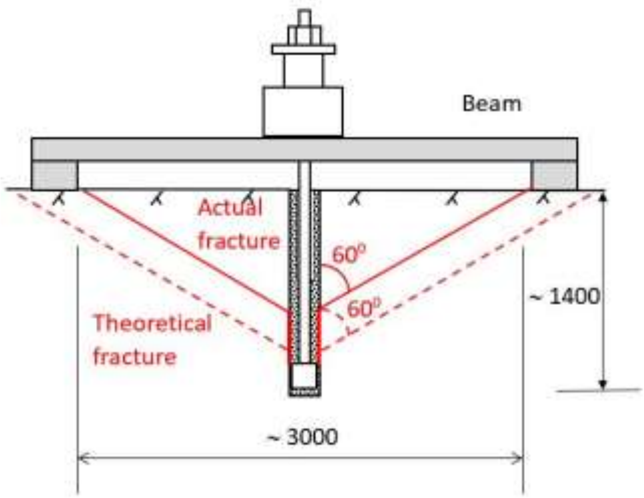

Figure 8. Possible failure shape of the anchors tested.

The failure mode of the rock mass is complex. The failure shape is also affected by the pre-existing joints in the rock mass. During the tests, it was obvious that the pre-existing joints opened first, as shown in Figure 9. From the seismic measurements in Figure 6, the most part of the failure crater has been developed along the pre-existing joints. There are no or only very small events in the west, northwest, and north side of the crater, which indicate that the intact rock has not fractured in these parts. The colour of the failure surface of these parts are also slightly miscoloured which indicate weathering, which means that these are pre-existing joints in the rock mass.

Figure 9. Surface cracking around anchor B1.5m after the test finished.

3.2. Load capacity of the rock mass

The anchor capacity of the tests was calculated based upon the design methods given by the Norwegian Public Roads Administration (NPRA, 2018) and from back calculation of historical data. The design methods given by NPRA, which uses the dead weight of the overlying rock and presumptive shear strength of the rock mass, resulted in very conservative design. The recommended cohesion for a rock mass with three joint sets and less than 20 joints per square meter was 50 kPa. The historical data came from tests in intact rock (García-Wolfrum et al., 2007), carboniferous strata (Bruce, 1976), a very weak shale (Littlejohn and Bruce, 1977), and granitic mass (Dados, 1984). The rock mass strength used in the calculation was based upon an average from the historical data rounded down to the closest half MPa. The rounding down of the rock mass strength was done due to lack of data and the scale difference between the tests of García-Wolfrum et al. (2007) and the test performed here. The estimated uplift capacity, sum of weight and max shear resistance, from NPRA (2018) was 166 kN and 403 kN for 0.9 m and 1.4 m depth, respectively, while the capacity was 1049 kN and 2388 kN from the back calculation with historical data. The uplift capacity estimations are summarised in Table 2.

Table 2. Anchor uplift capacity estimation based upon presumptive values from (NPRA, 2018) and back calculation from historical data.

Depth (m)	Apex angle (degrees)	Cohesion from back calculation (MPa)	Presumptive cohesion from NPRA (2018) (kPa)	Weight force (kN)	Max shear resistance from back calculation (kN)	Max shear resistance from NPRA (2018) design (kN)
0.9	90	0.5	50	20.2	1029	146
1.4	90	0.5	50	76.1	2312	327

The measured uplift capacity was much higher than the estimate with the recommended method from NPRA (2018). Therefore, it is important to understand the difference between the measured uplift capacity compared to the estimated uplift capacity with the current design methods from a rock mechanics perspective. The current design method is very simplified and conservative. The rock mass characteristics are not used in the design, the design method only uses the density of the rock to calculate the weight of overlying rock, and the number of joint sets to estimate the shear strength of the rock mass through a table of presumptive values given by NPRA (2018). The estimated capacity based upon historical data was closer to the achieved capacities, but they underestimated the capacity of the anchors with short, bonded section and slightly overestimated the capacity of the anchors with a longer bonded section. The back calculated cohesion from García-Wolfrum et al. (2007), Dados (1984), Littlejohn and Bruce (1977) and Bruce (1976) showed large variations depending on the rock types and rock masses. There are many assumptions involved with the back calculations, it was assumed that the failure surface was an inverted cone, that the cohesion was uniform in the rock mass, and an apex angle of 90º when nothing else has been stated. All calculations have been done from the bottom of the embedment depth. The back calculations indicated that the cohesion is greatly influenced by the rock type and joint density in the rock mass. Unfortunately, there are very few full-scale tests that reports of rock mass failure in anchor uplift tests, this was also seen and reported by Xanthakos (1991) which wrote "there is an impressive scarcity of data on anchor failure in rock mass, hence documentation of stability theories is not readily available". Due to this lack of data, the design methods against rock mass failure have been on the conservative side.

In Norway, the rock masses are mostly strong and unweathered. These rock masses have high load carrying capacities, which will result in underestimations of the load capacity with the current dimensioning method, as has been shown in these tests in a medium strong rock mass. Bruce (1976) concluded with that the uplift capacity was very sensitive to the degree of weathering, and much less sensitive to the rock mass structure. Since the design method is supposed to work for all rock masses, it is made to work in weathered rock masses which is why it is so conservative in unweathered rock masses. Therefore, there is a need to update or make a new design method for areas which have strong and unweathered rock masses. This could reduce the size of the anchors, which would be more environmentally friendly and more cost effective.

3.3. Stress distribution in the rock mass

The induced stresses in the rock mass have been questioned by Brown (2015). These tests show a slight increase in the horizontal stress around the anchor during the uplift tests before the peak load has been reached. The increase in horizontal stress is an indication that a load arch is formed in the rock mass during the pulling of the anchor. This has formerly only been shown in small scale laboratory tests with concrete blocks by Grindheim et al. (2022). The load arching in the rock mass contribute to increased rock mass capacity and therefore also making the current design method against rock mass uplift even more conservative.

4. CONCLUSIONS

Rock mass uplift tests has been performed in a limestone rock mass to investigate the rock mass uplift capacity and failure process. The rock mass capacity was much higher than what was calculated with presumptive values found in the recommended guideline in Norway. The estimations based upon back calculations from historical data was more accurate. The apex angle measured, 120-140º, was higher than the recommendation in literature, 60-90º. The horizontal stress in the rock mass increased during the tests, which indicates the formation of a load arch around the anchor as described in Grindheim et al. (2022).

These field tests shows that the current design method for rock mass uplift failure is very conservative and inaccurate for a medium strong rock mass. This has also been shown in literature earlier, but the method has not been updated due to very few documented cases of rock mass failure. In areas with medium strong or stronger rock masses, the rock mass capacity is much higher than the current design and results in over dimensioned anchors.

5. FURTHER RESEARCH

These field tests demonstrated how the rock mass fails around shallow anchors installed in a medium strong rock mass. The endplates of the anchors combined with the steel beam resulted in rock mass failure. The rock mass heaved close to the anchor with a distance less than 150 cm and the fracturing was greatest above the endplate at a depth of 60-80 cm at distances 40 cm to 100 cm from the anchor. The pre-existing joints in the rock mass affected the failure shape. In future research, it would be necessary to test anchors at increasing depths to see if or how the failure shape and mechanism changes with depth. Brown (2015) argued for that the joints in the rock mass would have less effect on the failure shape and mechanism at large depths. One could also argue that the rock mass is much stronger than the grout and steel so at a certain depth the grout or steel would always be the weakest part of the anchoring system, testing to find this depth level would be very useful for anchor design. Bruce (1976) saw that the rock mass in most cases was the strongest part of the anchoring system when installed at greater depths (>2 m).

6. ACKNOWLEDGEMENTS

The authors acknowledge the financial support of the Research Council of Norway through the research project ROCARC, project number 303448. The partners of the project are NTNU, SINTEF, NGI, The Arctic University of Norway (UiT), Norwegian Association of Rock Mechanics (NBG), Norwegian Public Roads Administration (NPRA), Multiconsult AS, Norconsult AS and NORSAR. The authors thank Simon Alexander Hagen in SINTEF and Jon Runar Drotninghaug for their enthusiastic participation in the field tests and Noralf Vedvik for his technical assistance in manufacturing. The authors are also grateful to Verdalkalk AS, especially Ørjan Sjöström, for the use of their quarry and all their help.

REFERENCES

Brown, E.T., 2015. Rock engineering design of post-tensioned anchors for dams - a review. Journal of Rock Mechanics and Geotechnical Engineering 7, 1–13. DOI: doi.org/10.1016/j.jrmge.2014.08.001.

Bruce, D.A., 1976. The Design and Performance of Prestressed Rock Anchors with Particular Reference to Load Transfer Mechanisms (As reproduced by ProQuest LLC 2014 (UMI U433767)). Ph.D. thesis. University of Aberdeen. Aberdeen, Scotland.

Dados, A.T., 1984. Design of anchors in horizontally jointed rocks. Journal of Geotechnical Engineering 110, 1637–1647. DOI: doi.org/10.1061/(ASCE)0733-9410(1984)110:11(1637).

Grindheim, B., Aasbø, K.S., Høien, A.H., Li, C.C., 2022. Small block model tests for the behaviour of a blocky rock mass under a concentrated rock anchor load. Geotechnical and Geological Engineering 40, 5813-5830. DOI: doi.org/10.1007/s10706-022-02251-1.

García-Wolfrum, S., Serrano, A., Olalla, C., 2007. Model failure tests on rock anchors, in: 11th Congress of the International Society for Rock Mechanics: The Second Half Century of Rock Mechanics, Taylor & Francis Group, Lisbon, Portugal. pp. 339–342.

Hanna, T.H., 1982. Foundations in Tension: Ground Anchors. Trans Tech Publications and McGraw-Hill Book Company, Clausthal, Germany.

Ismael, N.F., 1982. Design of shallow rock-anchored foundations. Canadian Geotechnical Journal 19, 463-471. DOI: doi.org/10.1139/t82-050.

Ismael, N.F., Radhakrishna, H.S., Klym, T.W., 1979. Uplift capacity of rock anchor groups. IEEE Transactions on Power Apparatus and Systems 98, 1653–1658. DOI: doi.org/10.1109/TPAS.1979.319483.

Kim, H.K., Cho, N.J., 2012. A design method to incur ductile failure of rock anchors subjected to tensile loads. Electronic Journal of Geotechnical Engineering 17, 2737–2746.

Littlejohn, G.S., Bruce, D.A., 1977. Rock anchors - state of the art. Foundation publications LTD., Brentwood, Essex, England.

Mothersille, D., Littlejohn, S., 2012. Grouting of anchors to resist hydrostatic uplift at Burnley tunnel, Melbourne, Australia, in: Proceedings of the Fourth International Conference on Grouting and Deep Mixing, American Society of Civil Engineers, New Orleans, Louisiana, USA. pp. 1073– 1084.

NPRA, 2018. Handbook V220 - Geotechnics in Road Construction (in Norwegian). Norwegian Public Roads Administration (Statens vegvesen), Oslo, Norway.

Pease, K.A., Kulhawy, F.H., 1984. Load Transfer Mechanisms in Rock Sockets and Anchors. Project 1493-1 EPRI EL-3777. Electric Power Research Institute. Ithaca, New York, USA.

Roesen, B.S., Trankjær, H., 2021. Permanent uplift anchors in Copenhagen limestone, in: IOP Conference Series: Earth and Environmental Science 710, IOP Publishing, Helsinki, Finland. p. 10.

Shabanimashcool, M., Olsson, R., Valstad, T., Lande, E.J., Berzins, A., Tuominen, K., Lapsins, J., 2018. Numerical modelling of anchored foundation for wind turbine generators, wtg (in Norwegian), in: Fjellsprengningsdagen - Bergmekanikkdagen - Geoteknikkdagen, NFF, NBG, NGF, Oslo, Norway. pp. 18.1–18.24.

Tayeh, B.A., El dada, Z.M., Shihada, S., Yusuf, M.O., 2019. Pull-out behavior of post installed rebar connections using chemical adhesives and cement based binders. Jorunal of King Saud University - Engineering Sciences 31, 332–339. DOI: doi.org/10.1016/j.jksues.2017.11.005.

Thomas-Lepine, C., 2012. Rock bolts - Improved design and possibilities. Master's thesis. Norwegian University of Science and Technology (NTNU). Trondheim, Norway.

Weerasinghe, R.B., Littlejohn, G.S., 1997. Uplift capacity of shallow anchorages in weak mudstone, in: Ground Anchorages and Anchored Structures: Proceedings of the International Conference, Thomas Telford Publishing, London, England. pp. 23–33.

Wyllie, D.C., 1999. Tension foundations. E & FN SPON, London and New York, England and USA. capter 9. pp. 310–359.

Xanthakos, P.P., 1991. Ground Anchors and Anchored Structures. Wiley Interscience, John Wiley & Sons, Inc., New York, USA.

Yan, S., Song, B.C., Sun, W., Yan, H., Yu, Q.L., 2013. Stress state analysis on a rock anchor rc foundation of wind driven generator, in: The 2013 World Congress on Advances on Structural Engineering and Mechanics, Daejeon Techno-Press, Jeju, Korea. pp. 2202–2213.

Proceedings of the NROCK 2023
The IV Nordic Symposium on
Rock Mechanics and Rock Engineering
ISBN 978-9935-9436-2-0
DOI 10.33112/nrock2023.13

Large-scale laboratory model tests simulating rock mass uplift failure

Bjarte Grindheim (bjarte.grindheim@ntnu.no)

B. Grindheim, C. C. Li
Department of Geoscience and Petroleum, Norwegian University of Science and Technology (NTNU), Trondheim, Norway
A. H. Høien
Norwegian Public Roads Administration (NPRA), Bergen, Norway

ABSTRACT

Rock anchors are high-capacity reinforcement measures used to stabilise large-scale infrastructure. There are four main failure mechanisms for rock anchors, which are: (1) rock mass uplift failure; (2) grout-rock interface failure; (3) tendon-grout interface failure; and (4) steel tendon tensile failure. A large-scale laboratory test rig has been developed to test block models which simulates rock mass uplift failure (failure mode 1). The design methods against failure mode 1 are the most conservative and least satisfactory design methods according to literature. The full-field displacements of the models were monitored with digital image correlation (DIC). The block model tests had higher capacities than what was calculated with the current design methods using the weight of overlying rock cone and presumptive shear strength values along the assumed failure cone. The capacity and failure shape in the block models showed to be structurally dependent on the block model pattern. The horizontal stress in the models increased during the tests, which showed that load arches were induced in the block models during the uplift. The load capacity of the block models increased with model height and horizontal stress level.

KEYWORDS

Block model, anchor pullout, load arching, failure mode, influence of joint pattern.

INTRODUCTION

Rock anchors has been used as load carrying elements for large-scale infrastructures since the first-time usage on Cheurfas dam in Algeria in 1934 (Merrifield et al., 2013). Later, the usage has been expanded to stabilisation of bridges (Schlotfeldt et al., 2013), wind turbines (Shabanimashcool et al., 2018), slopes (Choi et al., 2013), stadiums (Jordan, 2007), large statues (Koca et al., 2011), reinforcement of underground caverns (Aoki, 2007), and anchorage of submerged buildings (Roesen and Trankjær, 2021) and tunnels (Mothersille and Littlejohn, 2012). The loads from the structures are transferred to the stable rock ground by rock anchors. The anchor is loaded in tension, and it transfers the structural load to the stable rock through shear stresses along the two surfaces tendon-grout and grout-rock (Brown, 2015).

According to literature can a rock anchor fail in one of four principal ways (Littlejohn and Bruce, 1977; Brown, 2015). These are (1) rock mass uplift failure, (2) grout-rock interface failure, (3) tendon-grout interface failure, and (4) tensile failure of the anchor steel. The failure modes are showed in Figure 1. The capacity of an anchor is equal to the failure mode with the lowest capacity (Brown, 2015). The capacity of the failure modes 2-4 are calculated for individual anchors, while for failure mode 1 the interaction between adjacent anchors must be considered if they are installed in close vicinity (Brown, 2015).

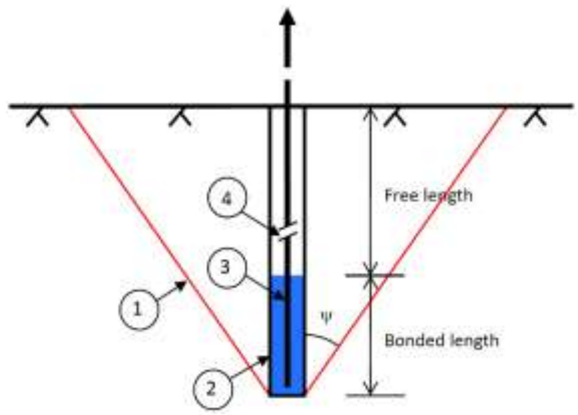

Figure 1. Grouted rock anchors can in principle fail in four ways: (1) rock mass uplift failure; (2) grout-rock bond or interface failure; (3) tendon-grout bond or interface failure; and (4) steel tendon tensile failure.

Brown (2015) carried out a thorough review on the design of rock anchors. In the review, it was concluded that the design against failure mode 1, failure of the rock mass from uplift, was based upon simplified assumptions on the stress distribution and volume of rock mass influenced, which has resulted in a design method that is excessively conservative and represents poor engineering practice. To make a precise design of rock anchors, it is required to understand the mechanisms and interaction between the anchor and the rock mass (Showkati et al., 2015). To improve the design of rock anchors, there is a need to increase knowledge on the stress distribution and failure mechanisms of the rock mass around rock anchors.

The failure mechanisms of rock anchors have been investigated formerly in the laboratory to some extent. Failure mode 3 has been well tested in the laboratory, for example by Barley (1997), Kim and Lee (2005), Ivanovic and Neilson (2008) and Akisanya and Ivanovic (2014). For the more uncertain failure modes 1 and 2 testing have not been performed to the same degree in the laboratory. The mentioned Barley (1997) also tested failure mode 2 as well and failure mode 1 has been tested on intact rock blocks by García-Wolfrum et al. (2007) with anchors of small dimension (up to 10 cm length), which showed that the failure surface was not conical but expanding towards the surface. Dados (1984) and Grindheim et al. (2022) tested failure mode 1 on block models with aluminium and concrete blocks, respectively. The tests by Dados (1984) showed that the blocks close to the anchor bulged upward and the vertical joints tended to open when the anchor was pulled upward. Grindheim et al. (2022) showed that load arches are induced in each layer of a laminar block model when pushed upward, which increased the block model capacity compared to the estimated anchor capacity with the current design methods.

The ground rock mass contains fractures, geological discontinuities and foliation that may function as weakness planes. These discontinuities divide the rock into blocks of various sizes. In such blocky rock masses, the failure often occurs along the geological structures (Grindheim et al., 2022). Grindheim et al. (2022) demonstrated that load-arching is induced in a blocky and laminar block model under a concentrated load, which enhanced the capacity of the block model. These tests only tested one type of block pattern with continuous horizontal joints and discontinuous vertical joints. It is therefore important to investigate how the load is transferred from an anchor to blocky rock masses with varying block patterns as well as the load capacity of the different block patterns.

This paper is a continuation of the work by Grindheim et al. (2022). The paper investigates the deformation behaviour of blocks set in different patterns and the failure mode of the patterns through laboratory pull tests on a specially designed test rig. The effect changes in the block pattern and stress conditions have on the arching effect and model capacity will also be investigated. All tests were monitored by digital image correlation (DIC) to get the full field displacements in the models.

1. TEST ARRANGEMENT AND PROCEDURE

1.1. Test setups

A specially developed laboratory rig was built to test the load distribution and failure pattern of several block models with varying joint patterns, the test setups are shown in Figure 2. The test rig consisted of a steel frame with inner dimensions of 223 × 153 × 30 cm (width × height × depth). Inside the steel frame, there is 10 hydraulic cylinders fastened on the left inner vertical wall and 16 hydraulic cylinders fastened on the top horizontal wall, which can provide horizontal and vertical stress, respectively. The hydraulic cylinders have a capacity of 142 kN each, 10 cm stroke and there are fastened 3 cm thick steel plates on ball mounts towards the test material. At the bottom centre of the frame, there are fastened two large pistons with a steel block of 10 × 10 × 25 cm (width × height × depth) in between, which represents a rock anchor. The steel block will from now on be termed anchor. The pistons around the anchor have a capacity of 225 kN each, which results in an anchor capacity of 450 kN. The working area inside the hydraulic cylinders in the frame is 190 × 120 × 30 cm. Inside the working area, the block material is placed which represents a rock mass. The hydraulic system is servo controlled. The movements of the blocks in the model are monitored by digital image correlation (DIC) technology with two cameras. The hydraulic pressure is monitored on the horizontal hydraulic cylinders and the anchor pistons which is used to calculate the horizontal stress and anchor force. The displacement of the anchor pistons is measured by thread extensometers, which also is used for anchor displacement control.

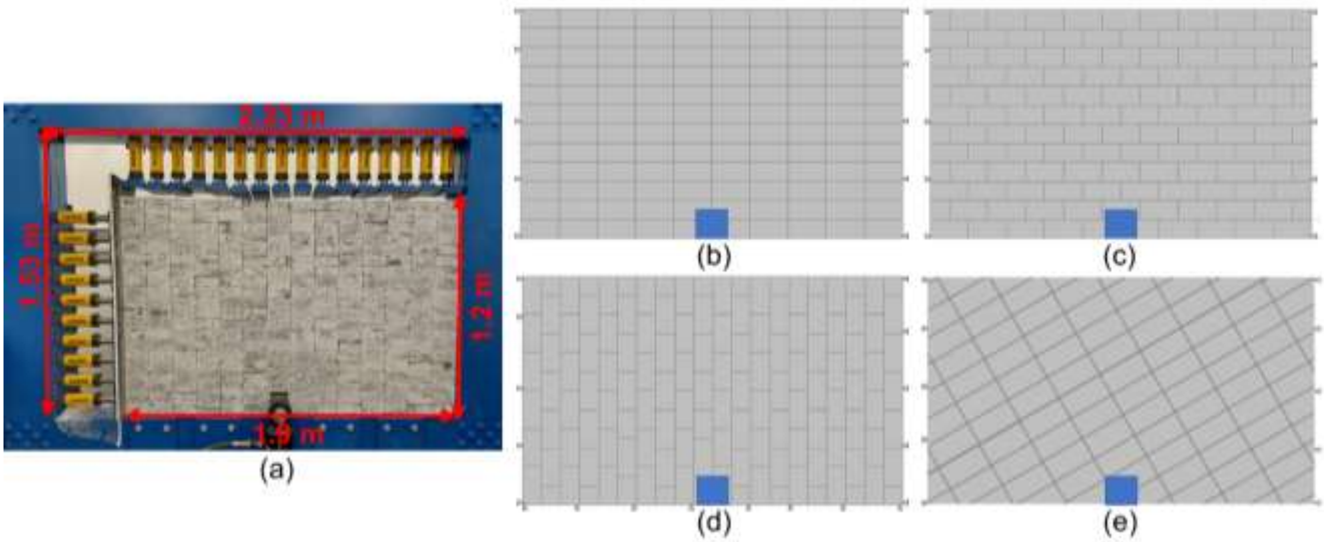

Figure 2. (a) Test setup of the laboratory tests with concrete blocks within the steel frame, the concrete blocks were placed in different patterns as sketched: (b) block pattern 1 - continuous horizontal and vertical joints, (c) block pattern 2 - continuous horizontal and discontinuous vertical joints, (d) block pattern 3 - discontinuous horizontal and continuous vertical joints, and (e) block pattern 4 - 25° tilt on the horizontal and vertical joints.

Monitoring of the tests with DIC cameras required preparation of the blocks. A speckle pattern had to be applied to the blocks on the side facing the cameras. First the blocks were painted white, then the speckle pattern was applied which was non-repetitive 50/50 black and white with high contrast. The size of the speckles should be at least 3-4 pixels to avoid aliasing (Correlated Solutions, 2020). The cameras were placed in line with the outer edges of the concrete blocks at such a distance that the whole model was visible in both cameras, which resulted in an angle of 25.5° in between them. The cameras were set to take 5 images per second in the tests not run to failure and 10 images per second in the failure tests. The images of the tests were analysed with the software Vic-3D (Correlated Solutions, 2020) after the tests. The software calculated the displacements and strains in the models from changes in the speckle pattern by taking reference in an image from the beginning of the test.

The material used in the tests were 27 × 6 × 20 cm concrete pavement blocks. The pavement blocks were cut into smaller blocks of dimensions of 13 × 6 × 19 cm and 6.5 × 6 × 19 cm. Small errors occurred during the cutting of the blocks, which resulted in that not all the layers were in contact with the horizontal hydraulic cylinders. Therefore, to ensure contact between all the layers and the horizontal hydraulic cylinders, cement mortar was casted on the side to fill all the gaps. The cement mortar had a water-cement ratio (W/C) of 0.28.

The material properties of the concrete pavement blocks were found by drilling cores out of the blocks and test them under uniaxial compression as described in Bieniawski and Bernede (1979). The Young's modulus (E) and

Poisson's ratio (v) was calculated from the measured axial and radial strains. The average uniaxial compressive strength (UCS) was measured to 43 MPa, the Young's modulus 23 GPa, and Poisson's ratio 0.22. The density of the concrete was 2272 kg/m^3. The wooden plate was a formwork board with bending strength 58.6 MPa in the longest direction and 42.6 in the shortest direction.

The creation of block pattern 4 with tilted layers, Figure 2(d), required getting the tilt angle correct on the bottom of the frame. The diamond cutters used to cut the concrete blocks at the laboratory were not precise enough to get the right angle from the beginning. Therefore, the first layer in the tilted model were made from wood since the saw was more precise and easier to work with.

1.2. Test procedure

Multiple tests of the four block patterns (Figure 2) have been done in the test rig. On each of the block patterns, the wall height, vertical stress, and confinement has been varied. All the tests followed the same procedure, which is shown step by step here:

1. The blocks were placed in the frame with the wanted block pattern and height.
2. The left side of the model was evened out with cementitious grout and a wooden plate, the grout was left to harden for a week.
3. The wanted horizontal stress was applied to the blocks from the horizontal cylinders and then the valves were closed, to keep the model from deforming horizontally.
4. A vertical stress was applied to the blocks from the vertical cylinders if a height higher than 1.2 m were to be simulated. The valves were left open to keep the stress constant and let the model deform vertically.
5. If the tests were not run to failure a displacement limit of 25 mm was set on the system.
6. The DIC capturing was started.
7. The blocks were then loaded with a displacement rate of 0.5 mm/s with a force limit. The force limit was increased with 10 kN increments if the movement stopped. For the tests not run to failure, the test was stopped if a force of 50 kN was reached and the movement stopped, or the displacement reached the limit of 25 mm. The failure tests were run to the end of the stroke of the pistons.
8. The anchor was then unloaded slowly.
9. The DIC capturing was stopped.
10. The confining stresses were then removed.

2. RESULTS AND ANALYSIS

A total of 80 tests has been done in the testing rig. These tests have been done on the four block patterns shown in Figure 2. On each block pattern 20 tests without failure were done, except for block pattern 4 where only 16 tests were done, the results from these tests are presented in Tables 1-4. The last test on each block pattern was a failure test.

The test results from block pattern 1 with continuous joints horizontally and vertically are shown in Table 1. The tests shows that the load capacity of the block model is lowest when the height and horizontal stress are at a minimum. The block model capacity increased with increasing wall height and increasing horizontal stress.

Table 1. Results from the non-failure tests of block pattern 1. The colours indicate which tests was stopped by displacement (yellow) and load (green).

		Height (m)				
		0.6	0.9	1.2	4	8
Horizontal stress (MPa)	0	Load 11.7 kN Disp. 25.2 mm	Load 16.1 kN Disp. 25.1 mm	Load 27.1 kN Disp. 25.1 mm	Load 45.1 kN Disp. 25.1 mm	Load 47.8 kN Disp. 18.5 mm
	0.1	Load 14.9 kN Disp. 25.1 mm	Load 19.6 kN Disp. 25.1 mm	Load 33.3 kN Disp. 25.1 mm	Load 44.4 kN Disp. 25.1 mm	Load 47.0 kN Disp. 12.5 mm
	0.5	Load 20.4 kN Disp. 25.1 mm	Load 31.7 kN Disp. 25.1 mm	Load 46.3 kN Disp. 18.5 mm	Load 46.1 kN Disp. 13.3 mm	Load 48.9 kN Disp. 10.0 mm
	1	Load 23.6 kN Disp. 25.0 mm	Load 38.7 kN Disp. 25.2 mm	Load 46.0 kN Disp. 11.2 mm	Load 48.9 kN Disp. 9.6 mm	Load 49.0 kN Disp. 8.9 mm

The results from the tests on block pattern 2 with continuous horizontal joints and discontinuous vertical joints are shown in Table 2. The tests show similar results as for block pattern 1, that the load capacity of the block model is lowest when the height and horizontal stress are at a minimum. The block model capacity increased with increasing wall height and increasing horizontal stress.

Table 2. Results from the non-failure tests of block pattern 2. The colours indicate which tests was stopped by displacement (yellow) and load (green).

		Height (m)				
		0.6	0.9	1.2	4	8
Horizontal stress (MPa)	0	Load 14.1 kN Disp. 25.2 mm	Load 18.9 kN Disp. 25.1 mm	Load 16.3 kN Disp. 25.3 mm	Load 38.9 kN Disp. 25.2 mm	Load 43.0 kN Disp. 6.8 mm
	0.1	Load 15.3 kN Disp. 25.0 mm	Load 20.5 kN Disp. 25.3 mm	Load 26.7 kN Disp. 25.1 mm	Load 43.1 kN Disp. 25.1 mm	Load 47.4 kN Disp. 5.8 mm
	0.5	Load 20.3 kN Disp. 25.1 mm	Load 31.4 kN Disp. 25.1 mm	Load 44.7 kN Disp. 23.1 mm	Load 45.5 kN Disp. 11.7 mm	Load 47.8 kN Disp. 5.0 mm
	1	Load 23.4 kN Disp. 25.1 mm	Load 40.4 kN Disp. 25.1 mm	Load 44.3 kN Disp. 12.6 mm	Load 45.5 kN Disp. 8.1 mm	Load 49.9 kN Disp. 4.9 mm

Table 3 shows the results from the tests on block pattern 3 with discontinuous horizontal joints and continuous vertical joints. The tests show similar results as for the first two block patterns, that the load capacity of the block model is lowest when the height and horizontal stress are at a minimum. The block model capacity increased slightly with increasing wall height. The load capacity of block pattern 3 were much more sensitive to the increase in horizontal stress and the load capacity increased considerably with increasing horizontal stress.

Table 3. Results from the non-failure tests of block pattern 3. The colours indicate which tests was stopped by displacement (yellow) and load (green).

		Height (m)				
		0.6	0.9	1.2	4	8
Horizontal stress (MPa)	0	Load 12.9 kN Disp. 25.2 mm	Load 13.0 kN Disp. 25.3 mm	Load 15.0 kN Disp. 25.4 mm	Load 22.7 kN Disp. 25.2 mm	Load 29.6 kN Disp. 25.1 mm
	0.1	Load 21.3 kN Disp. 25.2 mm	Load 39.4 kN Disp. 25.3 mm	Load 40.8 kN Disp. 25.1 mm	Load 46.2 kN Disp. 25.1 mm	Load 42.6 kN Disp. 25.2 mm
	0.5	Load 39.7 kN Disp. 25.2 mm	Load 47.0 kN Disp. 3.6 mm	Load 50.2 kN Disp. 4.6 mm	Load 49.2 kN Disp. 2.6 mm	Load 47.6 kN Disp. 3.0 mm
	1	Load 47.8 kN Disp. 5.3 mm	Load 46.0 kN Disp. 1.1 mm	Load 48.1 kN Disp. 1.3 mm	Load 46.7 kN Disp. 1.5 mm	Load 48.1 kN Disp. 1.3 mm

The final block pattern tested was block pattern 4 with a tilt angle of 25°. The results from this block pattern are shown in Table 4. The tests show similar results as for the other block patterns, that the load capacity of the block model is lowest when the height and horizontal stress are at a minimum. The block model capacity increased slightly with increasing horizontal stress, the test with the lowest heights collapsed with the high horizontal stress and they could therefore not be done. The load capacity of block pattern 4 were much more sensitive to the increase in wall height and the load capacity increased considerably with increasing wall height.

Table 4. Results from non-failure tests of block pattern 4. The colours indicate which tests was stopped by displacement (yellow) and load (green).

		Height (m)				
		0.6	0.9	1.2	4	8
Horizontal stress (MPa)	0	Load 14.1 kN Disp. 25.5 mm	Load 16.6 kN Disp. 25.1 mm	Load 21.1 kN Disp. 25.1 mm	Load 45.2 kN Disp. 14.3 mm	Load 45.5 kN Disp. 3.9 mm
	0.1	Load 14.0 kN Disp. 25.3 mm	Load 15.3 kN Disp. 25.2 mm	Load 24.1 kN Disp. 25.1 mm	Load 45.4 kN Disp. 12.2 mm	Load 46.3 kN Disp. 3.5 mm
	0.5	-	-	Load 36.0 kN Disp. 25.1 mm	Load 46.4 kN Disp. 6.5 mm	Load 47.4 kN Disp. 2.5 mm
	1	-	-	Load 46.3 kN Disp. 18.7 mm	Load 46.6 kN Disp. 7.5 mm	Load 45.5 kN Disp. 2.0 mm

The displacement patterns of the different block models from the DIC measurements are shown in Figures 3-6. These are shown at the maximum displacement for the same loading condition for each block pattern. The loading condition is height 1.2 m and horizontal stress 1 MPa. For block pattern 1, a loading condition of height 1.2 m and horizontal stress 0.1 MPa is included to show the effect of the horizontal stress. The increase in horizontal stress reduced the vertical displacement towards the top of the block model for block patterns 1-3. While the increased horizontal stress led to a concentrated vertical displacement along or normal to the joints for the tilted block pattern 4 (Figure 6).

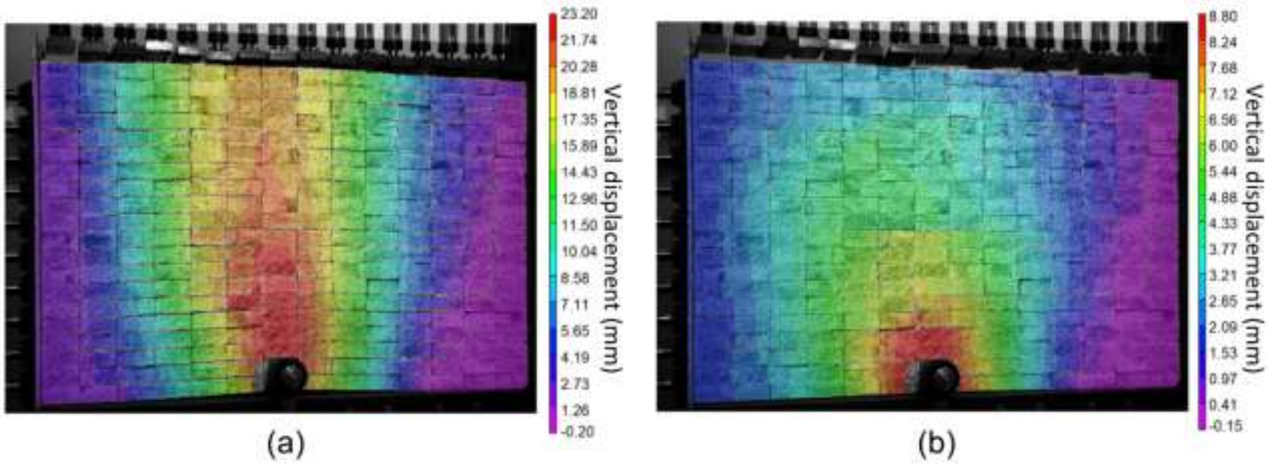

Figure 3. Vertical displacement pattern of two tests of block pattern 1: (a) height 1.2 m, horizontal stress 0.1 MPa; and (b) height 1.2 m, horizontal stress 1 MPa.

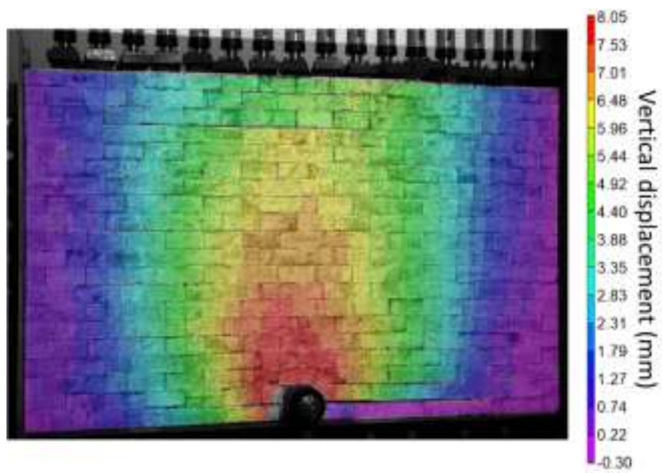

Figure 4. Vertical displacement pattern of block pattern 2 with height 1.2 m and horizontal stress 1 MPa.

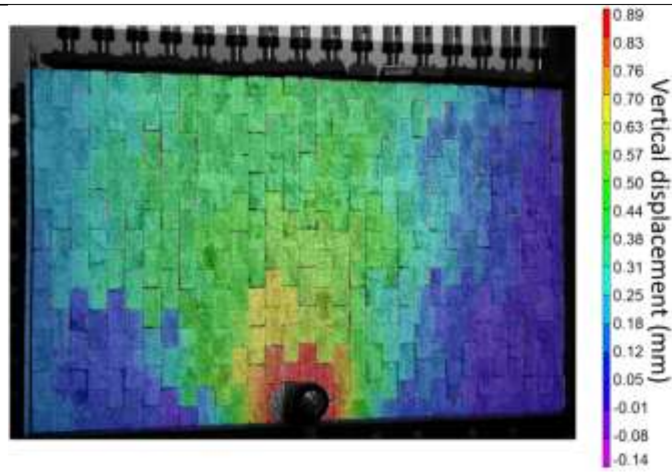

Figure 5. Vertical displacement pattern of block pattern 3 with height 1.2 m and horizontal stress 1 MPa.

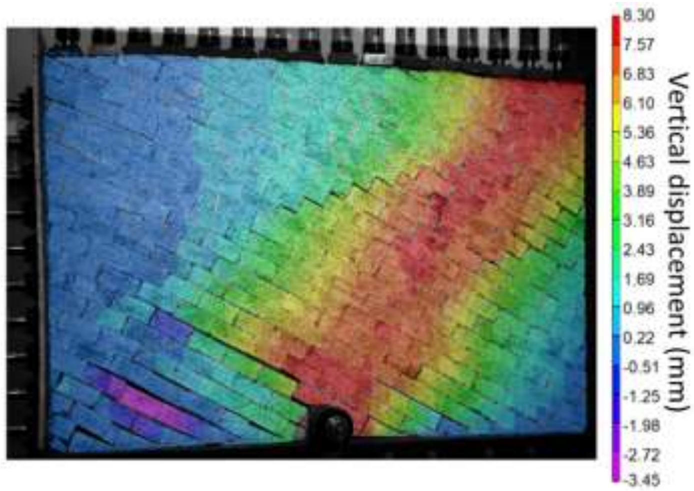

Figure 6. Vertical displacement pattern of block pattern 4 with height 1.2 m and horizontal stress 1 MPa.

Figure 7 shows the horizontal stress against time for the tests with 1.2 m height and 0.1 MPa applied horizontal stress. The plots show a slight decrease in the horizontal stress at the beginning after the cylinders were closed at the wanted stress level, this is likely due to some small leakages of oil in the cylinders. When load is applied to the anchor, the horizontal stress increases above the applied stress level in the models with block patterns 1-3 while it decreases in the model with block pattern 4. The increase in horizontal stress is highest for block patterns 1 and 2, these reached the same level of 0.31 MPa. The increase in horizontal stress in the models indicate that load arches are formed in the block models as described by Grindheim et al. (2022). The load arches increase the horizontal stress by 2-3 times. In the model with tilted blocks, the horizontal stress decreased when anchor load was applied.

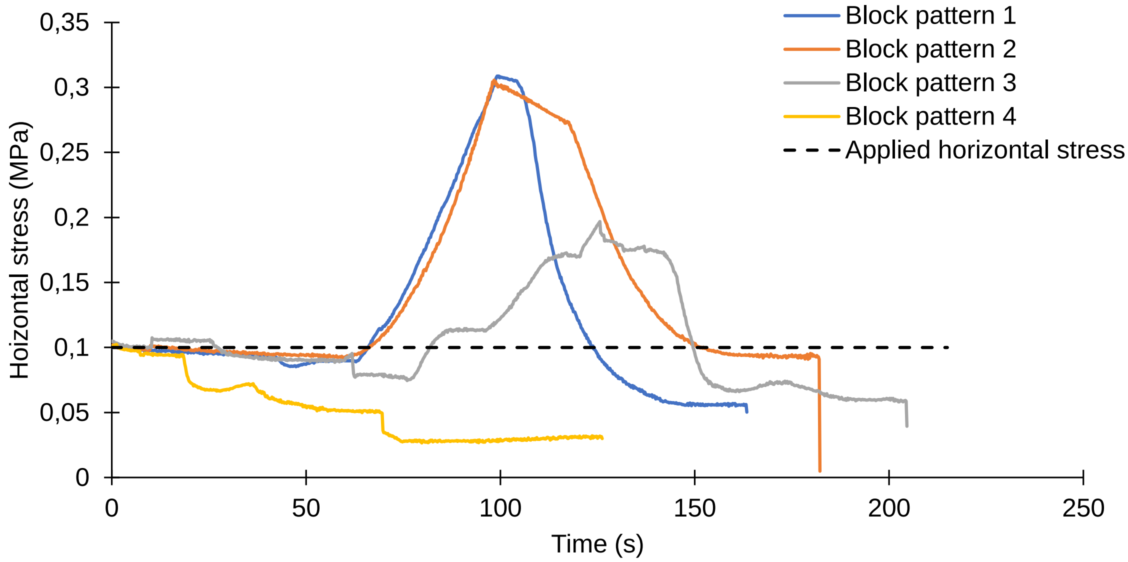

Figure 7. The average horizontal stress from the tests with 1.2 m height and 0.1 MPa applied horizontal stress of all the block patterns. The dashed line shows the applied horizontal stress at the beginning of the tests.

The block patterns were run to complete failure in the last test for each of them, the failures are shown in Figure 8. The failure tests were run with block model heights of 0.9m and horizontal stress of 0.5 MPa, for block model 4 the horizontal stress was reduced to 0.1 MPa since this block pattern gave in with a horizontal stress of 0.5 MPa. All the tests failed as an inverted cone and the fracturing followed the block patterns in all the failure tests. The apex angle of the failure cones varied from 90° -140°. The maximum load capacity of each of the block patterns were 29.71 kN for block pattern 1, 33.92 kN for block pattern 2, 75.15 kN for block pattern 3, and 19.35 kN for block pattern 4.

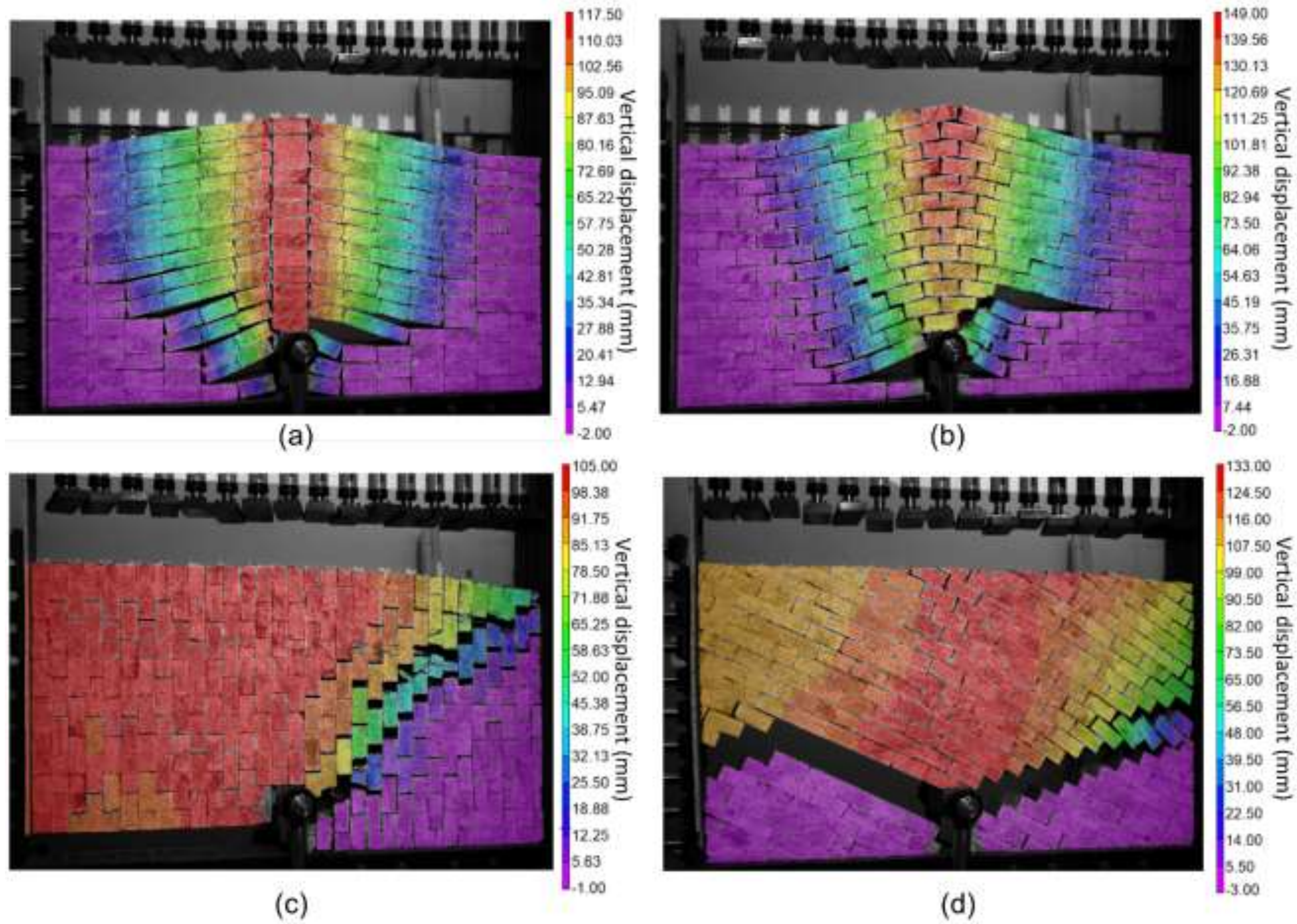

Figure 8. Failure of (a) block pattern 1 with an apex angle of 120°, (b) block pattern 2 with an apex angle of 100°, (c) block pattern 3 with an apex angle of 90°, and (d) block pattern 4 with an apex angle of 140°.

3. DISCUSSION

The laboratory tests aimed to develop a better understanding of how joint patterns in a rock mass affects the uplift failure around a rock anchor, failure mode 1 in Figure 1, through block models. The tests showed that the joint patterns had a visible effect on the vertical displacement in the block models with the same boundary conditions, shown in Figures 3-6. The displacement in the block models were greatest in the directions parallel or normal to the joints, which became evident with tilted pattern in Figure 6. The in-situ stresses also influenced the rock mass displacements, see Tables 1-4. In block pattern 3 the anchor capacity decreased with increasing vertical stress when the horizontal stress was low (see 4 and 8 m depth in Table 3) but not zero. The joint patterns also affected the failure shape. The failures followed the joints in the block model (Figure 8), and therefore the apex angles are also dependent on the joints.

The tests looked at the effect of in-situ stresses on the rock mass capacity by changing the boundary conditions on the block models, which is summarised in Tables 1-4. In general, the block model capacity increased with increasing wall height or increasing horizontal stress. For the individual joint patterns, the effect of the height and confinement varied. The capacity of the block models increased the most if the stresses normal to the longest axis of the blocks were increased. This can be transferred to in-situ rock masses, the rock mass capacity is high if the stresses in the rock mass are high and normal to the joint set with the shortest spacing, and the rock mass capacity is low when the stresses in the rock mass are low. In the failure tests, it was evident that block model 3 with the blocks oriented normal to the horizontal stress had the highest capacity.

The block model capacity of the failure tests was estimated with the current design method with the weight of overlying rock (Brown, 2015) and with a shear strength of 100 kPa along a failure surface with an apex angle of

80° from presumptive values given in NPRA (2018) for a rock mass with two joint sets. These gave a block model capacity of 3.8 kN and 26.2 kN for the weight force and presumptive shear strength, respectively, for a block model of height 0.9 m. The weight force is conservative by one order of magnitude from the measured capacities at the end of section 3. The presumptive shear strength is close to the measured capacities of block patterns 1, 2 and 4, while it is only one third of the capacity measured for block pattern 3.

A small-scale block model by Grindheim et al. (2015) showed that load arches are induced in a block model with continuous horizontal and discontinuous vertical joints. Figure 7 shows the horizontal stress development in the tests with 1.2 m height and 0.1 MPa applied horizontal stress. The horizontal stress increased in block models 1-3, which indicates that load arches were formed. The plots demonstrate that the joint patterns influence the development of load arches in the block model. Load arches are formed in the block models with horizontal and vertical joints, while for the block model with tilted joints there is no increase in horizontal stress, which indicate that no load arch is induced. This indicate that an unfavourable joint pattern in a rock mass may lead to no load arch being formed. It also possible that the load arch was formed in this model between the vertical cylinders and the right wall of the frame, but this was not captured as there were no stress measurement on the individual vertical cylinders and on the right wall.

In literature, the apex angle of the failure cone is assumed to be 60-90° depending on the rock mass strength (Littlejohn and Bruce, 1977; Brown, 2015). The apex angle is assumed to be 60° in weak rock masses and 90° in strong rock masses. The failure tests of the block patterns here had apex angles ranging from 90-140°, which is mostly higher than in literature. It was also the test with the highest capacity that had the smallest apex angle, block pattern 3. These tests indicate that the size of the apex angle is dependent on the joint pattern and not the rock mass strength, and that the failure cone follows the joints, as seen in Figure 8.

4. CONCLUSIONS

A total of 80 two-dimensional block model tests were carried out in the laboratory to investigate load arching, the load capacity, and failure of different rock masses. The tests showed increased horizontal stress (i.e., load arching) in the tests with horizontal and vertical joints, while it decreased in the test with a 25° tilt of the joints. The vertical displacement in the block models was greatest in the direction normal to or parallel to the joint sets. The load capacity of the block models increased with both increasing horizontal stress and increasing wall height (corresponding to an increase in depth). The joint patterns affected the load capacity of the models. The failure shape was affected by the joint patterns, the failure surface followed the joint pattern in all the failure tests. The apex angle of the inverted cone was larger than in literature for most of the tests and it was dependent on the joint patterns rather than the rock mass strength.

5. FURTHER RESEARCH

These tests described and discussed here have only used one kind of blocks. In the future, it is necessary to test blocks of different sizes and materials to see how they affect the capacity, deformations, and stresses in the block models. The results should also be transferred to real scenarios, which can be done through numerical models calibrated on these test results. The numerical models can also be used to test the effect of different materials through sensitivity analysis.

6. ACKNOWLEDGEMENTS

The authors acknowledge the financial support of the Research Council of Norway through the research project ROCARC, project number 303448. The partners of the project are NTNU, Norwegian Association of Rock Mechanics (NBG), SINTEF, NGI, The Arctic University of Norway (UiT), Norwegian Public Roads Administration (NPRA), Multiconsult AS, Norconsult AS and NORSAR. The authors thank Gunnar Vistnes, Jon Runar Drotninghaug, Noralf Vedvik, and Torkjell Breivik for their technical assistance in manufacturing and Brage Angell for his participation in the tests.

REFERENCES

Akisanya, A.R., Ivanovic, A., 2014. Debonding along the fixed anchor length of a ground anchorage. Engineering Structures 74, 23–31. DOI: doi.org/10.1016/j.engstruct.2014.05.013.

Aoki, K., 2007. Design and construction of large rock caverns supported by ground anchorages, in: Ground Anchorages and Anchored Structures in Service, Proceedings of the International Conference, Thomas Telford Publishing, London, England. pp. 188–198.

Barley, A.D., 1997. Properties of anchor grouts in a confined state, in: Ground Anchorages and Anchored Structures: Proceedings of the International Conference, Thomas Telford Publishing, London, England. pp. 371–383.

Bieniawski, Z., Bernede, M., 1979. Suggested methods for determining the uniaxial compressive strength and deformability of rock materials. International Journal of Rock Mechanics and Mining Sciences & Geomechanics Abstracts 16, 137–140. DOI: doi.org/10.1016/0148-9062(79)91451-7.

Brown, E.T., 2015. Rock engineering design of post-tensioned anchors for dams - a review. Journal of Rock Mechanics and Geotechnical Engineering 7, 1–13. DOI: doi.org/10.1016/j.jrmge.2014.08.001.

Choi, S.W., Lee, J., Kim, J.M., Park, H.S., 2013. Design and application of a field sensing system for ground anchors in slopes. Sensors 13, 3739–3752. DOI: doi.org/10.3390/s130303739.

Correlated Solutions, 2020. Vic-3D v7 Testing Guide. Correlated Solutions.

Dados, A.T., 1984. Design of anchors in horizontally jointed rocks. Journal of Geotechnical Engineering 110, 1637–1647. DOI: doi.org/10.1061/(ASCE)0733-9410(1984)110:11(1637).

García-Wolfrum, S., Serrano, A., Olalla, C., 2007. Model failure tests on rock anchors, in: 11th Congress of the International Society for Rock Mechanics: The Second Half Century of Rock Mechanics, Taylor & Francis Group, Lisbon, Portugal. pp. 339–342.

Grindheim, B., Aasbø, K.S., Høien, A.H., Li, C.C., 2022. Small block model tests for the behaviour of a blocky rock mass under a concentrated rock anchor load. Geotechnical and Geological Engineering 40, 5813-5830. DOI: doi.org/10.1007/s10706-022-02251-1.

Ivanovic, A., Neilson, R.D., 2008. Modelling of debonding along the fixed anchor length. International Journal of Rock Mechanics & Mining Sciences 46, 699–707. DOI: doi.org/10.1016/j.ijrmms.2008.09.008.

Jordan, L., 2007. Monitoring of multi-strand ground anchors at the City of Manchester Stadium, in: Ground Anchorages and Anchored Structures in Service, Proceedings of the International Conference, Thomas Telford Publishing, London, England. pp. 99–110.

Kim, D.H., Lee, S.R., 2005. Uplift capacity of fixed shallow anchors subjected to vertical loading in rock. International Journal of Offshore and Polar Engineering 15, 312–320.

Koca, M.Y., Kincal, C., Arslan, A.T., Yilmaz, H.R., 2011. Anchor application in Karatepe andesite rock slope, Izmir - Türkiye. International Journal of Rock Mechanics & Mining Sciences 48, 245–258. DOI: doi.org/10.1016/j.ijrmms.2010.11.006.

Littlejohn, G.S., Bruce, D.A., 1977. Rock anchors - state of the art. Foundation publications LTD., Brentwood, Essex, England.

Merrifield, C., Møller, O., Simpson, B., Farrell, E., 2013. European practice in ground anchor design related to the framework of EC7, in: Proceedings of the 18th International conference on soil mechanics and geotechnical engineering: challenges and innovations in geotechnics, Paris: Presses des Ponts, Paris, France. pp. 1835–1838.

Mothersille, D., Littlejohn, S., 2012. Grouting of anchors to resist hydrostatic uplift at Burnley tunnel, Melbourne, Australia, in: Proceedings of the Fourth International Conference on Grouting and Deep Mixing, American Society of Civil Engineers, New Orleans, Louisiana, USA. pp. 1073– 1084.

NPRA, 2018. Handbook V220 – Geotechnics in road construction (in Norwegian). Norwegian Public Roads Administration (Statens vegvesen), Oslo, Norway.

Roesen, B.S., Trankjær, H., 2021. Permanent uplift anchors in Copenhagen limestone, in: IOP Conference Series: Earth and Environmental Science 710, IOP Publishing, Helsinki, Finland. p. 10.

Schlotfeldt, P., Panton, B., Humphries, R., Elmo, D., 2013. New Park Bridge, Kicking Horse Canyon; pier 5 - a difficult foundation on rock, in: 47th US Rock Mechanics/ Geomechanics Symposium, American Rock Mechanics Association, San Francisco, California, USA. p. 8.

Shabanimashcool, M., Olsson, R., Valstad, T., Lande, E.J., Berzins, A., Tuominen, K., Lapsins, J., 2018. Numerical modelling of anchored foundation for wind turbine generators, WTG (in Norwegian), in: Fjellsprengningsdagen - Bergmekanikkdagen - Geoteknikkdagen, NFF, NBG, NGF, Oslo, Norway. pp. 18.1–18.24.

Showkati, A., Maarefvand, P., Hassani, H., 2015. Stress induced by posttensioned anchor in jointed rock mass. Journal of Central South University 22, 1463–1476. DOI: doi.org/10.1007/s11771-015-2664-x.

Proceedings of the NROCK 2023
The IV Nordic Symposium on
Rock Mechanics and Rock Engineering
ISBN 978-9935-9436-2-0
DOI 10.33112/nrock2023.14

Analysis of water ingress, grouting effort and pore pressure reduction caused by hard rock tunnels

Kristin H. Holmøy, (Kristin.holmoy@ntnu.no)
Department of Geoscience and petroleum / NTNU, Trondheim, Norway

ABSTRACT

Norwegian ground conditions with hard bedrock underlying soft, marine clay deposits are challenging with respect to the risk of settlements caused by water ingress to tunnels. Settlements in clay-filled depressions and damage to nearby buildings are one of the main risks associated with future upgrading of infrastructure. This paper presents a database and findings from 44 tunnels in the Oslo-region, excavated between 1975 and 2020. One of the main findings is that few of the tunnels in the database meet the strict leakage limits necessary to avoid settlements for future tunnel projects. Previously, water ingress of typically 3-7 l/min/100 m has been allowed to limit pore pressure reduction to 10-30 kPa (1-3 m water head), limiting settlements and building damage. In areas where the pore pressures already have been affected by water ingress to an existing tunnel, any additional leakage and pore pressure decrease due to a new tunnel will cause additional settlements. Previous reduction in pore pressure results in an even stricter water ingress limits for new tunnels. Hence, water control through improved pre-excavation grouting (PEG) techniques and better monitoring of pore pressure development during excavation is needed. To ensure necessary data-collection for future research it is important to increase the quality of collected data.

KEYWORDS

Urban tunnelling; Water ingress; Pore pressure; Settlements; Pre-excavation grouting.

1. INTRODUCTION

Norwegian ground conditions with soft marine clay deposits overlying hard bedrock are challenging with respect to risk of groundwater leakage to rock tunnels and deep excavations, which can cause severe settlements. Even small water inflow can cause considerable pore pressure reduction at bedrock level in the confined aquifers between the bedrock and soft clay. This will initiate a consolidation process in the clay, which can cause large settlements damaging overlying structures, buildings, and infrastructure. The problem is illustrated in Figure 1, showing water ingress to a bedrock tunnel, causing pore pressure reduction in a water bearing layer of sand and gravel at the bedrock surface, Δu. With time pore pressures, u, in the clay layer are affected, resulting in settlements.

This paper presents and discuss monitoring data from 44 tunnels constructed over 45 years in Norway, mainly in the Oslo region. The original database from Karlsrud et al. (2003) contained 29 tunnels, recently 15 tunnels were added, mostly from tunnels constructed after 2000. An overview of the complete database was published in 2022 (Langford et al., 2022). Main findings from analyses of this database will be discussed and presented.

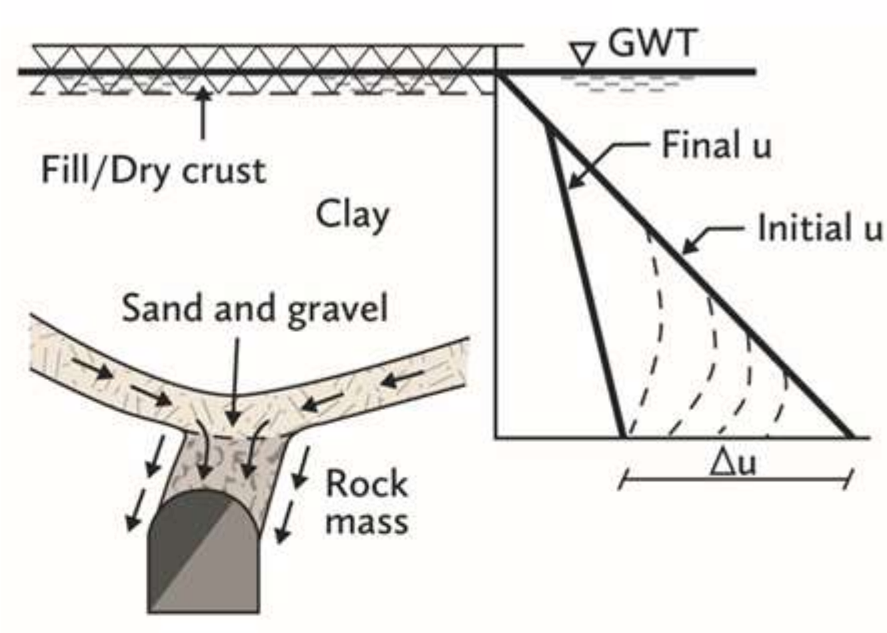

Figure 1 Illustration of water ingress to a bedrock tunnel causing pore pressure reduction in a water-bearing layer over the bedrock (revised from Karlsrud et al. 2003)

An increasing growth of population in the cities will require an increased need for upgrading of infrastructures, such as road-, railway-, and subway tunnels. These projects will pose challenges in avoiding consequences related to water inflow. In addition to underground rock tunnels, deep excavations will be necessary at stations and tunnel openings. The new tunnels will be built in areas already influenced by existing tunnels, where current drainage has caused settlements and thereby increased the risk associated with new projects. These conditions will result in even stricter requirements on inflow limits to avoid damage, which in turn will require improved performance pre-excavation grouting (PEG) procedures.

Pregrouting was the focus in the Norwegian research programmes “Tunnels for the citizens” (Lindstrøm and Kveen, 2005), and True Improvement in Grouting High pressure for Tunnelling (TIGHT). The latter project was completed in 2018 and had main goal to increase the understanding of rock mass grouting (Strømsvik, 2019). Another, R&D program, " REMEDY / BegrensSkade" has the aim to reduce the risk of damage to neighbouring buildings and structures caused by deep excavation and foundation works. In the projects, one of the main causes of damage is reported to be leakage to deep excavations, resulting in pore pressure reduction and settlements in soft clay (REMEDY, 2015). This fits well, since recent and ongoing projects also report difficulties with avoiding settlements and damage to nearby buildings.

2. TYPICAL ROCK AND SOIL CONDITIONS IN THE OSLO REGION, AND SENSITIVITY TO PORE PRESSURE REDUCTION

The geological conditions in the Oslo region consist of bedrock dating from the Precambrian, Cambro-Silurian, and Carboniferous and Permian periods. A graben structure was created by the Caledonian folding and Permian block faulting, resulting in the following main rock types:

- · Igneous rocks (including both plutonic and volcanic) – Carboniferous and Permian
- · Shale and limestone (sedimentary rocks) - Cambro-Silurian
- · Gneiss – Precambrian

A bedrock map of the Oslo region together with approximate locations of tunnels included in a big analysis presented in Langford et al. (2022) are shown in Figure 2. In the following sections analyses and main results will be presented.

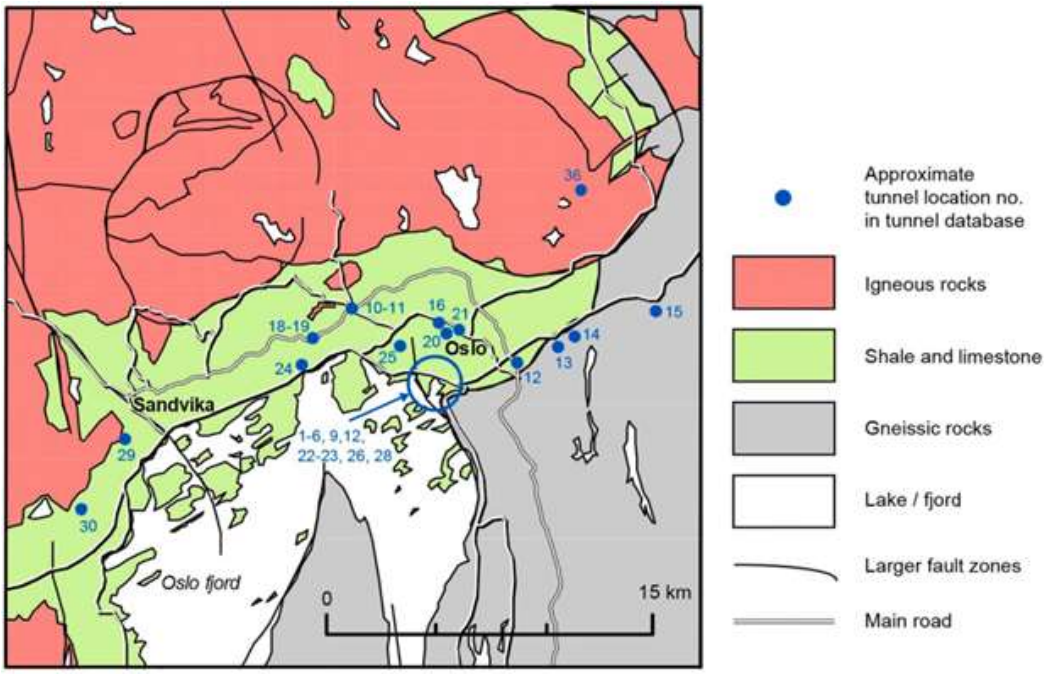

Figure 2 Location of the tunnels in the Oslo region in the database. Bedrock map modified from Bjørlykke (2004) and Langford et al. (2022).

The lower-lying areas of the city centre and nearby regions consist mainly of Cambro-Silurian sedimentary rocks such as shale and limestone. Igneous dikes (mostly syenite-porphyry and diabase) are common in these formations with thicknesses ranging from around half a meter to 50 m. The main igneous rocks in the Oslo region are syenite/monzonite, granite, and rhombus porphyry, which makes up the hills and ridges to the north and west of the city centre. Precambrian gneissic rocks dominate the areas south and southeast of the city centre.

Research has shown that igneous rocks are often more brittle and tend to have more open channels along the joints compared to other rock types (Klüver, 2000). As an example, in the Oslo region it has been documented that syenite (plutonic) and Permian dikes, such as syenite porphyry and diabase, have higher hydraulic conductivity than other rock types (Holmøy, 2008; and Lindstrøm & Kveen, 2005).

The soil deposits above the bedrock typically consist of soft marine clays (0–80 m thick) deposited at the end of the last glaciation, about 10,000 years ago. These clays have not been subjected to loads greater than the present overburden stress and are normally consolidated (Bjerrum, 1967), with an apparent over-consolidation ratio (OCR, the ratio between the pre-consolidation stress and the in-situ effective overburden stress) of 1.2–1.4 due to ageing (Bjerrum, 1973). Commonly there is a layer of glacial moraine between the bedrock surface and overlying marine clay. This layer exhibits significantly higher hydraulic conductivity than the clay deposit, and hence represents a permeable aquifer which extends along the bedrock surface. Pore pressure levels in such confined aquifers are sensitive to changes in water infiltration and extraction, such as water ingress to tunnels.

To illustrate the nature of time-dependant settlements, Figure 3 shows an example of calculated pore pressure reduction of 100 kPa at bedrock are performed using the Janbu modulus concept (Janbu, 1970), widely used in the Nordic countries to calculate consolidation settlements in clay (Andresen & Jostad, 2004). As the OCR is close to 1, minor changes in effective stresses, i.e., reduction in pore pressure, will cause significant consolidation settlements. The hydraulic conductivity of the clay is set to 5·10-10 m/s. The pore pressure reduction in the clay deposit is calculated for different time intervals. The low hydraulic conductivity of the clay layer results in a long consolidation process. From Figure *3* it is apparent that the pore pressures need to be monitored at the bedrock surface to detect any effects of water ingress to tunnels. In the example it will take more than 6 months for pore pressures at 10 m depth to be affected.

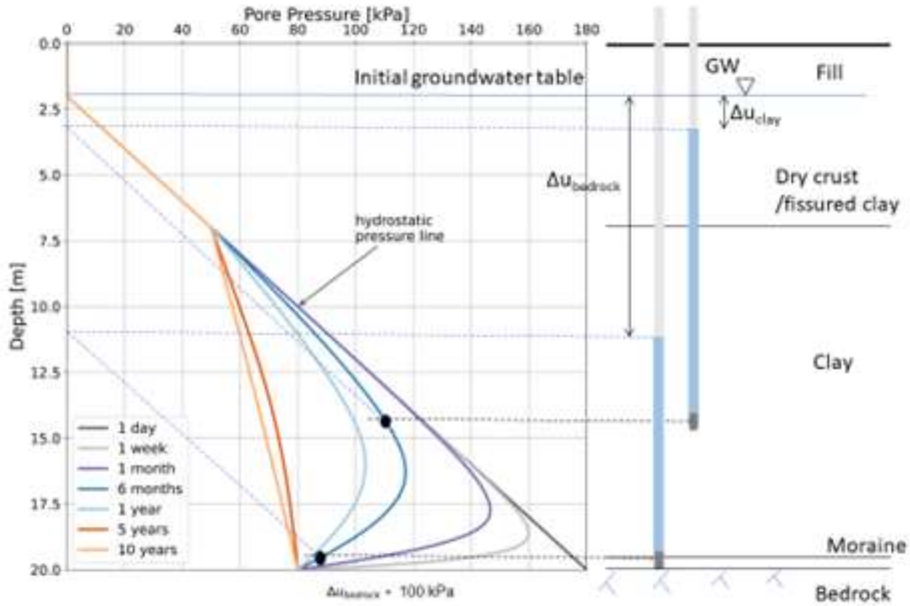

Figure 3 Example of calculated pore pressure profiles with time in a clay profile (Langford et al. 2022)

3. DATABASE

Data from 44 tunnel projects, mostly in the Oslo region, constructed between 1975 and 2020 have been collected (Langford et al., 2022). For some projects, data has been monitored in several sections along the tunnel, in other projects data has been monitored over the total tunnel length. In total, the database contains monitoring data from 56 sections. All tunnels have been excavated using drill and blast excavation technique. All sections have strict limits on water ingress, which has required extensive PEG. The locations of the tunnels in the Oslo region are shown in Figure 2, together with the three main bedrock types. The extent and quality of geological mapping varies across projects. In some cases, jointing, rock type and weakness- or fault zones were not described in detail. Hence, focus has been on assessing the data with respect to the main rock types in the Oslo region.

The data has been provided by the clients and consultants involved in the planning and execution of the projects. The extent of the monitoring and quality of the monitoring varies between projects. Since the data is collected from completed projects, it has not been possible to influence the extent of monitoring. The data collected is considered representative of the Norwegian state of-practice for monitoring of tunnelling projects in urban areas.

4. ANALYSES

Pore pressure reduction at bedrock level has been recorded in 14 tunnel projects. Figure 4 presents the measured decrease in pore pressure, in relation to horizontal distance from the tunnel centre. In many projects pore pressure reduction has been observed up to several hundred of metres from the tunnel centreline, typically up to 400 m. This large spatial influence is due to hydrogeological conditions with a confined aquifer over bedrock, which is sensitive to drainage. In the right-hand side of the figure the data is systemized with respect to the main bedrock type for the tunnels. There is no indication of a correlation between the magnitude of pore pressure reduction and bedrock type. One likely explanation for this is that the pore pressure response is primarily governed by the hydrogeological conditions of the confined aquifer underneath the clay, such as the orientation, areal extent, hydraulic conductivity and natural groundwater recharge. The scatter in data can also be explained by varying amounts of water ingress to the tunnels, as well as duration of the leakage to the tunnels with respect to time of monitoring. Despite the scatter, the data clearly highlight the potential for large reductions in pore pressure at significant distances from the tunnel centre line.

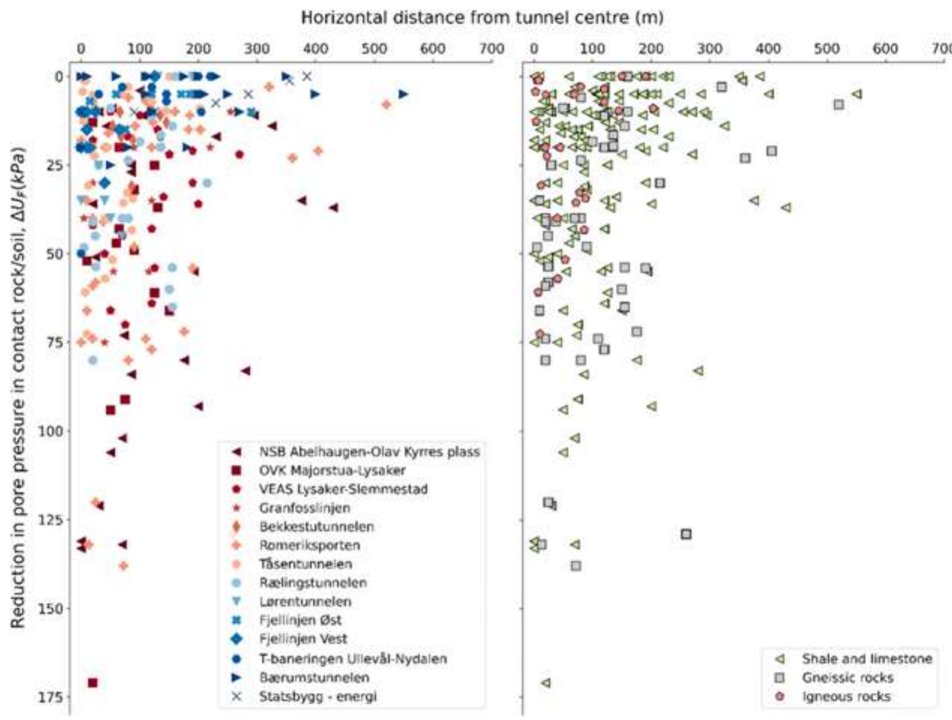

Figure 4 Relationship between measured pore pressure reduction at soil/bedrock interface in relation to horizontal distance from tunnel centre line. In the left-hand figure data is plotted for individual tunnels, in the right-hand figure data is systemized with respect to main rock type (Langford et al., 2022).

Figure 5 presents the measured decrease in pore pressure at bedrock along the centre line above the tunnel versus measured water ingress to the tunnel. This figure is used by the Norwegian tunnelling industry to determine water ingress limits in urban areas. Based on acceptance criteria for settlements, the corresponding pore pressure reduction for areas overlying the tunnel is determined. The figure is then used to choose the water ingress limit. Normally, a pore pressure reduction of maximum 10–30 kPa will result in small settlements in a clay deposit with an apparent OCR of 1.2 to 1.4 due to ageing. The shaded area indicates values “normally accepted” suggested by Karlsrud et al. (2003), with q in the order of 3 to 7 l/min/100 m, i.e. flow rates expected to result in ΔuF < 30 kPa and normally chosen as a water limit design value. It is important to note that in areas with existing tunnels or other underground structures, the pore pressures may already have been affected by leakage, causing an increase in effective stress level and a corresponding decrease in apparent OCR of the marine clay. Any additional pore pressure decrease will cause additional consolidation settlements. In these areas, limits on water ingress may be even stricter than indicated in Figure 5, down to 1–3 l/min/100 m.

The points indicate the average monitored values, the grey crosses show the range of measured pore pressure reduction and inflow rates for each tunnel. Red data points show projects without artificial water infiltration. Blue datapoints show projects with artificial groundwater infiltration in bedrock wells. For these cases, the water is infiltrated at a constant rate in drilled bedrock holes, with packers installed at approximately 5 m depth into the bedrock. The infiltration will recharge the confined aquifer through fractures the bedrock and contribute to maintaining pore pressure levels. For these projects, the decrease in pore pressure is expected to be lower for a given water ingress, compared to projects without water infiltration.

Figure 5 shows a considerable scatter in measured pore pressure reduction in relation to water ingress. This is likely caused by varying hydrogeological conditions previously described. In addition, there are uncertainties in the water ingress measurements, which are well-known to be challenging to perform. Nonetheless, there is a trend showing that pore pressure reduction increases with increasing water ingress. Based on the dataset a regression line has been derived for projects without water infiltration. This line is consistent with typical trendline previously suggested by Karlsrud et al. (2003). “Upper” and “lower” bound lines from Karlsrud et al. (2003) are shown in Figure 5. These indicate a characteristic area for the ΔuF to be expected, suggested in planning and design of tunnelling projects. The data from more recent tunnels (no. 19–26) are largely in agreement with previous data.

Projects with water infiltration were excluded when deriving these lines, as they are affected by artificial recharge.

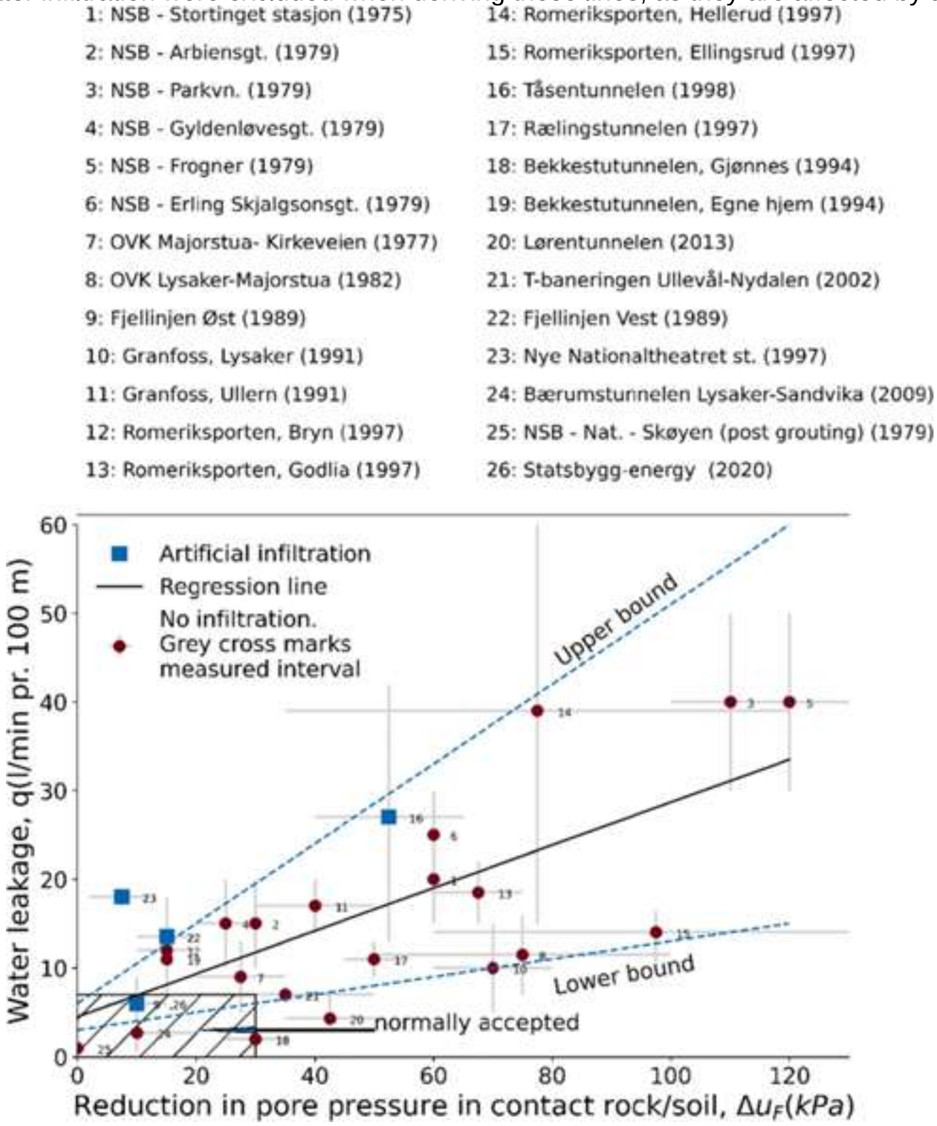

Figure 5 Relationship between reduction in pore pressure at bedrock level and water ingress. Normally accepted area is indicated as shaded area (Langford et al., 2022).

Several equations may be used for back calculating the hydraulic conductivity (El Tani, 2003, and Park et al., 2008). The equation given by Karlsrud et al. (2003) is used for back-calculation of the hydraulic conductivity in this paper, consistent with previous publications for tunnel projects in Norway. Karlsrud's equation has been shown to overestimate the water inflow rate for shallow tunnels with ratios of Re /h < 0.5 to 1.0 (El Tani, 2003). In the database, the tunnel depth below the groundwater table is more than twice the tunnel radius for all tunnel sections, with two exceptions. Hence, the approximation is considered sufficiently valid for this study.

$$Q = \pi k_i h \frac{2}{\ln\left(\frac{(R_e + t)}{R_e}\right)}$$

Where:
Q = water ingress to tunnel after PEG [m3/s/m].
ki = hydraulic conductivity of the grouted rock zone [m/s].
h = depth below the groundwater table [m].
Re equivalent radius of the tunnel [m].
t thickness of the grouted zone [m], assumed at 10 m for traffic tunnels and 5 m for sewage tunnels.

Langford et al. (2022) analysed how the grout effort (grout consumption and normalized drilling) influenced obtained K_i in different rock types. The data had significant scatter without clear correlations. A likely reason might be that K_i is back calculated from water ingress measurements over long sections, rather than measurements of leakage encountered in specific geological structures. Nevertheless, the figures imply that it is possible to obtain a hydraulic conductivity in the grouted zone of typically 4 to 6·10-9 m/s, when applying standard Norwegian practice. The most watertight tunnels after PEG has a K_i down to 1 to 2·10-9 m/s. Figure 6 indicates that the drilling effort has been larger in shale and limestone tunnels, without obtaining a more water tight grouted zone. Experience from execution indicates that the shale and limestone formations require more grouting effort in terms of drilling for PEG, to achieve a certain water tightness compared with igneous rock.

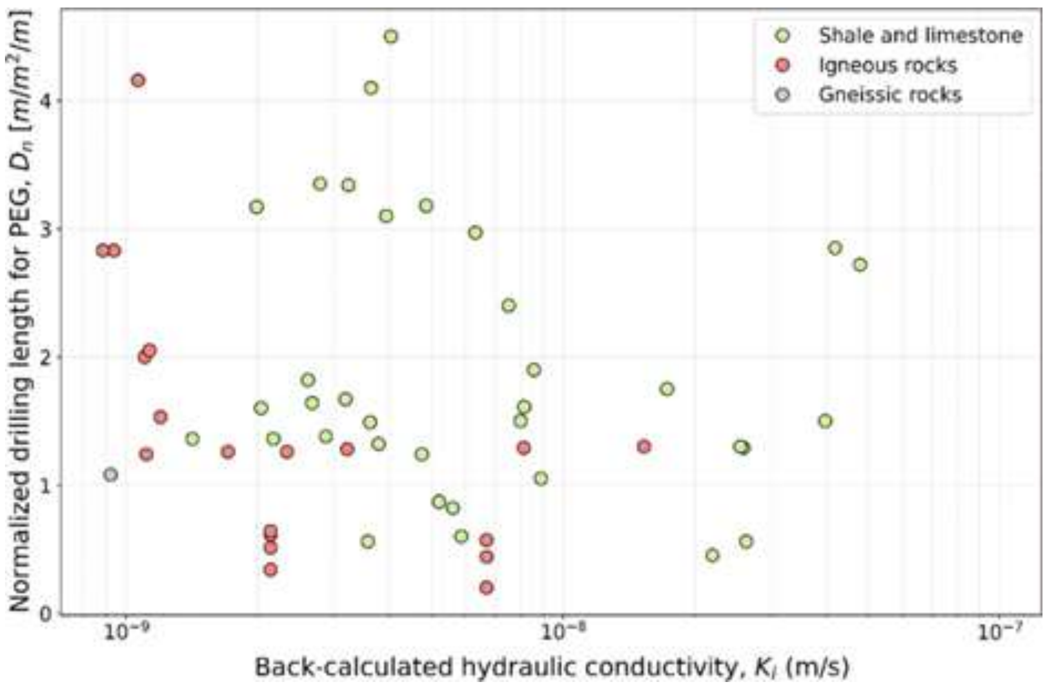

Figure 6 Plot of back-calculated hydraulic conductivity of grouted zone in relation to drilling length for grouting (Langford et al. 2022)

A timespan of 38 years gives a unique opportunity to check if it is possible to see any development for the grouting effort over time. Figure 7 shows normalized grouting consumption (kg/m2) versus back-calculated hydraulic conductivity over time. The colours gradually change from red in 1975 to blue in 2013.

The oldest projects (darkest red) have achieved hydraulic conductivity from 2 to 4 · 10-8 m/s with relatively low grouting effort (up to 65 kg/m2). While the newest projects (darkest blue) have achieved hydraulic conductivity from 1 to 4 · 10-9 m/s with grouting effort of ca. 25 kg/m2. The trend shows that almost all data from projects after 2003 have relatively low back-calculated hydraulic conductivity with mostly less than 50 kg/m2 in grouting effort. This is a good development and can be due to increased focus on grouting technique to reduce the water ingress and the risk of settlements in urban areas (Lindstrøm and Kveen, 2005; Strømsvik, 2019).

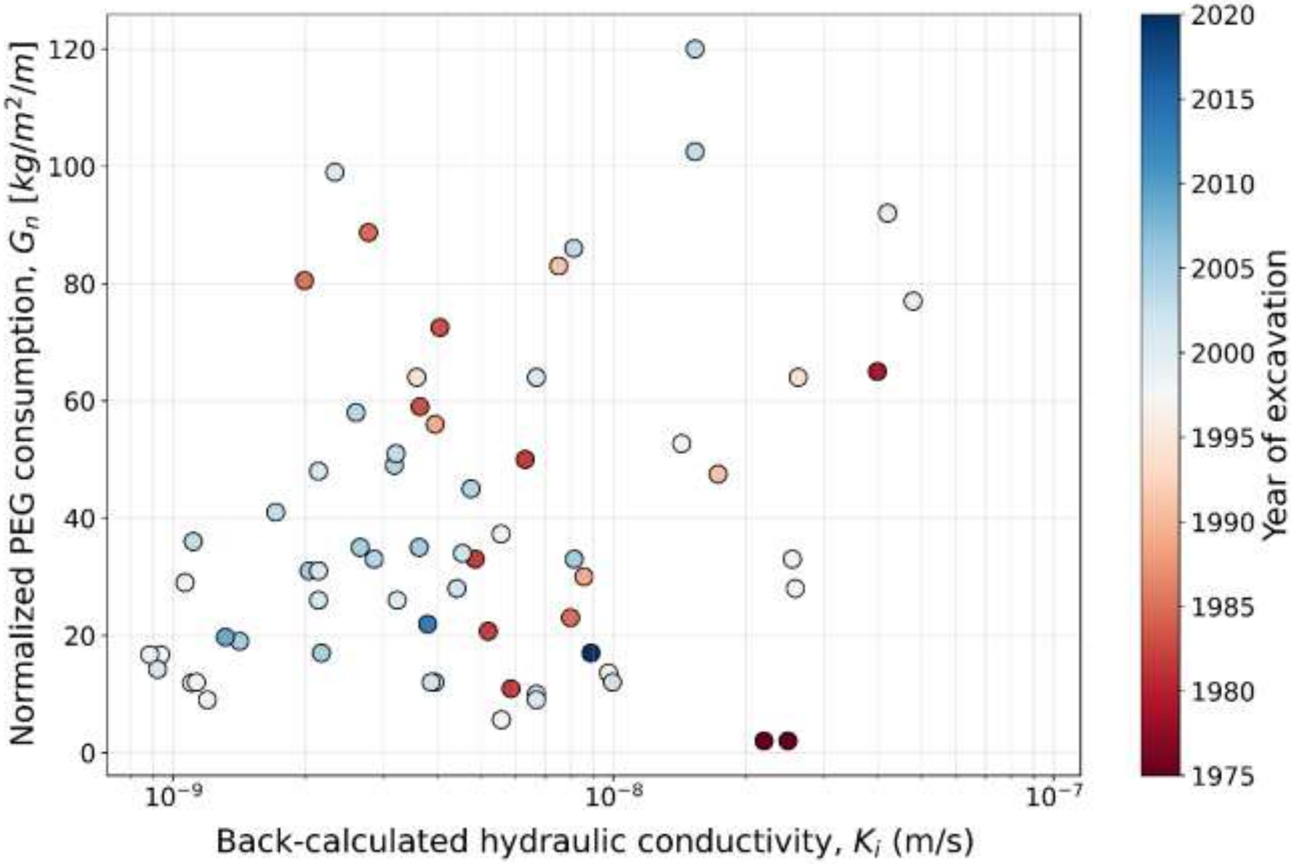

Figure 7 Relationship between achieved hydraulic conductivity and grouting effort with year of excavation shown in colours (Langford et al. 2022).

5. DISCUSSION

Much of the scatter in the database may be related to challenges in measuring water ingress, resulting in variations and uncertainty in the data itself. In addition, the measurements are average rates taken over distances ranging from hundreds of meters to several kilometres, whereas it is well known that the water ingress is often concentrated around local fracture zones. Also, the data is strongly influenced by varying geological and hydrogeological conditions for each project. Despite the scatter, the database provides unique insight into trends in terms of water ingress and pore pressure reduction and permits the suggestion of design limits for water ingress.

However, the data plotted in Figure 5 imply that estimating pore pressure reduction from water ingress levels is related to significant uncertainty. Hence, monitoring of water ingress is an insufficient measure to control pore pressure reduction. The resulting pore pressure reduction for a given leakage rate will vary depending on the hydrogeological conditions. An improved understanding of the sensitivity of pore pressure reduction in clay filled depressions could potentially be achieved with more detailed hydrogeological analysis. As an example, infiltration response tests (water loss measurements) can be performed during drilling of boreholes in bedrock for water infiltration wells. This requires installation of piezometers at bedrock level to monitor pressure levels during water infiltration. This type of test could be used to assess site-specific conditions, directly relating water infiltration rates to changes in pore pressure levels and allowing better understanding of the sensitivity of the areas to water ingress to tunnels.

6. CONCLUDING REMARKS

From the analysis it is apparent that focus should be aimed at monitoring pore pressure levels rather than water ingress, to reduce the risk of unacceptable pore pressure reduction and associated settlements. Furthermore, future projects will have stricter limits on water ingress and stricter requirements on water tightness. Real time monitoring of pore pressure during excavation and execution of PEG works, enable a more precise approach to PEG details, particularly the criteria for termination and decisions on further advance, having met the required result for maximum allowed water ingress. The following future developments are therefore proposed:

- Increased utilization of pore pressure measurements at bedrock level, to allow adjustments to PEG during construction.
- Continued research and development of PEG technology.
- Improved collaboration between geotechnical engineers, hydrogeologists, and engineering geologists. One common baseline report summarizing the hydrogeological situation, and all information related to risk of settlements (results from both geotechnical and geological investigations). In the same report mitigations such as grouting methods and pregrouting in both deep excavations and tunnels should be made.

7. ACKNOWLEDGEMENTS

The author would like to acknowledge the work carried out over years by former colleagues at NGI; Jenny Langford, Kjell Karlsrud and Vidar Kveldsvik. A special thanks go to clients of the tunnel projects studied.

REFERENCES

Andresen, L., Jostad, H.P., 2004: Janbu's Modulus Concept vs. Plaxis Soft Soil Model.
Nordic Geotechnical Meeting NGM 2004 – XIV.

Bjørlykke, K., (2004). Geology – The Oslo area. An over-view of the geology. University of Oslo

Bjerrum, L., 1967. Engineering geology of Norwegian normally consolidated marine clays as related to settlements of buildings. 7th Rankine lecture. G´eotechnique 17, 81–118.

Bjerrum, L., 1973. Problems of soil mechanical and construction on soft clays. State of the art report to Session IV. In: 8th International conference on soil mechanics and foundation engineering. Moscow, pp. 1–53.

El Tani, M., 2003. Circular tunnel in a semi-infinite aquifer. Tunn. Undergr. Space Technol. 18 (1), 49–55.

Holmøy K.H. (2008) "Significance of geological parameters for predicting water leakage in hard rock tunnels." Dissertation, Norwegian University of Science and Technology

Janbu, N., 1970. Grunnlag I geoteknikk. Trondheim. Tapir forlag.

Klüver, B.H. (2000) Pregrouting in hard rock. Internal Report No. 2151, Norwegian
Public Roads Administration, Oslo, 21 pp. In Norwegian

Langford, J., Holmøy, K.H., Hansen, T.F., Holter K.G., and Stein, E. (2022). "Analysis of water ingress, grouting effort, and pore pressure reduction caused by hard rock tunnels in the Oslo region" Tunnelling and Underground Space Technology 130, 12 pp.

Lindstrøm, M. and Kveen, A. (2005) " Tunnels for the citizen - Final Report" Norwegian
Public Roads Administration, Tunnels for the citizens, Report No. 105, 62 pp. In Norwegian.

Park, K.H., Owatsiriwong, A., Lee, J.G., 2008. Analytical solution for steady-state groundwater inflow into a drained circular tunnel in a semi-infinite aquifer: A revisit. Tunn. Undergr. Space Technol. 23, 206–209.

REMEDY (2015) "Damage limitations – Final Report" (Begrensning av skader som følge av grunnarbeid - Sluttrapport" In Norwegian.

Strømsvik, H. (2019): "Assessment of High Pressure Pre-Excavation Rock Mass Grouting in Norwegian Tunnelling", Doctoral thesis in the TIGHT project, Norwegian University of Science and Technology

Proceedings of the NROCK 2023
The IV Nordic Symposium on
Rock Mechanics and Rock Engineering
ISBN 978-9935-9436-2-0
DOI 10.33112/nrock2023.15

PU grouting in cold environment at fully operating Fljótsdalur Powerplant

Jóhann Örn Friðsteinsson (jof@verkis.is)

Verkís hf, Reykjavík, Iceland

ABSTRACT

Post grouting in rock was performed with polyurethane close to the pressure shaft valve chamber in the Fljótsdalur powerstation in autumn 2021 while the powerstation was in full operation. Sudden increase in leakage had been observed in the valve chamber during unit trips and associated water-hammering of the rockmass in the powerhouse area, in addition the total leakage in the tunnel system around the valve chamber, had gradually increased since commissioning of the powerplant in 2007 from 10 l/sec to 20 l/sec, going up to 50 l/sec during unit trips when the production is stopped. To prevent potential future problems caused by frequent transient state in the waterway, it was decided to perform grouting in the area. Detailed geological investigations of the rock mass between the valve chamber and the headrace tunnel gave premises for design of new grouting curtain and the choice of grouting material. Difficult conditions with cold water, highly permeable fracture zone and unpredictable changes in pathways resulted in challenging work where collaboration between contractor, client and consultants was essential. Roughly 17.000 liters of polyurethane was injected into the rock mass to seal the bedrock and the constant leakage was reduced down to 4 l/sec. Several unit trips have occurred since the work was completed and to-date, no increase in leakage has been observed.

KEYWORDS

Polyurethane; grouting, cold environment; hydropower plant

INTRODUCTION

The Fljótsdalur powerstation is a 690MW hydroelectric powerplant in eastern Iceland with a max gross head of 600 m. The hydropower plant consists of 40 km headrace tunnel (HRT) from the Halslón reservoir towards to the top of vertical shafts above the powerstation hall. Hraunaveita diversjon also supplies water to the powerplant. The pressure shaft valve chamber (PSVC) is located on the top of the vertical shafts where the water is divided into two vertical shafts of 400 m down to the powerhouse complex. This leaves approximately 200 m of water pressure in the headrace tunnel adjacent to the valve chamber.

Leakage has been constantly measured from the valve chamber area and in the rock next to the headrace tunnel concrete plug since the commissioning of the powerplant. During technical issues in the Aluminium smelter, the production in Fljótsdalur power station has been strongly reduced and frequently shut off causing sudden and heavy increase in water pressure (waterhammers) in the tunnel system. This has resulted in significant increase of leakage to the PSVC. Surveillance systems in the PSVC show increased leakage in the PSVC access tunnel immediately after shutdown. The volume of leakage has been high enough to overflood the drainage system in the PSVS and access tunnel. Under normal circumstances the recorded leakage is between 18 and 22 l/sec in a measuring weir downstream the valve chamber but increases to up to 50 l/sec during periods of unit trips.

A sudden increase in leakage can cause potential future problems for the operation and maintenance of the powerplant. To prevent this, a significant post grouting work with polyurethane (PU) was conducted in the area in 2021. The grouting design was done by Tomasz Najder at Najder Engineering in collaboration with Verkis consulting engineers and the owner Landsvirkjun, the grouting work was performed by Jan Najder at BESAB AB.

1. LAYOUT IN THE PRESSURE SHAFT VALVE CHAMBER AREA

The access to the valve chamber is through a roughly 1 km long Adit 1 tunnel from the top of the Fljótsdalur valley (Figure 1). There is a junction close to the valve chamber where the adit tunnel divides and continues to the right towards the headrace tunnel and concrete plug and left towards the access tunnel to the valve chamber. The shortest distance from the valve chamber to the pressurised headrace tunnel is 25 m. The drainage tunnel is located just upstream of the HRT manifold. The drainage tunnel drains water from the tunnel system to a creek in the valleyside in Fljótsdalur. Layout of the valve chamber area is shown in *Figure 2*.

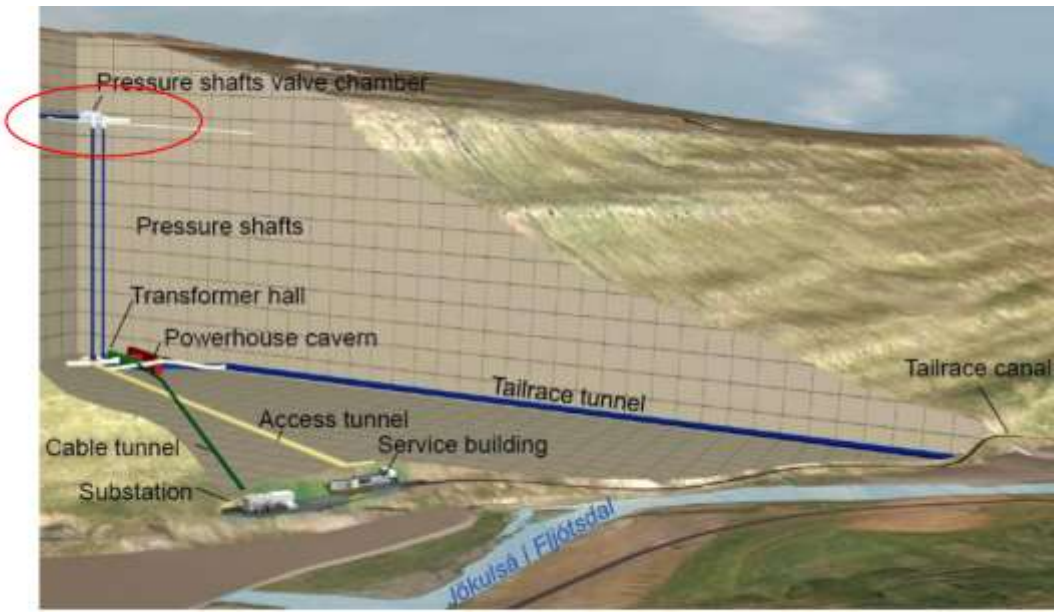

Figure 1. The powerstation area in Fljótsdalur valley. Pressure shaft valve chamber at the top of the vertical shafts.

The headrace tunnel is mostly unsupported, and limited lengths are supported with shotcrete at various places. A concrete lining was placed starting a short distance upstream the manifold, about 25 m upstream of the drainage tunnel centreline. The concrete lining is drained and after contact grouting, drain holes were drilled through the lining with 2x2 m grid above the springline, hence, leaving direct access for the water into the surrounding bedrock. Grout curtains, consisting of 3 row of grout holes for cement grouting in each curtain, were installed in the manifold tunnels, drainage tunnel and the concrete plug.

During pressurization of the headrace tunnel in 2007, there was a significant leakage from the Headrace tunnel into the valve chamber, to the main extent into the access tunnel. Additional grouting curtain with polyurethane (K-ring in *Figure 2*)) was performed in 2008 to seal off the inflow, when 8.500 liters of polyurethane was injected into the rock mass, and PVC membrane was placed on rock walls for protection of electrical equipment in the valve chamber and the access tunnel. The total leakage through the valve chamber after the grouting in 2008 was approximately 10 l/sec.

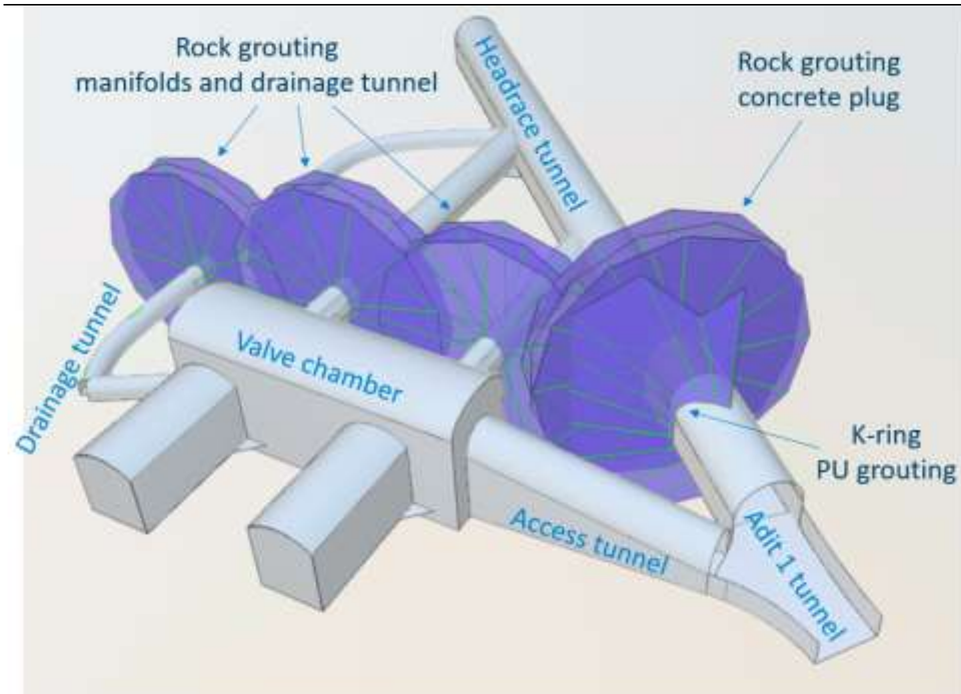

Figure 2. Layout in the valve chamber area and location of additional grouting curtain from 2008 (K-ring).

2. RECORDED LEAKAGE IN THE VALVE CHAMBER

A measuring weir was installed in the drainage tunnel at the downstream end of the valve chamber in 2010, for measuring all leakage water from the valve chamber and the Adit 1 tunnel. The leakage was recorded manually in the period from 2010 until in September 2018 when automatic measuring device was installed after sudden increase in leakage was first noticed.

Figure 3 shows records from the monitoring system and reflect the transient state in the waterway during water hammering pressure pulses and associated increased in leakage measured by the measuring weir. Pressure gauges installed at the top of the penstock are representative for the state in the pressurized headrace tunnel. Review of the data from the monitoring system and video records show that the leakage comes in three pulses where the top of the first pulse is measured 4-6 minutes after the first pressure peak in the penstocks, which then increases by up to 40 m (mH_20) during the episodes. The effects of the initial water hammer seems not to affect the leakage due to the short time that such a high pressure is occurring in the system. Considering 4-6 min delay in response time, leakage seems to start to increase when pressure in the penstock and headrace tunnel reaches roughly 20 mH_2O above normal state.

Review of records from CCTV cameras in the valve chamber show clearly that the leakage increases in both sides of the access tunnel as well as up through the center of the concrete invert. Leakage is also observed coming from the junction in adit 1 tunnel, under the portal between the access tunnel and the adit tunnel (*Figure 4*).

Study of as build documents and geological mapping from the construction time indicate that water is flowing through similar pathways as prior to the grouting of the K-ring, and the water is being transferred by joint sets and fracture zone orientated diagonal to the tunnel system. It was though uncertain if the water was flowing above or under the grouting curtains or even through them. Field investigations showed also signs of increased leakage during unit trips in the adit 1 tunnel. Orientation of possible leakage ways is shown in *Figure 5*.

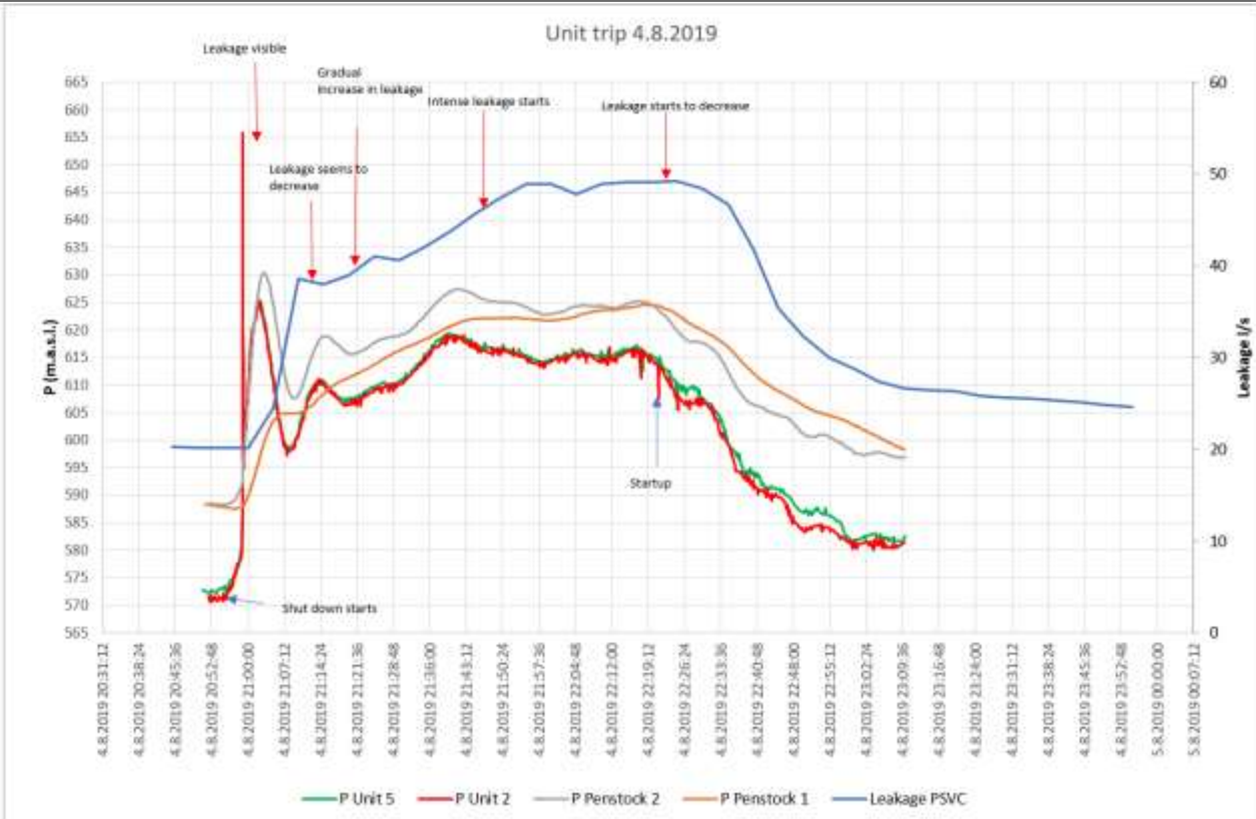

Figure 3. Graph showing water pressure at units and penstocks and during unit trip 4. august 2019 and recorded leakage from PSVC. Text above graph with observation on video records.

Figure 4. Observed increased leakage in access tunnel during a unit trip in august 2019. Note water flowing under portal door.

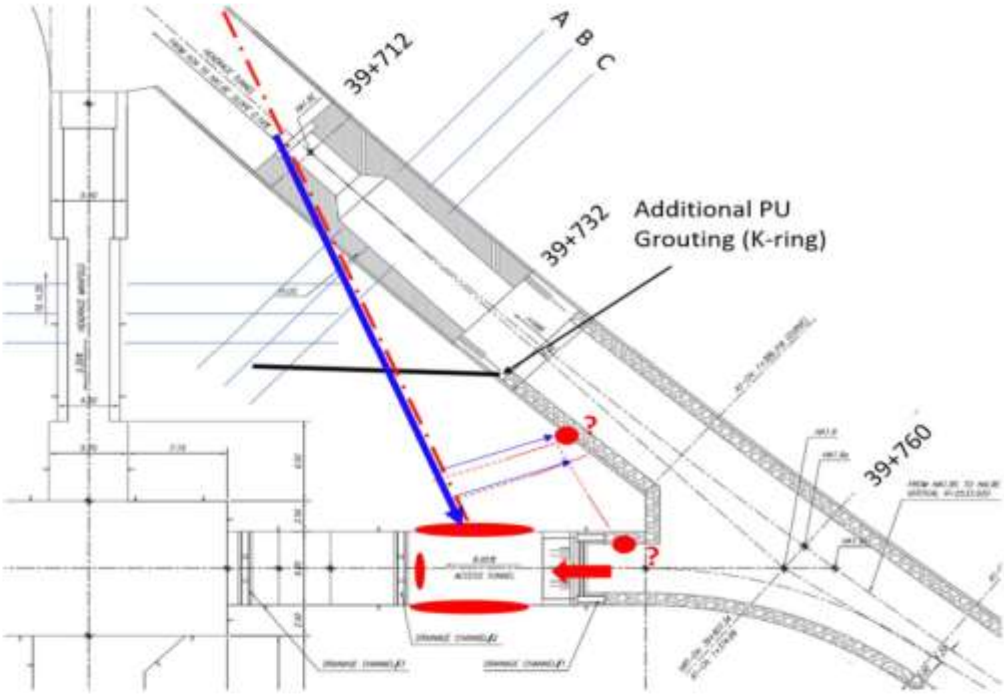

Figure 5. Possible flow pathway (blue) from the headrace tunnel to the access tunnel and adit tunnel. Note possible leakage areas with question marks in the adit tunnel outside the access tunnel to valve chamber.

3. INVESTIGATIONS 2021

Geological investigations were performed in March 2021 by probe drilling as permeability- and tracer tests were performed in all holes. The drilling was conducted from the adit tunnel, in the rock pillar between the headrace tunnel, and the access tunnel towards the valve chamber. The aim of the investigations was to identify possible leakage pathways from the pressurized HRT to the access tunnel in order to gather information about permeability in the rock mass for further use in detail design of a new grouting curtain. The measured temperature of the leakage water during the tests was between 1,5 and 2,1°C, but the temperature of the leakage water annually varies between 1 and 4°C.

The results from the investigations supported the assumption that the leakage from the HRT was confined to permeable joint zones both above and under the grouted K-ring, however, the rock mass itself has relatively low permeability. Permeable joints were observed outside of 18 m from the boreholes drilled in the same direction as the grouting curtain. Location of permeable zones in the boreholes with respect to the HRT and the leakage points in the access tunnel corresponded well to the previously mapped steep dipping (85-90°) joint set with strike direction diagonal to the adit tunnel.

Figure 6. Clear connection between probe hole and leakage in the access tunnel during permeability test.

Permeability tests indicated moderate to medium LU values (generally between 4-25 LU) with respect to the actual test sections. If the LU values are calculated with the assumed thickness of actual permeable zones, the leakage values could be classified as high or very high (50 to over 200 LU). Registration of flow with different pressure stages during permeability testing indicated that infillings in the joints were being pressed further into the joints causing lower flow rate with decreasing pressure stages. This was also seen in the access tunnel during permeability tests where brownish water was observed leaking from the joints during the tests.
Permeability tests with Fluorescein sodium blended into the injected water showed that the response time, from pumping until the colored water appeared in the access tunnel, was ranging between 9-15 minutes (*Figure 6*).

With respect to the test results, it was concluded that a new grouting curtain should be placed approximately 5-6 m downstream the K-ring curtain with grouting holes up to 24 m long to reach the permeable joint zones.

4. GROUTING DESIGN

4.1. Grouting curtain

In the original design it was planned to use the drill holes from the investigations in March as primary holes for grouting, and after completion of the grouting to drill secondary holes by forming a double array umbrella in the rock pillar between the headrace tunnel and the valve chamber (*Figure 7*). All primary and secondary holes were drilled to the minimum 24 m depth. Penetration rate and colour of flush water was registered to map in more detail the geology of the rock mass and permeability tests were performed with colored tracer material in all holes.

Grouting was performed through grout sets composed of steel pipes, two Bimbar packers and a plastic pipe to feed the grouting material to the desired depth in the hole, i.e. closest to the water bearing areas. The two components were mixed in 1:1 ratio in a static mixer before injected into the strata through the packers.

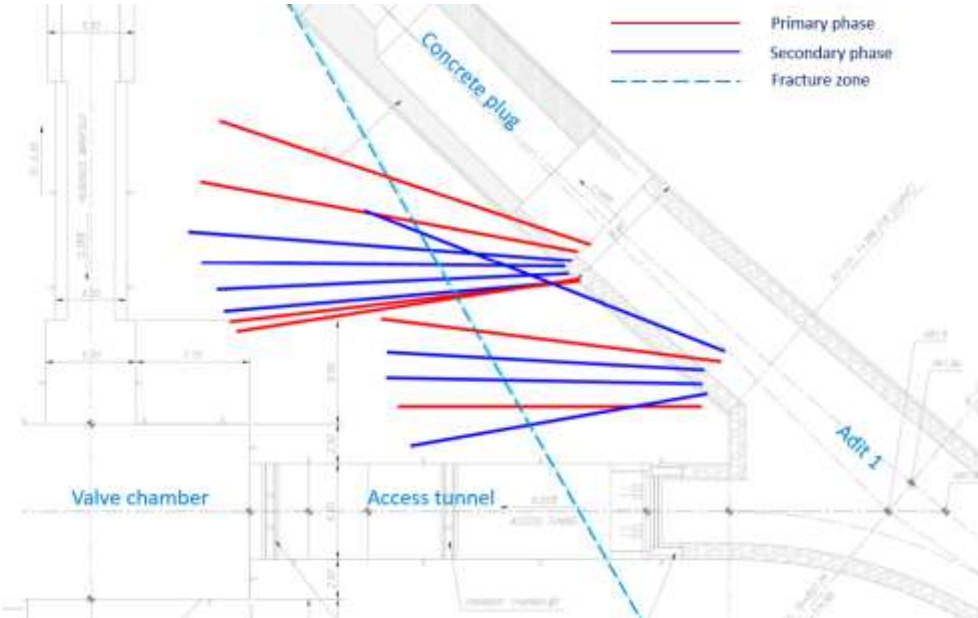

Figure 7. Original plan for grouting with primary (red) and secondary (blue) phase, location of potential fracture zone along dashed line.

4.2. Grouting material

Two component PU resin from DSI Schaum Chemie Ltd. was selected for the grouting. The PU properties were chosen based on the result of the investigation program in March 2021 with detailed information on permeability and response time. PU with the following properties was preferred for the grouting work:

Table 1. PU properties for grouting.

Product	Viscosity	Start foaming	End foaming	Foaming factor
DSI Inject PUR LV	70-100 mPas	180-300 s	ca 10 min	1,0 – 1,1
DSI Inject PUR HF	300±100 mPas	180-300 s	< 10 min	1,0 – 1,1
DSI Inject PUR HF ffx5	300±100 mPas	<60 s	< 3-4 min	5
DSI Inject PUR HF ffx10	300±100 mPas	<60 s	< 2 min	10 - 15

Grouting was mainly intended with low and medium expansion PU to avoid fracturing of shotcrete and rock during grouting and PU with higher foaming factor should be used for filling of cavities and high-water bearing joints. Additives, accelerator, and thixotropic agents for thickening, where also planned for challenging conditions.

The grouting was performed with pressure of 60 bar injection pressure above the groundwater pressure in the boreholes (measured at pump) giving a real overpressure of 3-5 bars when head loss in the hose system is taken into account. Refusal pressure of 100 bars (at pump) was used as a stoppage criterion or when grout take was exceeding 25 l of resin pr 1 m grouting length of the borehole. The grouting pressure was monitored closely during the work where the bedrock cover in the area is 120 m giving vertical stress about 3,2 MPa, and lowest stress in the area assumed even lower according to stress measurements down in the powerhouse area.

4.3. Preventive measures

The powerplant was planned to be in full operation during the grouting work. The tunnel system around the valve chamber includes drainage pipes and measuring weir which had to be protected from clogging. In addition, the leakage water is led through drainage tunnel to the slopes of Fljótsdalur Valley and the client posed strict restrictions for reacted PU in the leakage water to spill through the drainage tunnel onto the environment. Traps and dams composed of wooden planks, fishing nets and geotextiles were installed in the drainage tunnel to both calm the water in order to get the PU to react and collect reacted PU (*Figure 6,7 and 8*). The owner also monitored the outlet water from the powerplant to identify potential PU fragments and unreacted materials.

Figure 8. Provisional drainage system constructed on surface with open channel towards drainage tunnel to protect the permanent drainage system in the cavern.

Figure 9. Measuring weir (left) and drainage tunnel invert installed with fishing net and wooden planks to catch reacted PU downstream the valve chamber.

5. GROUTING WORK

The actual grouting work can be divided into three main phases; primary and secondary as described in the grouting design, and tertiary with changes in strategy after completion of original plan. Location of all boreholes and location of highly leaking zones was modelled in 3D after each day and the model frequently used for further decisions during the progress.

The grouting work started the 21st of October 2021 by extending and grouting the primary exploratory holes from the investigations. The grouting of all primary holes was finished grouted on the 26th of October with total consumption of 4880 l of PU. After this stage was finished, the constant leakage had decreased down to 15 l/sec in the drainage tunnel (*Figure 11*). Visible decrease in leakage was observed in the right wall of the access tunnel and the Adit 1 tunnel, but still high leakage was observed from the invert and left wall.

As for the secondary holes, in total of 9 holes were drilled in order to close two half umbrellas in the rock pillar between the HRT and the valve chamber. The secondary holes took almost the same amount of PU as the primary holes with no significant decrease in total leakage, as the constant leakage had actually increased up to 18 l/sec in the measuring weir (*Figure 11*). Results were whatsoever visible in the access tunnel where the right wall had at this point became almost completely dry. High leakage was though still coming from the left wall and the invert. Grouting of secondary holes was finished 4th of November.

Result from drilling and permeability testing of the primary and secondary holes showed that the water was clearly flowing through a subvertical fracture zone crossing diagonal through the rock pillar, now mainly below the invert. The highest change of completing the task was thereby to search for the water bearing part of the zone and grout directly in the main water source. By drilling directly into the water bearing zone, a leakage of 180-200 l/min with water pressure of up to 15 bars was measured. Grouting into this fracture zone was highly complicated as the leakage of this magnitude caused unreacted PU to flow out of the joints in the access tunnel and the polyurethane did not start to react until it was through the pillar and settling on the invert. The result of using higher foaming factor, adding accelerator or use thicker mixture resulted either in clogging of the holes or the water found new pathway through the fracture zone and into the tunnel. A unit trip occurring in the middle of the grouting process also gave leading information as now one could see which areas where tight and which were responding to the transient state in the headrace tunnel. As the result, it was decided to drill and grout umbrellas between the highly leaking zones and the periphery of the access tunnel where the water was leaking out, in the attempt to make a barrier closer to the tunnel and slowing the flowing rate through the rock mass before attacking the main water-bearing areas. After a reasonable tightness was accomplished, two additional holes were drilled in the main vain and packer with a valve was placed in one hole to control the water pressure and flow rate in the fracture zone while the other one was being grouted. This procedure proved to be successful and stopped the main leakage in the access tunnel. Location of grouted holes from all phases are shown in *Figure 10*.

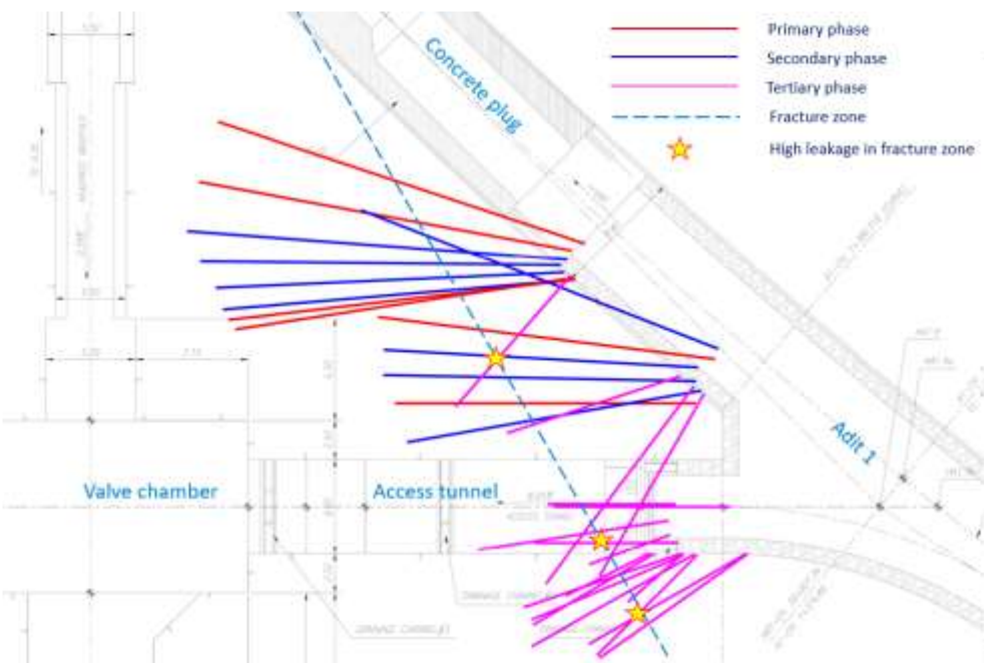

Figure 10. Final layout of grouting holes after all three phases. Tertiary phase with unregular pattern after chasing new pathways in the bedrock, mainly below the invert.

Seventeen holes were drilled and grouted in this tertiary phase of the grouting work and roughly 8000 liters of PU was injected, thereof 3000 liters in the main fracture zone. The total leakage measured at the measuring weir had at this point decreased down to 4 l/sec, the main leakage mainly coming from the 1 km long Adit 1 tunnel. The grouting work was finished 24th of November.

Total consumption of polyurethane was 17.410 liters injected into 46 boreholes. Total drilled length of probe- and grouting holes was 777 m, thereof were 583 m grouted length giving 29 liters grout pr meter in average.

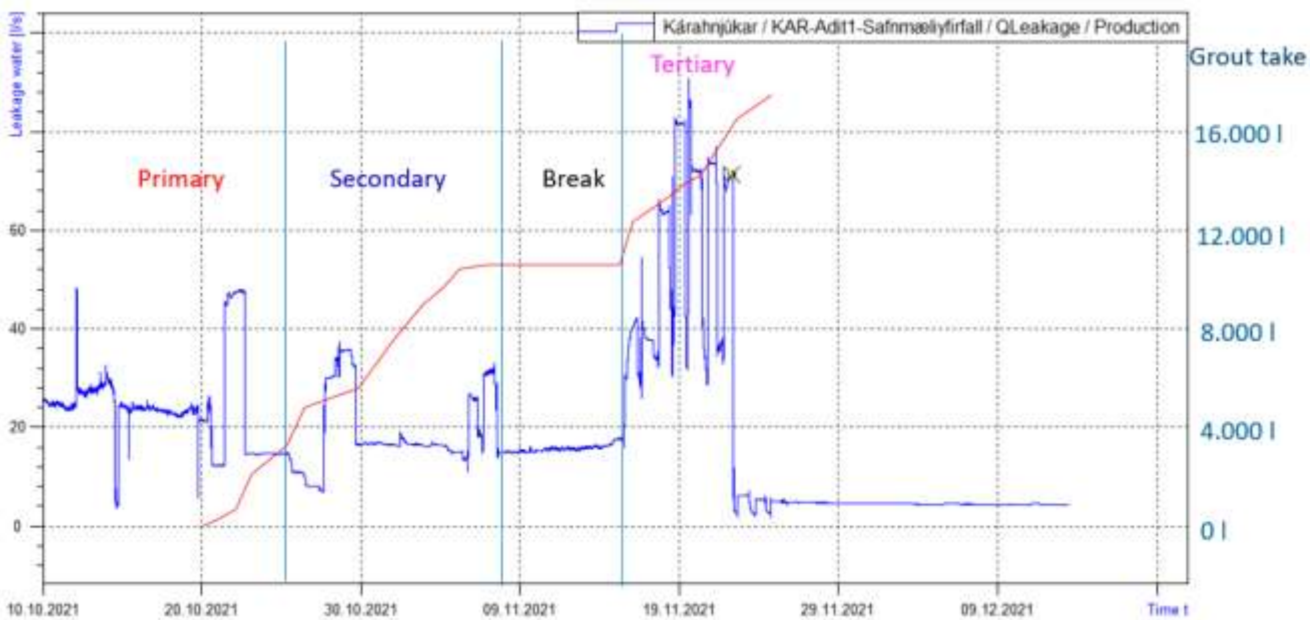

Figure 11. Total amount of leakage water from measuring weir (blue) and accumulated grout take (red) during grouting work. Irregularities due to preventive measures in the measuring weir (see Figure 9).

6. CLOSING REMARKS

Grouting of highly permeable fracture zones in cold environment with an operating hydropower plant close by is achievable with rigid polyurethanes. However, it requires good preparations and detailed investigations to accomplish with reasonable results. It is also vital to bring in experts in chemical grouting and flexible contractors, where decision making and evaluation on site must be taken frequently and change plans. All participants on site were aware of the complexity of the work and that results were not guaranteed. This time it was a success where remaining leakage after the work was mainly coming from leakage of groundwater in the roughly 1 km long adit tunnel and not the headrace tunnel itself. All remedial measures to reduce or eliminate polyurethane in the environment and the powerplant systems also worked as planned.

The main reason for good results was good and thorough preparations and daily meetings with all parts during the work. Location of all boreholes and results from permeability tests was modelled in 3D after each day giving valuable input in further decisions, especially in the tertiary phase of the work. The selected materials, both type of polyurethane, pumps and packers proved to be valid after several rounds with different suppliers. Above all, involving highly experienced specialists with knowledge about Icelandic conditions was a key factor.

A number of unit trips have occurred at the powerplant since the completion of the work and to-date, no increase in leakage has been observed.

7. ACKNOWLEDGEMENTS

Author thanks Dr.ing Tomazs Najder and Jan Najder for good cooperation, also thanks to Jón Smári Úlfarsson, Sindri Óskarson and Sigurbjörn Nökkvi Björnsson at Landsvirkjun and Þorleifur Páll Ólafsson foreman at Ístak.

Proceedings of the NROCK 2023
The IV Nordic Symposium on
Rock Mechanics and Rock Engineering
ISBN 978-9935-9436-2-0
DOI 10.33112/nrock2023.16

Spiling in unstable tunnel sections – a benchmark and case study review

Catrin Edelbro (catrin@itasca.se)
Itasca Consultants AB, Luleå, Sweden & Division of Soil and Rock Mechanics, KTH, Stockholm, Sweden

Fredrik Perman
Itasca Consultants AB, Luleå, Sweden

Fredrik Johansson
Division of Soil and Rock Mechanics, KTH, Stockholm, Sweden

ABSTRACT

In unstable ground, the tunnel can be pre-supported by driving spiles and forepoles into the crown and walls ahead of the excavation face with a small inclination angle upward. In Sweden, the nomenclature for this type of pre-support is "spiling". Spiling, which is a temporary support, is frequently used in Swedish tunnels. However, there is a lack of guidelines and international standardization for the design of spiling. This paper explores the design of spiling in unstable ground with focus on tunnels excavated in the Nordic countries with generally hard rock masses. Based on a benchmark, case and literature study review, example of guidelines and starting points in the design of spiling have been compiled. Cases, with different types of designed and installed spiling, are presented in the paper, followed by a discussion of when, and for what rock conditions, to use rebar spiles, pipe spiles, or self-drilling spiles to achieve a safe excavation progress. Analytical design methodologies used in Swedish cases are presented, including beam models for spiling sections between supporting arches or the face. Cases where numerical modelling have been used in the design of spiling are also described. The findings presented in this paper shows a lack of guidelines on how to design spiling. Future research work linked to model uncertainty, local arching effect and quality assessment is suggested, which will be beneficial for tunnel engineers in designing spiling in the future.

KEYWORDS

Spile, forepole, design, analytical, numerical

1. INTRODUCTION

In unstable ground, the tunnel can be pre-supported by driving spiles and forepoles into the crown and walls ahead of the excavation face with a small inclination angle upward. When the bearing capacity of the rock is insufficient due to weak rock, extensive weak zones, etc. an adapted and extensive reinforcement solution with spiling (longer bolts, pipes or braces) can be designed to secure the excavation, the working environment, and the surroundings (ground surface). Today, there is no clear compiled advice, recommended calculation methods or instructions for dimensioning of spiling (e.g., Oke et al., 2016; Strømsvik et al., 2016) even though excavating through complex passages involves a large cost. Based on previously completed and ongoing projects where spiling was used, examples of design and experience of temporary reinforcement with spiling have been compiled. The definition of spiling in this article is longer spiles (bolts or pipes) that are installed in the crown above the face, to create bearing capacity in the longitudinal direction of the tunnel (see Figure 1).

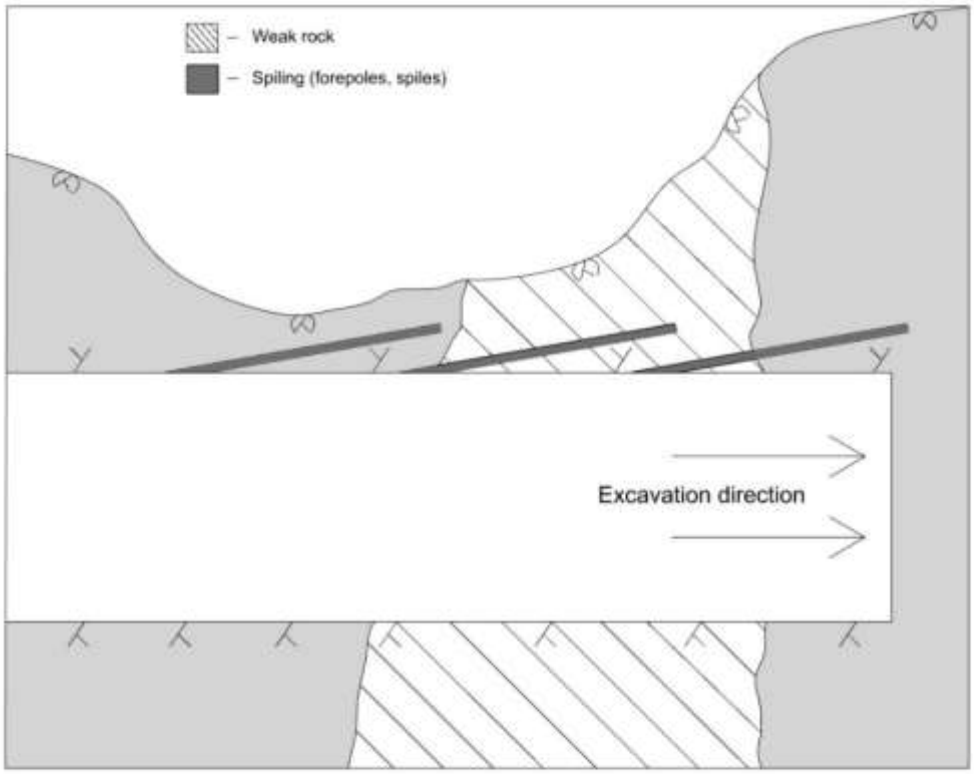

Figure 1. Example of a longitudinal section for a tunnel with spiling in weak rock and low rock cover.

The study does not address assessed risks and the actual risk management process associated with complex passages. The compilation does not deal with questions regarding durability, water and frost protection, form of contract and form of compensation. The compilation does not describe in detail other temporary reinforcement of the rock (e.g., fiberglass bolts) or changing its character (e.g., freezing, drainage, jet grouting) or other type of extraction (e.g., pilot tunnel, split fronts) when excavating through complex passages.

2. NOMENCLATURE

The concept of spiling, without further specification, is unclear. Within the concept of spiling, in our Swedish tunnel projects different terminology is used. Generally, spiling in Sweden means support added in the vicinity of the crown above the face; however, it does not specify the type of support nor its application or interaction with the rock mass. Typical used types of spiling (including the Swedish word in brackets), are rebar spiles (kamjärnsbultar), pipe spiles (rör), self-drilling spiles (självborrande stag, e.g., MAI, IBO, Ischebeck). Rebar spiles (bolts) are usually longer rebars that are cast into pre-drilled boreholes in hard rock where there is a risk of block failure or hammered into weaker, more earth-like material to provide a stabilizing effect. Pipes can be steel pipes, with a great diameter and larger thickness, which are installed in boreholes and where the pipe and the gap between the pipe and the rock is filled with concrete. The steel pipes are used and drilled into mainly heavily jointed rock or hammered into softer more earth-like material (Li, 2017). A certain risk with pre-drilled holes is that the holes collapse before steel pipes have time to be installed. Self-drilled spiles, to put it simply, are pipes that are left in the rock after drilling. Self-drilling spiles are often used for very weak rock to soil-like conditions.

Examples of terminology used in literature, when it comes to support in the crown above the face, are all from pipe roofing, pipe roof support, sub-horizontal jet grouting, steel pile canopy etc. Oke et.al. (2014a) presented a standardization proposal on the international nomenclature associated with support in the crown above the face to make everyone use the same words. The general term of the support in the crown have been suggested to be “umbrella arch”. In Oke et al., 2014a, "spiles" are defined as reinforcing elements whose length is shorter than the height of the rock tunnel. "Spiles" are installed closely (<30 cm distance) and at an angle of 5–40° from the axis of the tunnel. "Forepoles" are installed when longer stretches of weak rock are expected, which means that these are often thicker than "spiles" and longer (longer than the height of the rock tunnel).

3. DESIGN STRATEGY

Based on this study there is a lack of guidelines for calculation and analysis when designing spiling as well as lack of flowcharts in decision-making which considers if, what type, where and when spiling should be installed. A basic flowchart and some general principles that are suggested to be used in the design of spiling are proposed according to Figure 2. As part of the design strategy and during the entire work from identifying potential failure mechanisms to verifying the technical solution with calculations, a risk assessment is performed in parallel. Risks are identified, analyzed, and evaluated to decide how they should be treated and to discuss the possibilities to have back-up plans for unexpected occasions.

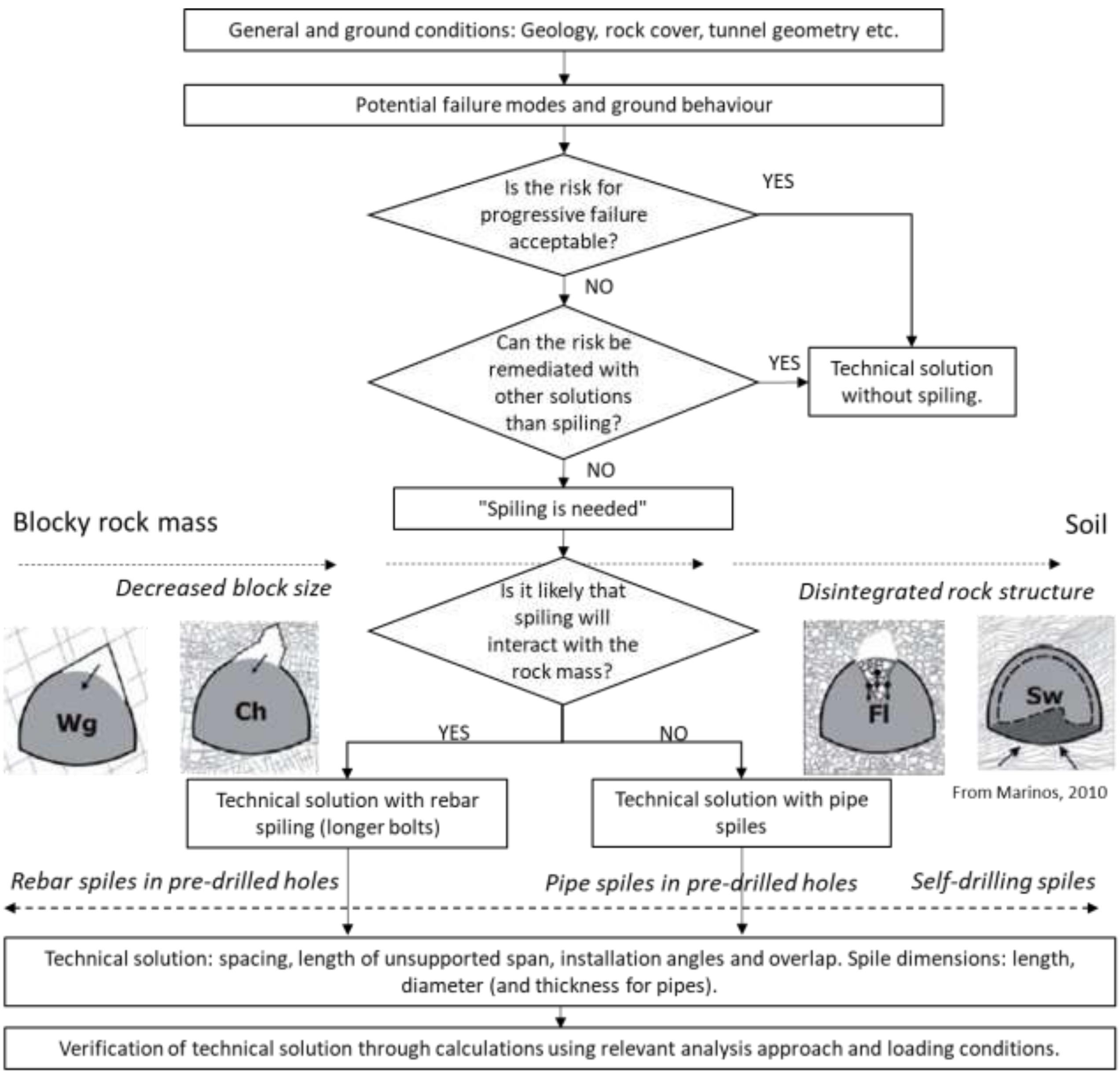

Figure 2. Proposed overall design strategy for temporary support using spiling.

All rock mechanical design requires an understanding of what ground behavior the rock mass can be expected to exhibit when excavating the tunnel. This behavior is due to a combination of rock mass composition, rock mass conditions and tunnel geometries etc. (Stille & Palmström, 2008). Ground conditions that must be considered include e.g., geology (lithology, structure, weathering), structures, groundwater conditions, rock cover, stress conditions and orientation of fracture groups in relation to the orientation of the tunnel. Decisions, whether spiling is needed, should be suggested based on the expected behavior of the rock mass, potential failure mechanisms, the accepted risk for raveling ground and if other temporary support measures (such as freezing, jetgrouting etc.) would be more applicable.

In Strømsvik et al. (2016) an attempt was made to study any correlation between rock mass quality (*Q*-value) and design of umbrella arches. According to Strømsvik et al. (2016), it was not possible to concretize any relationship between *Q*-value and choice of diameter of spiling pipes, distance between pipes nor the overlap over the pipe shields. A poor rock, say $Q < 1$, could represent all from a very blocky rock with intermediate water and clay problems to a sandy/soil like material. These two types of rock masses have different behaviour, potential failure modes and thereby different need for temporary support. For the Hallandsås tunnel in Sweden, eight scenarios were set up for *Q*-values < 1, based on expected geology (Sturk & Brantmark, 1998). For each scenario, geological risks were identified linked to potential failure mechanisms (e.g., loosening of the rock mass (raveling ground, running ground, swelling ground, etc.)) as well as how excavation and temporary reinforcement was expected to take place. Based on the above issues, and how to address the issue of low-quality rock masses, a thorough risk assessment is of importance. The risk assessment should include defined potential scenarios based on expected geology.

Once it has been decided that some type of spiling is required, the next decision is what type of spiling to use. The completed literature study shows that there are two fundamentally different reinforcement principles to choose from. The first principle is to use cast-in spiling rebar (bolts) that interact with the rock mass according to the same principle as for a reinforced concrete beam. An interaction between bolt and the rock mass can be expected for a blocky rock mass. The second principle is based on that the spiling carries through its ability to absorb moment. This principle is primarily used in rock masses of very poor (soil and/or sand) quality, to achieve the required load-bearing capacity. For this purpose, it is common to use thicker pipes.

When a suitable spiling solution has been chosen, a proposal for a technical solution can be produced, which is then verified through calculations. The verification of the technical solution through calculations requires that both load conditions and bearing capacity are considered through a suitable model, which is discussed in more detail in section 4. During the construction phase (not shown in Figure 2 above), the design conditions are continuously checked using e.g. geological mapping; and a final verification of the technical solution is obtained through monitoring of the rock mass and support behaviour.

4. TUNNELS WITH SPILING

There are several published cases of tunnels in rock masses with consistently weak rock and/or soil-like material (on the right in Figure 2) close to the surface where spiling has been used. In most of these cases, the focus has been on the evaluation of spiling as an effect to counteract settlements in an urban environment. It is also for these cases that most numerical analyzes have been performed. However, there are fewer examples of cases with a similar geology to hard Fennoscandian rock masses with passages through zones of weaker rock.

Examples of cases in Sweden where spiling pipes have been installed in tunnels are presented in Table 1. In all these cases, the rock mass structure has been disintegrated having a potential of raveling ground or chimney type failure. One of the most difficult technical challenges for the Stockholm Bypass project was the passage under the Lake Mälaren and the regional fault zone in the Fiskar fjord. The uncertainties and risks associated with this fault zone in the Fiskar fjord originated from limited information about the rock cover, the rock quality in the fault zone, possible large water leakages and existing in-situ stresses together with the relatively large width of the tunnels. To secure the excavation of the tunnels, a pipe umbrella with a length of 15 m, an overlap of 5 m and drilled at c/c 500 mm spacing was used. The steel pipes have a diameter of 140 mm and a thickness of 10 mm. In addition, to avoid stability problems at the tunnel face during excavation through the fault zone, self-drilling rock bolts installed at c/c 1.5 m were considered necessary (Stille et al., 2019). During the excavation of the rock tunnels in the Northern link project a critical part with soil within the profile of the rock tunnel was challenging. The excavation was completed with a temporary support using injection anchors above the crown (as spiling), lattice girders and sprayed fiber concrete together with short excavation steps (Andersson et al., 2011).

Examples of spiling bolts in intersections and tunnels with large span can be found, among others, from Västlänken (Eriksson & Fransson, 2022), New subway in Stockholm (Söder & Åkerlind, 2022), Götatunneln (Stille & von Matérn, 2003) and Hallandsås (Sturk & Brantmark, 1998). For the cases where bolts have been installed, the rock mass structure is very blocky to blocky. The compilation from the case study review shows that the design strategy and the design of spiling differ, and that different calculation methods, elementary cases and load cases have been chosen for the same expected behavior of the rock mass.

Table 1. Some examples of cases and projects in Sweden where spiling pipes have been applied.

Case (Project)	Quality of ground	Length of pipe [m]	Angle of application [°]	Overlap/Round length [m]	Spacing [m]
Yxhugget (Northern Link, Stockholm) *	Soil and rock	15 m (9-25 m)	8	-/3	0.4 (soil), 0.8 (rock)
Södra randzonen (Hallandsås tunnel) **		16 m (ø 140 mm)	5-10	-	0.4
Sätra-Kungshatt (Stockholm Bypass) ***	RMR_{base} 29 – 40	16 m (ø 140 mm)	7	5/2	0.5
Södermalmstunneln (Citybanan, Stockholm) ****	Soil	15 m (ø 139 mm)	7	5/1 pilot top heading	0.3 0.45
Kungsgatan (West link, Gothenburg) *****		18 m			

* Andersson et al., 2011, ** Sturk et al., 2005, *** Stille et al., 2019 **** Eriksson et al., 2016; Hjälmbacken & Söderberg, 2011, ***** Eriksson & Fransson, 2022

5. CALCULATION METHODS

5.1. Load cases in analytical calculation

To assess the size of the load on the spiling during excavation, there are several different examples of assumptions that can be made. Most ways to calculate the load have been compiled in, among others, Lukic & Zlatanovic (2019) and Moses & Malik (2019). Spiling bolts installed in tunnels with “good rock” and where the purpose is to hold a large span, or a crossing, must generally be capable of carrying loads from a block. The weight of the load can be derived from e.g., arrow height, interpretation of block size, etc. When calculating the loads on shallow tunnels, it is suggested (Franzén, 2003) that the strength of the surrounding soil/rock is not used, and the load is calculated in these cases as the overlay pressure (and water pressure). How large this pressure from above is assumed to be, should be based on the nature of the rock or soil. Furthermore, the pressure from above depends on the ability to receive an arching effect above the tunnel caused by the horizontal stresses. From the examples in the case study review, for loose rock masses, the pressure from above has been estimated based on, for example, numerical analysis, Terzaghi's methodology (Terzaghi, 1946) or rock cover height.

The well-known empirical method for assessing load from soil and rock is Terzaghi's compilation from 1946 where calculation of load (Figure 3) has its basis in the nature of the rock divided into nine rock classes. In this work, rock classes V-IX are in focus. There are several calculation examples for spiling where the Terzaghi theory is used as a basis for assessing the load. The height of the zone with loose soil or rock mass, H_p is a function of the tunnel's width, B, and height, H_t, according to Figure 3. The material above this zone is assumed not to load the tunnel roof. The shear strength is assumed to counteract the weight of the loose rock. Terzaghi's theory is applicable for tunnels with a width of up to 6 meters.

For tunnels in rock and soil located above the water table, the actual loads are significantly lower (50%) than those calculated according to Terzaghi's method (Franzén, 2003; Singh & Goel, 2011). The reason is believed to be that a quickly installed support and good contact with the soil/rock causes only a small deformation and the pressure arch in the soil/rock can then be formed quickly (Franzén, 2003). For a fictitious example, the uniform distributed vertical (non-sustaining) load, q, is as a function of rock material density, ρ, gravity acceleration, g, and overburden height, H_p, according to equation (1).

$$q = \rho \cdot g \cdot H_p \tag{1}$$

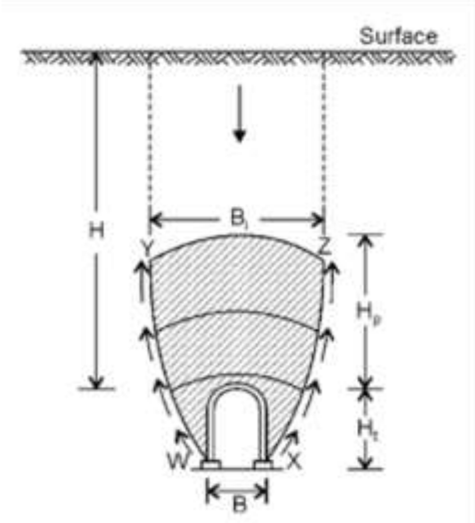

Rock class	Rock condition	H_p	Remarks
V	Very blocky and seamy	(0.35 to 1.10) $(B + H_t)$	Little or no side pressure.
VI	Completely crished, but chemically intact	1.10 $(B + H_t)$	Considerable side pressure. Softening effects of seepage toward bottom of tunnel. Requires either continuous support for lower ends of ribs or circular ribs.
VII	Squeezing rock, moderate depth	(1.10 to 2.10) $(B + H_t)$	Heavy side pressure. Invert struts reqired. Circular ribs are recommended.
VIII	Squeezing rock, great depth	(2.10 to 4.50) $(B + H_t)$	
IX	Swelling rock	Up to 80 m	Circular ribs are required. In extreme cases, use of yielding support recommended.

B = tunnel span in meters, H_t = height of the opening in meters,
H_p = height of the loosened rock mass above tunnel crown developing load

Figure 3. Left: Load from loose material above a tunnel (after Terzaghi, 1946). Right: Height of the loose rock mass based on rock classes (after Sing & Goel, 2011).

5.2. Analytical beam calculation

Analytical calculations for the bearing capacity are mainly based on the beam theory. When using beam theory, the rock mass is divided into strips where each strip consists of a spiling bolt/pipe and has a width corresponding to the c/c distance to the next bolt/pipe, alternatively calculated per meter in width. The assumption is considered conservative as the bending moments and loads are determined for the worst possible geometry (Stille & von Matérn, 2003).

Based on the bending moments to which the spiling is subjected, it can be assumed that it is a beam that is loaded according to four load cases, A to D according to Figure 4. The proposed load cases depend on excavation step and support or non-support at the near-end of the beam. The uniformly distributed load per spile, $q \cdot s$, is a product of the loose rock/ground pressure, q (as in equation 1), and the spacing between spiles, s. Analytical calculations using load case A and B for the different excavation steps (see example in Figure 5) and by assuming near-end support have been applied for, among others, the New Subway in Stockholm and the West Link in Gothenburg, Sweden.

Another way of looking at bearing capacity is that it is a simply supported beam (hereafter named case C) where the support of the beam consists of the reinforced rock vault (excavated tunnel) and the rock mass in the unexcavated tunnel. A fourth way used in the design is a cantilever beam (hereafter named case D,) which could represent the spiling before installing the first supporting arch. In case D, the spiling is only supported by the rock ahead of the front. Spiling is in such case installed at the bottom of the beam to sustain bending moments and the calculation method has been used for example for the Göta tunnel in Gothenburg, Sweden (Stille & von Matérn, 2003). The different load cases that may be relevant in analytical beam calculation, are described according to classical beam theory as four elementary cases:

A. Beam fixed at one end and simple support at the other, with uniform distributed load.
B. Beam fixed at both ends, with uniform distributed load.
C. Beam simple support at both ends, with uniform distributed load.
D. Cantilever beam, that is fixed at one and free at the other, with uniform distributed load.

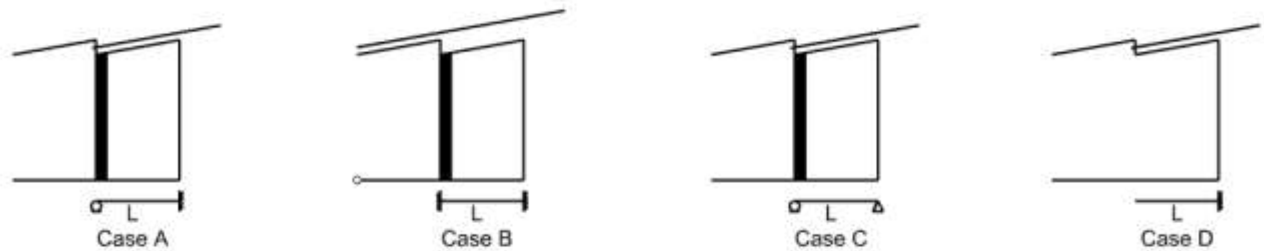

Case A	Case B	Case C	Case D
$M_{max} = M_B = \frac{q \cdot s \cdot L^2}{8}$	$M_{max} = M_A = M_B = \frac{q \cdot s \cdot L^2}{12}$	$M_{max} = M_{mid} = \frac{q \cdot s \cdot L^2}{8}$	$M_{max} = M_A = \frac{q \cdot s \cdot L^2}{2}$
$V_{max} = V_B = \frac{5 \cdot q \cdot s \cdot L}{8}$	$V_{max} = V_A = V_B = \frac{q \cdot s \cdot L}{2}$	$V_{max} = V_A = V_B = \frac{q \cdot s \cdot L}{2}$	$V_{max} = V_A = q \cdot s \cdot L$

Figure 4. The four different elementary cases for spiling and equations for the maximum bending moment and shear force.

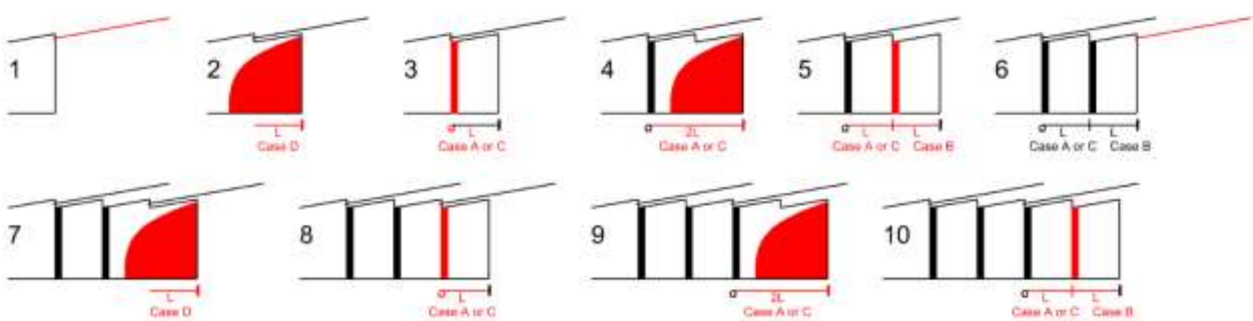

Figure 5. Excavation and installation sequence for spiling together with example of applicable elementary cases. L is the distance between ribs.

To assess the load-bearing capacity of the spiling, one (or more) of the following criteria has been used in the different case studies: moment (2), shear force (3) or normal and shear force (4):

$$M_{Ed} \leq M_{Rd} \tag{2}$$

$$V_{Ed} \leq V_{Rd} \tag{3}$$

$$\left(\frac{N_{Ed}}{N_{Rd}}\right)^2 + \left(\frac{V_{Ed}}{V_{Rd}}\right)^2 \leq 1 \tag{4}$$

where:
M = moment, V = shear force, N = normal force (tensile or compressive force), $_{Ed}$= design load effect and $_{Rd}$ =design load resistance. To determine the diameter and length of the spile, the moment, shear force and/or normal force to which the spiling will be exposed to, is compared with its capacity.

5.3. Numerical calculations

Internationally, spiling and its effect on ground movements been studied, using numerical modelling, mainly for near-surface tunnels in consistently weak rock or soil in e.g., Klotoé & Bourgeois, 2019. In Sweden, spiling in tunnels has been studied and designed through both 2D and 3D numerical calculation models. The evaluation of the results from numerical modeling is often done using moment-normal force interaction diagrams. Since the spiling is installed in front of the face, it is exposed, compared to permanent reinforcement installed in the tunnel, to all deformations caused by the rock excavation. The compilation has shown that numerical modeling in 2D does not capture the arching between spiling elements, the change of rock stress along the spiling element, and the response of the rock element in the longitudinal direction (e.g., Volkmann & Schubert, 2007; Peila, 2013; Oke et al, 2014b). The change in stress and response is especially important to consider in 3D if the tunnel is excavated in steps and partial face with heading-and-bench (which is common in complex passages) is used. However, it is recommended to use 2D modeling to design distances between spiles. This local arching effect has been studied in 2D models for properties corresponding to soil and sand (e.g., Doi et al., 2009) but there is nothing in the literature showing similar results for a fractured and blocky rock mass.

6. DISCUSSION

The literature and case study review have shown that there is a need for clarity regarding nomenclature and definition of what we refer to as spiling. When choosing spiling as a technical solution, the following should be described (i) function and mode of action, (ii) type and dimension, (iii) casting of the spile, (iv) interaction with other reinforcement and (v) installation (angles, single arch or double arch with spiles etc.).

The compilation focused on Swedish cases. For other Nordic countries, there may be other proposals for design strategies and more ways to design and calculate that are not publicly published. In general, the overall principles for design of spiling are well described in the literature, the main difficulties lie in: (i) being able to determine when spiling is needed, (ii) choosing the correct technical solution that works for the prevailing ground conditions, and (iii) being able to estimate design load and (iv) set up an acceptable bearing capacity model and calculation method. However, the model uncertainty of the bearing capacity model and its impact on the dimensioning in combination with other uncertainties linked to the rock mass mean that the probability of failure is difficult to determine, which also means that it is difficult to assess whether the dimensioning is associated with an unacceptable risk.

The compilation from literature and the case study review shows that the design of spiling differs, and that different calculation methods, beam models and load cases have been chosen for the same expected behavior of the rock mass. Material parameters in general, both regarding relevant material parameters for loose rock masses and surrounding rock but also parameters that describe the spiling interaction with the rock are difficult to assess. According to Andersson et al. (2011), the calculation method itself when calculating spiling and its accuracy is not decisive for the result. What is decisive is the interpretation and assumptions of the strength parameters of the rock and the soil along the tunnel and whether the material behaves as a friction material or is cohesive. To capture the variation of strength parameters, they proposed sensitivity analysis.

In the design stage, it is important to consider how the proposed technical solution can affect the construction stage, but also relative to other technical disciplines. When designing spiling, the following aspects should be considered:

- Grouting
  How is the developed grouting solution affected, considering location, length, direction, angle of spiling?
- Work environment when installing long spiling bolts.
- In terms of work environment, it is heavy and tiring, and thereby nonacceptable from a health and safety perspective to install 32 mm bolts. It is rarely or never that there are machines to install these bolts. Long bolts with ø 32 mm are not suggested to be designed if they are to be installed manually. Furthermore, there is a risk that long bolts will start sway, which partly makes it difficult to hit the hole, but which also risks creating motion sickness for those working from a sky lift.
- Investment cost and time required for special machines.
- Installation of pipes requires special machines. Investment cost for special machines constitutes a noticeable cost. Furthermore, installation of pipes gives extra time compared to simpler reinforcement installations.

7. CONCLUSION AND RECOMMENDATION FOR FUTURE WORK

The main conclusions of the literature and case study review are:

- The literature and case study review has shown that there is a need for clarity regarding nomenclature and definition of what we refer to as spiling.
- When describing spiling as a technical solution, the following should be described: (i) function and mode of action, (ii) type and dimension, (iii) grouting and spiling, (iv) interaction with other type of rock support and (v) installation (single or double arch for a pipe umbrella arch).
- There is a need for advisory documents for dimensioning spiling and flow charts for decision-making about: if, where and when spiling should be installed. The principle flow chart shown in this article can be used as a basis in future advisory documents. In the design of spiling, it is important to consider, among other things, the following aspects compared to other disciplines and in the construction phase: grouting, working environment, investment cost and time consumption.
- To address the issue of low-quality rock masses, a thorough risk assessment is recommended. The risk assessment should include defined potential scenarios based on expected geology.
- The preliminary study shows that the design of spiling differs, and that different calculation methods, beam models and load cases have been chosen for the same expected behavior of the rock mass.
- Material parameters in general, both regarding relevant material parameters for loose rock masses and surrounding rock, and parameters that describe the spiling interaction with the rock, are difficult to assess.
- According to the compilation, modeling of how spiling is loaded regarding excavation method and split front should be studied with a numerical 3D model. Numerical 2D modeling should only be used to study the arch effect to dimension pipe spacing.

The recommendation for future work includes:

- Linked to model uncertainty, it is suggested that one or more practice cases be studied regarding approach, calculation methodology, variation in parameter values through sensitivity analysis and reliability-based design.
- A similar compilation of how to dimension, and how to follow up, the developed technical solution in the construction phase should be made for the support arch themselves, such as shotcrete and lattice arches.
- This local arching action should be studied for jointed rock in 2D models to study block size and its connection to the arching action and thus the need for either bolt or pipe and the distance between them.
- Since classification systems, such as the Q system, are applied in tunnel construction, different probable scenarios for Q values below 1 should be described, which can be linked to the relevant choice of temporary reinforcement solution.

8. ACKNOWLEDGEMENTS

The presented paper is based on a pilot study in spiling and forepoling. The pilot study was partly funded by BeFo and the authors would like to thank Helen Andersson (Huth & Wien Engineering), Magnus Felldin (Implenia), Eric Hegardt (Trafikverket), Miriam Isaksson Mettävainio (AFRY), Charlie Li (NTNU), Björn Stille (TriEng), Carl-Olof Söder (Sweco) and Patrik Vidstrand (BeFo) for their contribution as reference group members for the pilot study.

REFERENCES

Andersson, H., Borchardt, P. & Dalmalm, T. 2011. *Bergtunnel utan bergtäckning*. Fjellsprengningsdagen 2011, NFF, s. 30.1-30.10.

Eriksson, M., Bertilsson, R., Sjöberg, J., Mas Ivars, D. & Lope Álvarez, D. 2016. *Tunneldrivning i heterogena förhållanden – översiktlig studie av styrande egenskaper avseende deformationer*, BeFo Rapport 150, ISSN 1104-1773, Stockholm, 87 p.

Eriksson, M. & Fransson J. 2022. *Komplexa passager i Västlänken*. Oral presentation at the Swedisk rock mechanics autumn seminar 2022, Stockholm, 2022-11-23.

Franzén, T. 2003. *Betonginklädnad av tunnlar.* Tekniköversikt-Förstudie. SveBeFo Rapport 62.

Hjälmbacken, P.-Å. & Söderberg, C. J. 2011. *Södermalmstunneln – en utmaning*. Svenska Bergteknikföreningen. Bergteknik (BK-Dagen) 2011.

Klotoé, CH. & Bourgeois, E. 2019. *Three dimensional finite element analysis of the influence of the umbrella arch on the settlements induced by shallow tunneling*. Comput Geotech 110:114–121.

Li, C. 2017. *Principles of rockbolting design*. Journal of Rock Mechanics and Geotechnical Engineering 9, 396-414.

Lukic, D. & Zlatanovic, E. 2019. *Load analysis in construction of tunnels by the pipe umbrella system*. 7th international conference. Contemporary achievements in civil engineering 23-24. April 2019. Subotica, Serbia.

Marinos, P.V. 2010. *Geological behaviour of rock masses in Underground excavations*. Bulletin of the Geological Society of Greece, Vol. 43:1238-1247.

Oke, J. 2016. *Determination of nomenclature, mechanistic behaviour, and numerical modelling optimization of umbrella arch systems.* PhD thesis. Department of Geological Sciences & Geological Engineering, Queen's University Kingston, Ontario, Canada.

Oke, J., Vlachopoulos, N. & Marinos, V. 2014a. *Umbrella Arch Nomenclature and Selection Methodology for Temporary Support Systems for the Design and Construction of Tunnels*. Geotech Geol Eng, 32:97–130.

Oke, J., Vlachopoulos, N. & Diederichs, M.S. 2014b. *Numerical analyses in the design of umbrella arch system*. J Rock Mech Geotech Eng 6(6):546–564.

Peila, D. 2013 *Forepoling design*. In: Ground Improvement, Pre-support and Reinforcement Short Course. Geneva: International Tunnelling and Underground Space Association (WTC 2013); 2013. (I Oke m.fl., 2014a).

Stille, B., Johansson, F., Rios Bayona, F., Batres Estrada, R. & Roslin, M. 2019. *Stockholm Bypass Project - Passage under Lake Mälaren*. In: Proceeding of the WTC 2019 ITA-AITES World Tunnel Congress (WTC 2019), May 3-9, Naples, Italy.

Stille, B & von Matérn, M. 2003. *Dimensionering av 'spiling' under Rosenlundshuset, Götatunneln.* Bergmekanikdag 2003 — Föredrag (Stockholm, Mars 2003), s. 79–89. Stockholm: SveBeFo.

Stille, H. & Palmström, A. 2008. Ground behaviour and rock mass composition in underground excavations. *Tunnelling and Underground Space Technology* 23, pp. 46–64.

Strømsvik, H, Grøv, E & Andersson, H. 2016. *Rørskjerm – dimensjonering og design*. Bergmekanikdagen 2016.

Sturk, R., Annertz, K. & von Matérn, M. 2005. *Tunnelling through a regional weakness zone with extremely poor rock at the Hallandsås Project*. Bergmekanikdag 2005 — Föredrag (Stockholm, Mars 2005), s. 149-159.

Sturk, R. & Brantmark, J. 1998. *Rock mechanical aspects on tunnelling through extremely poor rock at Hallandsås*. Papers presented at Rock Mechanics Meeting in Stockholm, March 18. ISSN 0281-4714.

Söder, C-O. & Åkerlind, A. 2022. Oral presentation at the Swedisk rock mechanics autumn seminar 2022, Stockholm, 2022-11-23.

Terzaghi, K. 1946. *Introduction to tunnel geology.* In R.V. Proctor & T.L. White (Eds), Rock tunnelling with steel supports (p.271). Youngstown, OH: Commercial Shearing & Stamping Co.

Volkmann, G.M. & Schubert, W. 2007. *Geotechnical model for pipe roof supports in tunneling*. In: Proceeding of the 33rd ITA-AITES World tunneling congress, underground spaced the 4th dimension of metropolises. London: Taylor & Francis Group; p. 755-60.

Proceedings of the NROCK 2023
The IV Nordic Symposium on
Rock Mechanics and Rock Engineering
ISBN 978-9935-9436-2-0
DOI 10.33112/nrock2023

Extended ABSTRACT 22
Session 4.5

TIGHT – A research project on modern rock mass grouting techniques

By Chief Scientist Professor Eivind Grøv
(Eivind.Grov@sintef.no)

One important element of tunnelling in urban areas or elsewhere where a strict requirement applies for water control is the technique of rock mass grouting. Norway is one of the countries globally that has been the driver for this development whilst on the other hand the technology is mainly empirical based.

Different approaches exist in the tunnelling industry to reduce groundwater ingress to tunnels to achieve specified leakage limits. The project TIGHT was established to improve Pre-Excavation Grouting techniques though a research-based approach and to take forward detailed understanding of improving high-pressure grouting in tunnels through a combination of work by academics, a PhD, and site-based studies on construction projects. TIGHT aimed at building upon empirical field experience to scientifically optimise the approach to pre-excavation grouting (PEG).

Rock mass grouting is a common method for reducing water inflow in tunnelling projects in hard rock, using cementitious grouts being carried out during excavation. The cost related to grouting constitute 20-30% of the tunnelling costs in projects where the groundwater level must be maintained at a certain level due to urban areas and/or in order to prevent damage to the environment. However, there is a significant unforeseeable aspect of grouting for all parties involved which needs to reduced. Increased knowledge is therefore crucial for optimising the existing grouting methods by reducing the amount of grouting materials used and the time spent on grouting operations. The future in tunnelling would likely implement pre-excavation grouting or rock mass grouting as a standard procedure integrated into the tunnelling cycle.

The official report from TIGHT was issued in Norwegian in 2020, presented to the country's national tunnelling industry over recent months, and its findings have been shared with the national and international tunnelling societies in various ways.

Some of the key outcomes of TIGHT are that even with the risk of jacking the use of high pressure grouting will continue but with an apparent reduction and increased caution to obtain effective spread of the injection. In this context the need of addressing properly cost, time and environmental concerns has an impact on the decision on grout pressure to be applied. While some may view high flow rates of grout to be a good thing due to jacking, it may not therefore always be so effective.

The outcome of the research suggest that the Norwegian approach to grouting would preferably be shifted to have more focused, site-specific designs and procedures. By that, high pressure is a need, but the pressure needs to be balanced with circumstances like in-situ stress, rock overburden and other elements that cause resistance on the grout penetration.

The TIGHT project aimed at combining studies of both theory, laboratory testing and practical tunnelling work to analyse, and better understand, the interplay of multiple variables in the task of high-pressure grouting of rock mass. Researchers looked at variables in particular such as materials, geology, rock mechanics and experience in the field. A vital threshold zone in the studies was the tipping point where hydraulic jacking by the high pressure suddenly opens up cracks wider in a local rock mass, leading to much greater grout consumption.

From numerical simulation it was found that the angle of borehole incidence to crack orientation has little influence on the spread of grout, whilst viscosity has more bearing. The penetration point needs to be open enough to permit and not throttle flow. Water in cracks has some positive effect on grout dispersion.

Enlarged cracks allow the viscous properties of cement to become more dominant to flow behaviour with ensuing consequences for pressure control, especially in small cracks. Grout, then, is also partly diverted from the intended zones, but there can be instances where jacking opens up filled cracks in aid of grouting.

Further, there is no doubt that finding the optimal cement mix is challenging and products with seemingly the same properties behave differently. Therefore, a much more intensive testing would be needed both before commencing the grout works as well as during the works to control that the wanted behaviour of the grout mix is actually achieved and also maintained during the execution of the works.

The research project TIGHT (True Improvement in Grouting High pressure Technology for tunnelling) has improved the understanding and procedures for pre-excavation grouting in such a way that it produces more cost- and time-effective grouting methods that benefit all the participants in this research project, including the public owners who finance the building of road- and railway tunnels through the national budget. Other owners and operators of tunnels and underground openings will benefit from the results of TIGHT as well.

Based on the results from TIGHT, the project-specific solutions should seek local, site-specific approaches to grouting based on a comprehensive design approach covering all elements of the grouting system and controls and held to consistently. By continuously employing the same cement mix design for grout, the same mixing method and equipment, and a faster more rigorous management of jacking risk the workflow processes would have better opportunity to minimise variations in grouting performance. Including the understanding that high or moderate pressure is required to be able to insert cement into cracks and joints in the rock mass, but still have control on the flow. Jacking may not be the key of the problem, rather control of the grouting procedures that follow immediately upon such instances being triggered and this is where research is currently ongoing, ie. how to detect an incident and how to react on the alarms that go off. Widespread and uniform methods from a general solution would not be the expected outcome, whilst project-specific solutions will continue to be required.

TIGHT may have led to development of technology and also benefit projects on time and cost aspects of grouting, however the field of pre-excavation grouting of the rock mass is a huge theme to investigate. There are still lots of issues that could have been developed and dealt with in other research projects; like the understanding on how contract conditions could better reflect grouting quality and quantity; how can the industry better establish relevant laboratory testing on grout penetration on cracks and joints in the rock mass to mention a few, and last but not least, how can we take benefit and learn from the endless amounts of data that is collected at the drilling jumbo and the grouting rig for each grouted hole in the rock mass.

TIGHT is a project that has been financed by the Norwegian Research Council as a competence building project (KPN-BIA) involving a number of participants from the tunnelling industry in Norway; Statens Vegvesen, Jernbaneverket, BASF, Mapei, Geovita, LNS, ITS, Normet, Bever Control, AMV and Veidekke together with NGI, NTNU and SINTEF.

Picture shows preparations for pre-excavation grouting at Implenia/Acciona tunnel face in Moss. Picture by AMV

Proceedings of the NROCK 2023
The IV Nordic Symposium on
Rock Mechanics and Rock Engineering
ISBN 978-9935-9436-2-0
DOI 10.33112/nrock2023

Savilahti Underground Sport and Event Center

Paula Pohjanperä (paula.pohjanpera@ains.fi)
AINS Group
Espoo, Finland

Pieti Haapala, Veera Tasapuro, Erik Johansson,
AINS Group
Espoo, Finland

ABSTRACT

An underground sport and event center is being constructed in the area called Savilahti, located in the city of Kuopio. The facility is designed for 2500 people but it also serves as a civil defence shelter for 7000 people. This type of concept is very common in Finland. The span of the largest cavern hall is 50 m which is the largest underground span in Finland. The length of the cavern hall is 88 m, height 17 m and total volume 88 000 m^3. Interesting feature is, and also a challenge that Savilahti cavern utilizes the old existing underground caverns that were built already in late 1930's and served for military purposes. Savilahti cavern is situated relatively close to the rock surface with minimum rock roof around 15 m. The cavern is situated in tonalitic gneiss and granite with good properties and quality, but the area has also joints and several fracture zones that needed rock investigations and special attention in the design process. Rock mechanics simulations were performed with 3DEC-code to ensure the cavern stability and fulfill the requirements for the civil defense shelter.

At the time of writing this abstract the construction works are underway. The cavern was excavated during 2021-2022. The photogrammetry was intensively used e.g. for rock mapping, modelling, grouting and rock support design The rock monitoring with several extensometers were also performed during excavation. The results showed that the measured displacements were close (a bit less) to the anticipated ones. Savilahti underground sport and event center will be completed and ready for use in spring 2024.

Figure 1. Savilahti Underground Sport and Event Center (Photo: LUOLA, www.savilahti.com).

Proceedings of the NROCK 2023
The IV Nordic Symposium on
Rock Mechanics and Rock Engineering
ISBN 978-9935-9436-2-0
DOI 10.33112/nrock2023

EXTENDED ABSTRACT
Session 3

Extreme Challenges in Vadlaheidi Road Tunnel Case History

Oddur Sigurðsson (osha@vegagerdin.is)
Icelandic Road and Coastal Administration

ABSTRACT

Vadlaheidi road tunnel is in the Northern part of Iceland. The tunnel's cross-section is according to Norwegian design guidelines and is called T9.5, with a cross-sectional area of approximately 66 m^2. The total length of the tunnel in rock is 7.2 km and it connects Eyjafjordur in the west to Fnjoskadalur in the East.

Figure 1. Location of Vadlaheidi road tunnel

Tunnel excavation started in July 2013 and the tunnel was opened for public traffic late December 2018, about two years later than originally scheduled.

There were two main reasons for this delay. Firstly, high water temperature and inflow of hot water that caused extremely poor working conditions and frequent grouting operations during the tunnel excavation from the west side. Secondly, an extreme collapse in the tunnel on the East side, causing a large inflow of relatively cold water resulting in filling and closing the tunnel for months.

Tunnel excavation from the West side started on July 3rd, 2013. On February 15th, 2014, a large inflow of 46°C hot water, approximately 350 l/s, occurred. The total length of the tunnel was at that time 1870 m. The excavation was continued with very frequent grouting operations, increasing water temperature and rapidly decreasing working conditions. It was therefore decided to post grout the area. The grouting work was executed in June and July of 2014. Although a relatively successful post-grouting operation the working conditions were extreme due to water and rock temperature up to around 63°C. Late

August the contractor decided to stop the excavation and move to the East side. The tunnel length at the west side was at that time 2695 m.

Figure 2. Inflow of 46°C hot water, total of 350 l/s.

Tunnel excavation from the East side started on September 5th, 2014. After relatively successful tunnel excavation work, an extreme collapse occurred on April 17th, 2015, from a 10 m wide fault zone. The tunnel length was at that time 1475 m.

Figure 3. Collapse in the tunnel

Shortly after the collapse, an inflow of 7°C cold water of up to 518 l/s followed. The tunnel was filled with water and tunnel excavation consequently stopped.

Pumping of water from the tunnel started in October 2015 and preparation work for continuing tunnel excavation started in January 2016. After successful grouting and consolidation grouting work, as well as very heavy reinforcement of the roof part, using a pipe umbrella, to excavate through the fault zone, tunnel excavation commenced on the East side on October 19th, 2016 and break-through was obtained on April 28th, 2017.

Proceedings of the NROCK 2023
The IV Nordic Symposium on
Rock Mechanics and Rock Engineering
ISBN 978-9935-9436-2-0
DOI 10.33112/nrock2023.17

Digitalization in rock mechanics: A parametric design for numerical models in Norway

Mario Morales C. (mario.morales@sintef.no)

Mario Morales C.
SINTEF Community, dept of Rock and Soil Mechanics, Trondheim, Norway
Yared Bekele
SINTEF Community, dept of Rock and Soil Mechanics, Trondheim, Norway

ABSTRACT

Determination of stress magnitude and orientation plays a vital role in rock mechanics and the underground works industry. Local stress fields are disturbed during excavation and new induced stresses influence the surrounding rock mass. Information about their magnitude and orientation is crucial because in some cases the rock strength is exceeded, resulting in instabilities which can have undesired consequences. In turn, the stress state of the rock mass may vary with diverse locations because of factors such as regional tectonics, geology, and/or topography. A rule of thumb points out that on early stages the engineer should search for stress information on a radius of 50 km. Due to scarce and restricted information this is not always possible. For example, Norwegian hydropower depends on knowledge of local rock stresses in order to find the best location and design of solutions in the underground, and to minimize the need for steel lining in pressurized tunnels.

As part of the NoRSTRESS project, the authors have created a shallow 3D model of Norway where it is possible to extract a given area by centre and square side size on a 20 m resolution. This allows for fast and accurate creation of volumes and meshes for further numerical modelling on different scales. There is no evidence of such an effort in the literature for any other country. The results are expected to help evaluating stress magnitude and orientation on early project stages as well as to contribute to develop a 3D stress map of Norway. To have a better overview and understanding of the ground conditions to come will be useful, not only for the hydropower industry, but also for the emerging mining business.

KEYWORDS

parametric design; rock mechanics; numerical modelling; rock stress

INTRODUCTION

The preparation of 3D models is an important step in the analysis and design process. It could contribute to significant time savings in the long-run (and thereby cost) if done efficiently. Parametric 3D modeling is a method of creating 3D models that uses parameters or variables to define and control the shape, size, and other properties of a model. In parametric modeling, relationships between different parts of the model are established through mathematical formulas and algorithms, allowing for quick and easy adjustments to be made to the model, thus eliminating the need for constantly redrawing a design every time changes are made to the model. This approach contrasts with traditional 3D modeling, where shapes are created and modified directly through manipulation of the model's geometry, allowing for greater control, flexibility, and efficiency in the design process. The method has been widely used in civil engineering for structural analysis and design, infrastructure design, water resources management, and geotechnical engineering. Various software tools are available for this purpose and some of the most commonly used ones include Solidworks and Rhino with Grasshopper.

Within geotechnical engineering, 3D models are created for various underground infrastructure projects such as excavations, deep foundations and tunnels. Design and construction of such geostructures could benefit greatly from parametric modelling through time savings and seamless collaboration between project stakeholders. In rock and soil mechanics, parametric modeling has been employed to study the behavior of soil and rock masses and to design foundations, slopes, and retaining structures. This can involve using software such as FLAC 3D, PLAXIS or GEO5 to create numerical models of soil and rock behavior and simulate their response to loads and boundary conditions. Detailed knowledge of stresses is an essential component in rock mechanics to improve numerical modeling and understanding of rock behavior in underground mining, civil engineering, and geological applications. Several cases of utilization of parametrical modelling for design of underground structures can be found in the literature: an underground parking project in an urban area in Lisbon [1], and the subway extension in Stockholm [2] are two good examples of such utilization. No evidence of application of parametrical modelling for the preparation of numerical models has been found in the literature.

By using parametric design in numerical modeling for rock mechanics, engineers and geologists can streamline the process of model building and meshing and dedicate more time to gain a more comprehensive understanding of rock stress behavior, and make informed decisions on design, construction, and stability of underground structures. This is in accordance with an important premise of the use of parametric modeling in underground infrastructure projects: to improve the basis for decision making at early stages to reduce project risks and thereby reduce project costs. This can be conveniently illustrated by the so-called MacLeamy's effort curve in Figure 1, which illustrates the effects of decision making at different stages of an infrastructure's lifecycle.

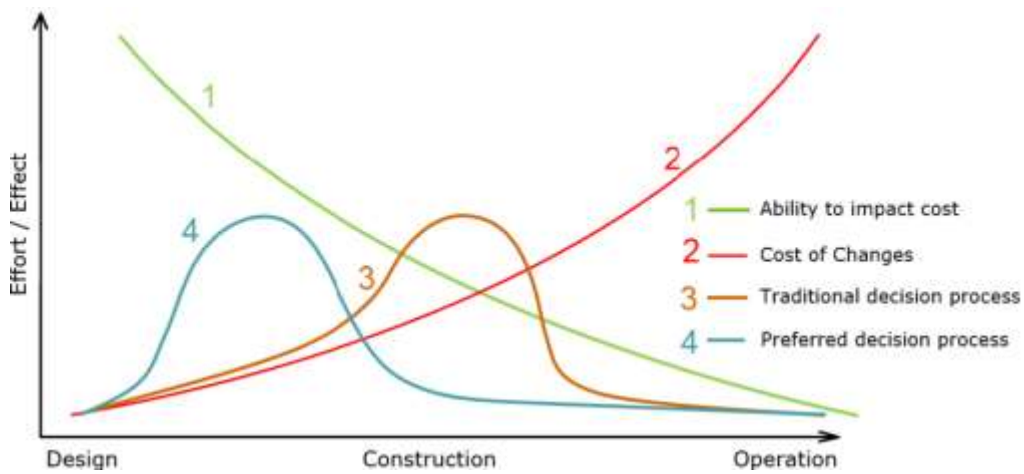

Figure 1: MacLeamy's effort curve [1].

While there has been substantial progress in the use of parametrical modeling for infrastructure above the ground, application to subsurface infrastructure in soils and rocks started receiving attention only in recent years [3]. Unforeseen ground conditions are often the most common source of uncertainty in large infrastructure projects with 37% of project overruns being due to ground problems [4]. It is estimated that 70% of public projects were delivered late and 73% were over the tender price [5]. Some estimates further show that unforeseen ground conditions could increase project costs for example by up to 8% and extend project duration by about 10% [6]. In the context of the present article, the purpose of applying parametric design solutions for the subsurface should be reducing the risk from unforeseen ground conditions due to rock stresses [3][1]. In addition to aiding the challenges related to ground conditions, the application of parametric design has a huge potential towards contributing to the green shift and sustainable infrastructure development.

1. SOFTWARE AND HARDWARE

The study has been done in a last generation computer with the following specifications:

- Intel-I9 12900KS CPU
- 64GB DDR5 RAM at 5200MHz.
- Asus ROG Maximus Z690 motherboard.
- Gigabyte GeForce GTX 1660 Ti video card.

- 2TB solid state drive (SSD) and 12TB hard disk drive (HDD).

Parametrical modelling has been done with the use of Rhino and Grasshopper, while the creation of FLAC 3D-compatible meshes has been done with a Rhino plugin called Griddle. Rhino and Grasshopper are both popular tools for parametric 3D modeling, especially in architecture and design fields. Rhino is a 3D modeling software that provides a comprehensive set of tools for creating and editing 3D models. It has a strong emphasis on precision and accuracy, and is widely used for industrial design, jewelry design, and architectural visualization. Grasshopper, on the other hand, is a visual programming language that runs as a plugin for Rhino. It allows users to create complex and dynamic 3D models using a graphical user interface, without the need to write code. In Grasshopper, users can define geometric relationships between different parts of a model using nodes, which represent mathematical operations or geometric transformations. Finally, the Griddle plugin for Rhino is a tool that is primarily used for creating parametric surfaces and meshes in Rhino. It allows users to create custom grids, or "grids of points," that can be used as a base for creating a variety of surfaces and meshes. The plugin also includes several tools for manipulating and refining the grid, such as the ability to add or remove points, adjust the spacing between points, and create irregular grids. Anyway, depending on the complexity of the mesh and the processing power of your computer, this process may take some time and require some optimization to ensure that the mesh is suitable for use in FLAC 3D.

By using Griddle and Grasshopper in combination with Rhino, users can create highly flexible and responsive 3D models that can be adjusted and updated based on changing design requirements and lately exported to a FLAC 3D-compatible format. The automatized process can significantly speed up the design and avoid engineers to focus on repetitive tasks.

2. METHODOLOGY

The following is the methodology for creating the parametric 3D model of an area of a given size from an orthophoto of Norway using QGIS and Rhino. Note that this is a general approach, and the specific steps may vary depending on the details of the project and the versions in use of QGIS and Rhino, Grasshopper and Griddle. The general steps are:

1) Import the orthophoto into QGIS. The orthophoto used is based on European Terrestrial Reference System 1989 ensemble (EPSG:6258). It has a limited accuracy of at best 0.1 meters.
2) Extract contour lines at different intervals from the orthophoto in QGIS. Intervals were chosen thinking on the future use and extension of the model, at 200m, 100m, 50m, 20m and 10m.
3) Import the desired contours into Rhino. Assign them to a surface feature on Grasshopper. This gives the flexibility to alternate between different contour resolutions without repeating the design process.
4) Define the area of interest by selecting a point on screen and assigning it to the initial point feature on Grasshopper. These areas were selected based on an internal rock stress measurement database from SINTEF, shown in Figure 2 as a heatmap. Exact locations cannot be disclosed due to confidentiality reasons. The ultimate idea is to be able to calibrate the numerical models based on actual measurements in areas with good availability of information and afterwards run it in areas with few or no datapoints and check the degree of accuracy of the predictions. Therefore, it is extremely useful to be able to quickly shift areas and sized during the design phase.

The following steps were automatized and parametrized on Grasshopper based on the initial selection on 4).

5) Contour clipping. This involved selecting and cutting contour lines that can be fully or partially inside the area of interest.
6) Create the surface terrain model. Meshes were created using Delaunay triangulation and regular squares.
7) Extrude the surface to create a box for a 3D representation of the area of interest.
8) Identify possible fault zones and at its correspondent surface lines. Manually define dip and direction. The algorithm generates the rest of the geometry based on faults crossing the whole block or just partially contained on it.
9) Export the terrain model from Grasshopper to Rhino.

To export the 3D model created in Rhino for use in FLAC 3D, one needs to export the model in a format that is compatible with the latter. The most common format for this purpose is the f3grid format. This was done using the Griddle plugin and the following steps:

10) Select the 3D box from 6) and the faults from 8) and create the initial mesh. The initial mesh is not very good, but it will be remeshed in future steps.
11) Intersect all meshes. The process allows to define a tolerance for the intersection. All other parameters were kept at defaults.
12) Select all objects again with and use Griddle Surface command to remesh the meshes from 11). It is very important to select eventual fault borders as well, because they will serve as hard edges to preserve conformity with the 3D box mesh. Parameters such as the overall block shape, and minimum and maximum edge length were found to be very relevant for further steps.
13) Do the volume meshing with the Griddle Volume. This tool typically marks parts of surface meshes causing meshing errors with red outlines.
14) Open FLAC 3D and import the f3grid file exported from Rhino. The 3D model should now be ready to use in the FLAC 3D simulation.

Using the Griddle tools to create a mesh from the contour lines or point data is a finicky process and the selection of parameters highly influences the corrections to be done and errors to be solved for achieving a successful geometry export.

Note that this is a general methodology, and the specific steps may vary depending on the details of the project and the versions in use of QGIS and Rhino, Grasshopper and Griddle.

Figure 2: Locations of existing rock stress measurements (red) and parametric model areas (boxes in blue) in Norway.

3. RESULTS

3.1. Processing Times

3.1.1. Contour lines

The processing time for generating contour lines from an orthophoto of the whole of Norway (4Gb in size) in QGIS depends on several factors such as the processing power, complexity of the terrain, and the selected contour interval. A rough estimate of the processing time for generating contour lines at different intervals might vary from a few seconds (in 200m scale) to minutes in extent (in 10m). In general, it is obvious than the shorter the interval the longer to process. These estimates are rough and may vary depending on several factors, as mentioned earlier. Actual processing time for the different cases are shown in Table 1:

Table 1. Processing time for contour line extraction

Contour [m]	Time [s]
200	53
100	104
50	231
20	694
10	1345

From the table, we can conclude that the processing time increases significantly as the interval between contours decreases. This is expected as the calculations become more complex and computationally intensive when the intervals are smaller. We can also see that the difference in processing time between intervals of 200 meters and 100 meters is relatively small compared to the difference between intervals of 50 meters and 20 meters or 20 meters and 10 meters. This indicates that the processing time do not increase linearly with decreasing interval size. Extrapolating processing times for intervals of 5 meters and 10 centimeters based on the given data is straightforward with a power regression (R2 = 0,997). We can estimate that the processing time for a 5-meter interval may be around 2 983 seconds (or 50 minutes) and the processing time for a 10 centimeter interval may be around 222 303 seconds (or 2,6 days). The latter may not be possible to reach due to floating storage/memory constraints.

Even though the orthophoto can be clipped to a minor extent in QGIS, and therefore allow for extraction of contour lines on intervals of 10m and even smaller, this creates a repetitive task for each time a new location and area is to be chosen.

3.1.2. Computing time versus square side/area

Equally as the case of contour lines, the processing time for a parametric model clipping contour lines at 20m interval for a given area depends on several factors such as the processing power, complexity of the terrain, and the selected contour interval. Figure 3 presents an overall overview of the four squares side sizes tested during the project: 25, 10, 5 and 1km. Table 2 presents the processing times in minutes for contour curves of whole Norway being clipped at specific locations with different sizes using a parametric model in Grasshopper. The first and second columns indicates the side of the square and its area, with the previously mentioned values of 25, 10, 5 and 1 kilometers. The next three columns show the processing times for each area, namely North, West, and East. Table 2 can be used to compare the processing times for different area sizes and regions, which may be useful for optimizing workflows and improving efficiency in contour curve processing.

Table 2. Processing time for contour clipping and 3D model building.

Side size [km]	Surface [km^2]	Processing time [min]		
		North Area	West Area	East Area
25	625	8,0	11,1	2,4
10	100	17,3	39,8	3,0
5	25	9,1	1,2	12,7
1	1	6,8	5,8	25,3

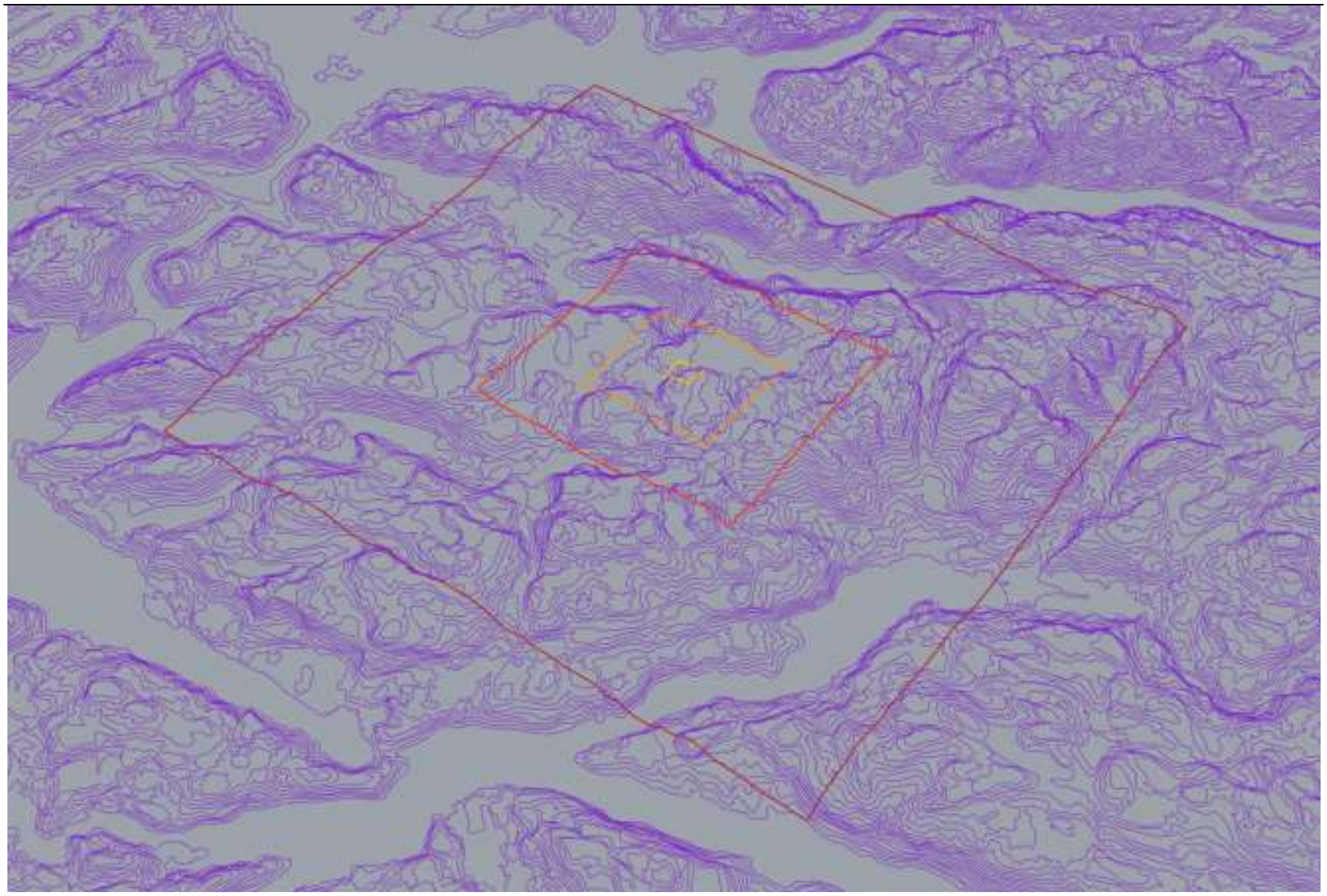

Figure 3: Areas for testing parametrical model building (square side 1km (yellow), 5km (orange), 10km (red), and 25km (dark red)).

Based on the data in the table, it appears that the minimum processing time varies depending on the size of the square area and the specific region of Norway being processed. Upon closer inspection of the table, it appears that the processing times for the East Area of Norway are actually longer for the 5 km and 1 km square side sizes compared to the 25 km and 10 km sizes. This suggests that the processing time is not solely determined by the area size, but also influenced by other factors such as data density, complexity of terrain, and algorithm efficiency.

Furthermore, the minimum processing time for each area is not consistent across different area sizes. In the North area, the minimum processing time is for the 1km area size. In the West area, the minimum processing time is for the 5km area size. Finally, in the East area, the minimum processing time is for the 25km area size. Therefore, the minimum processing time varies for different area sizes and regions, and it may be necessary to optimize the area size based on the specific region and processing requirements. The times obtained can be useful information to select an appropriate square size for generating 3D models in numerical simulations, where computational efficiency is crucial for obtaining results in a reasonable amount of time.

Additionally, two supplementary models were generated for the East Area, for 50km and 100km sizes, with processing times of 2.9 and 4.4 minutes, respectively. These results suggest that larger area sizes may lead to more efficient processing times, with a significant reduction in processing time observed at the 25km size. The findings may be useful for optimizing workflows and improving efficiency in contour curve processing for the East Area of Norway. These phenomena was not observed on the other areas and calls for future analysis.

3.1.3. Minimum element size to model side ratio versus meshing errors

Each of the 12 squares (4 on each region) were used to automatically generate 3D models of a region. In turn, these 3D models were used to generate 3D volumes to be exported to FLAC 3D. The overall block shape, was kept the same, while the minimum and maximum edge length were iterated at different ratios with respect to the edge size and compared to the number of errors. The minimum edge length determines the smallest allowable edge length in the mesh, while the maximum edge length determines the largest allowable edge length. By adjusting these parameters, it is possible to create a mesh with the appropriate level of detail for the intended use case while minimizing errors. There is no universal optimal edge size that works for all meshing applications, even though There are several publications that discuss mesh generation and optimization for different applications [7][8][9], none of them are in rock mechanics. The appropriate edge size depends on various factors such as the geometry of the object being meshed, the desired level of detail, and the computational resources available.

The errors considered were Meshing Error, Naked Edges and Clashing Faces. Meshing errors, naked edges, and clashing faces are common issues that can arise when using Griddle. Meshing errors occur when the mesh is not properly formed or has inconsistencies, such as overlapping vertices or incorrect face connections. These errors can result in an irregular or distorted mesh, making it difficult to create accurate and precise models. Naked edges are edges of a mesh that are not connected to any faces, which can occur when creating or modifying a mesh. Naked edges can create problems during the volumetric meshing process, as they can cause gaps or holes in the final exporting of the model. Clashing faces occur when two or more faces of the mesh intersect or overlap each other, which can also cause issues during the meshing and exporting process. It is important to identify and fix clashing faces to ensure the mesh is accurate and can be printed properly. Errors are shown in the red screen as illustrated in Figure 4. No faults or weakness zones were considered during the process.

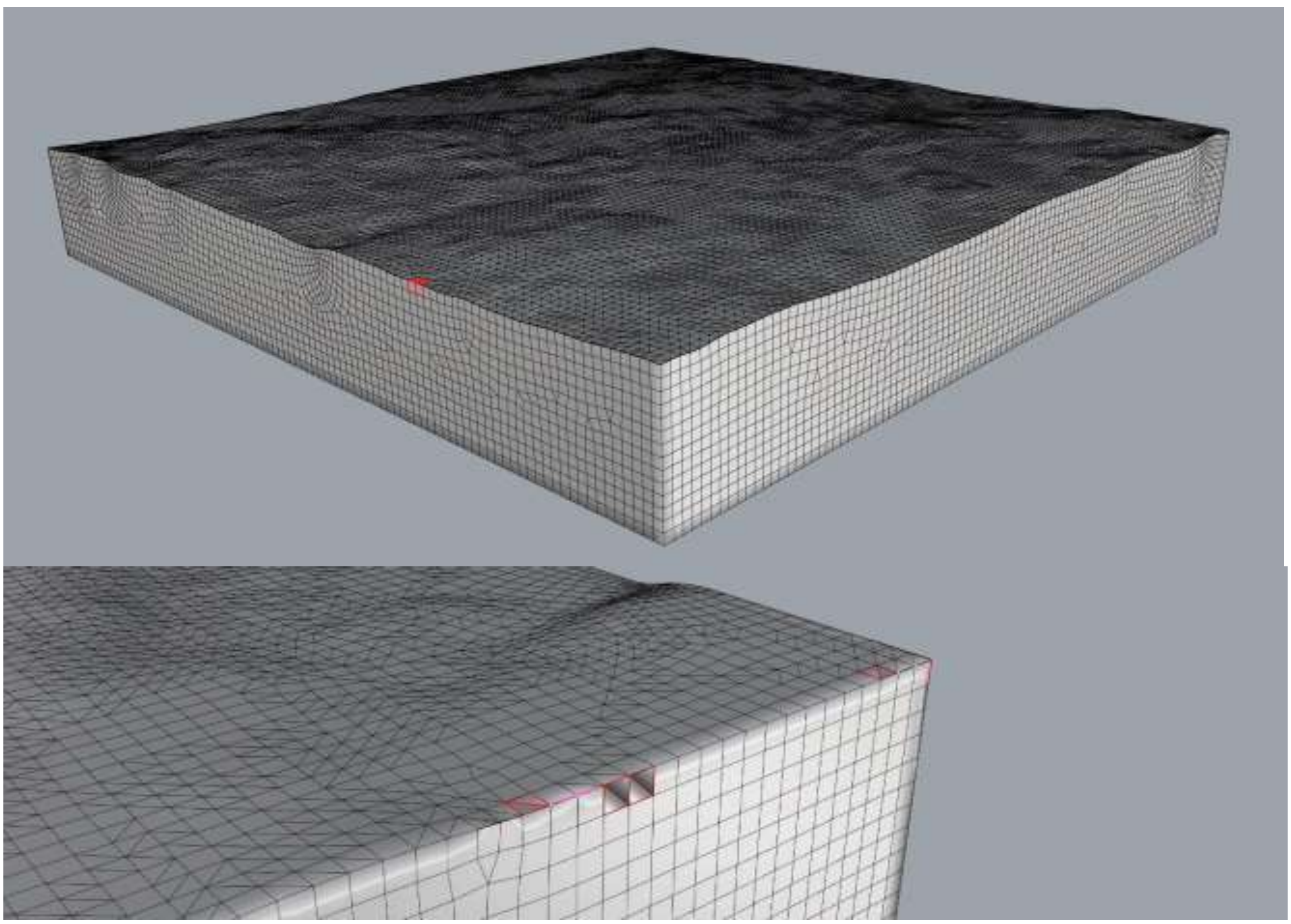

Figure 4: Meshing errors for one of the 3D models (Top: general overview; bottom, detail of clashing faces (red), meshing errors (dots) and naked edges (pink)).

Table 3 presents information on the squares side size, ratio, minimum and maximum edge length, meshing errors, naked edges, clashing faces, and status of the exporting process of the 3D models for the Eastern Area. The ratio column represents the aspect ratio of the minimum edge size of the mesh elements, while the maximum has been fixed at 10 times the minimum. The status column provides information on the final outcome of the export process without further healing of the meshes. Meshing errors, naked edges, and clashing faces are also reported in the table, which may help identify potential issues with the mesh. This information can be useful for assessing the quality of the mesh and making any necessary adjustments to optimize its performance.

Table 3. Summary of errors and status outcome.

Side size [km]	Ratio	Minimum edge [m]	Maximum edge [m]	Meshing Errors	Naked Edges	Clashing Faces	Status
25	1 to 20	1250	12500	25	1	0	Not Meshed
	1 to 100	250	2500	2	0	2	Meshed
	1 to 200	125	1250	12	0	1	Not Meshed
10	1 to 20	500	5000	17	1	0	Not Meshed
	1 to 100	100	1000	5	0	1	Meshed
	1 to 200	50	500	12	2	0	Not Meshed
5	1 to 20	250	2500	2	5	0	Meshed
	1 to 100	50	500	1	2	2	Not Meshed
	1 to 200	25	250	12	5	6	Not Meshed
1	1 to 20	50	500	29	4	2	Not Meshed
	1 to 100	10	100	1	0	1	Meshed
	1 to 200	5	50	4	5	4	Not Meshed

The table shows that meshing with a minimum edge to side size ratio of 1 to 100 results in the lowest number of meshing errors, naked edges, and clashing faces, while maintaining an acceptable range for the minimum and maximum edge lengths. Comparing it to a ratio of 1 to 20, we see an increase in all error types and a decrease in the maximum edge length, indicating that the mesh is too coarse. On the other hand, comparing it to a ratio of 1 to 200, we see a decrease in errors, but also a significant decrease in the minimum edge length, indicating that the mesh is too fine. Therefore, it can be concluded that a ratio of 1 to 100 provides the optimal balance between mesh quality and computational efficiency. Furthermore, it should be noted that using a minimum edge to side size ratio of 1 to 100 not only reduces meshing errors, naked edges, and clashing faces, but also leads to more successful exports to FLAC 3D.

4. CONCLUSIONS

Object - based parametric modelling is a major change for the building industry that is greatly facilitating the move from a drawing - based and handcraft technology to one based on digitally readable models that can be exchanged with other applications. Parametric modelling facilitates the design of large and complex models in 3D but imposes a style of modelling and planning that is foreign to many users. Like CAD, it is most directly used as a documentation tool separate from designing. A growing number of companies, however, use it directly for design and for generating exciting results.

As expected, the present work shows that processing times for generating contour lines from an orthophoto of the whole of Norway in QGIS increases significantly as the interval between contours decreases. Anyway, the difference in processing time between intervals of 200 meters and 100 meters is relatively small compared to the difference between intervals of 50 meters and 20 meters or 20 meters and 10 meters, indicating that the processing time does not increase linearly with decreasing interval size. This supposes a trade-off between resolution and computing times. On this side, clipping the orthophoto to a minor extent in QGIS allows for extraction of contour lines on intervals of 10m and even smaller, but this creates a repetitive task for each time a new location and area is chosen.

Once the contour lines have been generated, the processing time for a parametric model clipping such contour lines at a given area depends on several factors such as the processing power, complexity of the terrain, and the selected contour interval. The processing times for different area sizes and regions may vary depending on data density, complexity of terrain, and algorithm efficiency. The minimum processing time for each area is not consistent across different area sizes, as it varies for different area sizes and regions, and it may be necessary to optimize the area size based on the specific region and processing requirements. The times obtained can be useful information to select an appropriate square size for generating 3D models in numerical simulations, where computational efficiency is crucial for obtaining results in a reasonable amount of time. The results show that there seem to be an inflection point on all three areas, but at different sizes. Further research on these findings may be useful for optimizing workflows and improving efficiency in contour curve processing for the East Area of Norway.

On the exporting side, it is found that using a minimum edge to side size ratio of 1 to 100 not only reduces meshing errors, naked edges, and clashing faces, but also leads to more successful exports to FLAC 3D. It seems that the 1 to 100 ratio strikes a good balance between mesh density and computational efficiency, resulting in smoother and more accurate numerical models. Therefore, based on the findings and the surface topography and conditions it is recommended to use a minimum edge to side size ratio of 1 to 100 when building surface meshes for numerical modeling in FLAC 3D or similar software. Adjusting the minimum and maximum edge length in the mesh can create a mesh with the appropriate level of detail for the 3D models of the region. The optimum ratio of minimum element size to model side length may vary depending on the specific region, and a high ratio may lead to an increase in meshing errors.

Overall, the article discusses the advantages and challenges of object-based parametric modeling in the building industry, which enables the design of complex 3D models that can be exchanged with other applications. Even though the processing time for generating contour lines from an orthophoto in QGIS increases significantly as the interval between contours decreases, the clipping time of such contour lines at a given area depends on several factors such as processing power and complexity of terrain. These results are expected to help building a baseline for estimating the maximum radius of influence of stress measurements to accurately forecast stress conditions in other location.

The authors are of the opinion that the full potential of this enabling capability within Geotechnics and Engineering Geology is to be developed during the next decade because its implications and new uses are discovered gradually. What is currently known is that object - based parametric modelling resolves many of the fundamental representational issues in architecture and construction and allows quick payoffs for those transitioning to it, even with only partial implementation. These payoffs include a reduction in drawing errors due to the built-in consistency of a central building model and the elimination of design errors based on spatial interferences. The same is expected to be developed for Geotechnics and Engineering Geology over the coming years.

5. ACKNOWLEDGEMENTS

This paper is written as part of research project NoRSTRESS. The authors would like to thank The Research Council of Norway and partners (Hafslund E-CO AS, Hydro Energi AS, Sira-Kvina Kraftselskap DA, Skagerak Kraft AS, Statkraft AS, and NTNU) for financially support for the project.

REFERENCES

[1] Gondar, J., A. Pinto, and Z. Sampaio, Study of BIM applied to a geotechnical project - a 5D/BIM approach. 2019.
[2] Stelzer, M., et al., BIM processes and workflows using the example of the subway extension in Stockholm. Geomechanics and Tunnelling, 2018. 11(4): p. 340-347.
[3] Morin, G., et al., Case study–the real life benefits of geotechnical building information modelling. 2014: p. 95-102.
[4] Office, N.E.D., Faster building for commerce. 1988, HMSO London.
[5] Office, N.A., PFI: Construction performance. Rep. by the Comptroller and Auditor General, HC 371, Session 2002-03, 2003.
[6] Tawelian, L.R. and S.B. Mickovski, The implementation of geotechnical data into the BIM process. Procedia engineering, 2016. 143: p. 734-741.
[7] Liu, Y., Zhang, Y., & Zhang, W. (2017). Numerical simulation of airfoil flutter under gusty conditions. Journal of Aerospace Engineering, 30(2), 1-10. https://doi.org/10.1061/(ASCE)AS.1943-5525.0000665
[8] Jones, B., Smith, K., & Lee, T. (2019). Optimizing wind turbine blade design for enhanced efficiency. In Proceedings of the International Conference on Renewable Energy (pp. 100-105). Springer. https://doi.org/10.1007/978-3-030-12549-0_12
[9] Anderson, J. D. (2017). Computational fluid dynamics: The basics with applications. McGraw-Hill Education

Proceedings of the NROCK 2023
The IV Nordic Symposium on
Rock Mechanics and Rock Engineering
ISBN 978-9935-9436-2-0
DOI 10.33112/nrock2023.18

Strategic management of water-filled tunnels

Andrius Rimsa (andrius.rimsa@loxus.com)

Andrius Rimsa
Loxus Consulting, Stockholm, Sweden
Dave Malak
Hibbard Inshore, LLC, Auburn Hills, MI, USA
Mikko Simola
Loxus 3D Tunnel Inspections, Helsinki, Finland

ABSTRACT

In Scandinavia and worldwide, rock tunnels are largely used to transport water in many industries and municipal activities, e.g. hydro and nuclear power, water transport for drinking and wastewater, raw water supply to industrial facilities, etc. These tunnels are usually constantly filled with water but need monitoring and maintenance inspections at regular intervals.
According to the Swedish Energiforsk report (2021:730) "Inner waterways in a hydropower plant commonly have very limited access for inspections and some have never been inspected since the commissioning. Many plant owners lack systematic management of the inner waterways”. We do believe that this problem exists not only in Sweden and not only in hydropower plants.
Degradation of tunnel structure has many similarities in dry and water-filled tunnels; in the water-filled state, however, the hydrostatic pressure and its variation as well as physical erosion by flowing water are also added as possible negative factors.
Tunnel inspections must affect operations as little as possible. This can be achieved by performing inspection and maintenance with a ROV (Remotely operated vehicle) equipped with sonar, cameras and measuring instruments without emptying the tunnel of water and under safe working conditions. The combination of the correct size of the ROV and the length of the cable allows the inspection of tunnels of up to 20 km from a single-entry point.
We present the technical capacity of ROVs equipped with 3D sonar and examples of geological interpretation of inspection results from water-filled tunnels and maintenance solutions. We argue that a ROV equipped with 3D multibeam sonar is currently the most advanced instrument for performing inspections of water-filled tunnels in a safe work environment manner and should be considered as one of the tools for strategic management of inner waterways.

KEYWORDS

Hydropower; ROV; sonar; inspection; tunnel

INTRODUCTION

In Scandinavia and worldwide, rock tunnels are largely used to transport water in many industries and municipal activities, e.g. hydro and nuclear power, water transport for drinking and wastewater, raw water supply to industrial facilities, etc. These tunnels are constantly filled with water but need monitoring and maintenance inspections at regular intervals. Due to limited accessibility, challenging dewatering procedures and associated work environment risk, conventional inspections in dry conditions are rare or executed at irregular intervals.
The strategic management plans for any industry must indicate the risks and plan for mitigating actions to secure continuous operations and long-term safety. An accident that affects operation can cause a long rehabilitation

time and associated high costs as well as production break which can become more costly than rehabilitation itself.
When it comes to tunnels, many parameters must be encountered to produce a reliable risk assessment. Some of these parameters depend on geotechnical conditions, construction methods or material types and can be challenging to assess without proper documentation and monitoring.
Developing a strategic management plan with regular inspection and maintenance plans might contribute to secure operation and avoidance of unexpected failures. In water-filled tunnels, an inspection with the ROV should be considered an important tool and should be considered a necessary part of the management plan.

1. DEGRADATION OF TUNNEL STRUCTURAL INTEGRITY

Degradation of a tunnel structure has many similarities, regardless of whether it occurs in dry or water-filled tunnels. In a water-filled state, the hydrostatic pressure and its variations, as well as abrasive water flow, are added as possible influencing factors. The main features affecting the structural integrity of a water-filled tunnel can be summarized as:

- Degradation of the rock mass (e.g. due to poor rock quality, swelling clays, blasting damage and rock stresses).
- Degradation of rock bolts (e.g. corrosion of unmolded bolts, leaching of cement mortar, chemical degradation of cement mortar)
- Degradation of shotcrete/cast concrete/lining (e.g. carbonation, leaching, erosion, corrosion of fibers/mesh, spalling).
- Variations in hydrostatic water pressure (e.g. pressure stroke, swelling or negative pressure during load changes or shutdowns).

2. MAINTENANCE STRATEGY FOR WATER-FILLED TUNNELS

At present, to our knowledge, there are no industry practices, manuals/guidelines or international/national regulatory requirements for the inspection of water-filled tunnels. Tunnel owners handle the maintenance based on their own best practice. The Swedish Energiforsk report (2021) suggested minimum inspection intervals for inner waterways in Hydropower plants depending on different parts of the power plant. The parts between the intake gates and the draft tube gate should be inspected at an interval of 6 to 12 years. The parts outside these gates should be inspected for at least the interval of 25-50 years. The advice on planning, requirements, and execution is suggested in the report. It remains to see if the suggested management strategies will be adopted by the industry.

3. ROV/AUV

An ROV can operate in a tunnel without dewatering and under safe working conditions. A so-called ROV (Remotely Operated Vehicle) or AUV (Autonomous Underwater Vehicle) equipped with sonar, cameras, and instruments for measuring and sampling is used. The main difference between these vehicles is that ROV is operated with an external power supply and AUV is powered by an internal battery. An AUV (Figure 2) can run in fully automatic mode or be operated by a pilot. In piloted setup, the AUV uses a fiberoptic cable to enable communication between the pilot and a vehicle. An ROV has the advantage of an unlimited amount of time for operation but has distance limitations due to the power supply tether. A distance of up to 7 km from the entrance point is reachable with the ROV. An AUV, on the other hand, has a limitation on battery capacity and time of operation is limited, however distances of more than 20 km from the entrance point can be reached.
For tunnel inspections, so-called ‘inspection’ or ‘mid-sized ROVs’ are most often used (Figure 1). They usually weigh between 100kg and 1,000kg and are optimized for medium depth and long range.
The ROV/AUV can be adapted to specific needs and tunnel dimensions. Factors to be considered in the choice of ROV/AUV are tunnel length, size and layout; the size of the inspection hatch; and possible obstacles in the tunnel. The challenge is to achieve an optimal balance between the size and thrust power to be able to navigate in close spaces, and at the same time in the case of ROV, be able to pull the tether (data cable and power supply) for long distances from the access point.
The access point to the tunnel varies and can be an open water basin, swell tower, inspection hatch or access tunnel. At the water surface, the ROV/AUV is released and moves submerged in the water using thrusters. Tether for power and data transmission has the same density as water, providing neutral buoyancy and permitting long-distance runs. ROV/AUVs typically move at an average speed of 1km/h.

Figure 1. Several types of ROV. Loxus Explorer (left) 3D sonar, remote cameras, LED lights, range up to 7km; SEAMOR Marine Chinook - multibeam sonar, cameras, lighting, range up to 2000m.

Figure 2. AUV (Saab Sabertooth. Double hull) can be equipped with 3D sonar, remote cameras, LED lights, range of more than 20 km.

An important feature for correct sonar data calibration is an Inertial Navigation System (INS) used in ROV/AUV. Inertial Positioning System continuously calculates the position, orientation, and velocity, of the moving vehicle and associated sensors without the need for external references (Figure 3). The INS consists of a Ring Laser Gyro (RLG) or Fiber Optic Gyro (FOG) and a Doppler Velocity Log (DVL).

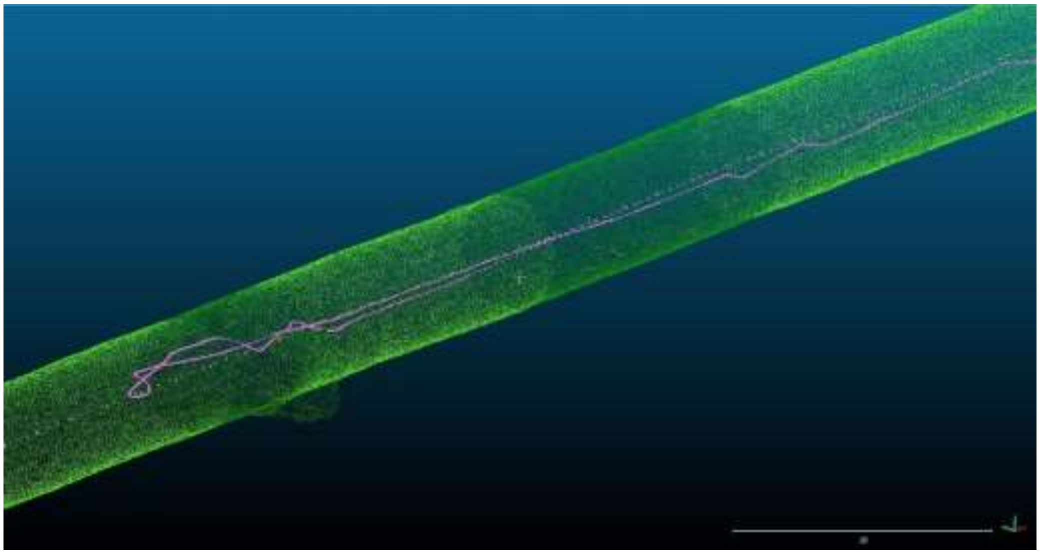

Figure 3. 3D model of a circular tunnel with the path of ROV. The 3D data set was collected in an 11.5 km water diversion tunnel, and the purple line shows the flight path of the ROV. The onboard INS system allows for the data set to remain smooth and consistent even if the path of the vehicle is irregular.

4. SONAR TECHNOLOGY

A device using sound to identify objects in the water column is referred to as a SONAR (SOund NAvigation and Ranging). Active sonars produce their specific sound waves and analyze the reflection of the emitted waves. The multibeam sonar is used to visualize surfaces and objects. With low-frequency waves generated image can have a lower resolution but covers large area scans as compared to ultra-high-resolution imaging with high-frequency waves which has a limitation of a small view field and a short distance to the object. Equipping an ROV/AUV with sonar makes it possible to scan tunnel geometry and produce ultra-high-resolution imaging even in poor or zero-visibility conditions.

5. INSPECTIONS DATA

During the inspection, tunnel condition is assessed by a rock/tunnel engineer via live streaming of sonar and video data. Video inspection is easy to interpret directly, however, may be unusable in high turbidity water and poor visibility. The biggest advantage of sonar data is that the technology works in poor visibility conditions and is independent of lighting and water quality.

5.1. Video data

During the inspection, the tunnel engineer has the opportunity to follow the ROV inspection through streaming video received from several cameras. The video streams are usually directed towards the tunnel bottom, walls and roof. In good visibility, these different streams can be important tools to evaluate geological parameters (e.g. lithology, blockiness etc.) and the status of the reinforcement (e.g. exposed parts on bolts, shotcrete, and concrete/steel elements) (Figure 4).

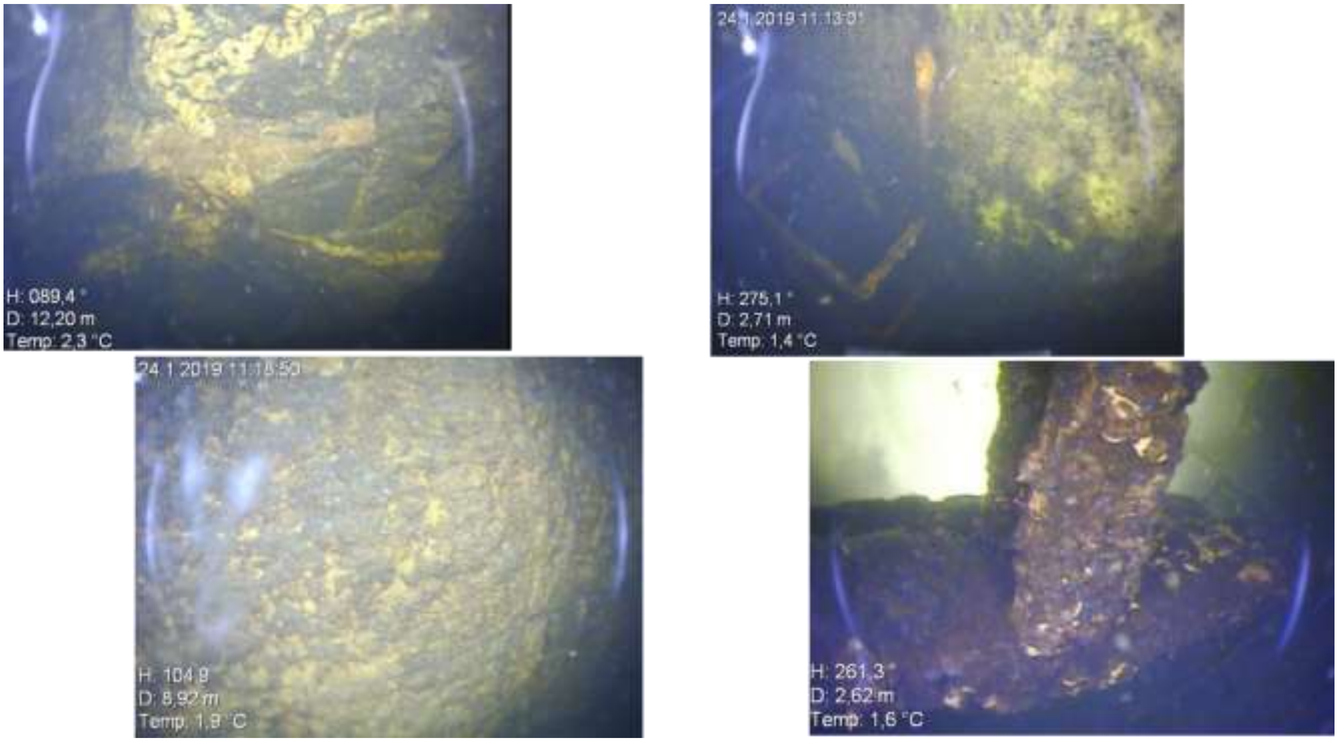

Figure 4. Still images from the video cameras. Top left- a lithological variation of the granitic gneiss; top right- cast concrete structure with an indication of porosity and miscolouring; lower left- the surface of the shotcrete reinforcement with no signs of degradation besides small cracks; lower right- heavily corroded steel structure.

5.2. Sonar scanning

A single beam-scanning sonar can be used to provide line profiles at periodic intervals. This required the ROV to be held in position for the conduction of every single scan. It generated limited coverage, pure data traceability and slow inspection speed. The development of multibeam sonar (ex. Teledyne Marine, BlueView T2250) proved to be ideal for tunnel inspections. Loxus 3D Tunnel Inspections was the first ROV operator to equip its ROVs with this new 3D multibeam sonar. The BlueView T2250 is a state-of-the-art, compact system, specifically designed to produce 3D data suitable for the inspection of tunnels with centimetre precision. The system uses high-frequency, low-power acoustic multi-beam technology and uses 2,100 overlapping narrow ‘beams’ to create a continuous 360° profile. The multibeam sonar operates at a frequency of 20Hz and creates a dense 3D point cloud. BlueView T2250 sonar is suitable for use in tunnels with a diameter of 2m-15m. Accuracy within the range of some centimetres that is achievable with 3D multibeam sonar is sufficient to document the tunnel geometry and the reinforcing elements of concrete/steel, and identify and quantify rock bursts, tunnel collapses, sediment accumulation and other phenomena (Figure 5).
The 3D sonar data can later be used to create a full 3D model of the whole inspection interval from the point cloud data. The detailed analysis of collected sonar data can be analyzed by a rock/tunnel engineer to indicate and qualify observed failures in a 3-D model (Figure 6).

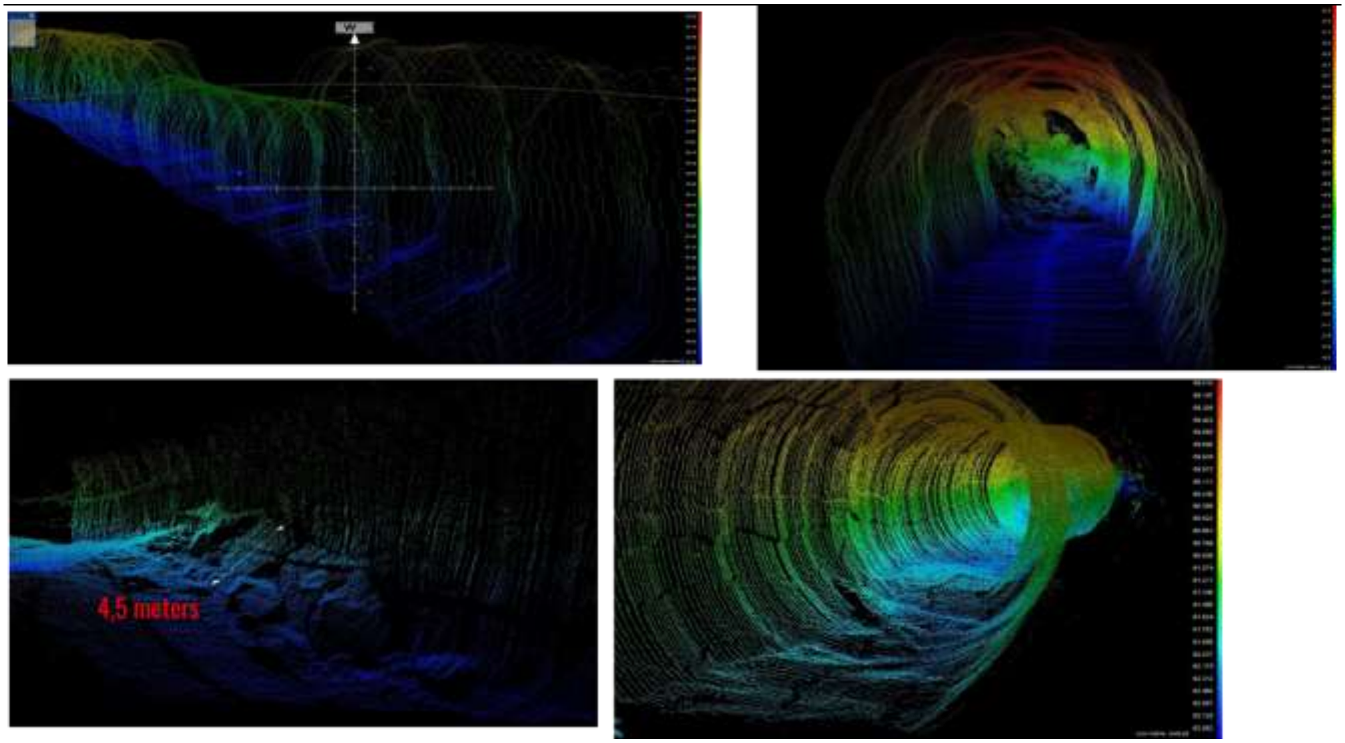

Figure 5. Multibeam sonar data showing various geometries of the scanned tunnel.

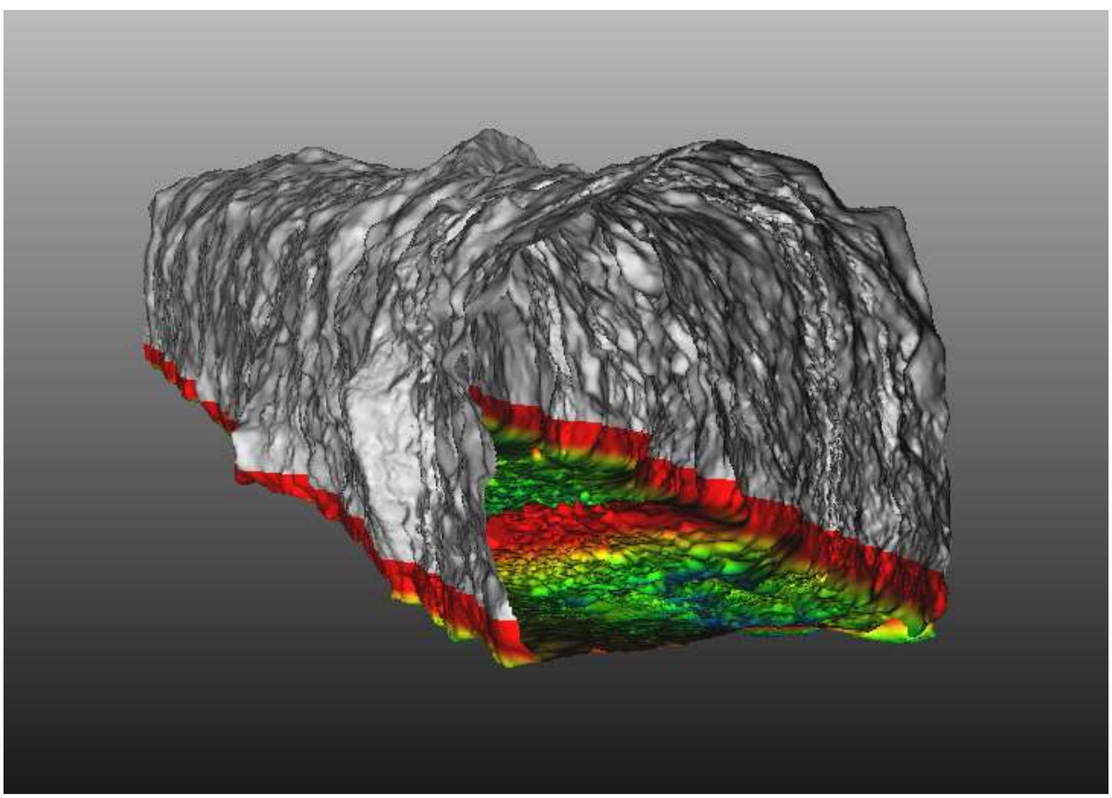

Figure 6. A 3-D model of the tunnel segment indicating the pile of debris under the crown feature.

The same multibeam data can even be used to create a digital twin model of a particular segment or elements of the facility. In hydro power plants an accurate model of ex. Penstock (Figure 7) or a draft tube (Figure 8) can be generated.

Figure 7. Model of a penstock generated from multibeam sonar data.

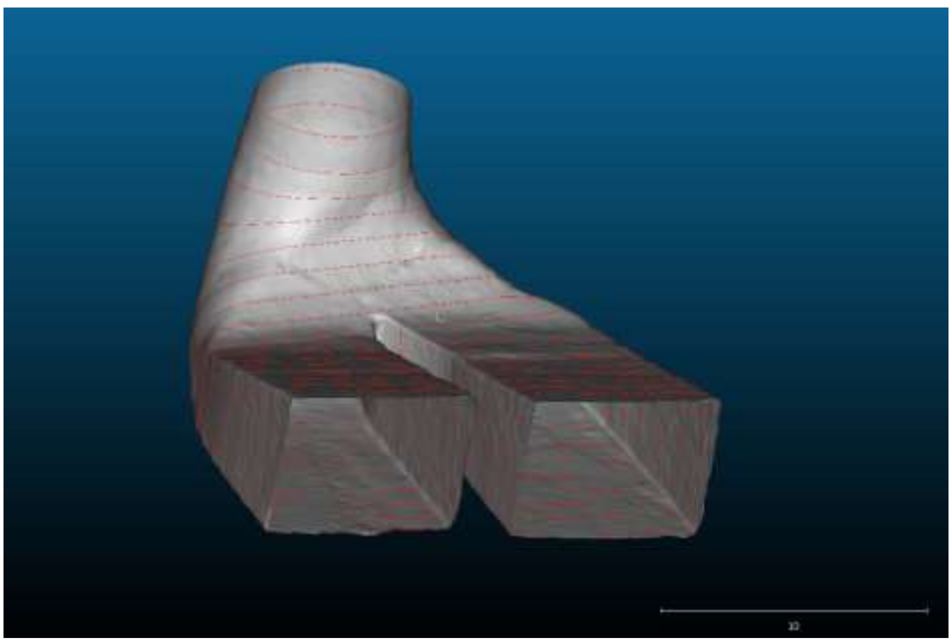

Figure 8. Model of a draft tube generated from multibeam sonar data.

5.3. Imaging sonar

High or ultra-high-resolution imaging sonar allows for images of damage underwater in low or zero-visibility conditions. These are also multibeam imaging sonar, only these are taken with a higher frequency unit. The downside of this sonar is that its field of view is smaller and most suitable to spot-check particular areas of known concern. This image data allows for smaller features such as cracking to be identified ex. inside pre-cast liner sections. This gives qualitative data on various features of interest along with allowing those features to be positioned by tunnel station and tunnel quadrant. These images (Figure 9) with feature locations identified allow comparing features in the same locations over multiple inspections to see if there have been any changes that may be cause for further monitoring or remediation.

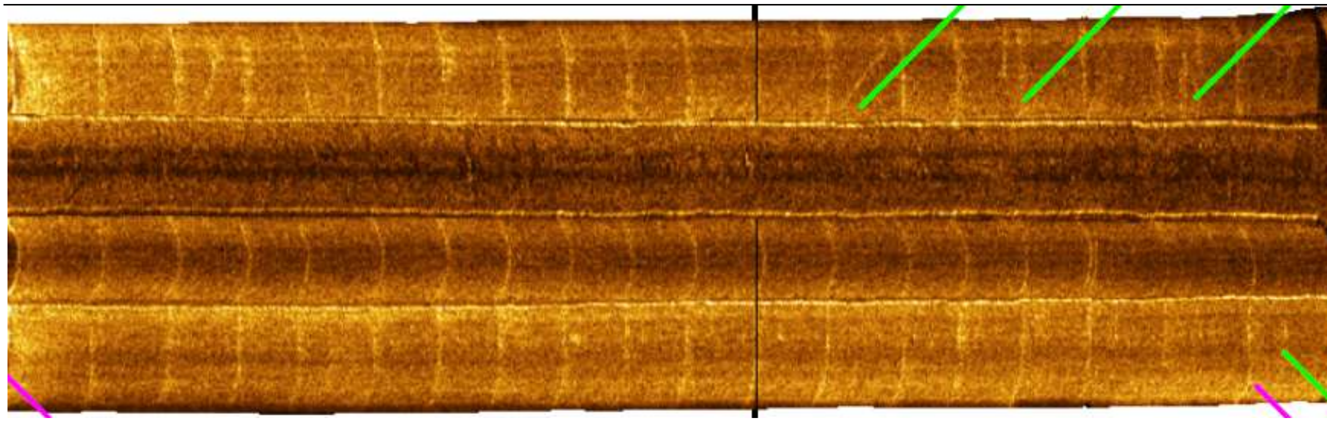

Figure 9. Sonar mosaic captured with multibeam sonar of unrolled concrete-lined tunnel (ca 50 m long section). Mosaicked multibeam imaging sonar images of the internal tunnel surfaces from the 9 o'clock, 12 o'clock, 3 o'clock, and 6 o'clock positions concurrently, geopositioned within the tunnel. This image data allows for smaller features such as cracking to be identified inside pre-cast liner sections.

This imagery can be collected at the same time as the 3D sonar scanning allowing for better characterization of anomalies that don't have large dimensional variance such as minor spalling (Figure 10), cracking and exposed steel structures (Figure 11).

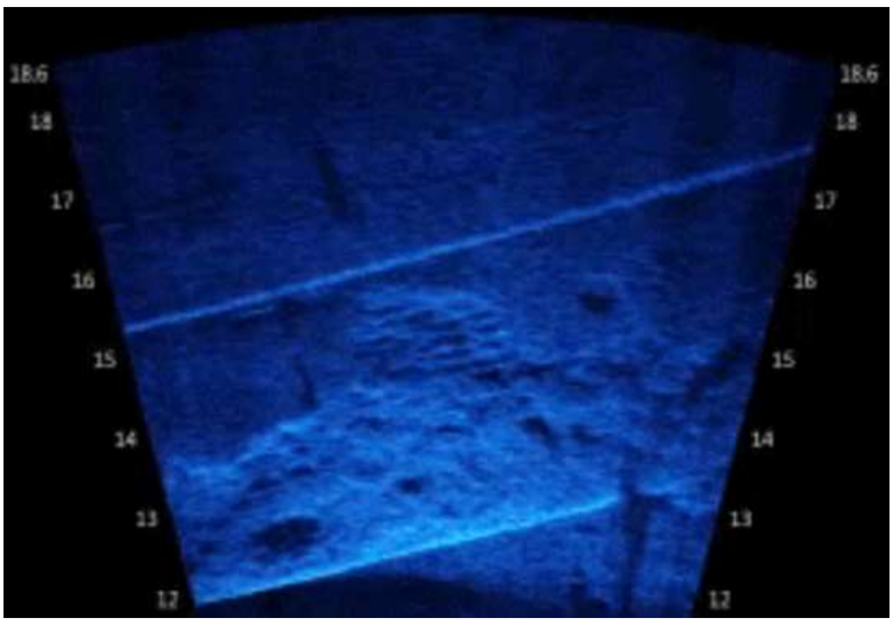

Figure 10. Spalling of cast concrete surface with exposed rebar shown with ultra-high-resolution imaging sonar.

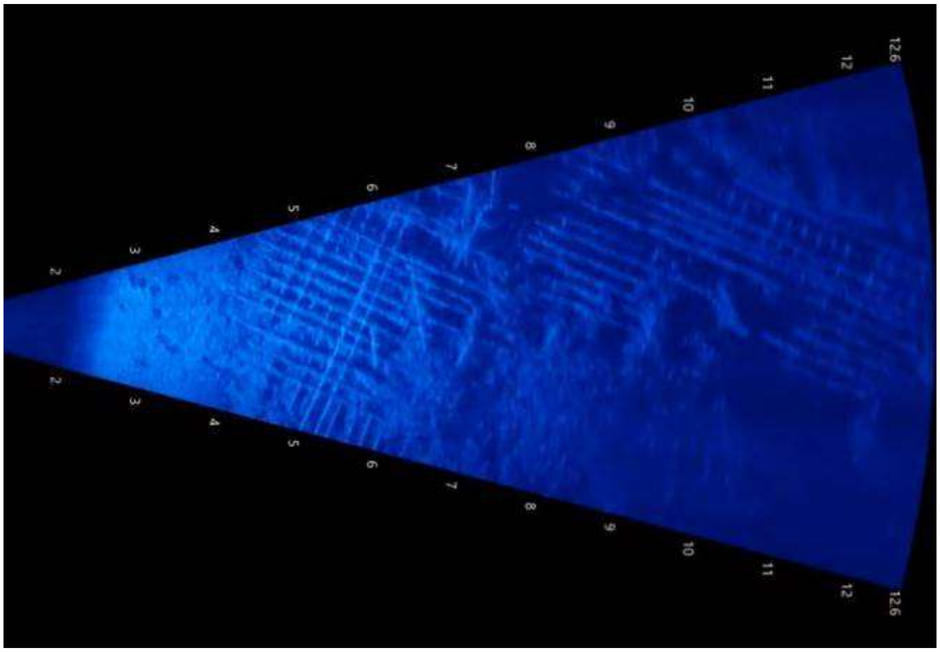

Figure 11. The exposed rebar is shown with ultra-high-resolution imaging sonar.

6. RISK ASSESSMENT OF STRUCTURAL INTEGRITY

Assessment of the structural integrity of the tunnel based on sonar and visual data collected with the ROV/AUV without dewatering brings an opportunity to identify and quantify the damages and base a risk assessment on actual observations rather than on historical data if any or subjective opinion. Relatively easy accessibility and short-time effect on facility operations caused by ROV/AUV inspection allow monitoring of the damage and assess its propagation on regular bases. Geological parameters (e.g., lithology, blockiness, orientation and character of fractures or weakness zones etc.) and the status of the reinforcement (e.g. exposed parts on bolts,

shotcrete, and concrete/steel elements) or cracks and spalling in lining structure is a list of parameters which have to be used to evaluate the probability and possible consequences of the failure. Therefore, access to an experienced and trained rock/structural engineer and a careful analysis of all available data is required to be able to make an overall assessment of the structural integrity of the tunnel.

7. RECOMMENDATIONS ON ACCESS POINTS

Inspection with ROV/AUV requires access to the water surface at the waterway. The access point has to be formed in a way that allows to raise and lower the ROV/AUV directly to the water surface. There is a large variation between facilities concerning the access point for the ROV/AUV inspection. In general, access points can be summarized in the following groups:
-access from an open water reservoir,
-access through service tunnel,
-access through inspection hatch (indoor or outdoor).
Each type of access point requires a specific approach and detailed planning. In existing facilities preparation must be made by means of assess roads, lifting equipment, electricity supply etc.
In the case of the design of new facilities or major reconstruction works of the existing ones comes an opportunity to design the facility that includes even planning for future inspection works. Each type of access point requires a specific approach, but general recommendations could be summarized as follows.
1 -The access point has to be accessible by road design for truck transport.
2- At the access point outdoor requires an area for unloading the equipment, an establishment area for equipment and control center and if needed lift crane.
3- If access is through a service tunnel, the slope and pavement must be suitable for the wheel loader.
4- The size of the inspection hatch should be at least 2x3 m for easy access with any type of ROV/AUV.
5- If the inspection hatch is indoors there should be a possibility to transport the equipment with a wheel loader or traverse.

8. CONCLUSIONS

An ROV/AUV equipped with a multibeam sonar is currently the most advanced tool for the inspection of water-filled tunnels in an efficient and HSE-safe manner and should be considered one of the crucial tools for the Strategic management of inner waterways.
The combination of the sonar and video data provides an opportunity for a trained tunnel engineer to make an overall assessment of the structural integrity of the tunnel without the extremely costly and time-consuming process of dewatering and executing a physical inspection. Geological parameters, the status of the reinforcement or lining structure is a list of parameters which have to be used to evaluate the probability and possible consequences of the failure. Experienced and trained rock/structural engineers and a careful analysis of all available data are required to be able to make an overall assessment of the structural integrity of the tunnel.

REFERENCES

Nordström, Erik (2001). *Strategi för förvaltning av inre vattenvägar*. Rapport 2021:730: Energiforsk (in swedish)

Proceedings of the NROCK 2023
The IV Nordic Symposium on
Rock Mechanics and Rock Engineering
ISBN 978-9935-9436-2-0
DOI 10.33112/nrock2023.19

Deep learning application in characterization and prediction of overbreak geometry in tunnels using point cloud data

Jorge Alvarez (jalvarez@srk.cl)

Jorge Alvarez
Sebastian Veloso,
Esteban Hormazabal
SRK Consulting Chile, Santiago, Chile

ABSTRACT

An overbreak during the construction of underground mining tunnels is a common geotechnical and operational problem, which is caused by a combination of geological, geotechnical, structural and operational factors, in which partial or reduced information is available, thus conditioning tunnel stability and consequently the safety of personnel during construction. Additionally, studying an overbreak during early stages allows to validate assumptions applied during engineering stages.
Throughout history, different methods have been proposed for the overbreak estimation, these ranging from an empirical, analytical (including numerical modelling), observational or even through the application of machine learning.
This work proposes a different approach to most of the studies carried out, which usually consider an average or expected value of overbreak. On this occasion, Deep Learning architectures are used to characterize and predict the complete geometry of the tunnel based off of a training carried out using point clouds of the sectors already excavated.
The results obtained show that it is possible to use autoencoder-type architectures to carry out the characterization and prediction of the tunnel's geometries from point clouds of previously excavated sectors, which has a relevant value for back analysis and potentially predictive analysis, which would in turn impact tunnel stability and/or safety in the different operation cycles during the construction of underground mining galleries and/or tunnels and civil works' projects and operations.

KEYWORDS

Tunnels; Overbreak; Point Cloud Data; Deep Learning; Autoencoders

INTRODUCTION

Overbreak is the zone around the tunnel with a larger cross-section than necessary according to the original design. This has important implications in terms of stability, costs and construction time in civil and mining projects. Although different methods have been used to address this issue, a definitive solution has not been found due to the difficulty of establishing a clear relationship between overbreak and its causes. In this paper, an approach is presented in which the complete 3D geometry of the excavated tunnel is used and artificial intelligence techniques, such as Deep Autoencoder Network (Vincent P., et al., 2010) are applied to characterize overbreak geometries and potential prognosis.

The central idea associated with the characterization of overbreak geometries is that during the engineering stages of a civil or mining project, different assumptions are established as input parameters, which are later evaluated during the construction process, which can result in significant differences between the expected behavior according to design and reality. Given the above, the application of an artificial intelligence algorithm oriented to the geometric segmentation of a tunnel aids for progress in terms of a zoning tool, which added to the design assumptions and as-built conditions, enables new forms of analysis. Figure 1a), presents the proposed analysis outline. For example, in Figure 1b), the geometric shape of a tunnel is conditioned by the insitu stress field, activating zones of potential spalling towards one side or the other according to the

orientation of the principal stresses (Wahid Ali, et al., 2022). This information allows validating or refuting the expected behavior according to design, thus when a contradiction is observed, it is possible to recommend in this particular case, further stress measurements in the area to corroborate the phenomenon or the application of mitigation measures such as a different support design, but in general terms it translates into the need for a better characterization of the potential causes (validation of assumptions).

A second point to assess would be the possibility of predicting the overbreak associated geometry (see Figure 2a). The central concept would be applying an artificial intelligence algorithm in the horizontal progress cycle of a tunnel using, for example, the drill and blast method. As shown in the figure aforementioned, depending on the prediction, an assessment of the potential risks could be carried out and subsequently the necessary mitigation measures taken; modifying the arrangement of the advance per blast or other support alternatives. Additionally, this would also enable the possibility of estimating those areas that cannot be surveyed by 3D scanner, as shown in Figure 2b, since it is not uncommon that some areas cannot be surveyed topographically for operational reasons, for example, areas with debris that would prevent the completion of the surveys.

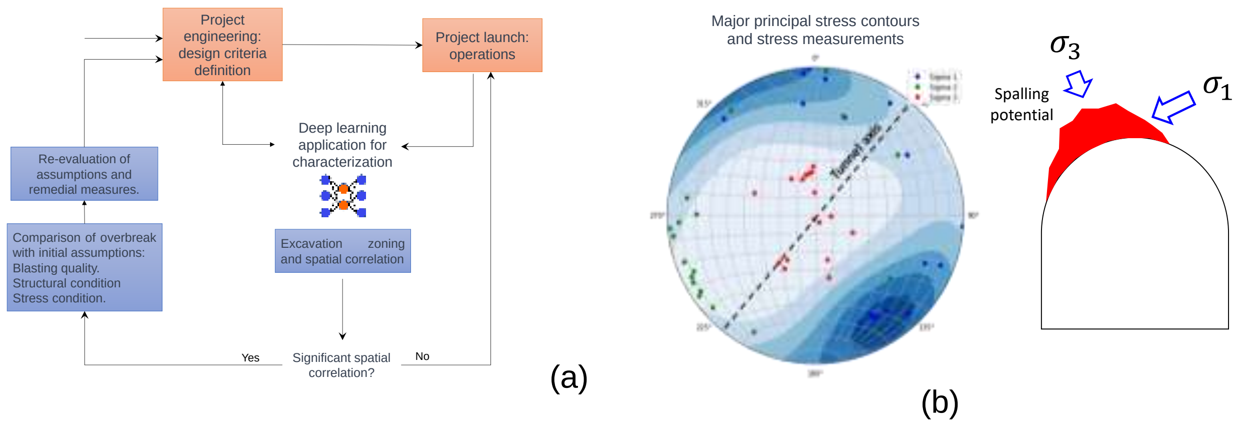

Figure 1. Application scheme of a characterization algorithm. (a) Explanatory diagram of a characterization algorithm applied in a UG project. (b) Example of a geometric characterization cross-referenced with stress measurements application.

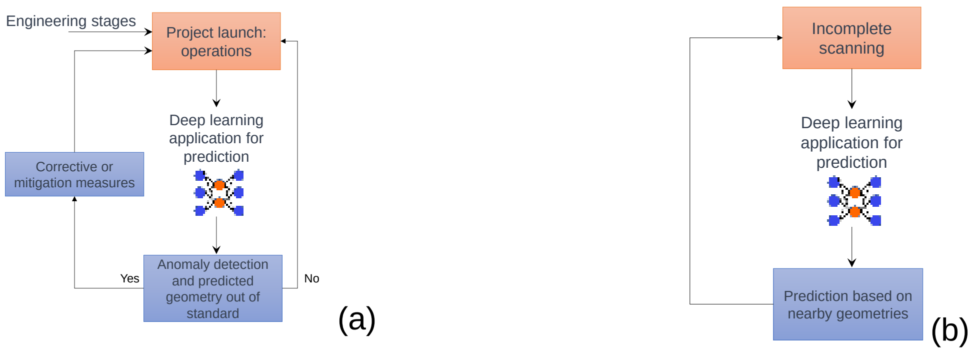

Figure 2. Application scheme of a prediction algorithm. (a) Explanatory diagram of a prediction algorithm applied during the horizontal advance per blast cycle (b) Explanatory diagram of an incomplete scanning estimation.

1. THEORETICAL DEFINITIONS

The following are some basic definitions for the development of a deep learning algorithm to characterize and predict overbreak using a complete geometry.

1.1. Machine Learning, Deep Learning and Autoencoders

Machine Learning and Deep Learning correspond to subfields of Artificial Intelligence (AI), while Machine Learning is the study of algorithms that improve task performance through experience making decisions without being explicitly programmed, Deep Learning, a subarea of Machine Learning, is often better suited for Big Data problems and has generated a paradigm shift in attribute extraction and compositional layer learning (Zhang A., et al., 2022).

Pattern discovery is an important task that allows to obtain useful information from large datasets (Alla & Kalyan Adari, 2019). One way to do this is by using autoencoders, which, in general terms, is a type of unsupervised neural network that aims to compress input data into a representation called latent space, which has a much lower dimensionality than input and that is characterized by preserving the most relevant information in an intelligent way. The main objective is to reconstruct the input from the latent space, seeking to minimize an error function. This can be thought of as a nonlinear version of principal component analysis or matrix factorization. In detail, autoencoders are divided into two components: one that encodes the data in the latent space and a decoder that reconstructs it from this encoding. Autoencoders can be used to reduce the complexity of the data and learn more abstract representations of it, which can be useful in various machine learning tasks. A basic architecture of an autoencoder can be seen in Figure 3.

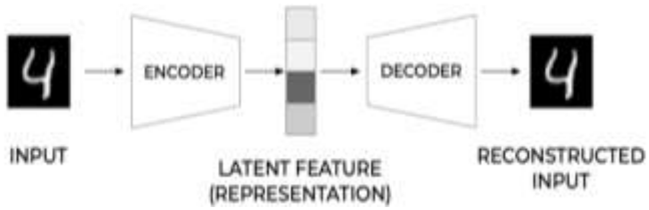

Figure 3. Typical autoencoder diagram (taken from Michelucci U., 2022).

1.2. Point Cloud Data Models

Artificial intelligence techniques for dealing with point clouds have evolved over time from the use of voxel grids for a structural treatment to architectures that are point cloud order invariant such as PointNet and PointNet++ (Charles R. Qi., et al, 2017). PointNet can handle cluttered point clouds and can be trained to classify, segment, and semantically analyze sets. PointNet++ uses a hierarchical architecture to improve local pattern capture (see Figure 4).

Other architectures such as FoldingNet (Yaoqing Yang, et al., 2018) also exist, which corresponds to a form of autoencoder, capable of transforming a 2D to 3D dimensional mesh. The input to the encoder is an n by 3 matrix, where each row of the matrix consists of the spatial position in three dimensions (x, y, and z). The output is an m by 3 matrix, representing the reconstructed point cloud.
Chamfer distance can be used to measure the reconstruction error, which measures the distance between the original and the reconstructed point cloud. The autoencoder computes a latent representation of each input point cloud and subsequently reconstructs the point cloud using this representation. Other architectures for point cloud processing, which have not been used in this work, include PCN and PointConv++ (Qi Yang, et al., 2021) which have used the PointNet and PointNet++ algorithms as their basis, respectively.

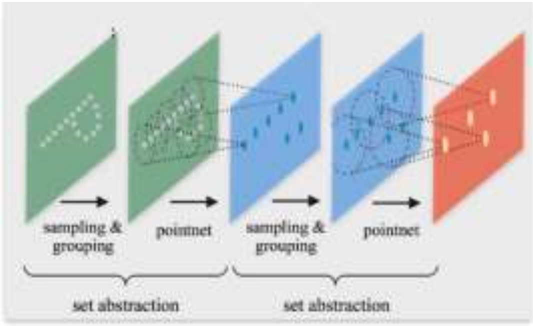

Figure 4. PointNet++ diagram, for capturing local and global attributes in a point cloud (taken from Charles R. Qi, et al., 2017).

2. MODEL SELECTION

FoldingNet base architecture is considered in terms of characterization and a modified architecture as an additional alternative, where a hierarchical extraction of both local and global attributes is incorporated through the use of PointNet++.

To evaluate the efficiency in the recognition of representations in the latent or compressed space (called code word), a public dataset is used where the different geometric categories to be recognized are known in advance like the ShapeNet dataset (Chang, et al., 2015) contains close to 17,000 3D point clouds with 16 different categories. The procedure consists of using the codeword of the latent space and then grouping in "n" clusters, to then compare these groupings with the actual categories of the dataset. Figure 5 shows the two architectures evaluated.

The results obtained indicate that the representativeness of the geometries in the latent space is higher with the modified architecture compared to the base, especially when the number of categories is lower. Therefore, a modified architecture is selected for the characterization task.

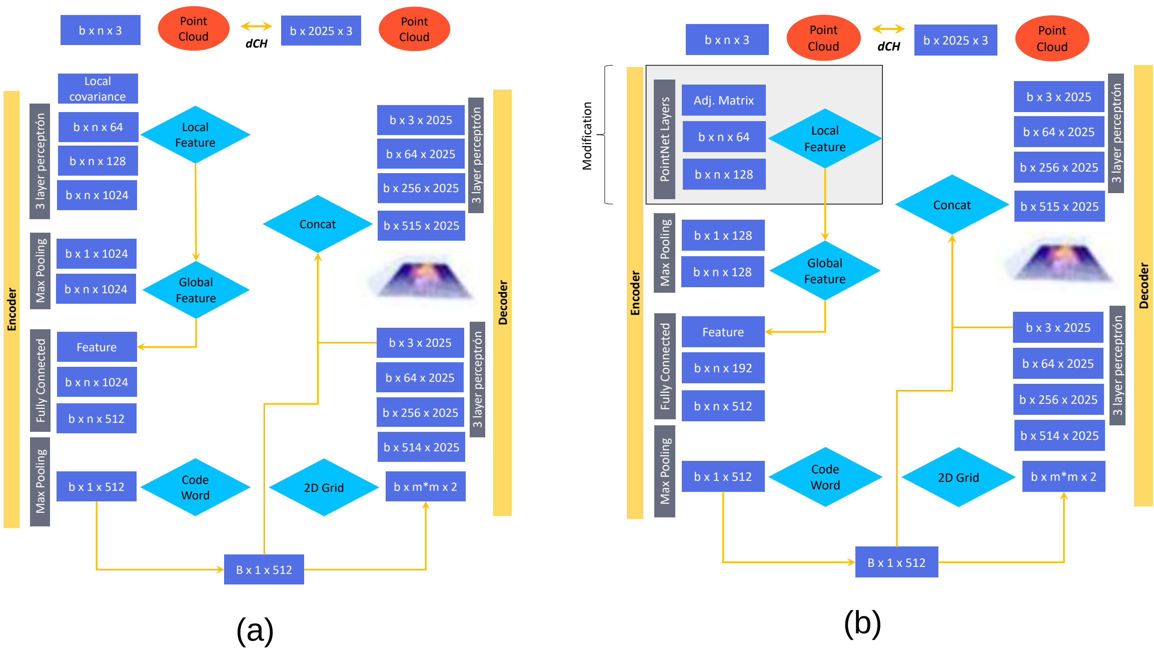

Figure 5. Deep learning neural architectures. (a) FoldingNet-type base architecture, (b) Modified architecture including PointNet++ (modified from Yaoqing Yang, et al., 2018).

Table 1. Geometry recognition comparison performance in latent space.

N° Categories	Base Architecture Accuracy (%)	Modified Architecture Accuracy (%)
4	84	99
6	81	96
8	79	82

3. CHARACTERIZATION RESULTS

3.1. Typical Outputs

Figure 6 displays a typical output using a modified architecture. The reconstructions obtained show a "clean" point cloud without disturbances or noise, and also allow extrapolating areas where the original point cloud has missing data.

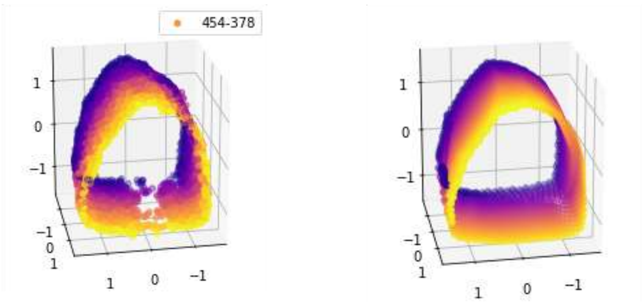

(a) (b)

Figure 6. Typical output from the model. (a) Input geometry in a model, (b) Output geometry of the model.

3.2. Results

After inserting 400 geometries corresponding to tunnel segments to the modified architecture and applying the codeword or latent space representation, it is possible to visualize each of these geometries in a 2 dimensional space by means of the commonly used PCA (principal component analysis). The graph on Figure 7, in addition to facilitating the visualization of the total geometries, has a logical order associated with the learned characteristics of the data set. The cluster with the highest density was sought using a DBSCAN type algorithm (Pedragosa F., et al., 2011) which indicates which geometries are repeated in greater quantity and have a certain degree of similarity. The exploration of the latent representations indicates that most of the geometries are within standard according to the design geometry (see Figure 7-1), while those far from the zone of higher density have biases in their shape (see Figure 7-2, 7-3 and 7-4), with the overbreak controlled by the presence of structural planes or joints in the roof area.

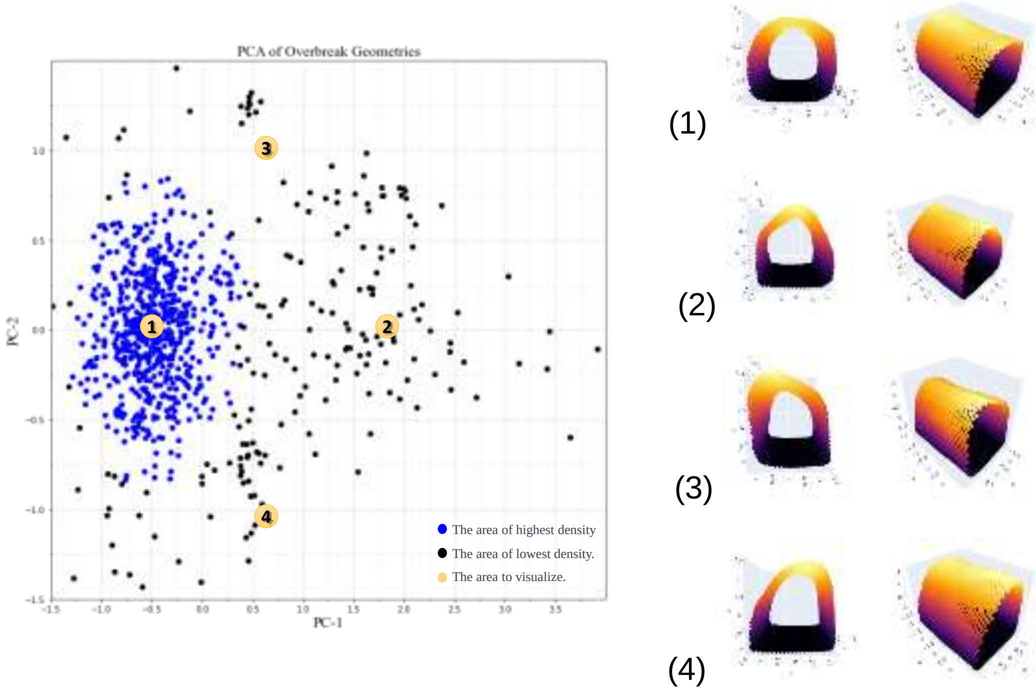

Figure 7. Recognition of overbreak features in latent space and their exploration in different zones.

Finally, it can be indicated that, from the observation of the latent space through a reduction of dimensionality, it is possible to characterize the overbreak associated geometries. Additionally, it can be seen that there is a logical order in the arrangement of the geometries, which can later be zoned in a layout of an underground project and/or allow a back- analysis of the initial design assumptions.

4. PREDICTION RESULTS

4.1. Geometry processing

For the overbreak prediction objectives, the same previous architecture was considered, with the exception that the data loading considers providing a point cloud used as input, which corresponds to a previous section of the tunnel to be predicted.
Figure 8, displays the difference between the data load associated with characterization and prediction.

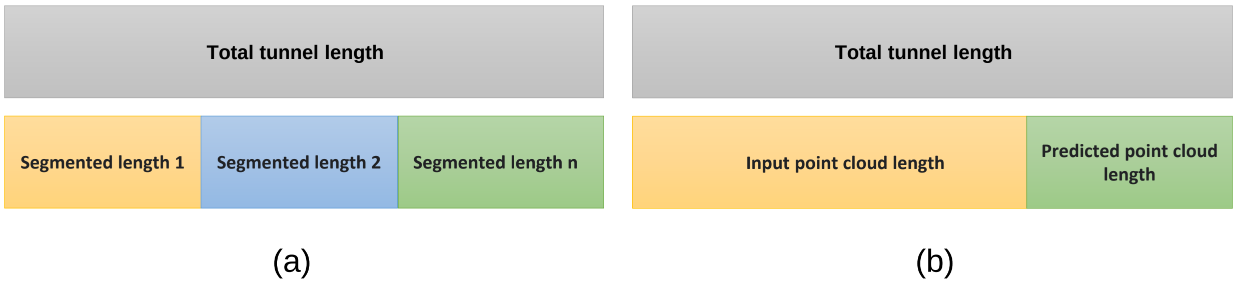

Figure 8. Data loader difference for prediction task and characterization task. (a) Data loader for characterization, (b) Data loader for prediction.

In this case, since the objective is not the characterization of geometries, the data processing does not consider a standardization of the points. A transformation of coordinates to the origin and a rotation were considered so that all geometries are aligned in the same direction, taking advantage of the largest amount of available data from excavations with different orientations.

4.2. Results

The results obtained indicate that there is no evidence of over-fitting in the training process, since both the training and validation loss curves decrease in a similar way and without separating from each other as the training is carried out (see Figure 9a). On the other hand, when reviewing a prediction of the validation set, a good agreement is seen in terms of distribution of the over-excavated distances, with an actual median of 0.16m and a predicted median of 0.19m, but with a higher variability (outliers). The association between the prediction and the actual point cloud can be seen in Figure 9b.

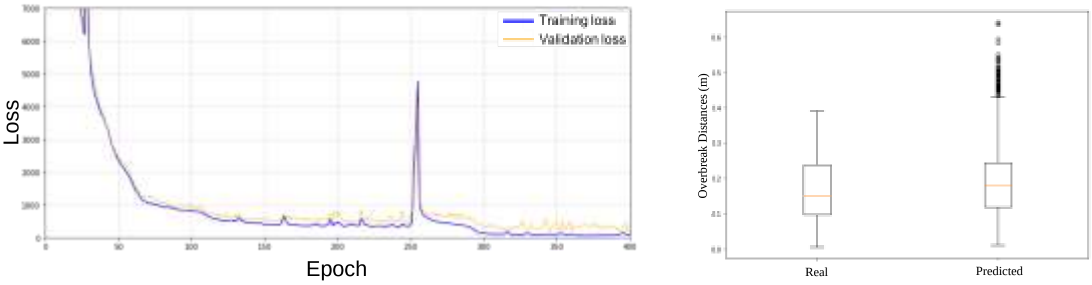

(a) (b)

Figure 9. Training metrics. (a) Loss curve of the training process (b) Overall comparison of validation, prediction of overbreak and actual overbreak.

The metrics associated with the loss function in the training process are the chamfer distance (CD), which measures the dissimilarity between two point clouds by summing the distances between corresponding points in each cloud, and the mean absolute error (MAE), and are presented in Table 2:

Table 2. Metrics associated with the prediction target.

Set	**CD Loss** (m^2)	**EAM** (m)
Training	57	0.18
Validation	118	0.21

Although the indicators seem to be favorable, there is still margin for result improvement, as can be seen in a validation example (see *Figure* 10), although there is a general agreement between the predicted and the real point cloud, in certain specific sectors the prediction level responds better than in other sectors. For example, in the roof area, at point A, there is a geometric depression that is captured by the model during the prediction, however, when moving to the right with point B, the major overbreak in the roof area is not captured.

As it is possible to observe, using a point cloud as input permits the learning of the neural network, furthermore, the prediction made adjusts quite well to the actual point cloud in terms of average overbreak, considering that causal factors/attributes such as: rock quality, structural condition, blasting quality among others, which all correspond to variables commonly used for a prediction task, were not used therefore these could enrich the results of an AI model.

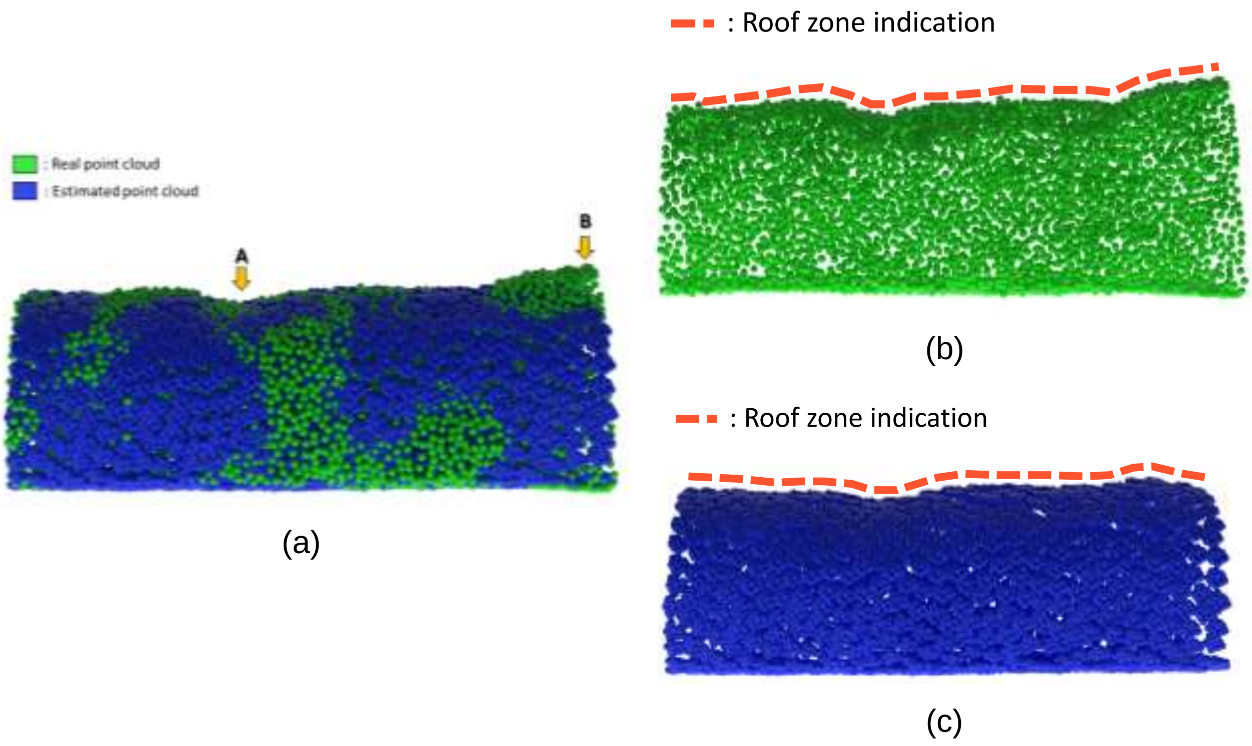

Figure 10. Tunnel Profile view. (a) Real and estimated geometry point cloud (b) Real geometry point cloud with roof zone indication (c) Estimated geometry point cloud with roof zone indication.

5. DISCUSSION OF RESULTS

Regarding the evaluation of architectures for characterization:

- Both base (FoldingNet) and modified (FoldingNet plus PointNet++) architectures were evaluated using the ShapeNet public dataset. The PointNet++ modified architecture performed better however, further performance evaluations with more batches and different public datasets are recommended to avoid a biased decision.
- The application to characterize overbreak geometries is effective and is simple to use, with interpretable results allowing to visualize the reconstructed geometries from the latent space.

Regarding the prediction of overbreak:

- The results show that a tunnel point cloud can be predicted when using another as input, and FoldingNet is flexible for this task. Overfitting was not observed for the prediction model and the prediction model could most likely be further improved after including causal factors/attributes such as structural condition, stress condition or blasting quality, among others.
- For this exercise geology and structural domains were not available so to improve the estimation, key factors/parameters such as structural conditions, in situ stresses, lithology or blasting quality, among others should be taken into consideration for future studies.
- Although the prediction model gave good results, it is recommended to evaluate alternative architectures that better capture local and global attributes of the input geometry, such as PointConv++ architecture. Additionally, the use of a PointMask-type architecture is suggested (Saeid Asgari Taghanaki, et al., 2020) to find those critical points that affect the output geometry, this in order to improve the interpretability of the results.

Applicability:
In terms of applicability AI models associated with characterization and prediction tasks, potentially applicable scenarios are:

Table 3. Potential applicability of AI algorithms in characterization and prediction.

Applications	When is it applicable?
Characterization	• For the purpose of a back-analysis of design parameters. • Apply when there is abundant scanning of excavations that have not been processed for analysis.
Prediction	• During the horizontal development cycle of a underground excavation. • When an estimate of zones with incomplete scanning is required.

6. CONCLUSIONS AND FUTURE WORK

Several Deep Learning algorithms for 3D point cloud analysis are currently available. This approach has great potential in areas of engineering, where geometries can enhance value. The modified FoldingNet model performed best for the task of characterizing overbreak geometries, based on the ShapeNet dataset and using a 4-element batch size. Autoencoders, especially FoldingNet, can be used to reproduce clean tunnel geometries that have incomplete zones.

Overbreak geometries point clouds can be predicted with other point clouds as input, which could be improved after including causal factors/attributes such as rock quality, blast quality, stress and structural conditions, among others.

In the field of geomechanics and particularly in overbreak analysis, AI can help us to discover patterns and features in the data more efficiently and with acceptable levels of accuracy, which can be considered as a tool for decision making.

Further performance evaluation of architectures using different public datasets, e.g., with ModelNet10 or ModelNet40 and with different batch size configurations, is recommended in order to detect possible biases in the model selection.

Regarding the characterization, an anomalous behavior detection analysis should be performed, in order to obtain a model that allows to automatically recognize those geometries that deviate from the ideal design. The incorporation of a variational autoencoder, which allows to generate a better distribution of geometries in the latent space and with the possibility of generating synthetic geometries for predictive numerical stability analysis (2D and 3D) could be considered.

In order to obtain a better interpretation of the inner workings of the neural network, an analysis of critical points should be incorporated to determine those geometric zones of the sections of the underground excavation that condition the results of the model. Regarding predictions, a larger data set should be used for the training process, as well as the incorporation of other explanatory variables and/or the evaluation of different architectures that better capture the local and global attributes of a point cloud.

7. ACKNOWLEDGEMENTS

The author would like to thank the various professors at Universidad Católica de Chile (Hans Lobel and others) and professionals at SRK Consulting Chile for their invaluable collaboration in the development of this research project and their generosity in providing information and giving their time for discussion and review of this work.

8. BIBLIOGRAPHY

Ali, W., Rehman, H., Abdullah, R., Xie, Q., & Ban, Y. (2022). Topography induced stress and its influence on tunnel excavation in hard rocks - a numerical a approach. *GEOMATE*, 9.

Alla, S., & Kalyan Adari, S. (2019). Beginning anomaly detection using Python-Based Deep Learning. Apress.

Asgari Taghanaki, S., Hassani, K., Kumar Jayaraman, P., Hosein Khasahmadi, A., & Custis, T. (2020). PointMask: Towards Interpretable and Bias-Resilient Point Cloud Processing. *ICML 2020*.

Chang, Angel X. and Funkhouser, Thomas and Guibas, Leonidas, & et al. (2015). ShapeNet: An Information-Rich 3D Model Repository. Chicago.

Charles R. Qi, Hao Su, Kaichun Mo, & Leonidas J. (2017). PointNet: Deep Learning on Point Sets for 3D Classification and Segmentation. *CVPR 2017*.

Charles, R. Q., Yi, L., Su, H., & J. Guibas, L. (2017). PointNet++: Deep Hierarchical Feature Learning on Point Sets in a Metric Space. *Computer Vision and Pattern Recognition*.

Fey, M., & E. Lenssen, J. (2019). Fast graph representation learning with Pytorch Geometric. *ICLR*, 9.

Michelucci, U. (2022). *An Introduction to Autoencoders.* Retrieved from Toelt.ai.

Pedregosa, F., Varoquaux, G., Gramfort, A., Michel , V., Thirion, B., Grisel, O., & et al. (2011). Scikit-learn: Machine Learning in Python. *Machine Learning Research*, 6.

Vincent, P., Larochelle, H., Lajoie, I., Bengio, Y., & Antoine Manzagol, P. (2010). Stacked Denoising Autoencoders: Learning Useful Representations in a Deep Network with a Local Denoising Criterion. *Journal of Machine Learning Research 11*, 38.

Yang, Q., Lin, Y., Li, J., Wang, Y., & Yang, F. (2021). PointConv++: A muti-resolutional network for point cloud classification. *Association for the Advancement of Artificial*.

Yang, Y., Feng, C., Shen, Y., & Tian, D. (2018). FoldingNet: Point Cloud Auto-encoder via Deep Grid Deformation. *CVPR*.

Zhang, A., C. Lipton, Z., Li, M., & J. Smola, A. (2022). *Dive into Deep Learning.*

Proceedings of the NROCK 2023
The IV Nordic Symposium on
Rock Mechanics and Rock Engineering
ISBN 978-9935-9436-2-0
DOI 10.33112/nrock2023.20

Rapid photogrammetric method for rock mass characterization in underground excavations

Mateusz Janiszewski (mateusz.janiszewski@aalto.fi)

Mateusz Janiszewski
Aalto University, Espoo, Finland
Markus Prittinen, Lauri Uotinen, Masoud Torkan, Mikael Rinne
Aalto University, Espoo, Finland

ABSTRACT

Underground excavation mapping and rock mass characterization are critical for ensuring the safety, proper design, and maintenance of underground infrastructure. Traditional mapping methods typically involve manual inspections and measurements that require contact with the tunnel surface, which can be time-consuming, expensive, and pose safety risks to personnel. In recent years, photogrammetry has emerged as an alternative method for generating high-resolution digital 3D models of tunnels, enabling rapid and remote rock mass measurements. In this paper, we present a method for tunnel and stope scanning using photogrammetry and remote rock mass mapping from 3D models. Two case studies are presented to demonstrate the effectiveness of the proposed method. In the first case, a multi-camera rig consisting of action cameras is used for video-based photogrammetric reconstruction of underground tunnel excavation. The rock mass data is then extracted from the model and visualized. In the second case, a drone workflow is used to map out rock mass features in stopes. Images taken with the drone are processed to create a 3D point cloud of the stope, which is then used to extract discontinuities from the rock mass surfaces. The orientation and spacing of these discontinuities are measured and visualized on top of the photorealistic 3D mesh of the stope for inspection. The proposed method significantly reduces the data capture process. The advancements in camera and software technologies have made it possible to acquire rapid and accurate 3D models of underground excavations that can be used as a source of rock mass data. Our results demonstrate that photogrammetry is a robust approach for underground rock mass inspection and remote mapping.

KEYWORDS

Rock mass characterization; fracture mapping; photogrammetry; underground; tunnel

1. INTRODUCTION

Understanding the behavior of rock mass in underground excavations is crucial for ensuring safe and efficient mining operations. Discontinuities in the rock mass, such as joints and fractures, play a significant role in governing its behavior. Mapping these discontinuities is essential for predicting and managing rock mass behavior, designing support systems, and planning mining activities. Traditionally, discontinuity mapping was done manually, which was a slow and time-consuming process that was prone to bias. In some cases, mapping was not even possible due to limited access to the area or safety concerns.

Recent advances in photogrammetry and in particular the Structure-from-motion Multi-view Stereo (SfM-MVS) photogrammetric method has shown great potential for digitizing the rock mass surface and extracting discontinuities using computer-assisted mapping methods (García-Luna et al. 2019). However, using photogrammetry in underground excavations poses many challenges, such as limited access, safety concerns, and the need for rapid and accurate data acquisition (Janiszewski et al. 2022).

In this study, we demonstrate a method for remote rock mass characterization in underground excavations using photogrammetry. Specifically, we show how a multi-camera rig can be used for quick data acquisition in underground tunnels, and a drone workflow can be used to digitize stopes. We then demonstrate how 3D point cloud data can be used for the digital mapping of joint planes using the 3D models of the rock mass surface. Our goal is to provide a comprehensive and practical solution to remote rock mass characterization that addresses the challenges posed by underground excavation environments.

2. RAPID TUNNEL PHOTOGRAMMETRY WITH A MULTI-CAMERA RIG

In this section, we describe the proposed tunnel photogrammetry method for rock mass characterization using a multi-camera rig. Traditional photogrammetry methods for tunnel mapping require capturing a large number of images from various positions and angles, which can be time-consuming and difficult to perform in narrow, unstable underground spaces.

2.1. Multi-camera rig

A multi-camera rig was constructed consisting of four GoPro Hero 8 cameras mounted on a PVC pipe frame (Figure 1) (Prittinen, 2021). The positioning of the cameras is optimized to capture the maximum area of the tunnel with sufficient overlap between images. The cameras are mounted horizontally with the top camera facing downwards and the bottom camera facing upwards, while the left side camera is slightly angled towards the right and the right camera is angled towards the left. This configuration allows for the rapid collection of data by taking four images at the same time and covering all tunnel surfaces.

An automatic shutter release GoPro smart remote is used to synchronize the start and end of recording across all four cameras. Optional battery-powered LED lights can be mounted on the frame to improve image quality in low-light conditions, but in this study, more powerful 360 lights and LED panels were used to illuminate the tunnel surface. The frame can also be mounted on a tripod and capture still images, but this was not done as the priority was to increase the acquisition speed as much as possible.

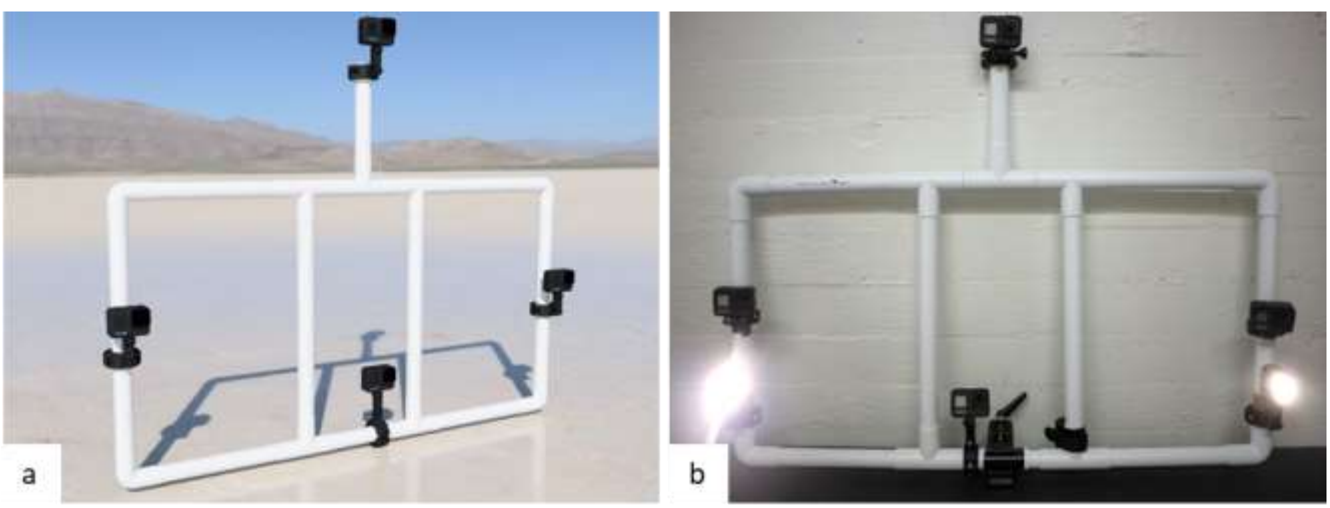

Figure 1. Multi-camera rig for rapid photogrammetric data acquisition in tunnels (modified after Prittinen, 2021).

2.2. Test site

To demonstrate the effectiveness of this method, a tunnel face of the Underground research laboratory of Aalto University (URLA) was scanned. Both walls of the tunnel are unsupported, and the area is used for engineering geology exercises to train fracture mapping. A tunnel drift measuring 4.4 × 2.9 × 4 meters was digitized using the proposed multi-camera rig (Figure 2a).

To illuminate the tunnel face evenly, the lighting setup included two DeWalt DCL074 360 lights and two Aputure Amaran Tri-8s LED light panels, which were positioned inside the tunnel drift (Figure 2b).

To orient and scale the model, an alignment board was designed according to Garcia-Luna et al. (2019), with five control points and known distances. The board is positioned horizontally, and the azimuth of one edge is measured so that the model can be oriented correctly (Figure 2c). In addition, to control the accuracy of the photogrammetric reconstruction, ten control points were mounted on the tunnel walls. Each control point consisted of a 20-bit circular marker generated with RealityCapture software that is automatically detected by the software from images, printed and laminated, and attached to a wooden platform that was attached to the wall.

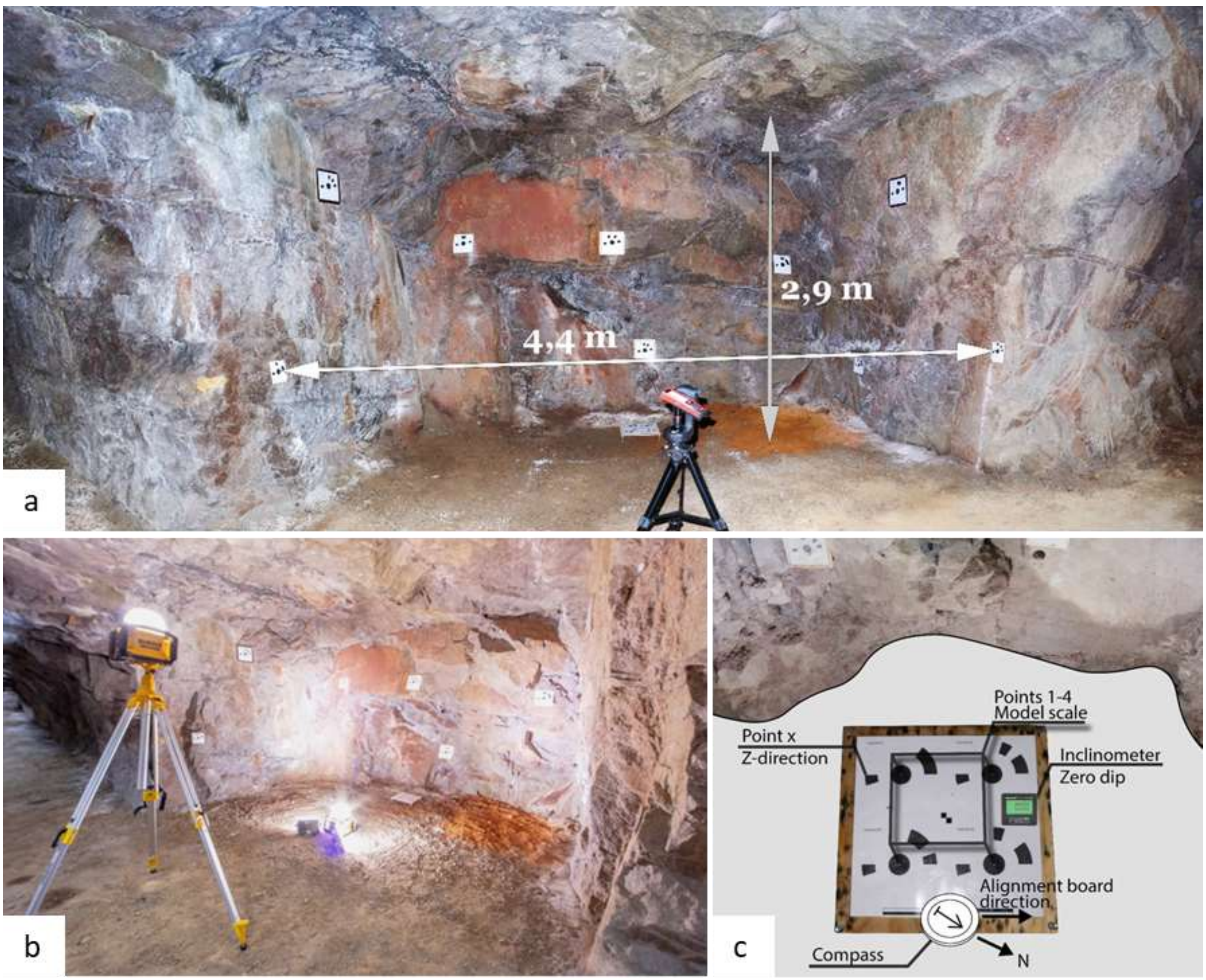

*Figure 2. Tunnel drift dimensions (a), the portable lighting setup (b), and the alignment board with control points and known control distances used to scale and orientate the 3D model (c) (*modified after Prittinen, 2021)*.*

2.3. Data acquisition and processing

Each camera recorded a 4K video with a frame size of 4000 × 3000 pixels. Due to low light conditions, a compromise between fast shutter speed and ISO was necessary. A shutter speed of 1/96 s and ISO of 800 were used. Frames were extracted from the videos at 1-second intervals using RealityCapture software, resulting in 480 frames (Figure 3a). The total time to capture all data was 172 seconds.

The extracted frames were processed using RealityCapture v.1.0.3 photogrammetric software, reconstructing the 3D model on Normal detail settings. The processing was done on a PC equipped with an AMD 3990x 64-core 2.9 GHz processor, 256 GB RAM, and 2 x GTX 1080 TI graphics cards. A total of 472 frames were aligned, and a mesh with 23.7M polygons and a point cloud with 11.9M points were produced. The processing times were as follows: alignment (4 min 33s), reconstruction (19 min 27s), and texturing (3 min 49s), totaling 27 min 49s. The point cloud was cropped and cleaned, leaving 9.1M total points with a mean point density of 14.8 pts/cm² (Figure 3b).

Reference distance measurements were taken using a Leica S901 laser distance measurement tool, comparing 13 distances measured between the control points mounted on the wall. The mean error was 3.7 mm, and the maximum error was 8.6 mm.

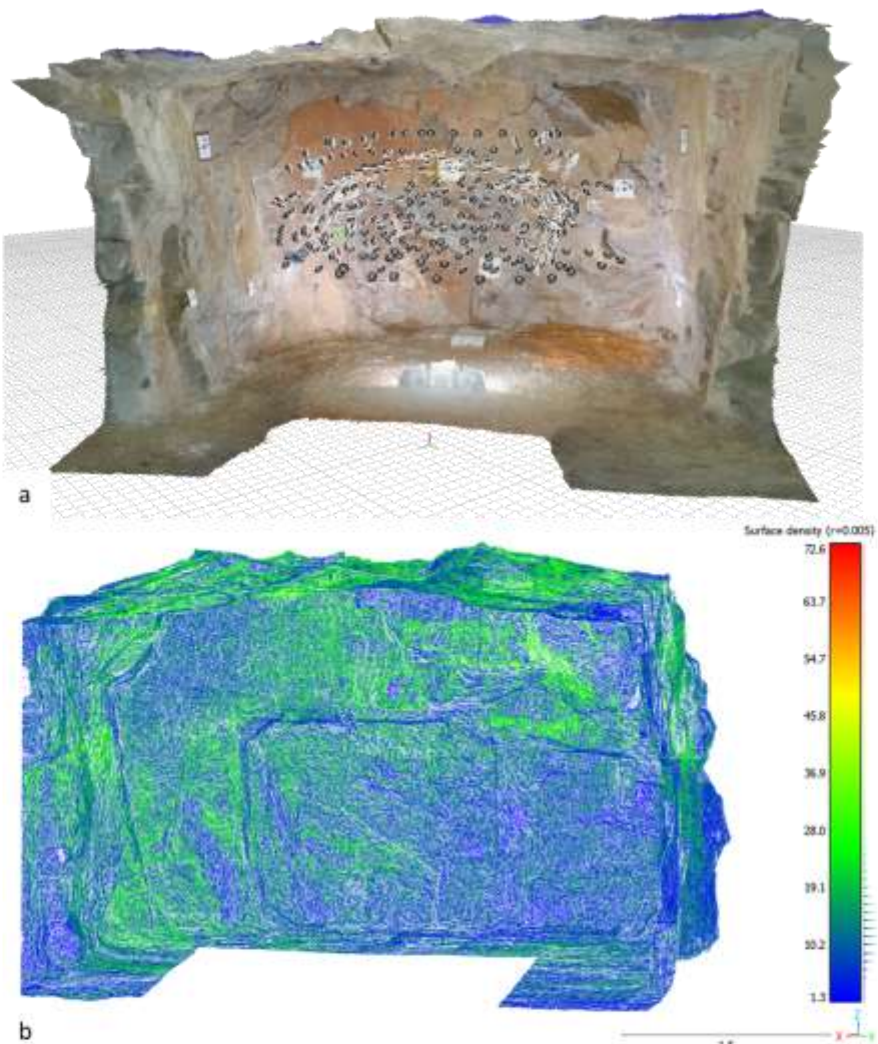

Figure 3. Photogrammetric model of the tunnel drift (a) and the cleaned point cloud colored by point density in pts/cm² (b).

2.4. Rock mass data measurement

The resulting 3D point cloud was then processed to extract the discontinuities in the rock mass surfaces. First, reference fracture orientation measurements were conducted manually using a geological compass, measuring seven planar and smooth discontinuity planes. Next, the orientation of the same fracture planes was measured digitally on the point cloud using the Compass plugin in CloudCompare software (Thiele et al. 2017). The mapping comparison against manual compass measurements showed a mean difference of 8.3 degrees for dip direction and 2.4 degrees for dip (Figure 4b).

The point cloud was then processed using a semi-automatic method in Discontinuity Extractor (DSE) software, which clusters the point cloud into discontinuity planes and extracts the mean orientation of discontinuity sets (Riquelme et al. 2014). Four discontinuity sets were identified, and their mean orientation was extracted (Figure 4a). The mapping comparison against manual compass measurements showed a mean difference of 10.4 degrees for dip direction and 3.6 degrees for dip. Thus, the orientation of discontinuity sets measured from the point cloud can be considered comparable to reality.

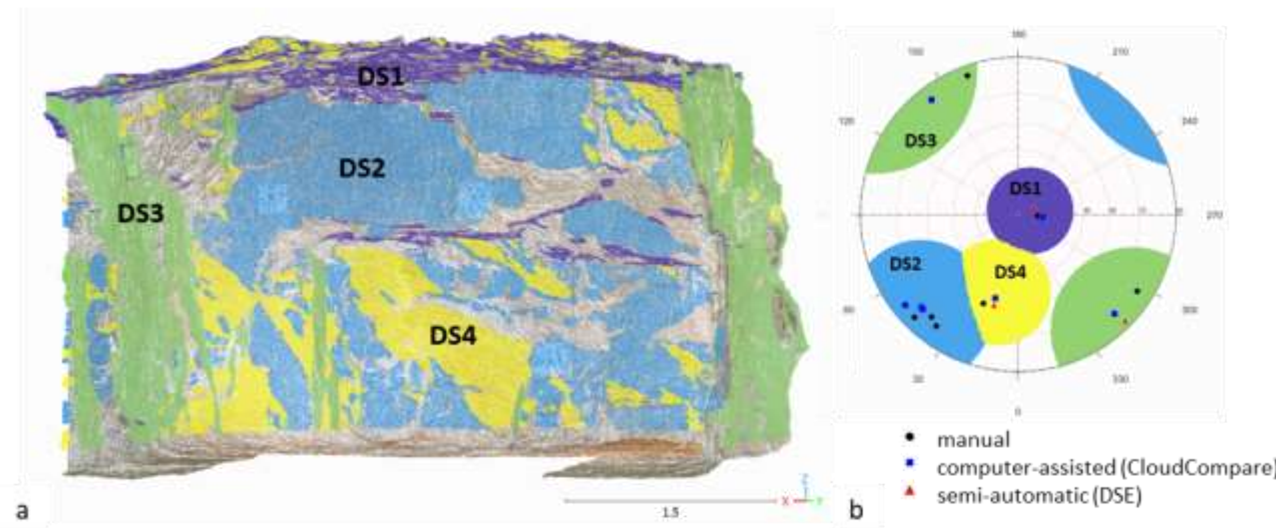

Figure 4. Discontinuity orientation results: visualization of the discontinuity sets extracted from the point cloud using the semi-automatic method in Discontinuity Set Extractor software (a), and comparison between the reference manual discontinuity measurements and digital measurements (b).

2.5. Discussion

The proposed multi-camera photogrammetric method for rock mass mapping in underground excavations demonstrates several advantages over traditional mapping methods. One of the primary benefits is the significant reduction in data capture time. In our case, the time to capture the entire drift was 172 seconds. This rapid acquisition enables efficient workflow, reducing the need for time-consuming manual inspections and minimizing safety risks to personnel. Another benefit of the proposed system is its low cost, with the total costs lower than a single high-resolution camera and lens combination.

In addition to its time and cost efficiency, the proposed method also yields accurate digital rock mass measurements. The reference distance measurements showed a mean error of 3.7 mm and a maximum error of 8.6 mm. The orientation of discontinuities measured from the 3D point cloud was comparable to reality, with a mean difference of 8.3 degrees for dip direction and 2.4 degrees for dip when using the Compass plugin in CloudCompare software. When utilizing the semi-automatic method in DSE, the mean difference for dip direction was 10.4 degrees, and for dip, it was 3.6 degrees. These results indicate that the accuracy of digital rock mass measurements obtained through the proposed method is within a reasonable range for engineering applications.

However, there are some limitations to the proposed method. Firstly, the proposed method requires a portable lighting setup to illuminate the tunnel surface. In consequence, setting up the lights reduces the acquisition speed. Such lighting is not necessary for scanning the tunnel face with a LiDAR, which can produce a grayscale point cloud in dark conditions. Secondly, there was no dust present at the test site, unlike active tunnels where construction activity generates fine dust particles that could interfere with photogrammetry. However, this problem would also affect laser scanning. Next, in operational tunnels or mines, photos may have to be taken from a larger distance due to safety precautions for working under unsupported roofs. This would reduce the point density, as pixels would represent a larger area on the tunnel surface. Finally, the point density of the resulting 3D model is lower compared to a model captured with a high-resolution camera. However, the resulting point cloud is still sufficient for accurate rock mass measurements and is significantly faster when comparing the time to capture the photos.

3. STOPE MAPPING WITH A UAV

Another rapid photogrammetry approach for underground excavations is to use an Unmanned Aerial Vehicle (UAV), which enables remote image capturing from a large area in a short amount of time. However, due to the confined space, low light conditions, and a lack of GPS signal underground, only special UAVs can perform photogrammetric missions successfully. This is especially difficult in underground spaces with restricted access, for example, open stopes, where mine personnel is prohibited from entering due to safety reasons. One example of a UAV that is capable of such missions in open stopes is Elios 2 from Flyability. The drone is equipped with a protective cage and a lighting system that enables photography of remote and hard-to-reach areas.

For the purpose of this study, an open dataset consisting of images taken inside a stope was downloaded from the drone manufacturer's website (Flyability, 2022). A stope in the Golden Sunlight Mine in Montana, USA, was scanned using the Elios 2 drone to explore the potential for stope photogrammetry in an active mine. The upper part of the stope with dimensions 10 × 30 × 100 m was scanned in 4 flights (~35 min total flight time) using the Elios 2 UAV. The drone was recording videos in 4K ultra high definition, which were then processed and 2105 frames with a size of 3840 × 2160 pixels were extracted. In this study, the dataset was reprocessed to test the remote rock mass mapping workflow to measure the orientation and spacing of discontinuities from a photogrammetric 3D model of an underground stope.

3.1. Data processing

The images were processed in Reality Capture photogrammetric software to reconstruct a 3D model of the stope. In total, 1755 images were aligned, and the processing times were as follows: alignment (14 min 08s), reconstruction (6 h 32 min), and texturing (3 min 42s), totaling 6 h 54 min. The resulting point cloud had 289.7 million points and a point density of 33.1 points per cm^2. However, to enable faster processing and ease of handling, the point cloud was cleaned and simplified to 11 million points with a point density of 1.6 pts/cm^2. In addition, a textured 3D mesh was also exported from the software for visualization (Figure 5).

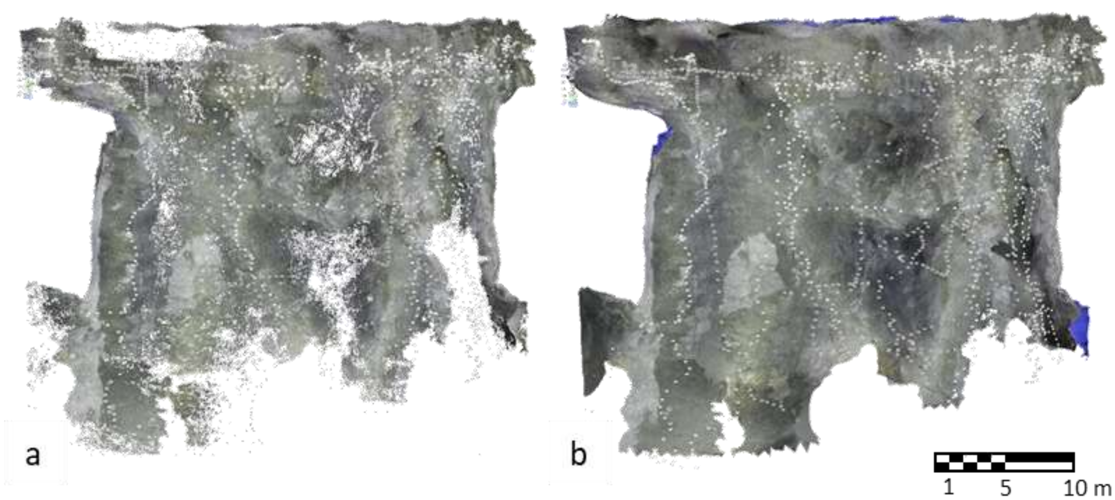

Figure 5. Stope 3D point cloud (left) and textured mesh (right).

3.2. Discontinuity mapping

Next, the goal was to identify the rock discontinuities inside the stope and measure their orientation using the semi-automatic method in the Discontinuity Set Extractor (DSE) software. The point cloud was further simplified to 1 million points. Four discontinuity sets were extracted and visualized on top of the stope 3D model, and their mean orientation was calculated (see Figure 6). Next, the spacing for each discontinuity set was calculated using the built-in function in the DSE software (Riquelme et al. 2015). The resulting histograms of spacing are presented in Figure 7.

The results confirmed the possibility of using drone photogrammetry for semi-automatic fracture mapping in stopes. The next step would be to filter out the data, compute the final measurements and visualize the 3D point cloud of the extracted discontinuities on top of the photorealistic 3D mesh, for example with the use of virtual reality as demonstrated in Janiszewski et al. 2020.

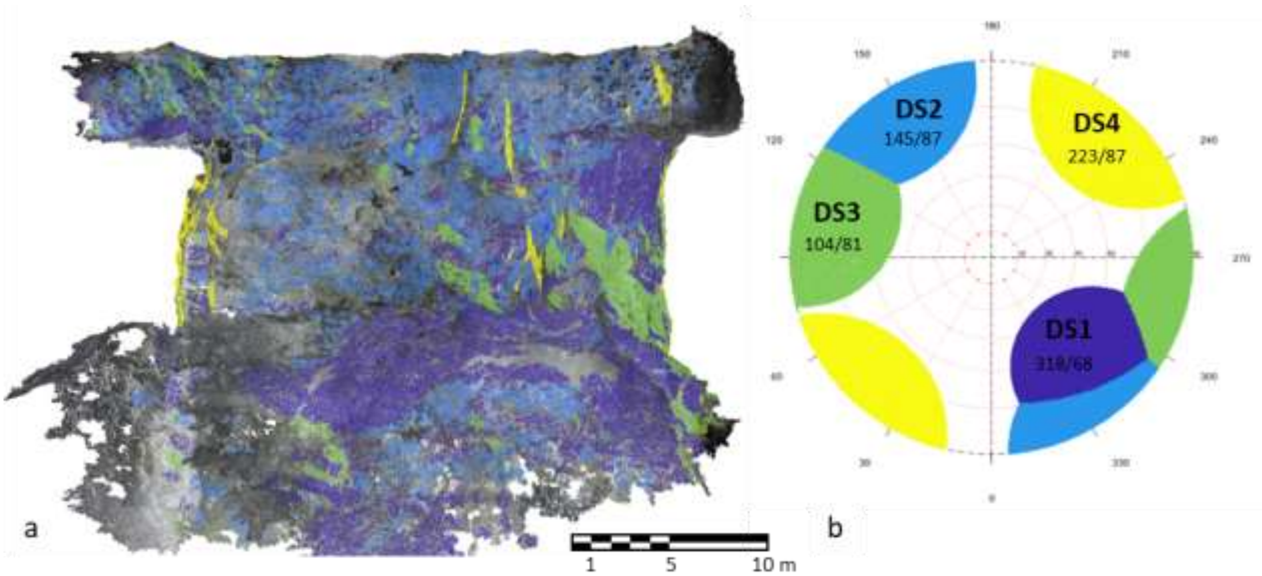

Figure 6. Discontinuity sets extracted from the stope 3D point cloud (left) and their mean orientation (right).

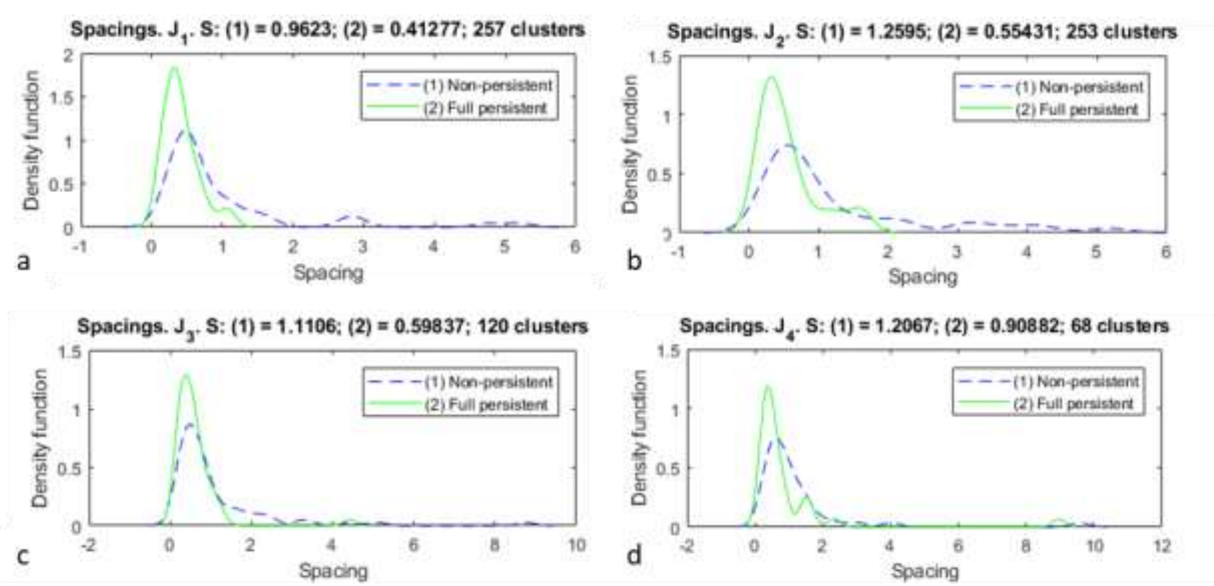

Figure 7. Normal spacing distributions of the four discontinuity sets extracted from the stope 3D model.

3.3. Discussion

The use of drone photogrammetry for stope mapping, as demonstrated in this study, offers several significant benefits for underground excavations. One primary advantage is the ability to remotely map rock mass features in open stopes, which was previously not possible due to access restrictions. This remote mapping capability not only reduces the time required for data acquisition but also opens up the possibility for automation, which can lead to further efficiency improvements. Furthermore, the use of a UAV for rock mass characterization reduces the risk of injury to personnel, as they do not need to enter potentially hazardous areas.

However, there are also limitations to this approach. The high cost of specialized UAVs, such as the Elios 2 drone used in this study, can be a barrier to widespread adoption. Additionally, the short battery life of drones poses a challenge, particularly for extensive underground excavations, as it may require multiple flights and battery changes to cover the entire area of interest.

Despite these limitations, there is significant future potential for UAV-based photogrammetry in underground excavations. The development of multi-camera UAV systems could increase acquisition speed and improve the quality of data, further enhancing the effectiveness of this method. Moreover, advancements in drone technology, including longer battery life and improved navigation capabilities, could further expand the applications of drone photogrammetry in underground excavations and other challenging environments. Ultimately, the combination of these advancements with the inherent benefits of remote mapping, automation potential, and reduced risk for injury positions UAV-based photogrammetry as a promising method for rock mass characterization in underground excavations.

4. CONCLUSIONS

The rapid photogrammetric method for rock mass characterization in underground excavations presented in this study offers an efficient, accurate, and remote alternative to conventional data acquisition techniques. This method not only reduces the time and costs associated with traditional mapping techniques but also provides reliable data for effective underground infrastructure design, maintenance, and safety assessments. Two case studies demonstrated the use of photogrammetry to rapidly acquire spatial data from the rock mass surfaces in underground tunnels and stopes. The photogrammetric 3D models allow for remote mapping of discontinuities to identify the number of joint sets and to measure their orientation and spacing for further analysis. By demonstrating this approach, we hope to enable more efficient and accurate mapping of underground excavations for rock mass characterization.

5. ACKNOWLEDGEMENTS

This research was funded by the Academy of Finland under grant no. 319798. The authors greatly appreciate the financial support.

REFERENCES

Flyability (2022). Photogrammetry dataset. https://info.flyability.com/photogrammetry-dataset (Accessed on 14 December 2022).

García-Luna, R., Senent, S., Jurado-Piña, R., Jimenez, R. (2019). Structure from Motion photogrammetry to characterize underground rock masses: Experiences from two real tunnels. *Tunnelling and Underground Space Technology 83* (2019) 262-273. https://doi.org/10.1016/j.tust.2018.09.026

Janiszewski, M., Uotinen, L., Baghbanan, A., Rinne, M. (2020). Digitisation of hard rock tunnel for remote fracture mapping and virtual training environment. in CC Li, H Ødegaard, AH Høien & J Macias (eds), *ISRM International Symposium - EUROCK 2020*, Trondheim, Norway, 14/06/2020.

Janiszewski, M., Torkan, M., Uotinen, L., Rinne, M., (2022). Rapid Photogrammetry with a 360-Degree Camera for Tunnel Mapping. *Remote Sensing* 14(21), 5494. https://doi.org/10.3390/rs14215494

Prittinen, M. (2021). Comparison of camera equipment for photogrammetric digitization of hard rock tunnel faces. Master’s thesis. Aalto University, Finland. http://urn.fi/URN:NBN:fi:aalto-202105236935

Riquelme, A.J., Abellán, A., Tomás, R., Jaboyedoff, M. (2014). A new approach for semi-automatic rock mass joints recognition from 3D point clouds. *Computers & Geosciences* 68, 38–52, https://doi.org/10.1016/j.cageo.2014.03.014

Riquelme, A.J., Abellán, A., Tomás, R. (2015) Discontinuity spacing analysis in rock masses using 3D point clouds. *Engineering Geology* 195, 185-195, https://doi.org/10.1016/j.enggeo.2015.06.009

Thiele, S.T., Grose, L., Samsu, A., Micketwaite, S., Vollgger, S.A., Cruden, A.R. (2017). Rapid, semi-automatic fracture and contact mapping for point clouds, images and geophysical data. *Solid Earth* 8, 1241–1253. https://doi.org/10.5194/se-8-1241-2017

Proceedings of the NROCK 2023
The IV Nordic Symposium on
Rock Mechanics and Rock Engineering
ISBN 978-9935-9436-2-0
DOI 10.33112/nrock2023.21

Geoscientific investigation for the site selection of high-level radiowaste disposal in South Korea

Dae-Sung Cheon(cds@kigam.re.kr)

Dae-Sung Cheon / primary author
Korea Institute of Geoscience and Mineral Resources, Daejeon, South Korea
Kwangmin Jin, You Hong Kihm, Won-Kyong Song, Jae-Yong Park
Korea Institute of Geoscience and Mineral Resources, Daejeon, South Korea

ABSTRACT

According to the 2nd master plan for high-level radioactive waste(HLW) announced by the South Korean government in 2021, the operation of the HLW disposal repository from site selection is planned to be carried out within 37 years. In particular, the site selection was decided within 13 years after the start of the project through a step-by-step process like other countries. Unlike Northern Europe such as Sweden and Finland, where crystalline rocks are the main composition, South Korea has various rock types similar to Switzerland. The Korea Institute of Geoscience and Mineral Resources published 8 types of geoenvironmental information maps, including rock types, lineament, faults, and geothermals etc., which can be used in the national screening stage. Geoscientific researches are being conducted for each rock type in consideration of the distribution area of rock types in the South Korea obtained from the geoenvironmental information map. Considering the depth of HLW disposal repository, drillings are performed at a depth of 750 m according to the rock types, and evaluation parameters for each research field used in basic and detailed investigations are obtained. Investigations using deep boreholes, which began in 2020, were conducted in granite, sedimentary rocks including mudstone and sandstone, and gneiss. Another investigation is planned for volcanic rocks next year. The evaluation parameters obtained during the geoscientific investigation include geological parameters such as lithology, joint and fault, hydraulic parameters such as hydraulic conductivity and storage coefficient, geochemical parameters such as hydrochemistry, sorption and nuclides, and geothermal parameters such as thermal conductivity and geothermal gradient. There are also mechanical parameters such as strength, and in-situ stress. These data are expected to be used as basic data for site selection for HLW disposal in Korea in the future.

KEYWORDS

high-level radiowaste(HLW); geoenvironmental information; site selection; evaluation parameter; rock type

1. INTRODUCTION

Since Kori nuclear power plant unit 1 started commercial operation in 1978, South Korea has operated a total of 25 nuclear power plants as of May 2017. As Kori unit 1 in June 2017 and Wolseong unit 1 in December 2019 entered the permanent shutdown phase, a total of 25 nuclear power plants are operating as of December 2022. Disposal of spent nuclear fuel generated from the operation of nuclear power plants is an important factor that must be considered indispensably in nuclear power generation, and a total of 504,809 bundles occurred by the third quarter of 2021. Considering the capacity of temporary storage facilities in power plants, discussions on interim storage or permanent disposal are inevitable as it is expected to be saturated sequentially starting with the Hanbit nuclear power plant in 2031.

According to the Korean government's second master plan for high-level radioactive waste (Figure.1), it aims to secure permanent disposal facilities within 37 years after the start of the site selection procedure, and to select sites for 13 years after establishing an investigation plan. Site selection for the deep geological disposal of high-level radioactive waste is considering a step-by-step approach worldwide, and South Korea also has a 3-step site selection procedure: exclusion of unsuitable areas, basic investigation, and detailed investigation, along with social consensus such as resident opinions and referendum for site.

This paper deals with the 8 types of geoenvironmental information maps that are expected to be used in the first stage of site selection and the geoscientific investigation according to the types of rocks required in the second and third stages.

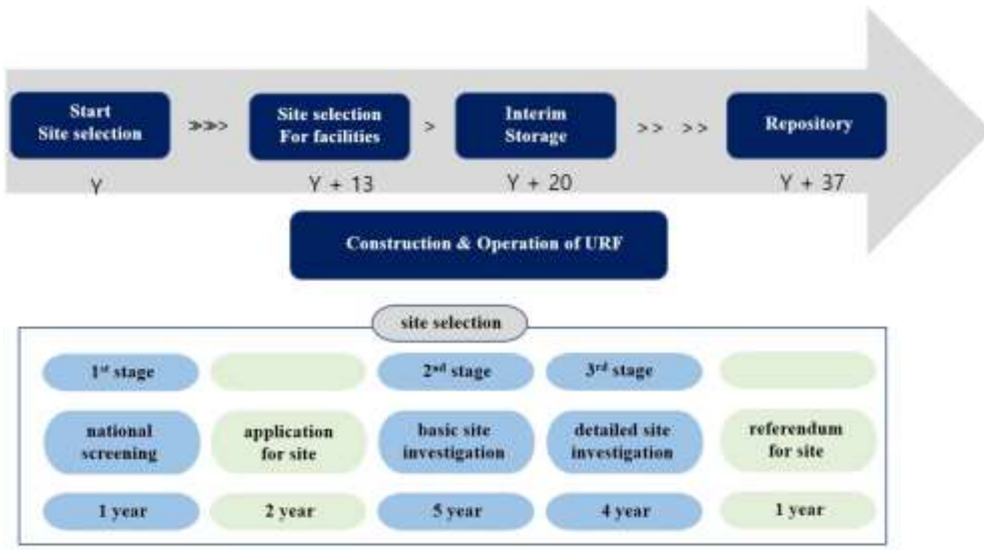

Figure 1. Site selection procedure in 2nd master plan for HLW management in South Korea.

2. NATIONWIDE GEOENVIRONMENTAL INFORMATION MAP

The Japanese government published a scientific feature map (Figure 2) in 2017 to promote public understanding the geological disposal of high-level radioactive waste. The “Scientific Features Map” is a rough view of what scientific characteristics need to be considered when determining geological disposal areas and how scientific characteristic values are distributed throughout Japan. Detailed maps can be checked on the NUMO(Nuclear Waste Management Organization of Japan) website, and individual geoenvironmental information maps were prepared for each criterion. These maps include volcanic activity, fault activity, uplift and erosion, geothermal activity, and mineral resources etc.

The Korea Institute of Geoscience and Mineral Resources(KIGAM), Korea's national research institute on geology and resources, comprehensively analyzed the items used by leading countries in high-level radioactive waste disposal projects when reviewing exclusion areas at the national level. Afterwards, considering the situation of Korea, geovironmental information maps were produced for all eight items, including rock types, mineral deposits, lineaments, faults, earthquakes, uplift, groundwater, and geothermal properties. Figure 3 presents an example of the geoenvironmental information map produced.

Since each rock type has different geological, thermal, and mechanical characteristics, the HLW disposal system is determined according to the rock type, and it is a very important item in site selection (Kim et al., 2020). Using the geological map(1:50K geological map, 1:250K geological map, 1:250K 1st integrated & harmonized geological map) published by the KIGAM, a 1:25K harmonized geological map(Figure 3 left) was produced through data integration and verification processes and investigation of boundary mismatched areas.

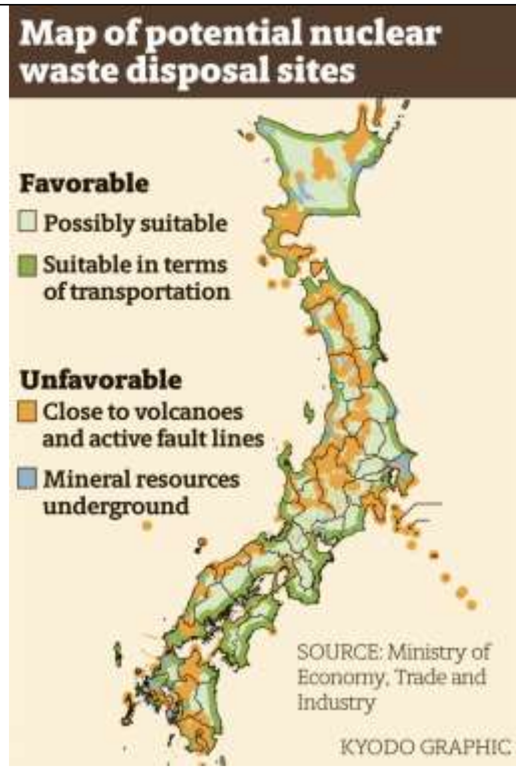

Figure 2. Nationwide map of 'Scientific features' relevant for geological disposal in Japan(www.numo.jp).

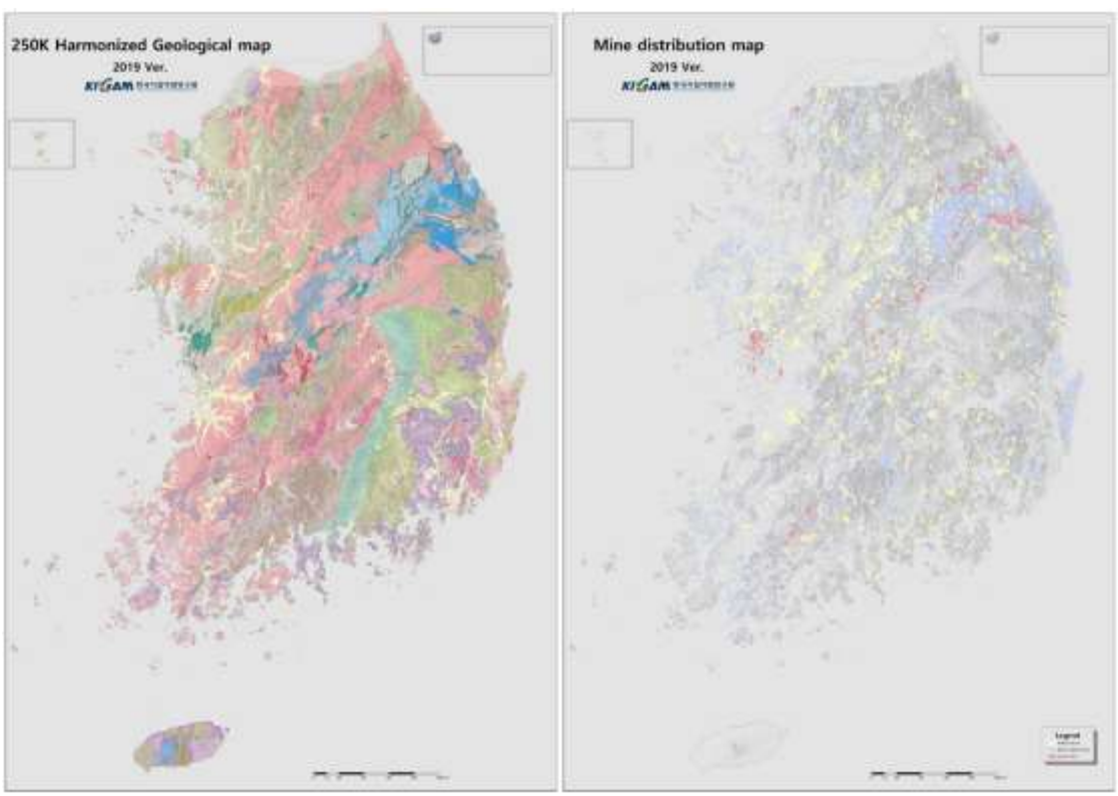

Figure 3. Examples of geoenvironmental information maps in South Korea(left: 250K harmonized geological map, right: mine distribution map, KIGAM 2019).

At least 100,000 years, the disposal period of high-level radioactive waste, is a very long time. The location of the previously developed mine is one of the important evaluation items because it is possible to search for useful deposits and excavate for mining in the high-level radioactive waste disposal facility in the future due to loss of information on the disposal site or other reasons. The mine distribution map(Figure 3 right) was produced through mutual verification using the data of Korea Mineral Resources Corporation, Korea Mine Reclamation Corporation, and KIGAM, which have mine information.

In the same way as above, the geoenvironmental information map for lineaments, faults, earthquake, uplift/subsidence, hydraulic conductivity, and geothermal was published in 2019.

When preparing the geoenvironmental information maps, a verification system (named GIVES) for the history and verification of data was produced together, and it was made accessible to the public through web services. Figures 4 presents an example of the overall flow of geoenvironmental information and verification system.

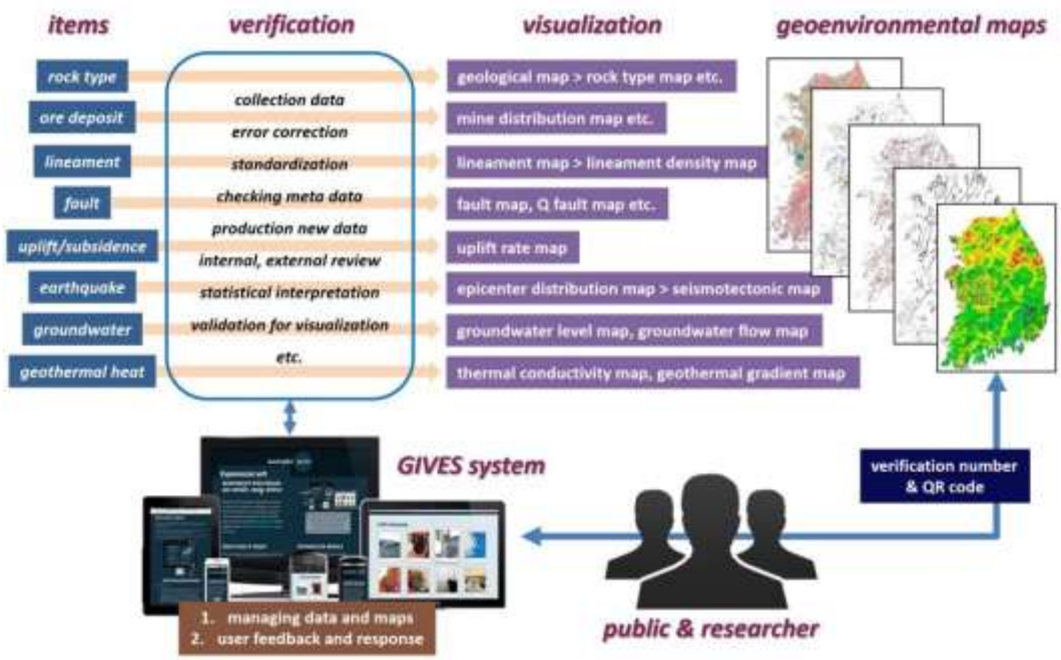

Figure 4. Overview of the nationwide geoenvironmental information maps and verification system (KIGAM, 2019).

3. GEOLOGICAL ENVRIONMENT OF SOUTH KOREA

For the safe geological disposal of high-level radioactive waste, it is very important to determine a disposal system suitable for the geological environment of South Korea. The most basic matter in determining the disposal system is the disposing host rock. This is because the disposal system is determined according to the disposing host rock type. Table 1 briefly presents the geological distribution of some countries and the disposing host rocks determined by them in the field of geological disposal of high-level radioactive waste.

Table 1. HLW disposing rock type and geological distribution in some countries.

	Determined disposing rock type	Major geological distribution
Finland	Crystalline rock	Crystalline rock
Sweden	Crystalline rock	Crystalline rock
Switzerland	Sedimentary rock	Crystalline rock/ Sedimentary rock
France	Sedimentary rock	Crystalline rock/ Sedimentary rock
South Korea	Not yet	Crystalline rock/ Sedimentary rock

Sweden and Finland used the KBS-3 system, which relies on multi-barriers for a crystalline rock as disposing host rock, while Switzerland determined a sedimentary rock as disposing host rock and developed a disposal system that relies on natural barriers. Unlike Sweden and Finland, the reason for the difference in the disposal system proposed by Switzerland and others is that it takes into account the local disposal environment, that is, geological characteristics. As can be seen from Figure 5, Sweden and Finland are mostly composed of crystalline rocks, while the geological distribution (Figure 6) in Switzerland is not only crystalline rocks, but also various types of rocks such as mudstone and sandstone.

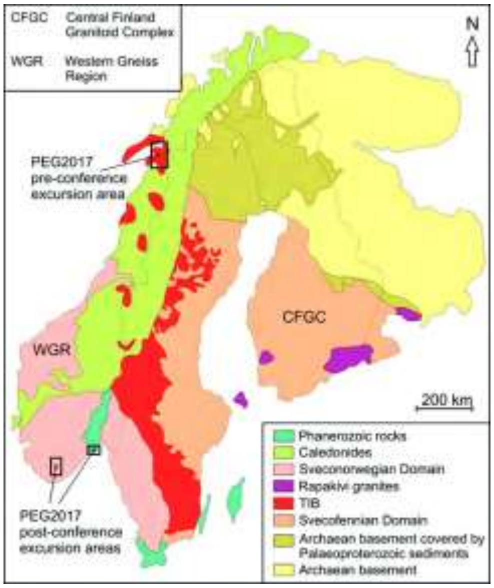

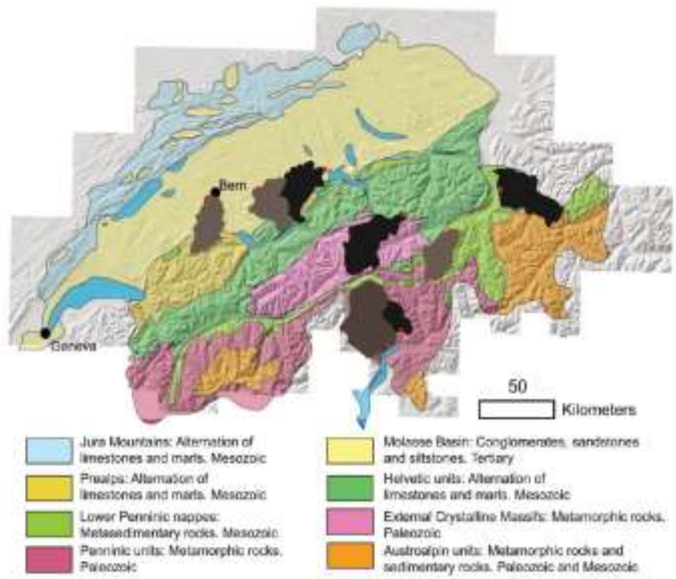

Figure 5. Generalized geological map of Scandinavia (Müller et al., 2017).

Figure 6. Simplified geological map of Switzerland (Litty and Schlunegger, 2017).

South Korea's geological environment is composed of complex geology such as those in Switzerland and France rather than Northern Europe, and no decision has been made on disposing host rock. Distributed rock types in South Korea are largely classified into the Precambrian metamorphic rock complex, Paleozoic sedimentary rocks, Mesozoic granite, and Cenozoic igneous rocks. Figure 7 presents the distribution area by rock type and era by classifying the rock types distributed in Korea based on the 250K harmonized geological information map published in 2019. Plutonic and metamorphic rocks occupy the largest area, each accounting for 30%, followed by sedimentary rocks, accounting for 25%.

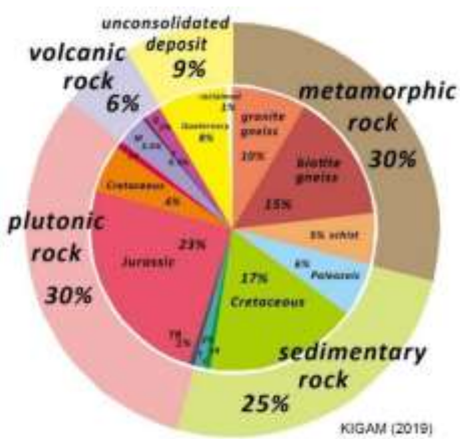

Figure 7. Rock distribution area in Korea by rock types and era(KIGAM, 2019).

The tectonic characteristics of the Korean Peninsula are located on the eastern edge of the Eurasian plate, and the tectonic structure is largely divided into the Gyeonggi massif, Yeongnam massif, Okcheon belt, and Gyeongsang basin (Kim et al., 2008; KIGAM, 2010; Cheong and Kim, 2012).

4. GEOSCIENTIFIC INVESTIGATION CONSIDERING TECTONIC STURCUTRE AND ROCK TYPE

Deep geological disposal facilities for high-level radioactive waste are generally assumed to be built at a depth of 300 to 500 m from the surface. Considering these target depths, at least 500 m deep drilling should be performed, and deep drilling at least 1 km corresponding to twice the disposal depth is recommended for modeling.

Deep drilling in South Korea is being carried out in various fields for the purposes of CCUS, geothermal energy, and seismic activity monitoring, in addition to the purpose of radioactive waste disposal. Depending on the purpose of drilling, there may be some differences in tests or methods performed during(or while) or after drilling, but there is no more certain way than drilling to identify the characteristics of deep rocks. Among them, only about 10 deep drilling drills were conducted for the purpose of disposing of high-level radioactive waste, mostly in crystalline rocks such as Goseong in Gangwon province, Yuseong in Daejeon city, and Andong city in Gyeongbuk province. As mentioned above, in order to determine the disposing host rock, it is essential to first understand the various rock types in Korea. This is because hydrological, geochemical, mechanical, and thermal characteristics, along with geological characteristics, appear differently depending on the type of rock.

Recently, KIGAM has been conducting more than two deep drilling every year since 2020 to investigate the characteristics of deep rock for the deep geological disposal of high-level radioactive waste. Table 2 summarizes the drilling status and plans for the deep geological disposal of high-level radioactive waste.

Table 2. Deep Drillings for HLW related purpose performed or planned according to tectonic structures and rock types(updated from Cheon et al., 2022).

	Gyeonggi massif	Okcheon belt	Yeongnam massif	Gyeongsang basin
Plutonic rock (Granite)	Chuncehon (1 hole) Goseong (2 holes) Goseong (planned)	Daejeon (7 holes) Wonju (1 hole)	NA	NA
Sedimentary rock (Mudstone)	NA	NA	NA	Daegu (1 hole) Jinju (1 hole) Changwon (1 hole)
Metamorphic rock (Gneiss)	Hongcheon(1 hole)	NA	Andong (2 holes) Taebaek (planned)	NA
Volcanic rock	NA	Mokpo (planned)		Tongyeong(planned)

In accordance with Kim et al. (2020), which suggested evaluation parameters for each step and field for site selection, major evaluation parameters that should be obtained first were selected and obtained through deep drilling in the selected area according to tectonic structure and rock type. In the field of geology, rock phase, fault, uplift rate, etc. are the key evaluation parameters. In the field of rock mechanics, uniaxial compressive strength, in-situ stress, joint distribution and rock mass classification are considered. In geochemistry, components, adsorption capacity, isotopes, etc. In the field of geophysical exploration, physical properties and discontinuities were selected, and in the field of geothermal thermal conductivity and geothermal gradient, etc. were selected. Figure 8 schematic presents the major evaluation parameters acquired by the different fields in the process of investigating the characteristics of deep bedrock.

Figure 8. Major evaluation parameters in the multidisciplinary fields for HLW geological disposal (KIGAM, 2021).

The drilling location was selected based on data such as geologic characteristics and era after identifying tectonic structure, distributed rock type, literature & surface geological survey, and lineament etc. The deep borehole investigation process is shown in Figure 9.

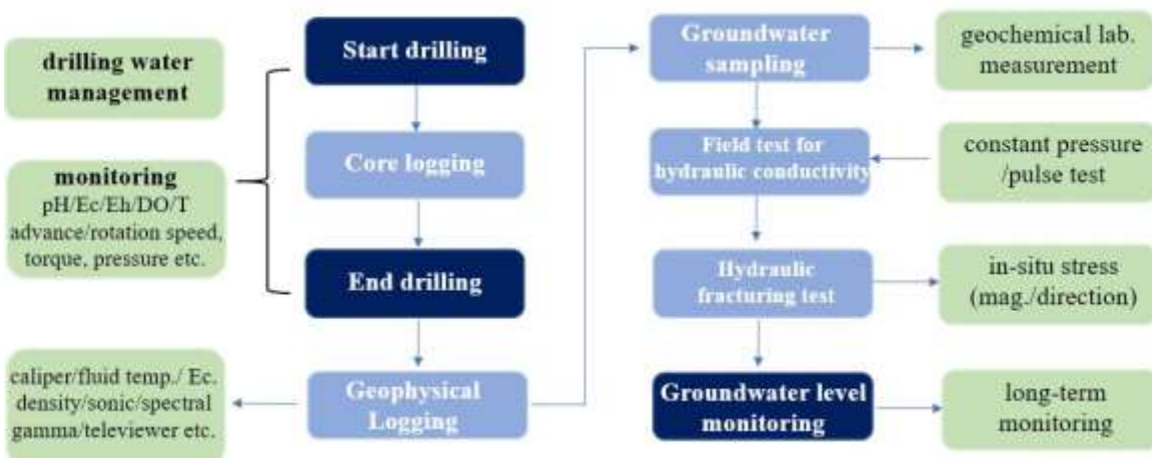

Figure 9. Deep borehole investigation and field tests process (Cheon et al., 2022).

While drilling, thrust and torque were monitored to understand the drilling conditions and mechanical characteristics according to the depth and bedrock, and the hydrogeological and geochemical effects were minimized by using a closed circulating water system. In addition, by dissolving a certain concentration of uranine in circulating water, the uranine concentration changes according to the depth, as well as hydrogen ion concentration (pH), electrical conductivity (Ec), dissolved oxygen concentration (DO), oxidation-reduction potential (Eh), temperature (T) etc. characteristics were monitored.

After drilling was completed, geophysical logging such as caliper logging, temperature-electrical conductivity logging, density logging, sonic logging, spectral gamma logging, acoustic televiewer etc. were performed to obtain rock properties according to the depth. Afterwards, geochemical analysis was performed using groundwater collected from boreholes to analyze geochemical characteristics in a specific section. In order to investigate hydraulic conductivity, hydraulic field tests using constant pressure test or pulse test were performed, and hydraulic fracturing tests were performed to determine the magnitude and direction of in-situ stress according to the depth.

Using the core recovered from the borehole, geochemical, geotechnical, mechanical, and hydrogeological characteristics were analyzed along with geological analysis such as drill log and structural geological characteristics including geological dating. For the intact rock, an analysis was performed for the thermal properties along with the mechanical properties.

This section introduces the case of a in-situ stress characteristic survey belonging to the field of rock mechanics among multidisciplinary investigations of deep bedrock. In-situ stress is also suggested as an important evaluation parameter necessary for site selection for the geological disposal of high-level radioactive waste in South Korea (Choi et al., 2017; Kim et al., 2020; Choi et al., 2020; Choi et al., 2021; Cheon et al., 2022). In-situ stress is estimated by hydraulic fracturing or overcoring methods, or by using fault or seismic mechanism.

According to the In-situ stress obtained with the depth at the disposal site in Finland or Sweden (Figure 9), even in the same area it was shown that magnitude and orientation of in-situ stress can change severely with the depth depending on the used method and geological structure.

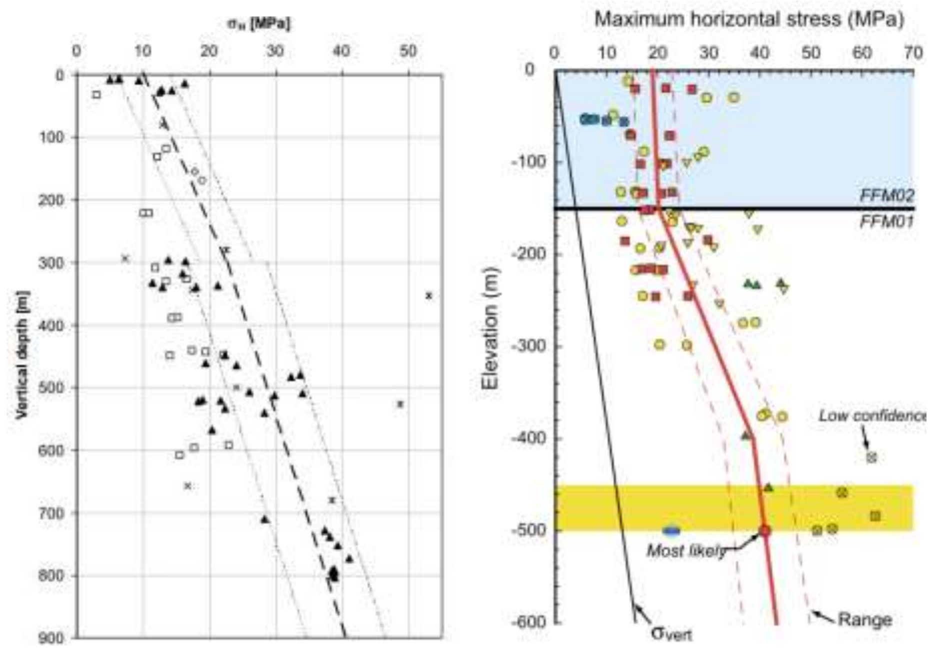

Figure 9. In-situ stress field model (left: Olkiluoto in Finland (Posiva, 2009), right: Forsmark in Sweden(SKB, 2007)).

The Korean stress map was published from field in-situ stress data conducted in Korea for the past 40 years (Kim et al. (2020)). The data used in the Korea stress map are obtained at a depth of less than 1 km underground. There are many data at a shallow depth above about 300 m, but relatively few at a depth below 300 m, which is considered a target depth for the geological disposal of high-level radioactive waste.

Considering that changes in in-situ stress may occur differently depending on the depth and that there is no experience in deep depth as an overcoring method in South Korea, the in-situ stresses were measured using a deep-depth hydraulic fracturing test system owned by KIGAM. The in-situ stresses were obtained by performing tests at more than 20 points for a 750 m test section using the HF (Hydraulic Fracturing) and HTPF (Hydraulic Testing of Pre-existing Fractures) methods. Figure 10 presents the magnitude of in-situ stress obtained in the Wonju area and Chuncheon area(rock type: granite) belonging to the tectonic structure of the Okcheon belt and Gyeonggi Massif, respectively. The trend of vertical stress, maximum horizontal stress, and minimum horizontal stress can be seen with depth, but as described above, it can be seen that the magnitude of the maximum horizontal stress may appear differently depending on some depth.

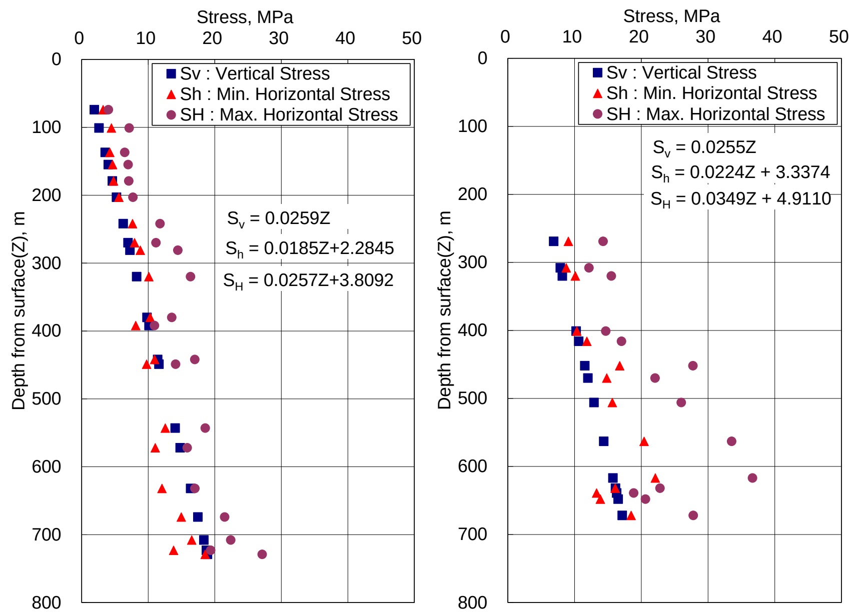

Figure 10. Magnitude and direction of in-situ stress in Wonju(left) and Chuncheon(right) area.

5. SUMMARY

The first step in deep geological disposal of high-level radioactive waste is the initiation of the site selection process. The site selection process begins with the establishment of a survey plan and the exclusion of unsuitable areas. For this purpose, geological data that can discriminate the exclusion and preference conditions on a nationwide scale must be the basis. Eight types of Korea's geoenvironmental information maps published by KIGAM in 2019 are expected to provide basic data for site selection like those of advanced countries.

This paper briefly introduced the 750 m deep drilling and related geoscientific investigations in order to obtain geoscientific evaluation parameters in relation to the deep geological disposal of high-level radioactive waste. The current deep drilling was selected in consideration of the South Korean policies and distribution of rock type, which had already been performed in 16 areas classified according to tectonic structure and type. In relation to the basic specifications for investigation research through deep drilling, drilling general, drilling circulation water management, measurement during drilling, and core management after drilling were presented. In addition, the contents and some results of multidisciplinary geoscientific investigations using deep boreholes were presented as examples. Multidisciplinary geoscientific investigations briefly introduced drill log reflecting geology and mechanical characteristics, geophysical logging to determine continuous physical characteristics, groundwater sampling to determine hydrochemical characteristics, constant pressure test to determine hydraulic conductivity, and in situ stress estimation. Evaluation parameters, that are considered important in site investigation or selection and must be obtained, are acquired and analyzed through the drilling process. It also is expected that analysis and research on specific methods and results for each field, as well as differences in characteristics according to rock type etc. can be utilized in site investigation, site selection, and generic URL construction for deep geological disposal of high-level radioactive waste in South Korea.

6. ACKNOWLEDGEMENTS

This research was financially supported by the Korea Institute of Energy Technology Evaluation and Planning(KETEP) grant funded by the Korea government Ministry of Trade, Industry and Energy (No. 20211710200010C), South Korea

REFERENCES

Cheon, D.S., Kihm, Y.H., Jin K., Song, W.K. and Choi, S., (2022). A study on nationwide maps with geoenvironmental information and geological characteristics of bedrock for HLW disposal, Journal of the Korean Society of Mineral and Enegry Resources Engineers, 59(3): 276-292.

Cheong, C., and Kim, N., (2012). Review of Radiometric Ages for Phanerozoic Granitoids in Southern Korean Peninsula, Journal of The Petrological Society of Korea, 21(2): 173-192.

Choi, J., Chae, B.-G., Kihm, Y.-H., Park, E.-S., Hyun, S., Kim, H.C., et al., (2017). Suggestion of site investigation method for HLW disposal facility, Journal of the Korean Society of Mineral and Energy Resources Engineers, 54(4): 303-318.

Choi, S., Kihm, Y.H., Kim, E., and Cheon, D.S., (2020). Rock Mechanical Aspects in Site Characterization for HLW Geological Disposal: Current Status and Case Studies, Tunnel & Underground Space, 30(2): 136-148.

Choi, S., Cheon, D.S., Jeong, H. and Jeon, S., (2021). Establishment of a basic DB of Korean intact rock properties applicable to site characterization for HLW geological disposal, Tunnel & Underground Space, 31(2), 83-97.

KIGAM, (2010). Construction of basic evaluation criteria for candidate HLW repository sites, NP2007-031-2010(1): KIGAM.

KIGAM, (2019). Development of nationwide geoenvironmental maps for HLW geological disposal, GP2017-009-2019: KIGAM.

KIGAM, (2021). Research on rock properties in deep environment for HLW geological disposal, GP2020-002-2021: KIGAM.

Kim, E., Kihm, Y.H., Cheon, D.S., Hyun, S.P., Jeon, J.S., Kim, H.C., et al., (2020). Development of Geoscientific Site Assessment Factors for the Deep Geological Disposal of HLW in South Korea, Journal of The Korean Society of Mineral and Energy Resources Engineers, 57(2): 215-233.

Kim, S.W., Lee, C. and Ryu, I.C., (2008). Geochemical and Nd-Sr Isotope Studies for Foliated Granitoids and Mylonitized Gneisses from the Myeongho Area in Northeast Yecheon Shear Zone, Econ. Environ. Geol., 41(3): 299-314.

Müller, A., Husdal, T., Sunde, Ø., Friis, H., Andersen, T., Johansen, T., et al., (2017) Geological guides (2017-6 Ed.), Trondheim: Norsk Geologisk Forening.

Posiva, (2009). Olkiluoto Site Description 2008, Part 1, Report 2009-1: Posiva Oy.

Litty, C. and Schlunegger, F., (2017). Geolgogical note: controls on pebbles' size and shape in streams of the Swiss Alps, J. Geol., 125(1): 101-112.

SKB, (2007). Quantifying in situ stress magnitudes and orientations for Forsmark; Forsmark stage 2.2, R-07-26: SKB.